Dense Core Survey toward Nearby Massive Star and Cluster Forming Giant Molecular Clouds: Origin of the Initial Mass Function

Norio Ikeda
Department of Astronomical Science
School of Physical Sciences
The Graduate University for Advanced Studies

2007

Acknowledgements

First of all, I would like to thank my supervisor, Yoshimi Kitamura, for his valuable suggestion on this work. I thank my practical supervisor, Kazuyoshi Sunada. Without his instructive advice, I would hardly have finished this thesis. I am very grateful to Sachiko Okumura, my formal supervisor. I also acknowledge the collaborators, Tsuyoshi Sawada, Satoshi Hongo, Takeshi Sakai, Takeshi Nakazato, Atsushi Miyazaki, Akiko Kawamura, and Tomofumi Umemoto. I thank Tomoki Saito for providing his $H^{12}CO^{+}(J = 1 - 0)$ data, and Yasutaka Kurono for his suggestive comments about the GCF. And, I would like to thank all of the members of Nobeyama Radio Observatory. Finally, I wish to thank my family for their support in both mental and financial ways.

Abstract

We have carried out $H^{13}CO^+(J = 1 - 0)$ core unbiased surveys in the nearby massive star- and cluster-forming giant molecular clouds Orion A, Orion B, and Cepheus OB3. Our observations were carried out using the Nobeyama 45 m radio telescope with the 25-BEam Array Receiver System (BEARS). Our surveys are very unique in that large areas (1.4 - 1.5 square degrees) of the clouds were covered with very high spatial resolutions of 20 - 27″, enough to resolve dense cores, and with deep integration ($1\sigma \sim 0.1$ K in T_A^*), resulting in the sensitive mass detection of 1.6 - 3.5 $M_\odot$ for dense cores in the clouds. These observational advantages allow us to derive reliable core mass functions (CMFs) with a good statistics of sample number $\sim$ 30 - 240 and a wide-mass range of $2 \leq M/M_\odot \leq 100$.

The morphology of the $H^{13}CO^+(J = 1 - 0)$ emission in the Orion A and B is very similar to that of the dust continuum emission. In addition, our observations of the Cepheus cloud is the first unbiased one of the dense gas with such a high spatial resolution. We identified 236, 98, and 31 dense cores from our data with the clumpfind algorithm in the Orion A, B, and Cepheus OB3, respectively. All the cores seem to be almost in virial equilibrium independently of whether the cores are thermal or turbulent. Furthermore, the majority of the cores in the three clouds has very similar distributions of the physical parameters. This suggests that the most of the cores are the common ones, while there are a few peculiar cores whose velocity widths and radii are larger than 1 km s^{-1} and 0.14 pc, respectively. We derived the

$H^{13}CO^+$ CMFs of the clouds and found that these are consistent with those by previous studies in the sense of their power-law indices in the high-mass part of -2.1 - -2.4 and the existence of turnovers near 5 - $10M_\odot$.

We showed that the dust CMF can be produced from the $H^{13}CO^+$ CMF assuming that the dust cores correspond to the inner denser ($> 10^6$ cm^{-3}) structures of the $H^{13}CO^+$ ones and the core density profile which is proportional to R^{-2}. Furthermore we predicted IMFs from the $H^{13}CO^+$ CMFs in the three clouds assuming that all the cores form stars simultaneously and the star formation efficiency is uniform over the cores. We also considered binary formations assuming that the core multiplicity is uniform over the cores. We found that the high-mass part power-law slope of the predicted IMFs agree well with that of the Orion Nebula Cluster IMF and of the Galactic-field averaged IMF for a star formation efficiency of $\sim$ 25 - 50 %. These findings suggest that the IMF is determined at the time of the $H^{13}CO^+$ core (the density of $\sim 10^{4-5}$cm^{-3} or less) formation, rather than that of the dust cores of $>10^6$cm^{-3}.

On the other hand, the predicted IMFs seem to have less number of stars considerably in the low-mass part below $2M_\odot$, resulted from the turnover of the CMFs. As one of the possible causes of the CMF turnover, we modeled confusion along the line of sight, mainly due to the shadowing of low-mass cores caused by massive cores. The shadowing-corrected predicted IMFs agree well with the IMFs. We found that the shadowing-corrected CMFs do not have turnovers, suggesting that the apparent turnovers in the observed CMFs may not correspond to those of the IMFs. On the other hand, their power-law indices of the shadowing-corrected CMFs are very similar to each other although the three clouds have apparent difference in star-forming activities. This implies a common core formation processes that is insensitive to environmental parameters, leading to the origin of the universality of the IMF.

We discovered four cores with large velocity widths, significantly wider

than those of the other cores, only toward the M42 H II region and the Cep-A compact H II region. The finding of the large-velocity width cores suggests that the energy input from the H II regions increases the velocity width. Since the large-velocity width cores can produce the most massive stars owing to their large mass accretion rates, the massive star formations in the Orion A and Cepheus OB3 clouds are likely to be caused by the environmental stellar activities. This may imply that the IMF have additional turnover at the high-mass end, although the statistical uncertainties of the observed IMF are too large to recognize the turnover. In the Orion B, on the other hand, there is no core with large velocity width significantly. One of the explanations is that stellar activities in the Orion B cloud, in which the most earliest star is O8, are less energetic than those of O6 and O7 in the Orion A and Cepheus, respectively. This may indicate that stellar energy sources earlier than O7 - O6 are required to influence the most massive stars of the next generation.

We conclude that the IMF originates from the CMF. It implies that investigating the CMF formation processes is equivalent to revealing the origin of the IMF. We tested the proposed core formation prosesses such as gravitational fragmentation, collision and coalescence, accretion, and turbulent fragmentation based on our core catalog. We conclude that the turbulent fragmentation is the most plausible one of them.

Contents

Chapter 1

Introduction

1.1 Motivation of the Present Study

Stars are the fundamental constituents of the universe, and hence understanding the star formation process is one of the most important issues in astronomy. Since the evolution of stars is characterized by their masses, we should know how the stellar mass is determined, or the origin of the stellar initial mass fucntion (IMF), which we focus in this study, to reveal the star formation processes. Since well-established evolution theory of stars cannot predict the IMF, the origin of the IMF must be revealed by the observational study. In the following we summarize the observed characteristics of the IMF and the relation between star-formation activities and them.

1.1.1 Observed Features of the IMF

The IMF has several remarkable features each of which is thought to be closely linked to the physical processes of the star formation. One of the most apparent features is it's power-law like shape in the high-mass ($> 1M_{\odot}$) side, and many authors have derived power-law relations, as indicated in Figure 1.1, taken from Miller & Scalo (1979). The pioneering work was done by

Salpeter (1955). He derived the IMF of the field stars in the solar vicinity and found that the IMF has a power-law form of $dN/dM \propto M^{-2.35}$ for 1 - 10 $M_\odot$. Miller & Scalo (1979) also derived a similar form with a power-law index of -2.7 for 1 - 10 $M_\odot$. Recent development in infrared astronomy allows us to observe embedded young clusters with an enough sensitivity, preferred to derive the IMF (Zinnecker et al., 1993): Muench et al. (2002) derived the IMF through the modeling of the K band luminosity function of the Trapezium cluster. Their IMF has an index of -2.1 above $0.6M_\odot$, which is consistent with the IMF by Salpeter (1955). As described above, the power-law indices of the IMF derived by many authors seem to fall in the narrow range from -2.1 to -2.7. In other words, the shape of the IMF seems to have an universality (e.g., Kroupa, 2001). Although the origin of the power-law index of ~ -2.3 have not been revealed yet, the power-law nature of the IMF in the high-mass side is very important for the evolution of galaxies and interstellar medium because the relation determines the number of high-mass stars, which cause a great deal of influence through kinetic feedback, i.e., energetic outflows, expanding H II regions, mass loss of the supergiant phase, and finally supernova explosions. High-mass stars also provide heavy elements at the center of them and through supernovae, determining the metalicity which can change the physics of the interstellar medium and is possibly related to the origin of planet and even life.

The power-law form of the IMF continues toward the low-mass side. At slightly less than 1 $M_\odot$ the IMF has a turnover and becomes flat below the turnover, i.e., the IMF has a characteristic mass, also seen in Figure 1.1. The variation of the power-law index as a function of stellar mass is indicated in Figure 1.2, taken from Kroupa (2001). Easily recognized in the figure, there is a apparent change of the power-law index in 0.5 - 1 $M_\odot$. More recent and detailed observations also show the same tendency. Muench et al. (2002) found that the slope of their Trapezium IMF becomes flat below $0.6M_\odot$, i.e., the IMF has a turnover at $0.6M_\odot$. The existence of the turnover means that

the stellar population is dominated by the stars of the characteristic mass of $\sim 1\ M_{\odot}$. Therefore, to understand the origin of the IMF we should also reveal this fundamental feature.

In contrast to these apparent features, the shape of the IMF at the low-mass and high-mass end is still under debate (Reid et al., 2002; Muench et al., 2002; Massey et al., 1995) because at the low-mass end a limited sensitivity and spatial resolution prevent one from counting low-mass stars without a considerable incompleteness, and at the high-mass end the statistical uncertainty of the observed IMF is too large to measure it's true form. However, the shape of the low-mass end determines the total number and mass of forming stars, i.e. related to the star formation efficiency (SFE) of cluster and the fraction of brown dwarfs. Furthermore, the processes to form the high-mass end of the IMF is very important because even if only one star having such a high mass is formed, surrounding molecular cloud and possibly the star formation within the cloud would be greatly influenced (e.g., Elmegreen & Lada, 1977; Motoyama & Yoshida, 2003). In other words, this may be connected to one of the difference of star-formation activities, the mass of the most massive stars (Dobashi et al., 2001). In the Orion A GMC the most massive stars to be formed is θ_1C, one of the trapezium stars, whose spectral type is O6 (Hillenbrand, 1997, and references therein). On the other hand that in the ρ Ophiuch cloud is a B0 star and in the Taurus region we only know low-mass (spectral types of G or later) star formations.

Another important feature is that the formation of the IMF seems to finish at the early stage of star formation. Lada et al. (1993) carried out an K band survey in NGC2264 embedded cluster and found that a large fraction (50±20 %) of the cluster members show infrared excess, i.e., most of the members are young stellar objects (YSOs). They showed that the K band luminosity function (KLF) of NGC2264 have a good agreement with a synthesis KLF with a underlying Miller & Scalo like IMF, implying that at the YSO phase, at least, the IMF have already been formed. More so-

phisticated method to derive a synthesis KLF from an underlying IMF was developed by Zinnecker et al. (1993); Muench et al. (2000). According to this method, the KLFs of many other galactic embedded clusters such as IC348 (Muench et al., 2003), NGC2362 (Lada & Lada, 1995), and Trapezium (Muench et al., 2002) were compared with the synthesis ones, and the KLFs of the three embedded cluster are likely to be reproduced from a very silimar underlying IMF adopting the plausible ages of the clusters, i.e., the universality of the IMF has emerged before the YSO phase (Lada & Lada, 2003). This encourages us to investigate molecular cloud core, more earlier stage of star formation.

1.2 Previous Surveys of Molecular Cloud Cores

One of the promising ways to answer the above issues is investigating the properties of molecular cloud cores, because the molecular cloud cores are the birthplaces of stars (Beichman et al., 1986). Therefore molecular cloud core mass function (hereafter we abbreviate this term to "CMF") is thought to be a key to revealing the physical meaning of the IMF. It is also natural to consider that the core properties are closely related to the charactaristics of stars to be formed.

Many authors have observed the molecular cloud cores with various spatial resolutions. Since the cores are compact ($\sim$ 0.1 pc) and dense ($\sim 10^{4-5}$ cm^{-3}), millimeter/submillimeter continuum emission or molecular lines that have relatively high critical density are often used to observe the molecular cloud cores. As for the continuum emission, large-field imaging observations of star forming regions such as Serpens (Testi & Sargent, 1998, 450 μm) , ρ Ophiuchi (Motte et al., 1998; Johnstone et al., 2000, 850 μm) and Orion B (Johnstone et al., 2001, 450 μm) were carried out. They identified 26 - 75 dust cores in each region. The continuum studies show that the compact ($\sim$ 0.01 pc) dust cores are probably protostellar condensations. As shown

in Figure 1.3 for example, the dust CMFs show power-law relations with power-law indices which are very similar to that of the stellar IMF (Testi & Sargent, 1998; Motte et al., 1998). This suggests that the IMF is determined by the core formation processes. For the latter, CS (e.g. Tatematsu et al., 1993), NH_3 (e.g. Barranco & Goodman, 1998), $H^{13}CO^+$ (e.g. Onishi et al., 2002), and N_2H^+ (e.g. Caselli et al., 2002) are often used. The $H^{13}CO^+$ CMF derived by Onishi et al. (2002) have a power-law index of -2.5, which is also similar to that of the IMF, suggesting that not only the submillimeter continuum emission but also the high-critical-density molecular lines can trace the protostellar cores (see Figure 1.3).

However, the previous studies have the following problems. (1) The surveys are limited to low- and intermediate-mass star forming regions except the studies by Tatematsu et al. (1993) and Johnstone et al. (2001). Since the majority of stars form in cluster forming regions in GMCs (Lada & Lada, 2003), dense core surveys in GMCs should be needed to reveal the formation of the most of stars. (2) The identifications of the cores and derivation of the physical parameters of them are different with each other. This prevents us from comparing the results between the studies directly and uniformly. (3) Some studies did not have spatial resolutions enough to resolve 0.1 pc-scale dense cores, other ones did not cover areas large enough to derive unbiased CMFs. (4) The continuum observations lack velocity information in spite of their high sensitivity. This may also cause a miss-identification of overlapped cores along the line of sight. To overcome this situation, systematic dense core surveys with a enough spatial resolution in cluster-forming GMCs are needed.

1.3 Strategy of This Thesis

The aim of this thesis is investigating the origin and meanings of the IMF features, such as the power-law slope in the high-mass side and the turnover

near $1M_{\odot}$, on the basis of the comparison between the IMF and CMF. The advantages of this study against the previous studies is deriving statistically-reliable CMFs in a few star-forming regions having various star-forming activities. To compare the physical parameters and CMFs uniformly over the regions, it is important to apply an uniform analysis to every regions. In other words, we would create fair and unbiased dense core catalogs in every regions. We employed the clumpfind algorithm (Williams et al., 1994), which is one of the automated analysis methods and is the most widely used. Such a systematic analysis allows us to estimate the core parameters uniformly and hence helps us to find out the region-to-region difference of the core paramters and CMFs if it exists.

The targets in which we would derive the CMFs are selected from the massive star- and cluster-forming GMCs, because the majority of stars are formed in clusters, often associated with massive-star formation (Lada & Lada, 2003). To derive CMFs with a good statistics, we should observe a large area enough to survey the whole cores in the GMCs. Observations also should be done unbiasly because, for example, observations only toward the active center of star-forming regions would detect more massive cores unfairly and would bring us a CMF flatter than as it is, on the analogy of the mass segregation in stellar clusters (e.g., Hillenbrand & Carpenter, 2000; Muench et al., 2002) which affects the shape of the IMF. This requires a great ability to carry out mapping observations, and one of the facilities to be able to execute our observations is the combination of the Nobeyama 45 m radio telescope and the 25-BEam Array Receiver System (BEARS) equipped on the telescope.

We observe dense molecular cloud cores, which have typical sizes of $\sim$ 0.1 pc and typical masses of several $M_{\odot}$. To trace the cores of dense gas $\sim 10^{4-5}$ cm^{-3}, we used the $H^{13}CO^{+}(J = 1 - 0)$ molecular emission line at the rest frequency of 86.75433 GHz, which is preferable for a molecular cloud core survey. The higher critical density (8×10^{4}cm^{-3}) and relatively

strong intensity of the line allow us to easily observe dense gas in a large area. This requires the distance to the target GMCs should not be farther than 1 kpc, because the angular resolution of the telescope at 87 GHz is 18″. We selected three nearby cluster-forming GMCs, the Orion A, Orion B, and Cepheus OB3 cloud. The Orion A and B GMCs are known to the most nearest GMCs and the most nearest ongoing massive-star-forming regions from the solar system $\sim$ 480 pc (Genzel et al., 1981; Wilson et al., 2005). The Cepheus OB3 GMC is one of the second nearest massive-star-forming GMCs $\sim$ 730 pc (Garmany, 1973), next to the Orion GMC complex. At their distances the linear resolutions are 0.06 - 0.09 pc (see Section 2.4), enough to resolve the dense cores in the clouds.

Following the above, our study has the following three advantages in contrast to the previous studies. (1) $H^{13}CO^{+}(J = 1 - 0)$ as an appropriate line for dense core surveys. A part of the advantage of using $H^{13}CO^{+}(J = 1 - 0)$ is described above. In addition, since the line is expected to be optically thin (see Section 3.4), we can estimate the mass of cores accurately. The molecular depletion is not a serious problem in our core survey because our resolution ($\sim$ 10000 AU) is larger than the scale in which the depletion is usually significant ($<$ 7000 AU) and because the high temperature of $\sim$ 16 - 20 K in the three clouds (see Section 3.5) prevents molecules from being depleted onto dust grains (Di Francesco et al., 2006). Furthermore, we can get the velocity information of the dense gas simultaneously. The velocity information allows us to separate overlapped cores more reliably and to know the internal motions of cores. (2) We observed a large area of 1.4 - 1.5 square degrees with a high spatial resolution of 23 - 27″. Furthermore, our sensitivity of mass is down to 1.6 $M_{\odot}$ in the Orion clouds and 3.5 $M_{\odot}$ in the Cepheus cloud as described in Section 4.1. For the three clouds, such a wide area, high spatial resolution, and high sensitivity have never been simultaneously realized in the previous studies. This point is very important to reveal the difference among the core properties in various regions and to derive the CMF

accurately, as mentioned above. (3) The unbiased dense core surveys were carried out in massive star- and cluster-forming GMCs Orion A, Orion B, and Cepheus OB3 clouds systematically. It is important that star formation activities in the three GMCs are different from each other as we will see in the next section.

1.4 Surveyed GMCs

In this section we review the star formation activities and the previous studies of the surveyed GMCs, the Orion A, Orion B, and Cepheus OB3 clouds.

1.4.1 Orion A Cloud

The Orion A cloud, 480 pc from the solar system (Genzel et al., 1981), has the following characteristics in star formation activity: low-mass star formation occurs all over the cloud, known as the aggregates and the distributed population (Strom et al., 1993; Stanke et al., 2002), while massive stars actively form in cluster at the northern part of the cloud ($Dec.(1950) > -5°40'$). Particularly, the Orion Nebula Cluster (ONC), one of the active cluster forming regions, is associated with the OMC-1/2 region in $Dec. \sim -5°10'$ - $-5°40'$. The IMF of the ONC is derived by Hillenbrand (1997) with a very wide mass range of $0.05 - 50 M_{\odot}$. The IMF has a power-law relation with a index of -1.9 for $0.3 - 50 M_{\odot}$, and becomes flat below $0.3 M_{\odot}$: a turn over at 0.3 $M_{\odot}$. In addition to the ONC, in the OMC-2/3 region, there are more than 10 intermediate-mass protostar candidates (Chini et al., 1997; Lis et al., 1998; Tsujimoto et al., 2003; Nielbock et al., 2003). On the other hand, in the southern part ($Dec.(1950) < -5°40'$), massive star formation is not known although there are a few of the aggregates of low-mass stars (Strom et al., 1993).

There seem to exist several stellar activities which significantly influence the star formation in the cloud. The bright M 42 H II region faces the most

massive OMC-1 cloud at *Dec.* $\sim -5°20'$ to $-5°30'$ (Kutner & Thaddeus, 1971; Felli et al., 1993). In addition, the Orion OB associations 1a and b (Blaauw, 1991) are located to the 3° north of the cloud (See Figure 1.4). These objects are expected to cause higher external pressure and energy input to the molecular cloud. In fact, this configuration of the OMC-1 cloud, M42 H II region, and Orion OB association exhibits a representative pattern of sequential star formation (Elmegreen & Lada, 1977; Blaauw, 1991). Consequently, the Orion A cloud has region-to-region variations in both the activity and environment of star formation, and thus we can investigate how the core properties depend on the local nature of the cloud.

Many molecular gas studies of the Orion A cloud have been done. The observations with low-density tracers such as ^{12}CO (J = 1 - 0, Bally et al., 1987) and ^{13}CO (J = 1 - 0, Nagahama et al., 1998) showed that the GMC is elongated along the galactic plane and has a very large extent of $3°.5 \times 2°$, while a dense region with $\geq 10^4$ cm^{-3} is limited to the northern part ($> -6°.5$). Then we refer to the dense region as the Orion A cloud in the following. The most remarkable filamentary structure in the Orion A, called as the "Integral Shaped Filament (ISF)" (Bally et al., 1987), is associated with the M42 H II region. The ISF including OMC-1, 2, and 3 has been observed with high-density tracers such as CS(J = 1 - 0) ($\sim 10^4$ cm^{-3}, Tatematsu et al., 1993), NH_3 ($\sim 10^4$ cm^{-3}, Cesaroni & Wilson, 1994) and H^{13}CO$^+$(J = 1 - 0) ($\sim 10^5$ cm^{-3}, Aso et al., 2000). Dust-continuum observations of the ISF have been also made: the whole ISF was mapped by Johnstone & Bally (1999, 850μm) and the OMC-2/3 region by Chini et al. (1997, 1.3 mm) and Lis et al. (1998, 350 μm).

1.4.2 Orion B Cloud

The star formation in the Orion B cloud, at the distance of 470 pc (Wilson et al., 2005), is more cluster-fashioned than that in the Orion A cloud. Almost all (96 %) of the young stellar objects (YSOs) associated with the cloud

belong to four major star-forming regions named NGC 2023, NGC 2024, NGC 2068, and NGC 2071 (Lada et al., 1991b) (See Figure 1.4). The most active cluster-forming region in the Orion B is NGC 2024. The NGC 2024 region is one of the typical massive star forming regions. associated with the flame nebula, an optical H II region ionized by an O8 - B2 star (Bik et al., 2003). The associated cluster has 309 members and the total stellar mass is $180 M_{\odot}$ (Lada & Lada, 2003), whose paramters are moderate among the galactic young cluster. However, the stellar number density is 4000 pc^{-3} (Lada et al., 1991b), as dense as the ONC. On the other hand, the clusters associated with the other regions are thought to be the intermediate-mass star forming ones: the NGC 2068 and NGC 2071 clusters, associated with reflection nebulae, have 192 and 105 YSOs, respectively. The total masses of them are $110 M_{\odot}$ and $60 M_{\odot}$ respectively. The stellar number densities are 440 pc^{-3} and 472 pc^{-3} respectively, one order of magnitude smaller than that of the NGC 2024 cluster. The remaining NGC 2023 is the smallest cluster in the Orion B: the number of YSOs in the cluster is 21, while the stellar number density is 945 pc^{-3}, twice larger than those of the NGC 2068 and NGC 2071 clusters. In short, in the Orion B GMC both of massive and intermediate-mass stars are formed in clusters, but the massive star-forming cluster is only seen in the NGC2024 region while the other clusters are intermediate-mass ones.

There are many studies of molecular gas in the Orion B cloud. The whole image of the cloud was taken with lower-density tracers of ^{12}CO (Maddalena et al., 1986) and ^{13}CO (Bally et al., 1991). The image shows that the cloud can be divided into the northern and southern parts. The northern part includes the NGC 2068 and NGC 2071 regions, and the southern part includes the NGC 2023 and NGC 2024 regions. The first dense gas survey in the cloud was made by Lada et al. (1991a) using the CS(2-1) line. Although the resolution is low (1′.8), they mapped the cloud unbiasly and found 42 CS clumps. The CS clumps seems to be associated with the clusters, while

a CS clump named LBS 23, one of the most massive CS clumps, seems not to associated with any active star formation. Aoyama et al. (2001) made mapping observations of the dense part of the cloud using the $C^{18}O(1 - 0)$ and $H^{13}CO^{+}(1 - 0)$ lines with the resolutions of 2'.7 and 3'.8, respectively. Johnstone et al. (2001) carried out a 850 μm continuum mapping observation of the northern part of the cloud. The continuum map reveals there are numerous cores in the CS clumps.

1.4.3 Cepheus OB3 Cloud

The Cepheus OB3 cloud is one of the second nearest massive-star-forming GMCs next to the Orion GMC complex. The distance is 730 pc from the sun (Garmany, 1973). Sargent (1977) firstly mapped the whole of the molecular cloud in the $^{12}CO(1 - 0)$ with a resolution of 2'.5, as shown in Figure 1.5. The cloud have a extent of $\sim 20 \times 60$ pc, and is elongated parallel to the garactic plane. The total mass of the cloud was derived to be 5×10^3 by her. She also created the nomemclature of Cep-A to F. For more dense gas, Yu et al. (1996) observed the cloud in the $C^{18}O(1 - 0)$ line with a resolution of 2'.7. On the other hand, The GMC is associated with the OB association Cepheus OB3. The Cepheus OB3 association have the two groups of the older group of $\sim 8 \times 10^6$ yr and the younger group of $\sim 4 \times 10^6$ yr. The younger group is located between the older group and the cloud. In addition, at the interface between the cloud and the younger group, an H II region S155 exists (see Figure 1.5). This configuration of the OB association, H II region, and the molecular cloud represents a typical view of the sequential star formation (Elmegreen & Lada, 1977; Sargent, 1977).

The Cep-B region faced to the S155 H II region is thought to be one of active massive star forming regions. Minchin et al. (1992) inferred the precense of a deeply embedded early type star of B1-B0.5 with a combination of a far-infrared and CO observations. Testi et al. (1995) found three centimeter continuum point sources in the region. They also argued that the

Cep-B region is more evolved than the other regions. The Cep-A region, located to the 35′ south of Cep-B, also shows several indicators of recent active star formation, such as H_2O masers, molecular outflows, compact H II regions and Herbig-Haro objects (Ho et al., 1982; Hughes, 1988; Garay et al., 1996). In addition, Cep-A is associated with a deeply embedded cluster, which have 580 stars and have a total stellar mass of $310 M_{\odot}$ (Lada & Lada, 2003). The Cep-F region, located 15′ northwest of Cep-A, also shows the following active star-forming features. A far-infrared source which is thought to be a B star (Sargent et al., 1983), and a compact H II region (Harten et al., 1981) are known. On the other hand, apart from the active star-forming regions mentioned above, an embedded cluster is known in the Cep-C region, located to the 1° east of the Cep-A/B region. The embedded cluster has a IRAS source and H_2O maser, suggesting ongoing star formation in Cep-C. In addition, in the other regions such as the Cep-E and L1211 regions there are IRAS point sources, millimeter continuum sources, powerful molecular outflows, and H_2O masers. Hence, active massive star formations occur all over in the Cepheus OB3 cloud, in contrast to the fact that the most active star forming region is limited near H II regions in the Orion A and B clouds.

1.5 Chapter Summary

To reveal the meanings of the stellar IMF, we have carried out the dense core surveys in the three GMCs Orion A, B, and Cepheus OB3, because the properties of the dense cores are expected to be related to the star formation processes. Our observations with the $H^{13}CO^+(1 - 0)$ molecular line emission, which is preferable for surveying the dense gas, are very unique in that we covered a large area of the GMCs with a high spatial resolution and deep integration.

We characterize the three GMCs as follows in the present study. Since the ONC is thought to be one of the typical galactic clusters (e.g., Kroupa et

al., 2001), the associated Orion A cloud is considered as the standard for the comparison between the clouds. The star formation activities in the Orion B cloud is less active: the spectral type of the most massives star in the cloud (O8) is later than that in the Orion A (O6), and the stellar number and total mass of the associated clusters are rather similar to those in intermediate-mass cluster forming regions, such as the ρ Ophiuchi cloud. Then in the Orion B cloud, we can sample the cores related to intermediate-mass star formation in GMC. Besides the Orion clouds, the Cepheus OB3 cloud is one of the best GMCs for us to sample dense cores related to the massive star and cluster formation because of it's nearness to the solar system of 730 pc. Furthermore, the Cepheus OB3 cloud has star forming regions all over the cloud as described in the last subsection in contrast to that active massive star formations in the two Orion clouds are limited near the H II regions.

Through the surveys in the three GMCs, we create dense core catalogs in nearby representative GMCs within the distance of 1 kpc. Since the catalogs are unbiased and uniform one, we can derive statistically-reliable CMFs and compare it with each other and the IMF to reveal the origin of the IMF in the solar neighborhood. We can also expect sample cores associated with various environments such as OB associations, (compact) H II regions, embedded clusters, molecular outflows, and starless clumps, or relatively quiet regions where are apart from such energetic phenomena. The catalogs would address whether the origin of such various star-formation activities are related to the properties of the dense cores or not.

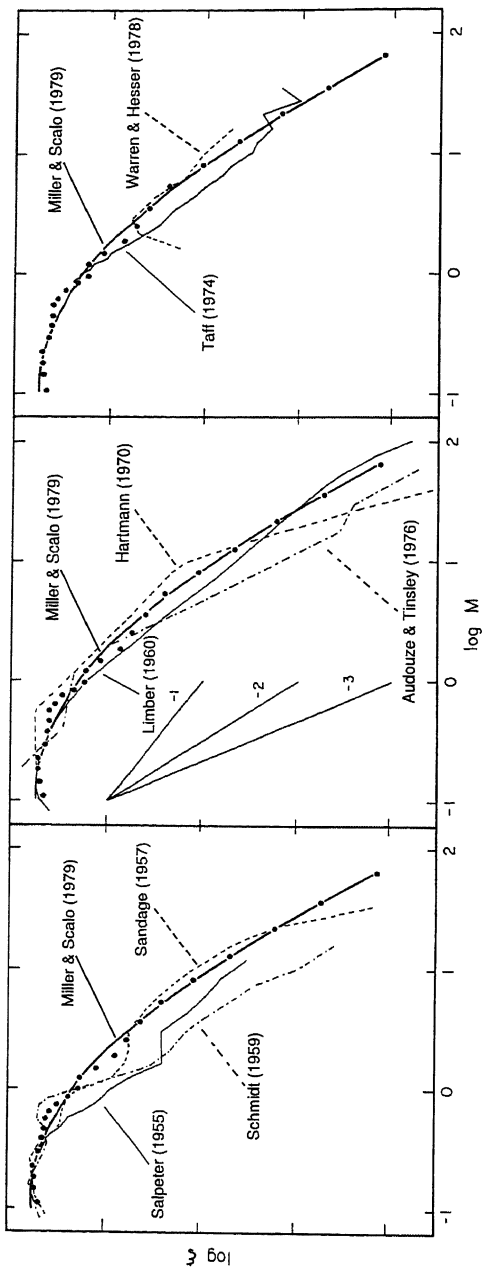

Figure 1.1 Various galactic field IMFs in the literature compiled by Miller & Scalo (1979). A notation ξ in the figure is equivalent to our notation of dN/dM in the later section. Note that the IMFs are arbitrarily normalized to agree at the low-mass end.

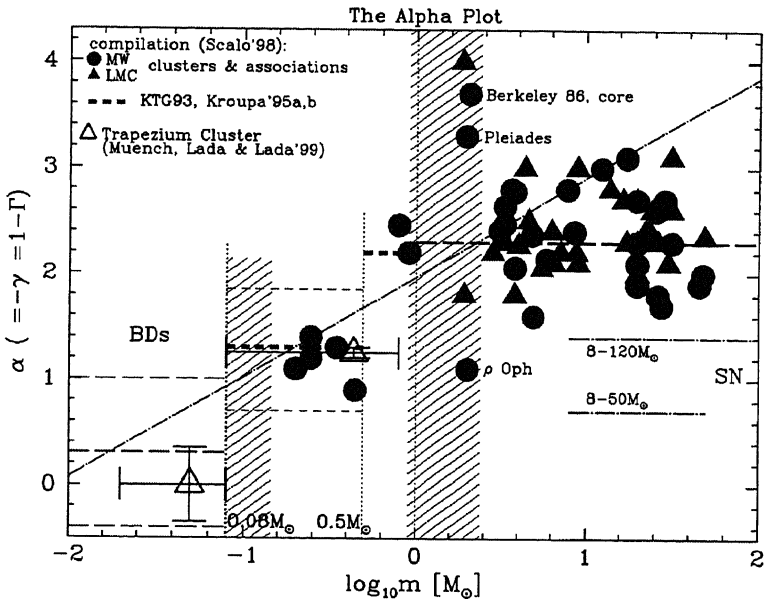

Figure 1.2 Figure 1 of Kroupa (2001), showing the power-law index α, equivalent to our notation of γ in the later section, as a function of stellar mass. The filled cirlcles and triangles show the power-law indices in the literature in the Milky Way and Large Magellanic Cloud, respectively. The diagonal dash-doted line represents the IMF by Miller & Scalo (1979), and the open triangles show those of the Trapezium IMF (Muench et al. 1999).

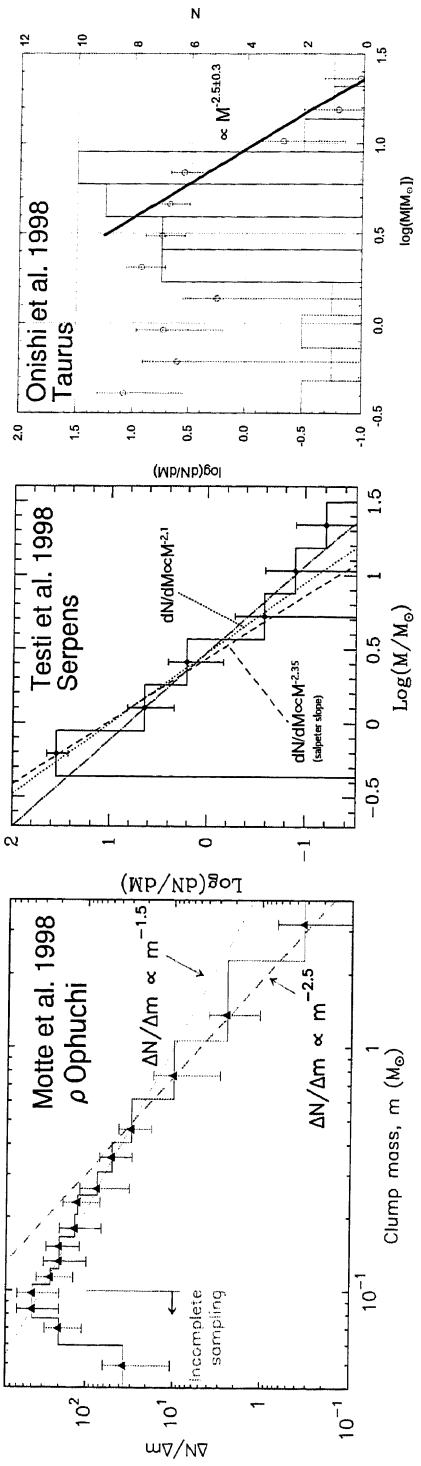

Figure 1.3 Examples of the dust and $H^{13}CO^+$ CMFs. The left, middle, and right panel shows the dust CMF derived by Motte et al. (1998), that by Testi & Sargent (1998), and the $H^{13}CO^+$ CMF derived by Onishi et al. (2002), respectively.

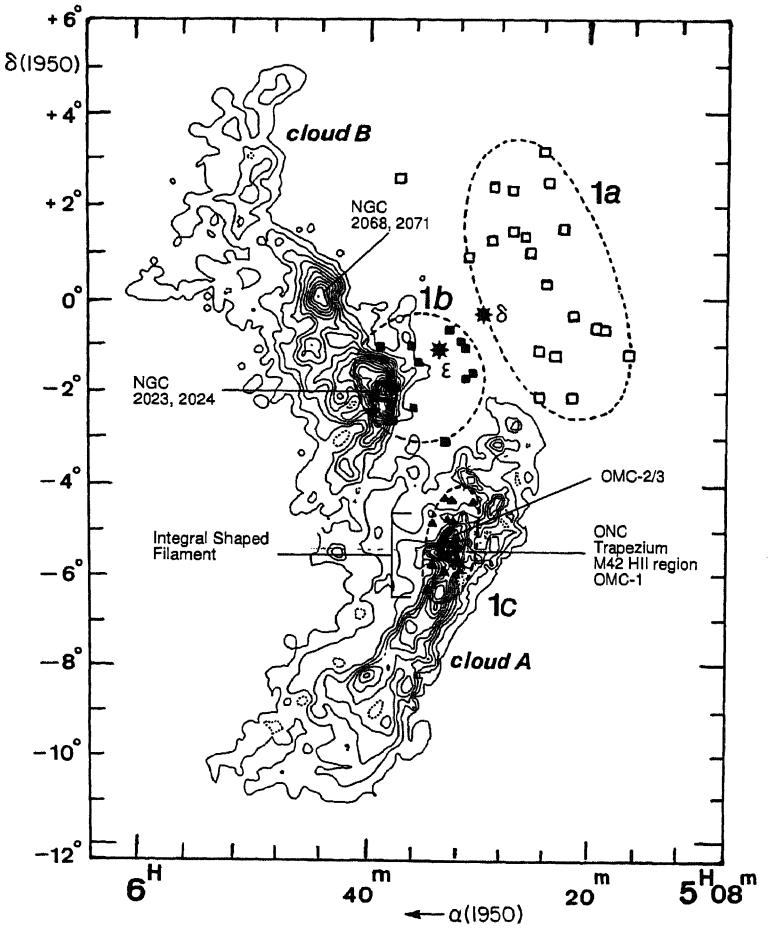

Figure 1.4 Spatial distribution of the Orion GMC complex with the contour map indicating the total integrated intensity of the $^{12}CO(1 - 0)$ emission, taken from Blaauw (1991). The open squares, filled squares, and filled triangles show the position of the stars of the Orion OB association 1a, 1b, and 1c, respectively.

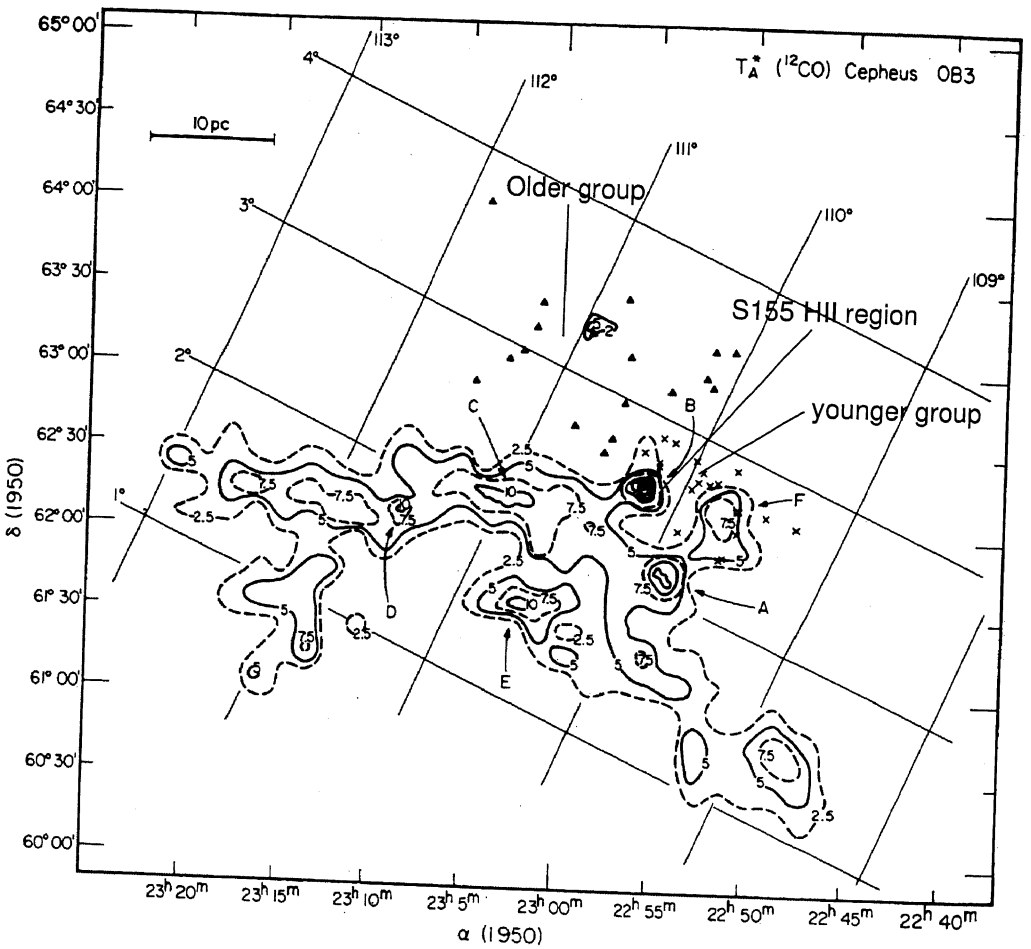

Figure 1.5 Spatial distribution of the Cepheus OB3 GMC with the contour map of the total integrated intensity of the ^{12}CO(1 - 0) emission (Sargent, 1977). The filled triangles and cross marks shows the position of the stars of the older and younger groups of the Cepheus OB3 OB association, respectively. The regions of Cep-A to F are also indicated.

Chapter 2

Observations and Data Reduction

All of our observations have been carried out with the Nobeyama 45 m radio telescope. The observations fall into the following three categories: (1) $H^{13}CO^+(J = 1 - 0)$ mapping observations to survey molecular cloud dense cores, (2) $HC^{18}O^+(J = 1 - 0)$ one-point observations to determine the optical depth of $H^{13}CO^+(J = 1 - 0)$, and (3) NH_3 mapping observations to derive the kinetic temperature distribution. Table 2.1 summarizes the parameters of the telescope, receivers and backends for each molecular line used for the observations. In the following the detail of the observations are presented.

2.1 $H^{13}CO^+$ Mapping Observations

The $H^{13}CO^+$ mapping observations were carried out toward the three clouds. For observing the Orion A, we used the position switching method. For the Orion B and Cepheus OB3, the On The Fly method was employed. The rest frequency of the $H^{13}CO^+(J = 1 - 0)$ emission is 86.75433 GHz. At 87 GHz, the half power beam width, $\theta_{\rm HPBW}$, and main beam efficiency, η, of the telescope were 18″ and 0.51, respectively. As the front end, we used the

BEARS in double side band (DSB) mode, which has 5×5 beams separated by 41″.1 in the plane of the sky (Sunada et al., 2000; Yamaguchi et al., 2000) . The 25 beams have variations of about 10 % in both beam efficiency and side-band ratio. To correct for the beam-to-beam gain variation, we calibrated the intensity scale of each beam by using a 100 GHz SIS receiver (S100) with a SSB filter. Furthermore, we observed the same grid point in mapping with different 9 beams to smooth the beam-to-beam gain variation. The standard chopper wheel method was used to convert the received intensity into the antenna temperature, $T_{\rm A}^{*}$. The telescope pointing was checked every 1.5 hours by observing the SiO maser sources Orion KL (Orion A and Orion B) or T-Cep (Cepheus OB3). The pointing accuracy was better than 3″. Table 2.2 summarizes the paramters of the mapping observations. In addition to the mapping observations, we took low-quality guide maps when the weather was bad. This is very important to achieve a unbiased dense gas survey as mentioned in Section 1.3, because we can use the low-quality guide maps to determine where we should observe.

2.1.1 Position Switch Mapping in the Orion A

The observations were carried out toward the Orion A molecular cloud in the period from December 1999 to May 2003. The mapping observations covered a 1.5 square degrees area of the Orion A GMC, shown in Figure 2.1. The mapping grid, $\Delta\theta_{\rm obs}$, has 20″.55 spacing, corresponding to a half of the beam separation of the BEARS, i.e., nearly full-beam sampling. For the observations in the period from 1999 to May 2001 we used, as the back end, 15 sets of 2048 channel Acousto-Optical Spectrometers (AOSs), which have a 40 MHz band width and a 37 kHz frequency resolution: the frequency resolution corresponds to a velocity resolution, $dv_{\rm spec}$, of 0.128 km s^{-1} at 87 GHz. In the period from December 2001 to 2003, we used 25 sets of 1024 channel Auto-Correlators (ACs), which have a 32 MHz band width and a 37.8 kHz resolution, corresponding to $dv_{\rm spec}$ of 0.13 km s^{-1} (Sorai et al.,

2000) . During the observations, the system noise temperatures were in a range between 200 and 600 K. The typical integration time at each grid point was 200 sec, and we achieved a uniform rms noise level of 0.1 K in T_A^*.

2.1.2 On The Fly Mapping in the Orion B and Cepheus OB3

The observations were carried out toward the two clouds in the period from December 2004 to May 2006. The mapping observations covered a 1.4 square degrees area of the Orion B cloud and a 1.4 square degrees area of Cepheus OB3, which are shown in Figure 2.2 and Figure 2.3, respectively. To reduce the scanning effect, we scaned each observing region along both the direction of the right acsension and declination, with the scan speed of the telescope in the celestial coordinates, $V_{\rm scan}$, of 30 arcsec s^{-1}. As the backend, we used 25 sets of 1024 channel ACs, which have a $dv_{\rm spec}$ of 0.13 km s^{-1}. The data dumping time of the backend, $t_{\rm dump}$, is 0.1 s. Then the spatial data sampling interval becomes 3″. During the observations, the system noise temperatures were in a range between 190 and 500 K. To achieve uniform noise level, we managed the integration time in the observations, resulting in a uniform rms noise level of 0.15 K and 0.13 K in the Orion B and Cepheus, respectively, in T_A^*.

2.2 $HC^{18}O^+$ One-point Observations

The $HC^{18}O^+(J = 1 - 0)$ one-point observations were carried out toward 4 peaks of the $H^{13}CO^+$ emission in the Orion B and 2 peaks of Cepheus during 9 - 14, May, 2006. We note that in the Orion A, to determine the optical depth we used the $H^{12}CO^+(J = 1 - 0)$ data provided by Saito (2002). The position of observing points are listed in Table 3.1 and are also indicated in Figures 3.6, 3.6, 3.11, and 3.12. The rest frequency of the $HC^{18}O^+(J = 1 - 0)$

is 85.1623 GHz. At 85 GHz, $\theta_{\rm HPBW}$ were 18″. As the frontend, we used the 80/100 GHz SIS receivers (S100/80) with SSB filters. At 85 GHz, η were 0.49 and 0.45 for the S100 and S80 receivers, respectively. The standard chopper wheel method was used to convert the received intensity into $T_{\rm A}^{*}$. The system noise temperature was typically 350 K. As the backend, we used the AOSs, which have a velocity resolution of 0.13 km s^{-1} at 85 GHz. The integration time of each point is typically 30 minites, resulting the RMS of 0.061 - 0.067 K in $T_{\rm MB}$. The telescope pointing was checked every 1.5 hours by observing the SiO maser sources Orion KL (Orion A and Orion B) or T-Cep (Cepheus OB3). The pointing accuracy was better than 3″.

2.3 NH_3 Mapping Observations

The NH_3 mapping observations were carried out toward the region where the $H^{13}CO^{+}$ emission is detected in the Orion B and Cepheus OB3 during Dec, 2005 to May, 2006. For the Orion A, we used the results provided by Cesaroni & Wilson (1994). The rest frequencies of the NH_3(1,1) and (2,2) are 23.6945 GHz and 23.7226 GHz, respectively. At 24 GHz, $\theta_{\rm HPBW}$ and η were 80″ and 0.8, respectively. As the frontend, we used the 20 GHz HEMT receiver (H20). The standard chopper wheel method was used to convert the received intensity into $T_{\rm A}^{*}$. The system noise temperature was 100 to 500 K. As the backend, we used the AOSs, which have a velocity resolution of 0.5 km s^{-1} at 24 GHz. We observed the NH_3(1,1) and (2,2) lines simultaneously by using two AOSs with the bandwidth of 32 MHz. The integration time of each point is typically 180 seconds, resulting the RMS of 0.04 K in $T_{\rm A}^{*}$. The telescope pointing was checked every 3 hours by observing the SiO maser sources Orion KL (Orion A and Orion B) or T-Cep (Cepheus OB3). The pointing accuracy was better than 15″.

2.4 Data Reduction and Construction of 3-D Cube Data

The reduction of the position switching data, i.e., the $NH_3(1,1)$, (2, 2), $HC^{18}O^+$ (1 - 0) data in the Orion B and Cepheus OB3, and the $H^{13}CO^+$(1 - 0) data in the Orion A cloud, were made with the "NEWSTAR" software, developped in Nobeyama Radio Observatory. First the raw data were integrated and calibrated with the task "LINTEG". Then the baseline fitting and subtraction of the baseline from the spectra were done with the task "BASELINE". For the $H^{13}CO^+$ mapping observation data in the Orion A with the BEARS, the beam distortion correction was applied with the task "Pos. Correct". To combine the spectra, we averaged the spectra at the neighboring observational positions weighted according to their spatial displacements with the task "AT for BEARS" with a 15″ Gaussian restricted mode. A 3-D $(\alpha - \delta - v_{\rm LSR})$ $H^{13}CO^+$ cube data in the Orion A was created with the task "Map(large)". The spatial grid size of the cube, $\Delta\theta_{\rm grid}$, is 20″.55, equal to the separation of the observational positions. We used "No interporation" mode to make the map, i.e., we did not apply any smoothing when we made the cube data. The resulting effective resolution, $\Delta\theta_{\rm eff}$, is calculated as $\Delta\theta_{\rm eff} = (\theta^2_{\rm HPBW} + 15''^2)^{1/2} = 23''.4$.

The reduction of the OTF data, i.e., the $H^{13}CO^+$(1 - 0) mapping observation data in the Orion B and Cepheus OB3, were made with the "OTF" reduction software, developped in Nobeyama Radio Observatory. For the OTF data, the beam distortion were automatically corrected during the observation. The baseline fitting and subtraction were made with the tasks "BASELINE" and "BASE(Batch)". The 3-D data were created with the task "Make Map". Since the spectra were taken with a very high spatial sampling rate of 3″, but with a very short integration time of 0.1 sec, we have to use a gridding convolution function (GCF) to integrate the spectra and to calculate the intensity at each grid point of the cube data. As a

GCF, we used a spheroidal function of $m = 6$ and $\alpha = 1$ (see the top panel of Figure 2.4). The spheroidal function is defined to maximize the suppression of the aliasing of the spatial frequency component higher than that of the telescope can sample (Schwab, 1984): the energy concentration ratio, which is the fraction of the power within the maximum spatial frequency of the telescope, is 99.9999 % (see the bottom panel of Figure 2.4). Since the spheroidal function have a FWHM of 20″.3 when $\Delta\theta_{\rm grid}$ is selected to be 9″, which is the nyquist grid spacing of the telescope, $\Delta\theta_{\rm eff}$ becomes to be 27″.1. Table 2.3 shows the summary of the parameters for the 3-D maps of the $H^{13}CO^+$ emission. Furthermore, to reduce the scanning effect, we combined the two maps scanned along the right ascension and declination with the task "Basket Weave", which is an implementation of the basket-weaving method (Emerson & Gräve, 1988). First, the FFT images of the two input maps are created. Next, the scanning effect components of the two FFT images are masked, and then the two FFT images are averaged. Finally the averaged FFT image is inverse-fourier-transformed to obtain a "basket-weaved" map.

In addition, we created the 3-D maps of the Orion A and Orion B with a spatial resolution of 41″.2 to compare directly with the Cepheus OB3, which is 1.5 times as far as the Orion clouds. Although we describe the detail in the subsect. 4.2.2.3, the paramters for the construction of the low-resolution cube data are also presented in Table 2.3.

2.5 Consistency Between the OTF and Position Switching Methods

We took the $H^{13}CO^+$ map of the Orion A cloud with the position switching method, while we employed the OTF method for the mapping observations in the Orion B and Cepheus OB3 cloud. Here we show the resultant maps obtained with the OTF and position switching methods are consistent with each other.

Figure 2.5 shows a part of the velocity channel maps of the $H^{13}CO^+$ emission in the Orion B cloud, taken with the OTF method. The whole of the maps are presented in Section 3.2. The observations of this area was carried out during 1st to 5th of December, 2004. The other observing paramters are described in Section 2.1 and the map preparing parameters are the same as described in the last section: a spheroidal function ($m = 6$, $\alpha = 1$) with a grid size of $9''$. The typical RMS of the map is estimated to be 0.14 K in T_A^*.

To compare with the OTF map, we observed the same area of Figure 2.5 using the position switching method in 29th of March, 2005. Since the OTF observations sampled the data without the lack of the spatial information, the observation of the position swithching one also should be: the observation grid were selected as $8''.22$, one fifth of the intrinsic beam separation of BEARS. Almost the nyquist sampling were achieved. For making map, we used a Gaussian with a FWHM of $14''$ as the GCF to have the same spatial resolution as the OTF map of $27''.1$. Figure 2.6 shows the velocity channel maps by the position switching method. The typical RMS of the map is estimated to be 0.09 K in T_A^*.

At a glance of Figures 2.5 and 2.6, the OTF and position switching maps have a good agreement with each other. Figure 2.7 shows the point-to-point correlation of Figures 2.5 and 2.6. Although the intensity range is relatively narrow, the correlation is good considering the typical RMSs of the maps. Furthermore, the maximum, minimum, mean values in the figures are also consistent with each other, as shown in Table 2.4. Consequently, the data obtained by the OTF and position switching method have a good agreement with each other.

2.6 Chapter Summary

We used the Nobeyama 45 m radio telescope for our all observations. Using the 25-beam receiver BEARS, $H^{13}CO^+(1 - 0)$ mapping observaions were carried out in the Orion A, Orion B, and Cepheus OB3 cloud with large areas of 1°.5, 1°.4, and 1°.4, respectively. The observations in the Orion A were done with the position switching method, while those in the Orion B and Cepheus OB3 were done with the OTF method. To determine the optical depth of the $H^{13}CO^+(1 - 0)$ emission, we observe the $HC^{18}O^+(1 - 0)$ emission at five points in the Orion B and Cepheus OB3 using S100/80 receiver. To obtain the kinetic temperature distribution of the clouds, we carried out the $NH_3(1, 1)$ and (2, 2) mapping observations in the Orion B and Cepheus OB3 using H20 receiver.

To make map with the data obtained with the OTF method, we used a spheroidal function ($m = 6$, $\alpha = 1$) as the GCF, which is defined to minimize the aliasing of the higher spatial frequency component. The resultant OTF maps have a spatial resolution of 27″.1 with the typical RMS of 0.14 K.

We checked the consistency between the OTF and position switching methods in the NGC2024 region. To compare the OTF map, we took the nyquist-sampled position switching data in the NGC2024 region anew. The appearance and point-to-point correlation between the OTF and position switching maps have a good agreement with each other, indicating that the OTF data is consistent with the position switching one.

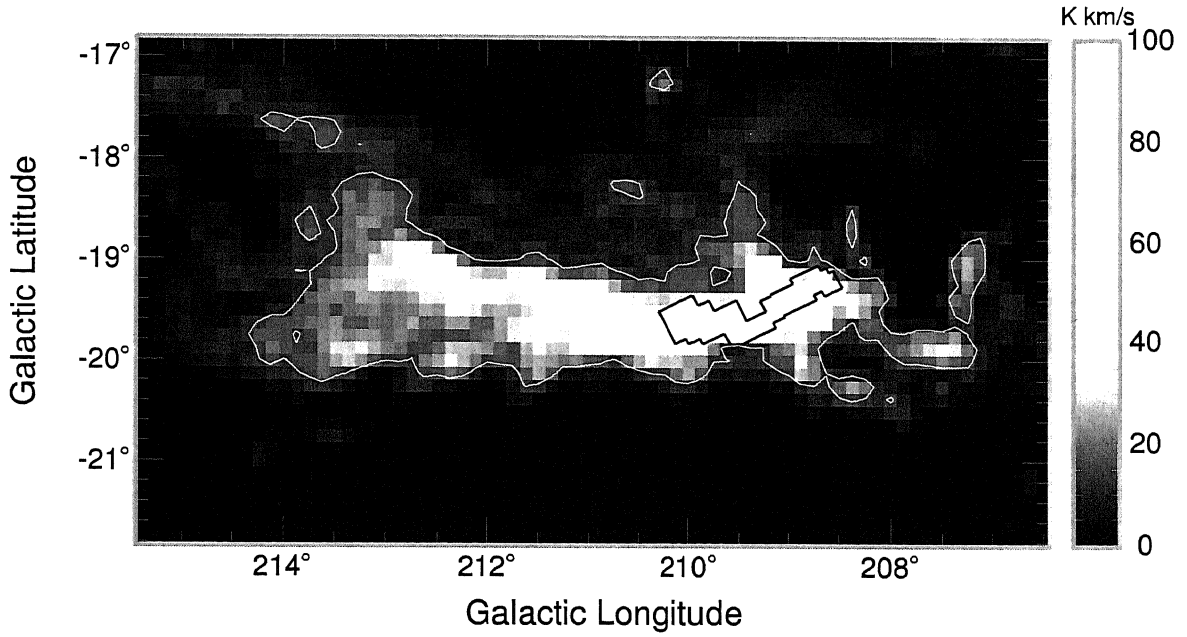

Figure 2.1 ^{12}CO total integrated intensity map of the Orion A cloud (Dame et al.2001, greyscale and contour). The cloud outline is shown with the 15 K km s^{-1} level contour. The black polygon in 208° $< l <$ 210° and -20° $< b < -19°$ indicates the region where our observations were carried out.

Table 2.1. Observational parameters 1. Telescope, receivers & molecular lines

	Frequency [GHz]	Receivers	η	$\theta_{\rm HPBW}$ arcsec	Pointing accuracy arcsec	Backend	$dv_{\rm spec}$ km s^{-1}
$H^{13}CO^+(J=1-0)$	86.7543	BEARS	0.51	18	≤ 3	AC/AOS	0.13
$HC^{18}O^+(J=1-0)$	85.1623	S100/80	0.49/0.45	18	≤ 3	AOS	0.13
NH_3	23.69	H20	0.8	80	≤ 15	AOS	0.8

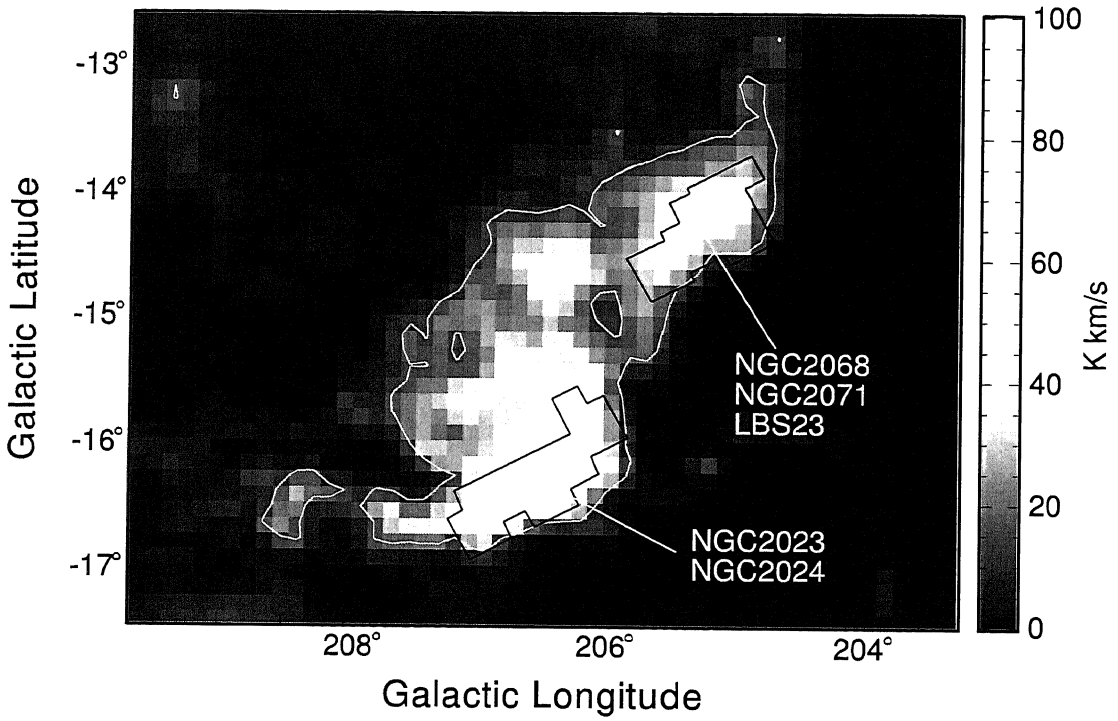

Figure 2.2 ^{12}CO total integrated intensity map of the Orion B cloud (Dame et al.2001, greyscale and contour). The contour paramter is the same as Figure 2.1. The black polygons in 206° < l < 207° and -17° < b < −15.5°, and 205° < l < 205°.5 and -15° < b < −13.5°, indicates the regions where our observations were carried out.

Table 2.2. Observational parameters 2. Observational methods for $H^{13}CO^+$ mapping

Cloud	Method	Area degree^2	$\Delta\theta_{obs}$ arcsec	V_{scan} arcsec s^{-1}	t_{dump} s	Pointing source
Orion A	Position Switch	1.5	20.55	-	-	Orion KL
Orion B	On The Fly	1.4	-	30	0.1	Orion KL
Cepheus	On The Fly	1.4	-	30	0.1	T-Cep

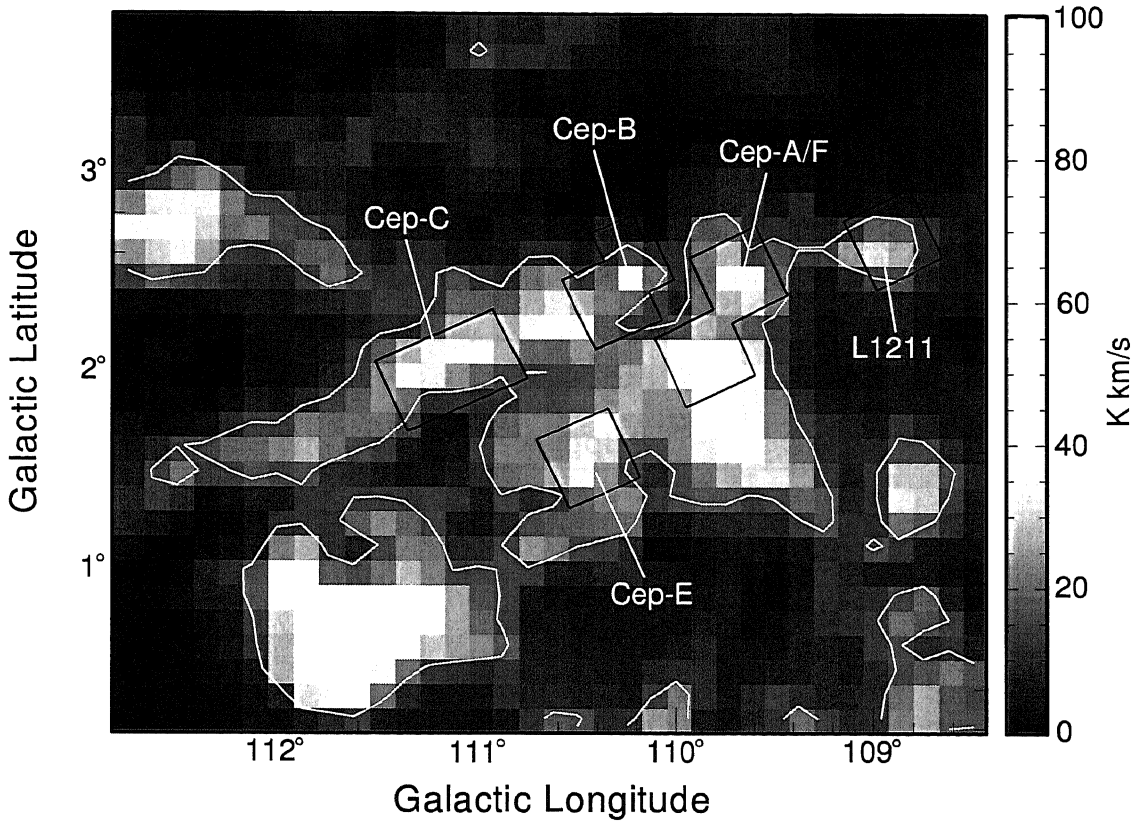

Figure 2.3 ^{12}CO total integrated intensity map of the Cepheus OB3 cloud (Dame et al.2001, greyscale and contour). The contour paramter is the same as Figure 2.1. The black polygons in $111.5° < l < 108.5°$ and $1.5° < b < 3°$ indicates the regions where our observations were carried out.

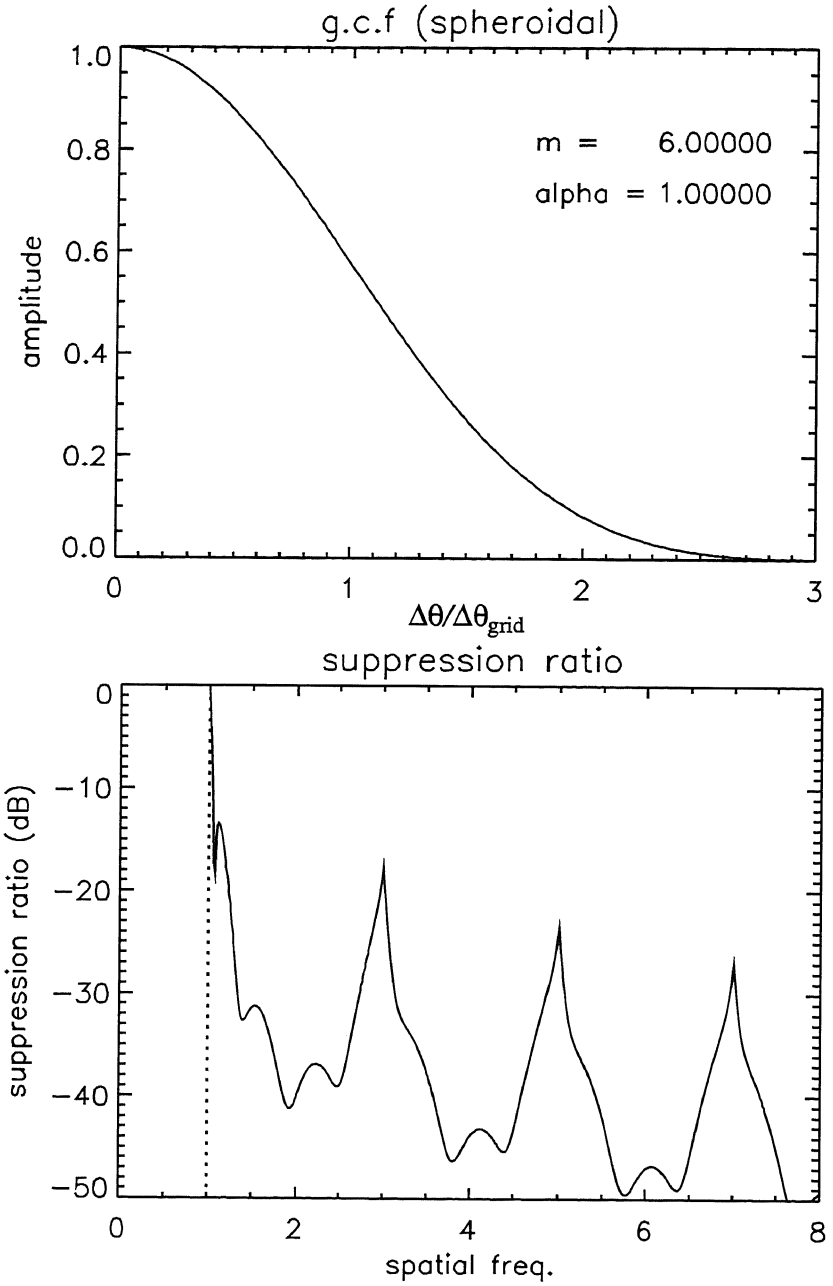

Figure 2.4 (*Top*) Radial profile of the spheroidal function of $m = 6$ and $\alpha = 1$. The unit of the horizontal axis is the grid size of the map, $\Delta\theta_{\rm grid}$. (*Bottom*) Suppression ratio of the spheroidal function of $m = 6$ and $\alpha = 1$. The unit of the horizontal axis is the spatial frequency of the telescope aperture.

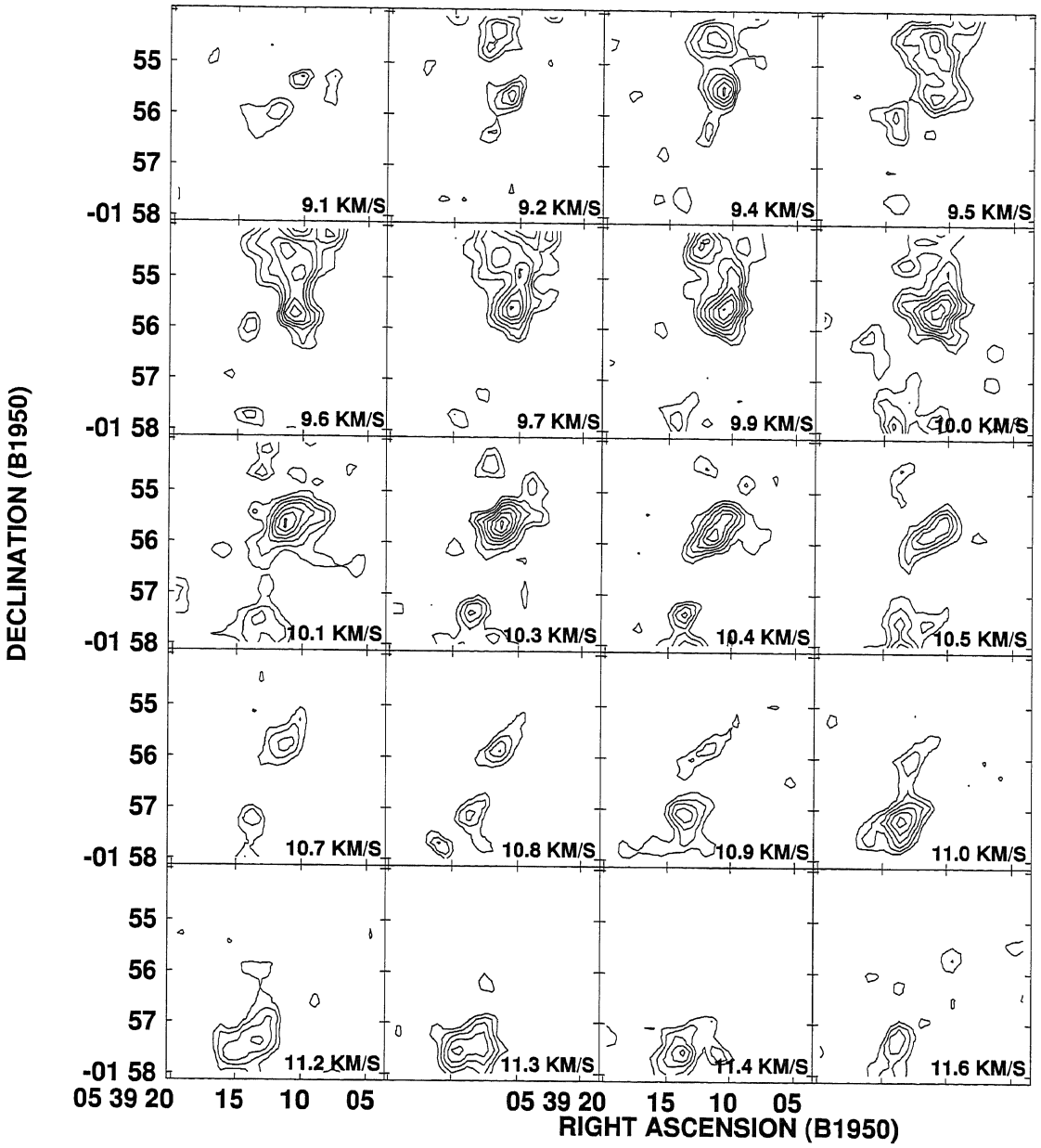

Figure 2.5 Velocity channel maps of the NGC2024 region with the OTF method. The contour interval is 0.14 K, corresponding to 1 σ. The lowest contour level is 0.42 K, corresponding to 3 σ.

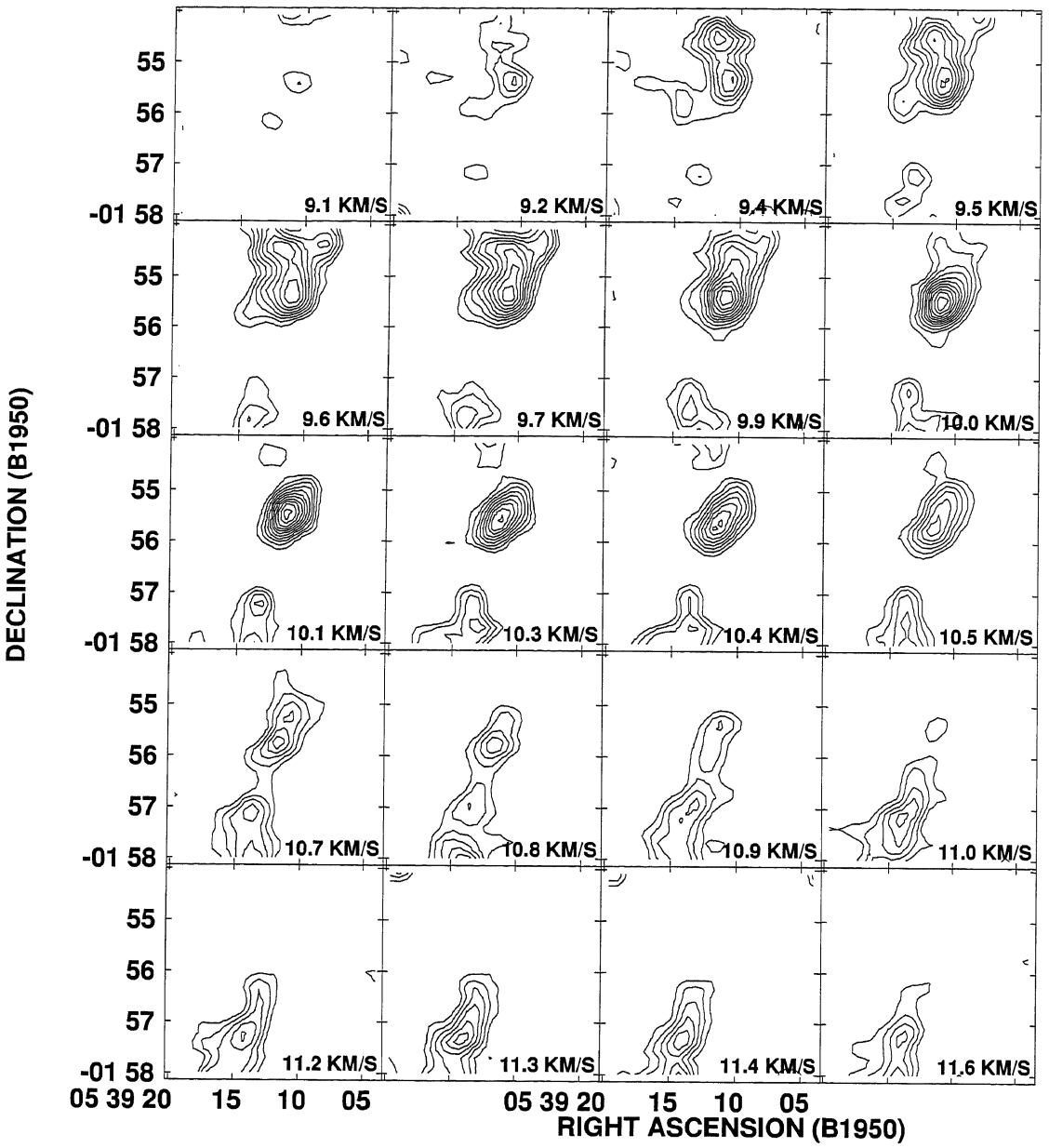

Figure 2.6 Velocity channel maps of the NGC2024 region with the position switch method. The contour interval is 0.09 K, corresponding to 1 σ. The lowest contour level is 0.27 K, corresponding to 3 σ.

Table 2.3. Map preparing parameters

Cloud	Method	$\Delta\theta_{\rm eff}$ arcsec	$\Delta\theta_{\rm grid}$ arcsec	GCF	Area degree^2	Typical RMS K, $T_{\rm A}^*$
Orion A	Position Switch	23.4	20.55	-	1.5	0.085
Orion B	On The Fly	27.1	9	Spheroidal($m = 6, \alpha = 1$)	1.4	0.115
Cepheus	On The Fly	27.1	9	Spheroidal($m = 6, \alpha = 1$)	1.4	0.13
Orion A	Position Switch	41.2	41.2	Gaussian($33''.9$)	1.5	0.06
Orion B	On The Fly	41.2	19.0	Bessel×Gaussian($37''.1$)	1.4	0.12

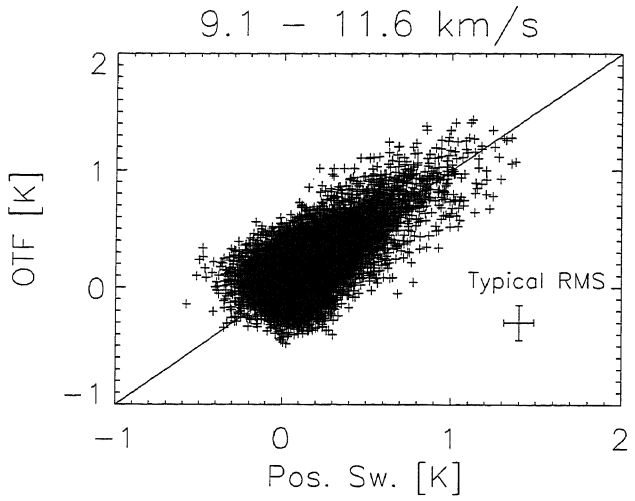

Figure 2.7 Point-to-point correlation between Figures 2.5 and 2.6. A cross mark with errorbars indicated bottom-right hand side of the panel shows the typical RMSs of each figure.

Table 2.4. Comparison between the OTF and position switch methods

Method	RMS	Maximum	Minimum	Mean
OTF	0.14	1.43	-0.57	0.07±0.24
Position Switch	0.09	1.38	-0.59	0.04±0.20

Note. — The unit of the listed values is K in $T_{\rm A}^{*}$.

Chapter 3

Results

3.1 $H^{13}CO^+$ Map of the Orion A Cloud

3.1.1 Intensity Distribution

Figure 3.1 shows a total integrated intensity map of the $H^{13}CO^+$ emission in the Orion A cloud. In the north region of the cloud ($-5°50' < Dec. < -4°50'$), the $H^{13}CO^+$ intensity is the most intense ($\sim$ 2 K km s^{-1}). One can clearly see the ISF, which was traced by NH_3 (Cesaroni & Wilson, 1994) and by submillimeter dust continuum emission (Chini et al., 1997; Lis et al., 1998; Johnstone & Bally, 1999). The distribution of the $H^{13}CO^+$ emission is remarkably similar to that of the submillimeter emission. The $H^{13}CO^+$ intensity becomes weak (<1 K km s^{-1}) toward the south ($Dec. < -5°50'$). We cannot discern a filamentary structure in the south region although the tenuous ($< 10^4$ cm^{-3}) filament is known (Bally et al., 1987; Tatematsu et al., 1993; Nagahama et al., 1998).

Our map shows that the ISF consists of several dense *clumps* with sizes of about 1 pc. Such a clumpy feature is also seen in the previous maps obtained with lower density tracers of ^{13}CO (Tatematsu et al., 1993) and $C^{18}O$ (Dutrey et al., 1991). In contrast to the ^{13}CO and $C^{18}O$ maps, the clumps can be

much clearly defined in our $H^{13}CO^+$ map. These distinct clumps are known as OMC-1, 2, 3, and L1641N (see figure 3.1). The most intense clump is OMC-1 ($\sim$ 3 K km s^{-1}), which is associated with the M42 H II region and includes the Orion-KL object, one of the nearest sites of on-going massive star formation. Furthermore, in each clump, we can recognize many small condensations with sizes of about 0.1 pc, which are referred to as *cores*.

In OMC-1, there exist some filaments extended from the Orion-KL object toward the west. These are known as "Molecular Fingers", also seen in the previous maps by the dust continuum emission (Johnstone & Bally, 1999) and by the NH_3 (Murata et al., 1990; Wiseman & Ho, 1998) and HC_3N (Rodríguez-Franco et al., 1992) line emission. The $H^{13}CO^+$ map, however, reveals several cores inside the molecular fingers. On the other hand, the Orion Bar region, which is thought to be a PhotoDissociated Region (PDR) around the M 42 H II region, cannot be seen in our $H^{13}CO^+$ map in spite of its prominence in dust continuum (Johnstone & Bally, 1999), CS (Tatematsu et al., 1993) and CN (Rodríguez-Franco et al., 1998). This suggests that the $H^{13}CO^+$ emission is not enhanced in a PDR, and is not biased to high temperatures in contrast to the dust continuum emission.

According to the optically thin $H^{13}CO^+$ emission shown in Section 3.4, the total H_2 mass of the dense gas is estimated to be 4300 $M_\odot$ from the $H^{13}CO^+$ map following the mass estimation described in Section 4.2.1. The mass of the corresponding ^{13}CO filament # 5 by Nagahama et al. (1998) is 19000 $M_\odot$, five times larger than our value. The total masses of the OMC-1, 2, 3, and the other regions is estimated to 1100, 520, 860, and 1800 $M_\odot$, respectively.

3.1.2 Velocity Structure

Figures 3.2, 3.3, and 3.4 show the velocity channel maps of the $H^{13}CO^+$ emission. The maps allow us to more easily recognize numerous cores in the cloud. Furthermore, the maps clearly show a distinct large-scale velocity

gradient along the north-south direction. The large-scale velocity gradients can be seen more easily in a declination-velocity diagram shown in Figure 3.5, which shows a gradient of 0.4 km s^{-1} pc^{-1}. The radial velocity tends to increase with increasing the declination. Similar velocity gradients were found along the ISF by the previous observations in ^{12}CO (Bally et al., 1987; Wilson et al., 2005) and ^{13}CO (Nagahama et al., 1998). Wilson et al. (2005) suggested that the velocity gradient is due to the compression of the cloud by the wind from the supernovae in the Orion OB association 1b subgroup on the basis of their ^{12}CO map. In addition to the overall structure, one can discern local structures deviated from the large-scale gradient. In the OMC-1 region, the velocity width in FWHM becomes as large as 3 km s^{-1} toward the blueshifted side. Particularly, the Orion S object ($R.A. = 5^h32^m45^s, Dec. = -5°26'$) has the largest velocity width of 3.4 km s^{-1} in the cloud. We will discuss this larger velocity width in the OMC-1 region in the context of the energy input from nearby massive stars in Section 6.1. In the other regions of ISF, the velocity width is not so large as that in OMC-1, and is typically ~ 1 km s^{-1}. Moreover, the south region ($Decl. < -5°.9$) shows smaller velocity widths of ~ 0.5 km s^{-1}.

3.2 $H^{13}CO^+$ Map of the Orion B Cloud

3.2.1 Intensity Distribution

Figures 3.6 and 3.7 show the integrated intensity distributions of the $H^{13}CO^+$ emission in the NGC 2023/2024 region and NGC 2068/2071 region, respectively. Although our spatial resolution is much higher, the distribution of the $H^{13}CO^+$ emision is very similar to those with the CS(2 - 1) (Lada et al., 1991a) and is consistent with the $H^{13}CO^+$ (Aoyama et al., 2001). The total mass of the $H^{13}CO^+$ emission is estimated to be $2500M_\odot$ (see sectiton 4.2.1), consistent with that of Aoyama et al. (2001) but is about a half of that in the Orion A cloud. We can find 5 distinct clumps in $5^h39^m.3$ and $-1°55'$,

associated with NGC 2024, $5^h39^m.0$ and $-2°20'$, associated with NGC 2023, $5^h44^m.3$ and $0°0'$, associated with NGC 2068, $5^h44^m.5$ and $0°20'$, associated with NGC 2071, and $5^h43^m.5$ and $-1°12'$, corresponding to LBS 23 (Lada et al., 1991a). The masses of the clumps range from 200 to $740M_\odot$. In addition to the clumps, there exists diffuse emission around them. In contrast to the $H^{13}CO^+$ map provided by Aoyama et al. (2001), which has a spatial resolution of 3'.8, our high-resolution (27") map resolves numerous cores, which is the substructures of the clumps.

The emission is the most intense ($\sim$ 2 K km s^{-1}) in the clump associated with NGC 2024 and having the LTE mass of $600M_\odot$. The clump shows a filamentary structure, called as "Molecular Ridge" (Chandler & Carlstrom, 1996), obscuring the NGC 2024 H II region, whose extent is about 15'. At the center of the H II region ($5^h39^m.3$ and $-1°50'$), the emission becomes weak. In the north side of the H II region ($5^h38^m.5$ and $-0°45'$) we also detected the $H^{13}CO^+$ emission although the intensities are weak. In the 20' south of the molecular ridge, we can see the clump associated with the NGC 2023 reflection nebula. This clump is the most massive ($740M_\odot$) one in the Orion B cloud. However, just at the position of NGC 2023 ($5^h39^m.0$ and $-2°17'$) the $H^{13}CO^+$ emission is not detected. The famous B33 horsehead nebula is located in $5^h38^m.5$ and $-2°30'$. We detected the $H^{13}CO^+$ emission toward B33, although the $H^{13}CO^+$ intensities are very weak. On the other hand, toward the 30' north of the NGC 2024 region, the $H^{13}CO^+$ intensities become weak and show diffuse distributions.

In the NGC 2068/2071 region, our map covers larger area than the mapping observation with 850 μm continuum (Johnstone et al., 2001). The morphology of the two maps are very similar to each other even for faint emission. The most intense clump in the region is NGC 2071 as well as the continuum map, and the clump mass is $410M_\odot$. The peak position is $5^h44^m32^s$ and 0°19'50", associated with the position of the NGC 2071 reflection nebula, $5^h44^m30^s$ and 0°20'17". The second intense clump is located to the 20' south

of the NGC 2071, associated with the NGC 2068 reflection nebula, $5^h44^m13^s$ and $-0°0'13''$. The dust continuum map revealed that the NGC 2068 clump is made of the chain of the dust cores (Johnstone et al., 2001). Our $H^{13}CO^+$ map also shows the chain of peaks. The LBS23 clump lies to the 10′ southwest of the NGC 2068 clump. The emission is more extended than those of the NGC2071 and NGC2068 clumps, but the clump mass of $380M_\odot$ is comparable to those of them. We also detected a relatively weak "northern clump" in $5^h45^m10^s$ and 0°37′, but this clump have been already found by Aoyama et al. (2001) (No. 1 of their $H^{13}CO^+$ clump).

3.2.2 Velocity Structure

Figures 3.8 and 3.9 show the velocity channel maps in the Orion B cloud. Unlike the Orion A cloud, the velocity channel maps do not show any distinct systematic velocity gradients and the emission is distributed around ∼10 km s^{-1}. This is consistent with the absence of the systematic velocity gradient in the CO(1 - 0) result (Wilson et al., 2005).

The largest velocity width of 2.5 km s^{-1} can be found in the molecular ridge, associated with the NGC 2024 H II region. We found an apparent local velocity gradient along the molecular ridge shown in Figure 3.10. The LSR velocity decreaces as the declination increases, i.e., toward the H II region. Since the dark lane of the optical H II region corresponds to the molecular ridge, the H II region is thought to lie behind the cloud. Then the expanding motion of the H II region would push the cloud toward the near side, and would cause the $v_{\rm LSR}$ decreaces toward the H II region. At the edge of the H II region, corresponding to the angular offset of 0′ of Figure 3.10, the velocity width becomes large. We can consider this large velocity width as a result of the energy input from the H II region, and will discuss this in Section 6.1. In the other region, however, we could not find any distinct velocity gradients. The typical velocity width in the other regions of the Orion B cloud is 0.5 - 1 km s^{-1}, except the NGC2023 region where the emission shows somewhat

larger velocity width of $\sim$1.3 - 1.5 km s^{-1}.

3.3 $H^{13}CO^+$ Map of the Cepheus OB3 Cloud

3.3.1 Intensity Distribution

Figures 3.11, 3.12, and 3.13 show the integrated intensity maps in the $H^{13}CO^+$ emission in the Cepheus OB3 cloud. The total mass of the $H^{13}CO^+$ emission is estimated to be $3800 M_\odot$, comparable to that of the Orion A cloud.

The emission is the most intense in the Cep-A region, reaching 1.5 K. (see Figure 3.11). The morphology of the emission is consistent with the $C^{18}O$ map obtained by Yu et al. (1996), although their resolution, 2'.7, is much larger than that of ours. The Cep-A embedded cluster and centimeter continuum sources are located at the peak of $H^{13}CO^+$.

In the Cep-F region, two distinct clumps can be seen (see Figure 3.11). Since a 130μm source, thought to be a B star (Sargent et al., 1983), was found at $22^h51^m22^s$ and 62°7'40" with a spatial resolution of 3', the FIR source seems to be associated with the northern clump. However, the intensity and size of the northern clump are weaker and smaller than those of the southern one. We note that the emission in the northern clump does not satisfy our core identification criterion (see sect. 4.1) because of their smaller size of 1'. The southern clump seems to be located near the center of the CO distribution (Sargent, 1977; Sargent et al., 1983).

In the Cep-C region the emission is more extended than that in the Cep-A (see Figure 3.12). Yu et al. (1996) found three $C^{18}O$ cores in the region. We detected the $H^{13}CO^+$ emission toward the three cores, while the emission toward the eastern core (core a of their nomenclature) is very weak. We resolved many smaller cores in the western (c) and center (b) cores with our high spatial resolution of 27". The location of the Cep-C embedded cluster, $23^h3^m45^s$ and 62°13'49" (Lada & Lada, 2003), corresponding to the position of a IRAS source IRAS23037+6213 and an associated H_2O maser (Harju et

al., 1993), is not on just the peak of the $H^{13}CO^+$ emission, but is surrounded by the $H^{13}CO^+$ cores.

On the other hand, in the Cep-B region the $H^{13}CO^+$ emission is very weak and compact: the intensity ranges from 0.3 to 0.6 K and the linear extent of the emission is as small as 30″ (see Figure 3.12). In contrast, the ^{12}CO emission in the region is the brightest in the cloud (Sargent, 1977), because the region would be heated by the S155 H II region that faces to the region and the optically thick ^{12}CO emission would trace the high temperatures. The dense gas, which is traced with the $H^{13}CO^+$, would be already dispersed due to the interaction with the H II region.

The top panel of Figure 3.13 shows that the region Cep-E contains a few small clumps. A clump ($\sim 23^h0^m.5$ and $61°26'$) in the Cep-E region seems to be associated with the IRAS23011+6126, which is thought to be an intermediate-mass YSO because the IRAS source has a bolometric luminocity of $\sim 80 L_\odot$ and drives an energetic outflow (Smith et al., 2003). The L1211 regions have two clumps (see the bottom panel of Figure 3.13). The southern clump in the L1211 region contains four 1.2 mm continuum sources. Two of them (MMS1 and 4), associated with CO(1 - 0) molecular outflows, are class 0 candidates (Tafalla et al., 1999). Although their resolution is about a half of ours, their 1.2 mm continuum map is similar to our $H^{13}CO^+$ one. On the other hand, the northern clump in the L1211 region have never been reported before. The total mass of the northern clump is estimated to be $80 M_\odot$, slightly less massive than that ($110 M_\odot$) of the southern one.

3.3.2 Velocity Structure

Figures 3.14, 3.15, 3.16, and 3.17 show the velocity channel maps of the Cepheus OB3 cloud. The Cep-A region has the most large velocity width of $\sim$4 km s^{-1} at $v_{\rm LSR} \sim -10$ km s^{-1}. On the other hand, the neighboring Cep-F region shows the $v_{\rm LSR}$ of -8 km s^{-1}, the most blueshifted LSR velocity in the cloud. These tendencies of the $v_{\rm LSR}$ are consistent with those with the

$C^{18}O(1 - 0)$ (Yu et al., 1996). On the other hand, the mean velocity width in the Cep-C region is 1 km s^{-1} and the typical velocity width in the other regions is 0.5 km s^{-1},

Figure 3.15 indicates that the Cep-B region contains two components in the north-east and south-west of the figure, which have different LSR velocities of -12.5 and -11.5 km s^{-1}, respectively. This velocity tendency can be also seen in the $C^{18}O$ spectrum (Yu et al., 1996) although they could not resolve the two components spatially. The size of both components are 30″, too compact to satisfy our criterion of core identification (see sect. 4.1). We note that we cannot find any more apparent velocity structures in the Cep-C, E, and L1211 regions.

3.4 Optical Depth of the $H^{13}CO^+$ Emission

We show here that the $H^{13}CO^+$ emission is optically thin in all the three clouds.

First, we estimate the optical depth in the Orion A cloud. Since the $H^{13}CO^+$ emission is the most intense toward OMC-1, we can estimate the upper limit of the optical depth in OMC-1. We estimated the optical depth of the $H^{13}CO^+(1 - 0)$ emission from the integrated intensity ratio of $H^{13}CO^+(1 - 0)$ to $H^{12}CO^+(1 - 0)$ (Saito, 2002) toward a region which is indicated in Figure 3.18. Let the optical depth of the $H^{13}CO^+$ and $H^{12}CO^+$ emission be $\tau_{H^{13}CO^+}$ and $\tau_{H^{12}CO^+}$, respectively. Then we have

$$\frac{I_{H^{13}CO^+}}{I_{H^{12}CO^+}} = \frac{1 - e^{-\tau_{H^{13}CO^+}}}{1 - e^{-\tau_{H^{12}CO^+}}}, \tag{3.1}$$

where $I_{H^{13}CO^+}$ and $I_{H^{12}CO^+}$ are the integrated intensities of the $H^{13}CO^+$ and $H^{12}CO^+$ emission, respectively. If we assume $\tau_{H^{12}CO^+}/\tau_{H^{13}CO^+} = [^{12}C]/[^{13}C] = 43 \pm 7$ (Savage et al., 2002), Equation 3.1 can be solved and we obtained the mean and maximum of $\tau_{H^{13}CO^+}$ in the region of 0.04 and 0.17, respectively.

Therefore we believe that the $H^{13}CO^+$(1 - 0) emission is optically thin in the Orion A.

For the Orion B and Cepheus, we estimate the optical depth using the $HC^{18}O^+$(1 - 0) emission. The observed positions are indicated in Table 3.1 and Figures 3.6, 3.7, 3.11, and 3.12. Figures 3.19 and 3.20 show the spectra of the $HC^{18}O^+$ and $H^{13}CO^+$ emission toward the Orion B and Cepheus, respectively. Since the $HC^{18}O^+$ emission is very weak, we only detected the $HC^{18}O^+$ emission whose intensity is more than 3 σ in 2 positions (the NGC 2023 and LBS 23 regions) in the Orion B, and marginally detected or not in the other positions. If we assume that $[H^{13}CO^+]/[HC^{18}O^+] = [^{13}CO]/[C^{18}O]$, and $[^{13}CO]/[C^{18}O]$ is equal to the terrestrial value of 5.5 (Harjunpää et al., 2004), we obtained $\tau_{H^{13}CO^+}$ of 0.70 $\pm$ 0.94 in LBS 23, and $\tau_{H^{13}CO^+} \ll 1$ in the other regions. Consequently, in the following discussion we consider that the $H^{13}CO^+$ emission is optically thin all over the three GMCs.

3.5 NH_3 Maps of the Orion B and Cepheus OB3 Clouds

Figure 3.21 and 3.22 show the $NH_3(1,1)$ and (2,2) total integrated intensity maps in the Orion B and Cepheus, respectively. The distributions of the NH_3(1,1) emission are similar to those of the $H^{13}CO^+$ emission although the spatial resolutions are 4.4 times larger than them. This is because the critical density of NH_3 is the order of 10^4 cm^{-3}, comparable to that of the $H^{13}CO^+$ emission of 8×10^4 cm^{-3}. The (2,2) maps show more compact distributions. One can see the strong peaks in the NGC 2024, NGC 2071, and Cep-A regions. These regions harbor young embedded clusters, and also are associated with an H II region, a reflection nebula, and a compact H II region, respectively, suggesting that the temperatures are raised by the stellar activities.

We estimated the kinetic temperature in the Orion B and Cepheus OB3

cloud as follows. The NH_3 inversion lines show hyperfine splitting, due to the interaction between the electric quadrupole moment of the N nuculeus and the electrons. For the (1,1) transition four quadrupole hyperfine satelites of ΔF= $\pm$1 are often strong enough to be detected. Since the optical depths of the inner satellites, $\tau(1,1,s_i)$ and those of the outer satellites, $\tau(1,1,s_o)$ have relations of $\tau(1,1,s_i) = 0.28\tau(1,1,m)$ and $\tau(1,1,s_o) = 0.22\tau(1,1,m)$, where $\tau(1,1,m)$ is the total optical depth of the ΔF= 0 hyperfine components. Then we can estimate the optical depth of the (1,1) line from the hyperfine intensity ratios, as

$$\frac{T_A^*(1,1,m)}{T_A^*(1,1,s)} = \frac{1-e^{-\tau(1,1,m)}}{1-e^{-\tau(1,1,s)}}. \tag{3.2}$$

For the (2,2) line, the ΔF= $\pm$1 hyperfine components are too weak to be detected because their intensities are expected to be only 6 % of that of the ΔF= 0 components. Therefore we deduce the (2,2) line optical depth, $\tau(2,2,m)$, from the intensity ratio of the (1,1) to (2,2) line,

$$\frac{T_{\rm A}^*(2,2,m)}{T_{\rm A}^*(1,1,m)} = \frac{1-e^{-\tau(2,2,m)}}{1-e^{-\tau(1,1,m)}}. \tag{3.3}$$

On the other hand, if the gas is under the local thermodynamic equilibrium, The ratio of the column density $N(1,1)$ at the (1,1) energy level to $N(2,2)$ at the (2,2) level is given by

$$\frac{N(2,2)}{N(1,1)} = \frac{g(2,2)}{g(1,1)} \exp\left(\frac{-\delta E_{1,2}}{kT_{\rm R}}\right), \tag{3.4}$$

where $g(1,1)$ of 3 and $g(2,2)$ of 5 are the statistical weights of the (1,1) and (2,2) levels, respectively, $\delta E_{1,2}/k$ the energy between the (1,1) and (2,2) levels of 41.5 K, and $T_{\rm R}$ the rotational temperature. With the Rayleigh-Jeans approximation, $T_{\rm ex} \gg h\nu/k = 1.14$ K, we have the general relation between

the optical depth and the column density,

$$\tau(J,K) = 6.13 \times 10^{-24} \frac{K^2}{J(J+1)} \frac{\nu^2}{\Delta\nu} \frac{1}{T_{\mathrm{ex},J,K}} N(J,K), \quad (3.5)$$

where ν is the rest frequency of the transition (J,K), $\Delta\nu$ the frequency width of the transition. Assuming the uniform T_{ex} and $\Delta\nu$ for both the (1,1) and (2,2) transitions, and combining Equation 3.3, 3.4, and 3.5, we have

$$T_{\mathrm{R}} = -41.5/\ln\left[\frac{-0.282}{\tau(1,1,m)}\ln\left\{1-\frac{T_{\mathrm{A}}^*(2,2,m)}{T_{\mathrm{A}}^*(1,1,m)}\left(1-e^{-\tau(1,1,m)}\right)\right\}\right]. \quad (3.6)$$

Ho & Townes (1983) showed a good empirical correlation between T_{R} deduced from the NH_3 data and T_{K} derived from CO observations. This suggests that T_{R} is a reliable indicator of T_{K}.

The T_{R} distributions are shown in Figure 3.23 and 3.24. The mean rotational temperatures in the Orion B and the Cepheus OB3 are 16.1±4.7 K and 17.0±4.0 K, respectively. The largest T_{R} of 29 K is derived in the NGC 2024 region. The high temperature is likely to be caused by the NGC 2024 H II region. In the Cep-A region, where ultracompact H II regions are associated, the temperature is also as high as ~24 K, consistent with the previous estimate of 22 K (Ho et al., 1982). On the other hand, the regions where the star formation activities are relatively quiet, such as the LBS 23 and Cep-C regions, the temperature is in the range from 11 to 17 K, comparable to low-mass star forming regions.

3.6 Chapter Summary

The $H^{13}CO^+$(1 - 0) maps are obtained in the Orion A, Orion B, and Cepheus OB3 clouds. Each of the maps covers a large ~ 1°.5 area of the clouds with a spatial resolution of 21 - 27″ and an uniform RMS noise level of 0.09 - 0.14 K in T_{A}^*. Such a large area, high spatial resolution, and high sensitivity

have never been realized simultaneously before. The morphologies of the $H^{13}CO^+$ emission in the Orion A and B clouds are very similar to those of the submillimeter continuum emission. The $H^{13}CO^+$ distributions consist of numerous 0.1-pc scale structures, referred as "cores".

The velocity width of the $H^{13}CO^+$ emission is typically 1 km s^{-1}. On the other hand, near the M42 H II region and the Cep-A compact H II region, the velocity widths reach up to 3 - 4 km s^{-1}. This larger velocity widths suggest the interaction between the stellar activities and the dense gas.

We showed that the $H^{13}CO^+$ emission is optically thin all over the clouds. For the Orion A case, we compared the intensity between the $H^{13}CO^+(1 - 0)$ and the $H^{12}CO^+(1 - 0)$ emission in the OMC-1 region, and found that the $H^{13}CO^+$ optical depth has the mean of 0.04 and the maximum of 0.17. For the Orion B and Cepheus cases, we observed the $HC^{18}O^+(1 - 0)$ at six points in the clouds and detected the emission at two points. The optical depths are found to be 0.7 ± 1.0 in the LBS23 region and $\ll 1$ at the other five points.

We derived the kinetic tempetature distributions in the Orion B and Cepheus OB3 clouds from the $NH_3(1, 1)$ and (2, 2) observations. The typical temperatures are 16 and 17 K of the Orion B and Cepheus OB3 clouds, respectively. Toward the H II regions NGC2024 and Cep-A, higher temperatures of 29 K and 24 K are derived. The derived temperatures are consistent with the previous results.

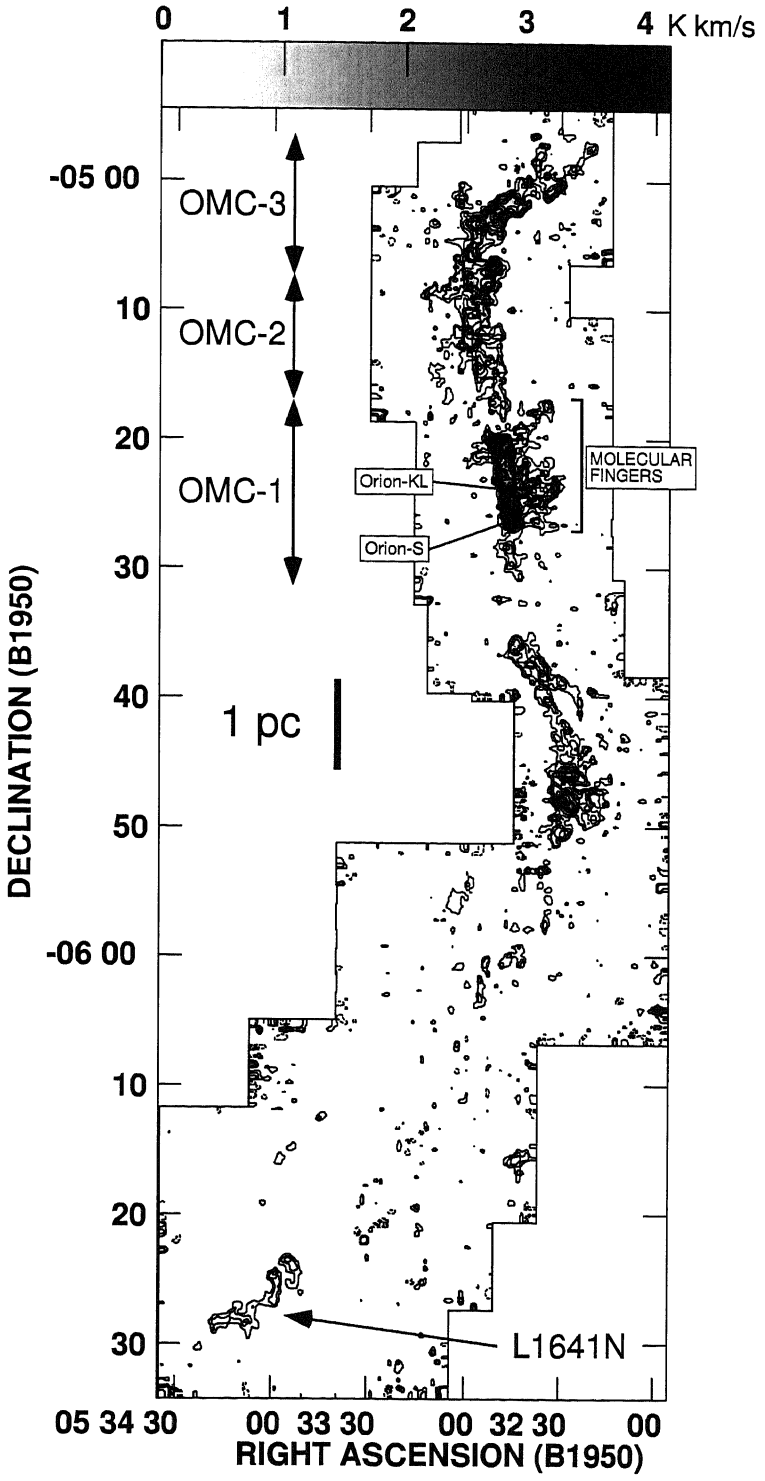

Figure 3.1 Total integrated intensity map of the $H^{13}CO^+(J = 1-0)$ emission ($v_{LSR} = 4 - 14$ km s^{-1}) in the Orion A cloud. The contour intervals are 0.2 K km s^{-1} (correspoinding to 2σ) starting at 0.2 K km s^{-1}. The unit of the grey scale is K km s^{-1}.

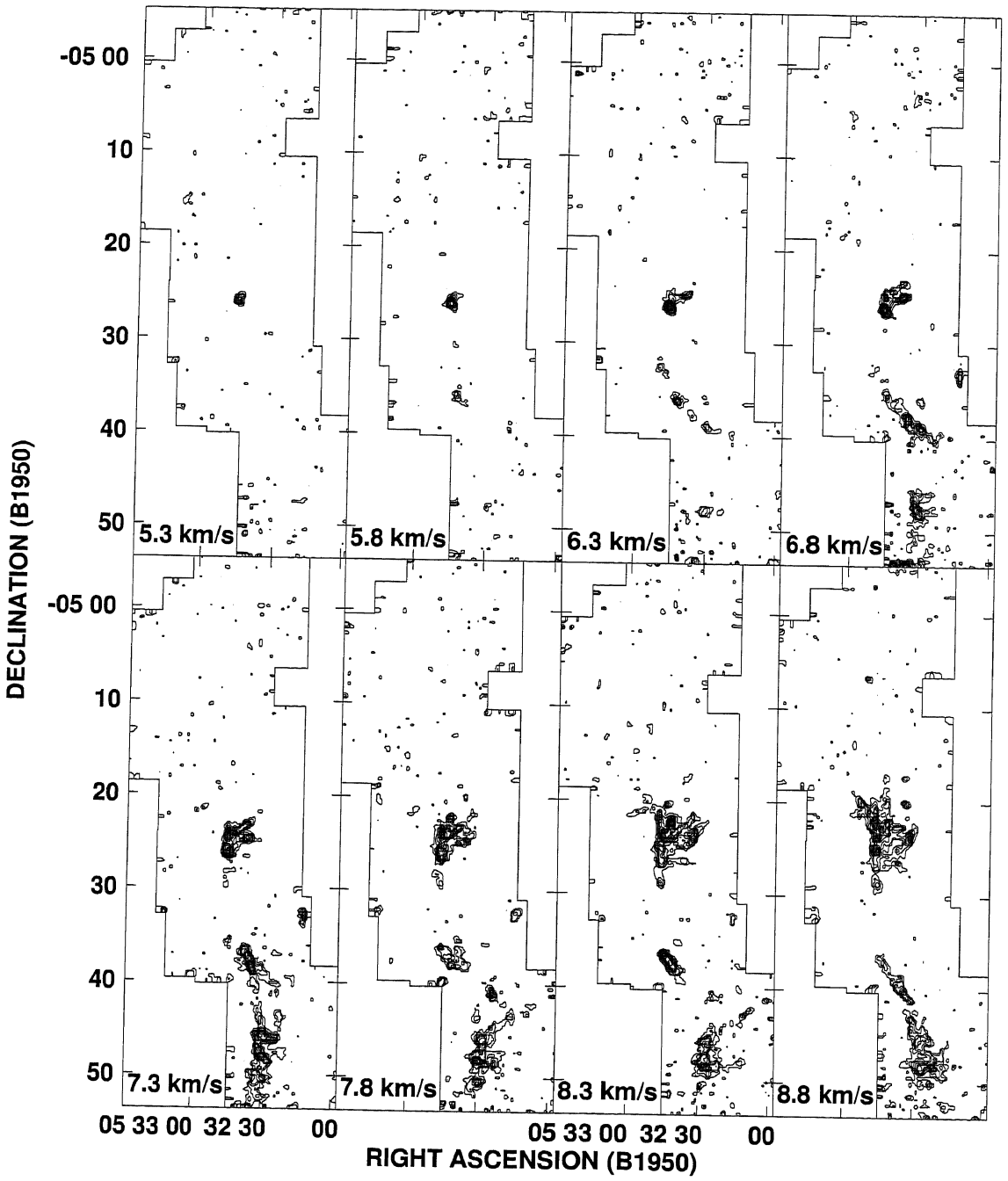

Figure 3.2 Velocity channel maps of the $H^{13}CO^+$ emission in the Orion A cloud for *Dec.* $> -5°50'$. The contour intervals are 0.3 K (correspoinding to 3σ) starting at 0.3 K. The LSR velocity is indicated at the bottom left-hand corner of each panel, and the velocity intervals are 0.5 km s^{-1}.

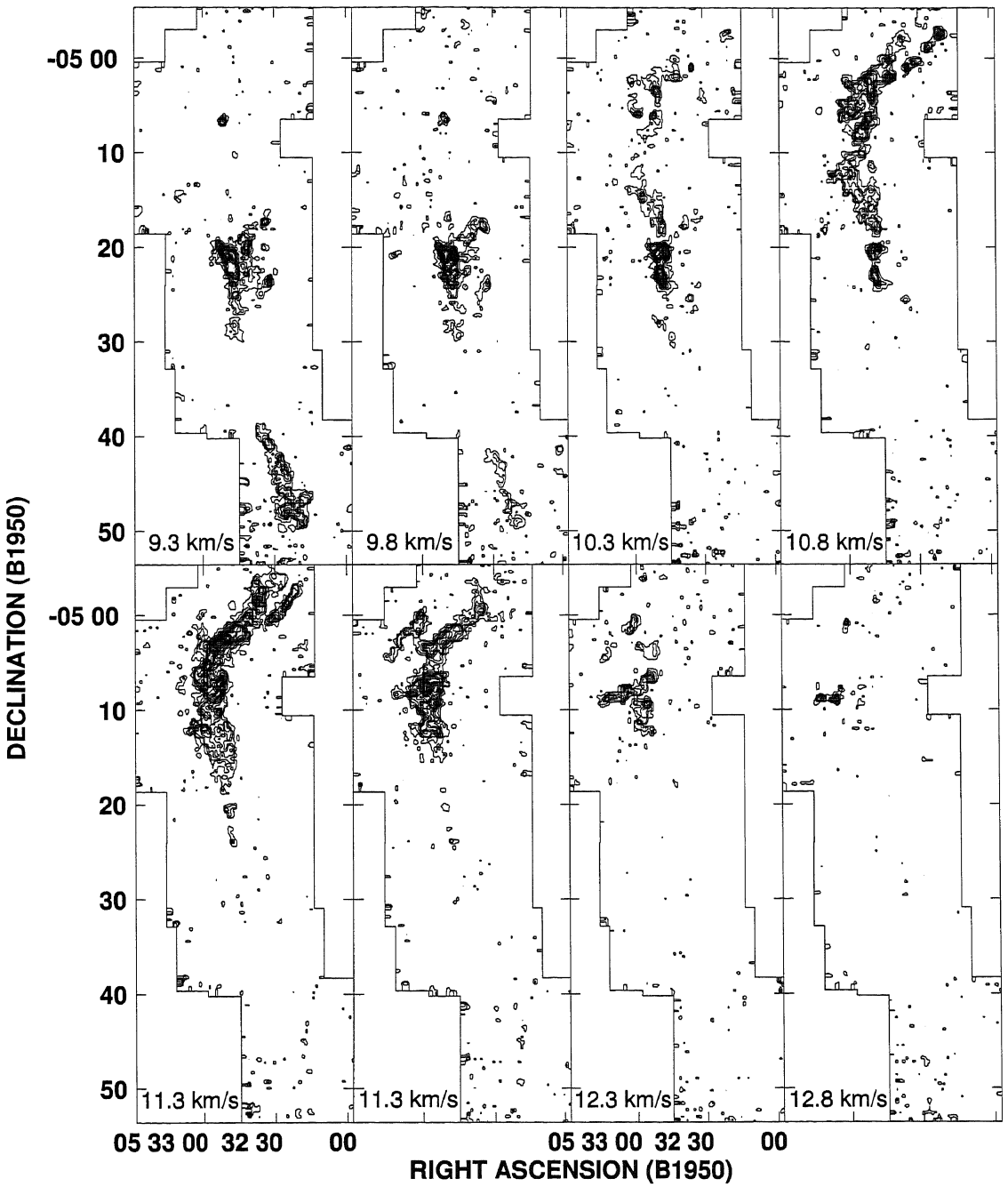

Figure 3.3 Velocity channel maps of the $H^{13}CO^+$ emission in the Orion A cloud for *Dec.* $> -5°50'$ (continued).

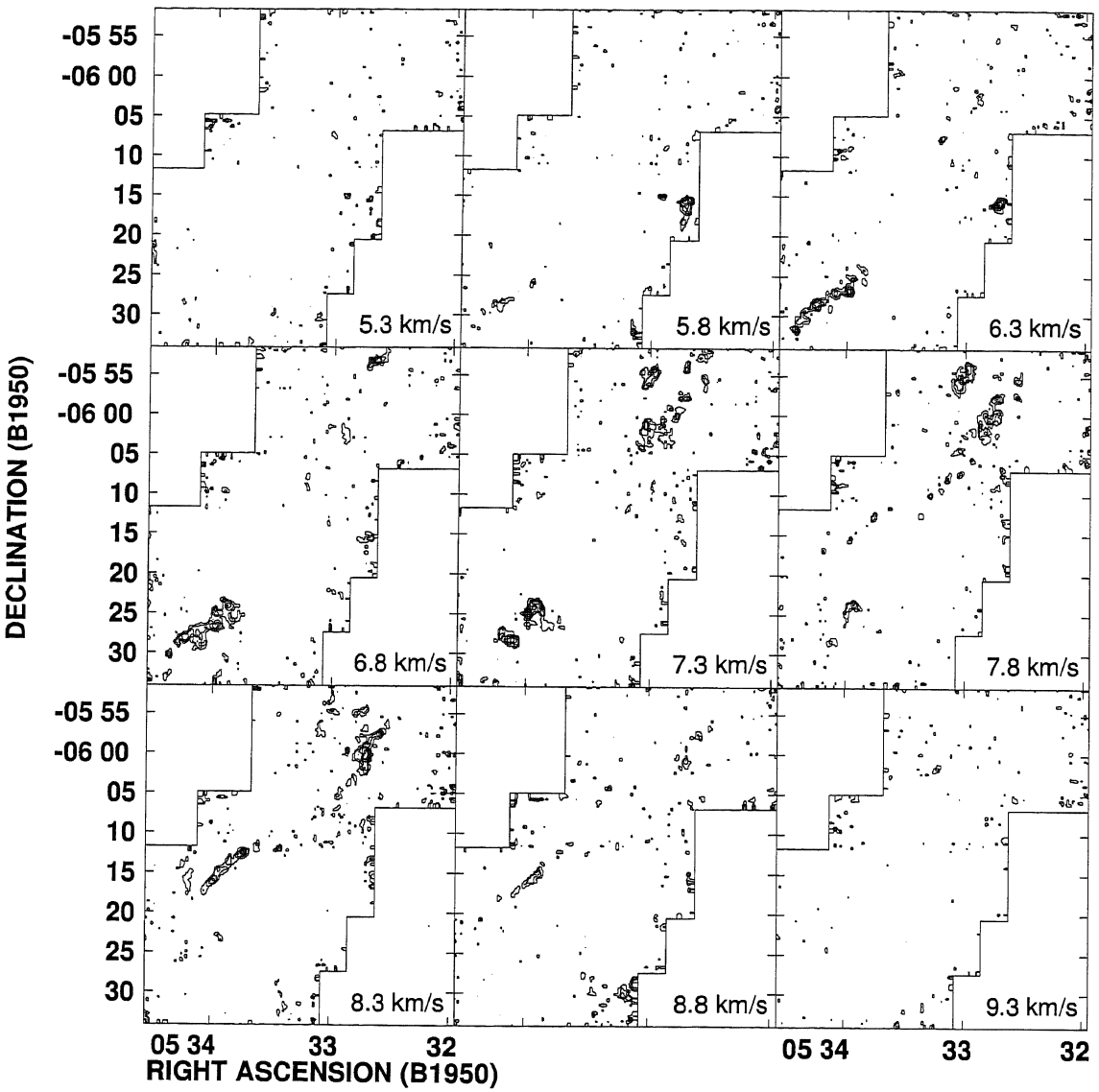

Figure 3.4 Velocity channel maps of the $H^{13}CO^+$ emission in the Orion A cloud for *Dec.* $< -5°50'$ in the same manner as in Figure 3.2.

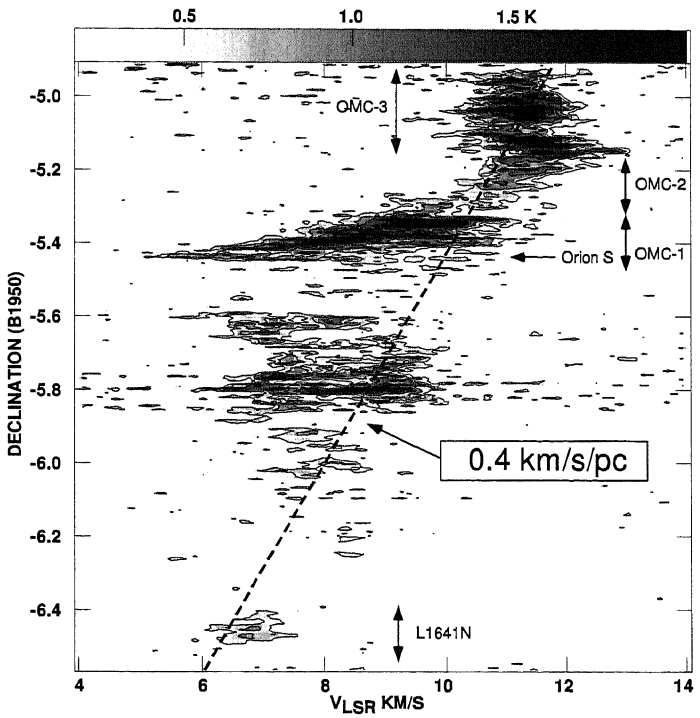

Figure 3.5 Declination-Velocity diagram of the $H^{13}CO^+$ emission in the Orion A cloud. The contour intervals are 0.2 K (correspoinding to 2σ) starting at 0.3 K (correspoinding to 3σ) . The dashed straight line represents the overall velocity gradient of 0.4 km s^{-1} pc^{-1}.

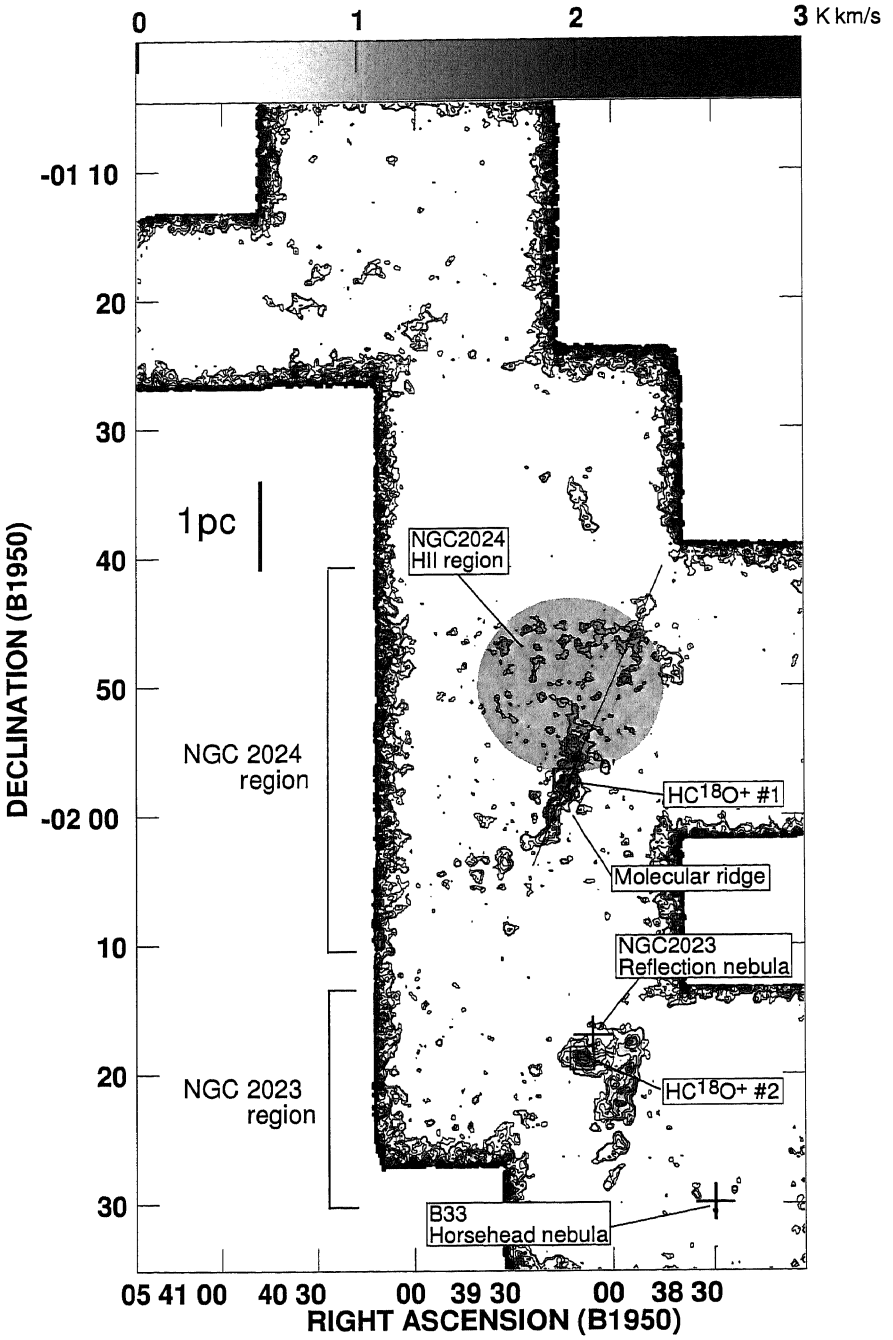

Figure 3.6 Total integrated intensity map of the $H^{13}CO^+(J = 1-0)$ emission ($v_{LSR} = 5-15$ km s^{-1}) of the NGC 2023/2024 region in the Orion B cloud. The contour intervals are 0.3 K km s^{-1} (correspoinding to 3σ) starting at 0.3 K km s^{-1}. The unit of the grey scale is K km s^{-1}. The straight line on the NGC2024 region shows the cutting line of the position-velocity map shown in Figure 3.10. The grey ellipse roughly shows the position and extent of the NGC2024 H II region.

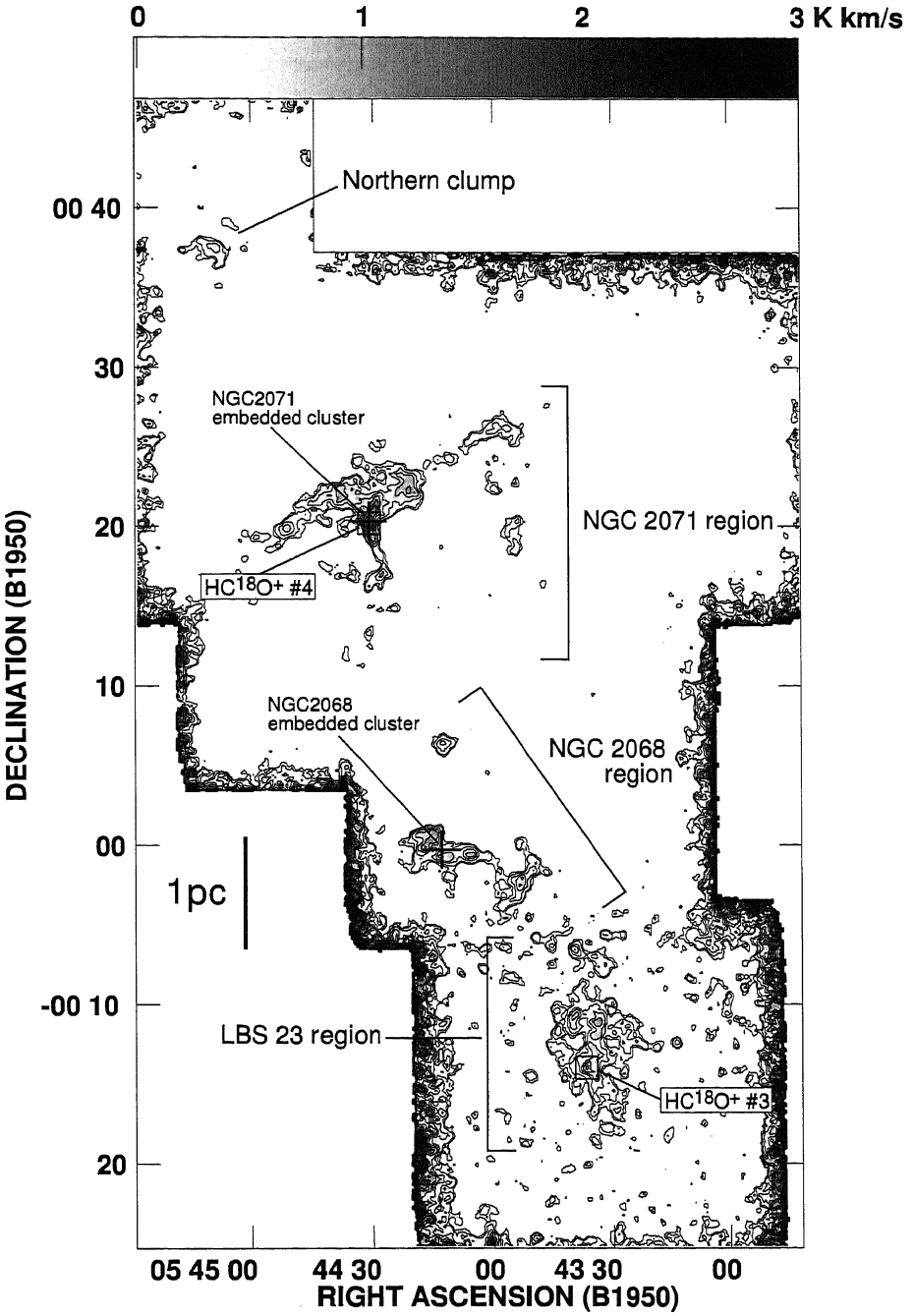

Figure 3.7 Total integrated intensity map of the $H^{13}CO^{+}(J = 1-0)$ emission ($v_{LSR} = 5 - 15$ km s^{-1}) of the NGC 2068/NGC 2071/LBS 23 region in the Orion B cloud. The contour intervals are 0.3 K km s^{-1} (correspoinding to 3σ) starting at 0.3 K km s^{-1}. The unit of the grey scale is K km s^{-1}.

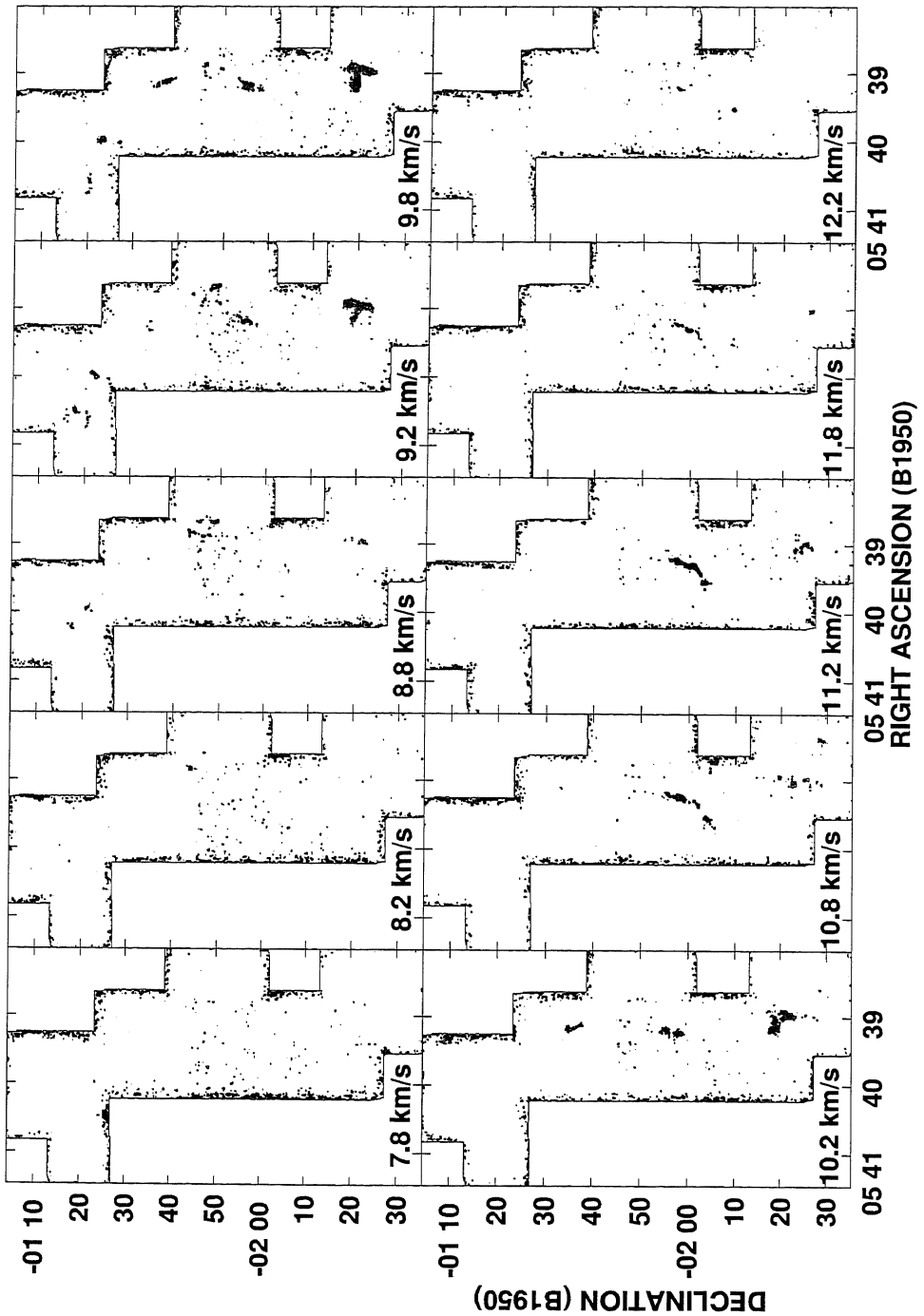

Figure 3.8 Velocity channel maps of the $H^{13}CO^+$ emission of the NGC 2023/2024 regions. The contour intervals are 0.3 K (correspoinding to 3σ) starting at 0.3 K. The LSR velocity is indicated at the bottom left-hand corner of each panel, and the velocity intervals are 0.5 km s^{-1}.

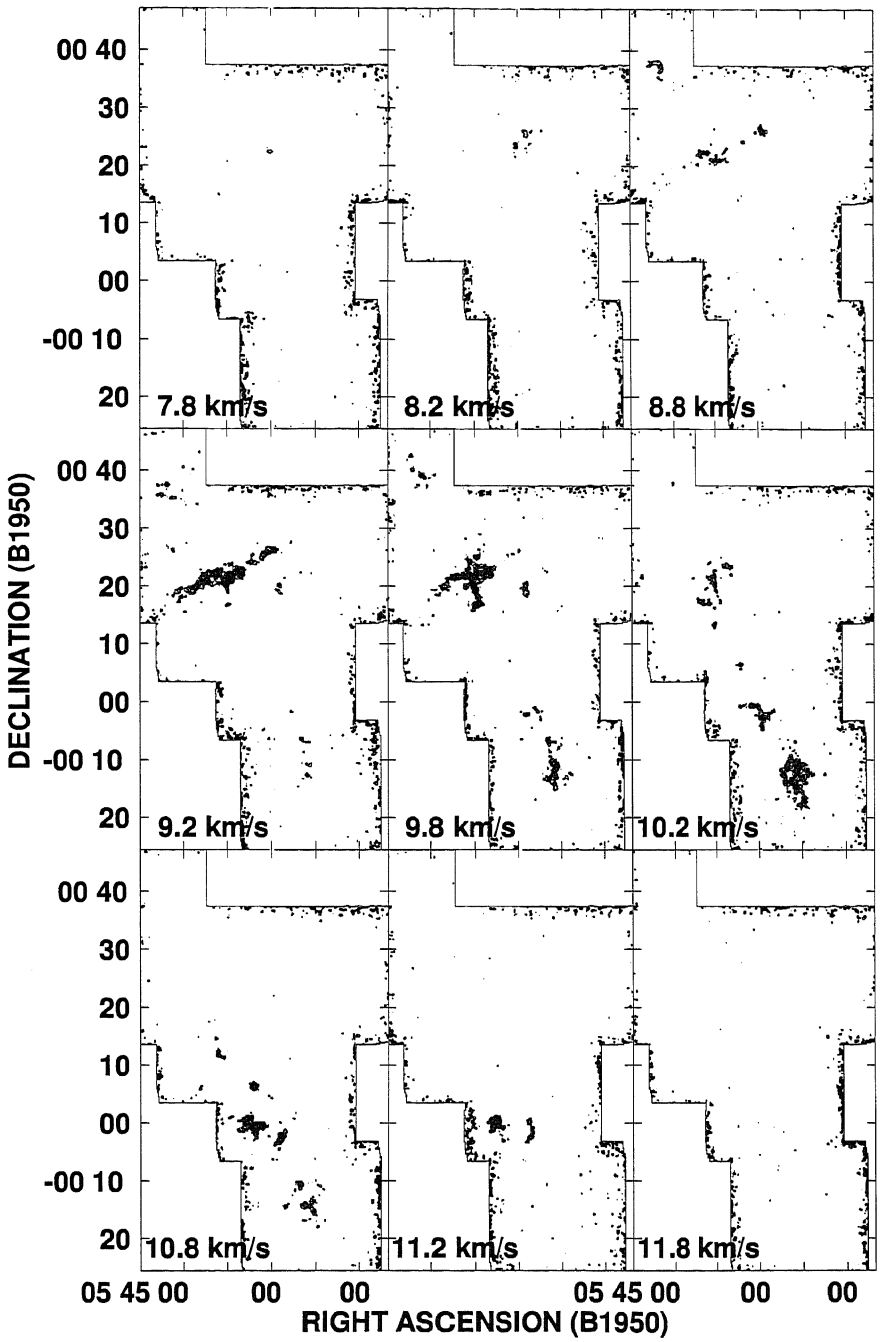

Figure 3.9 Velocity channel maps of the $H^{13}CO^+$ emission in the NGC 2068/NGC 2071/LBS 23 regions. The contour intervals are 0.3 K (correspoinding to 3σ) starting at 0.3 K. The LSR velocity is indicated at the bottom left-hand corner of each panel, and the velocity intervals are 0.5 km s^{-1}.

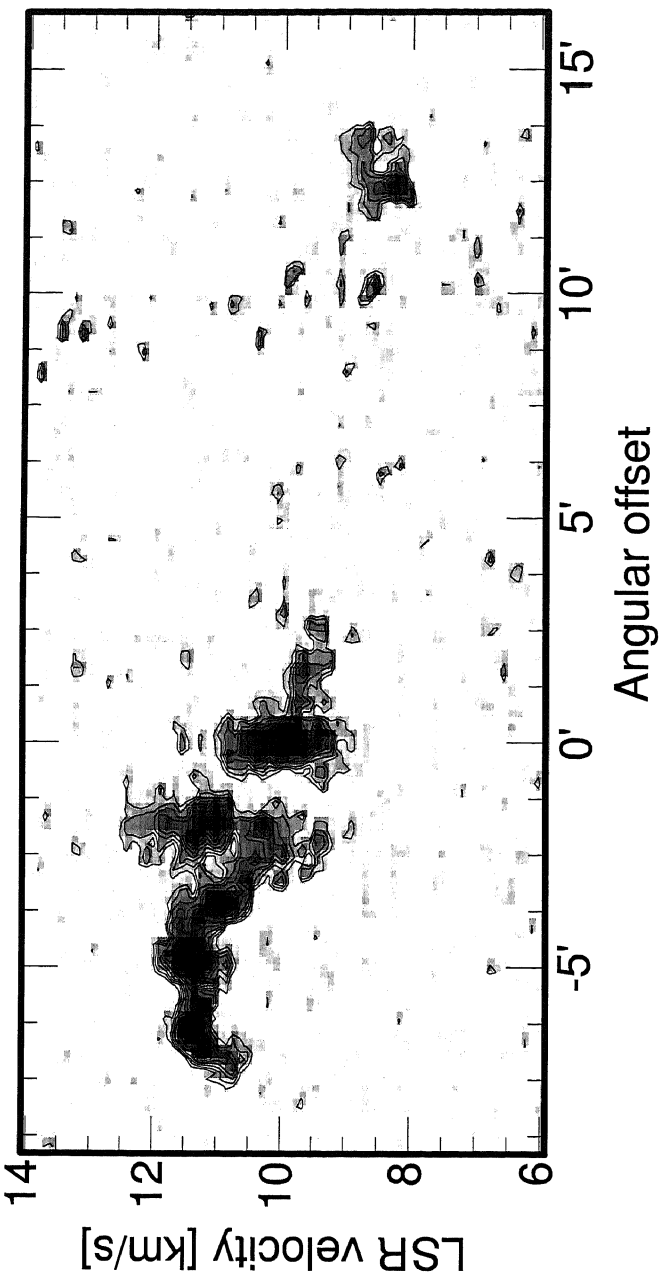

Figure 3.10 Position-Velocity map of the molecular ridge in the NGC2024 region. The contour intervals are 0.1 K, corresponding to 1 σ, starting at 0.3 K. The zero position is $5^h39^m10^s$ and $-1°56'57''$ (see also Figure 3.6).

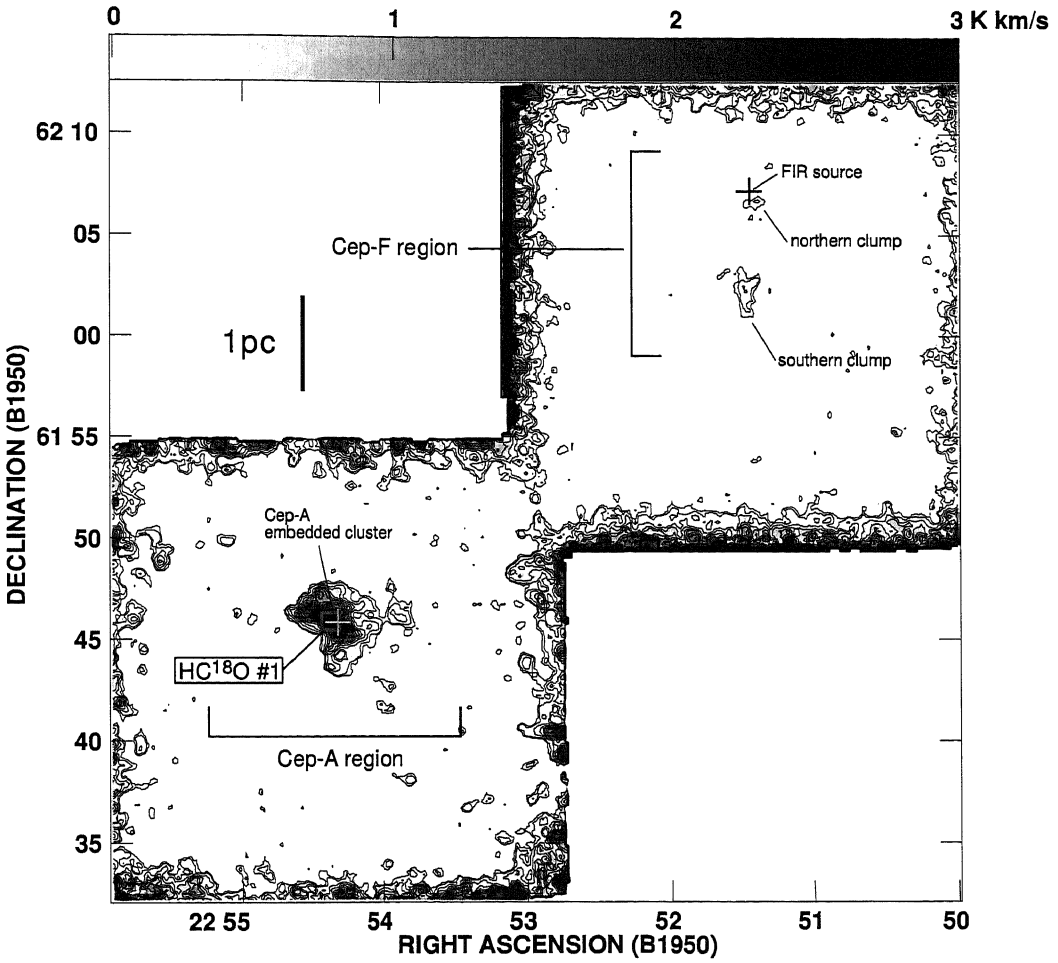

Figure 3.11 Total integrated intensity map of the $H^{13}CO^{+}(J = 1-0)$ emission ($v_{LSR} = -15$ - -5 km s^{-1}) of the Cep-A/Cep-F regions in the Cepheus OB3 cloud. The contour intervals are 0.08 K km s^{-1} (correspoinding to 1σ) starting at 0.24 K km s^{-1}. The unit of the grey scale is K km s^{-1}.

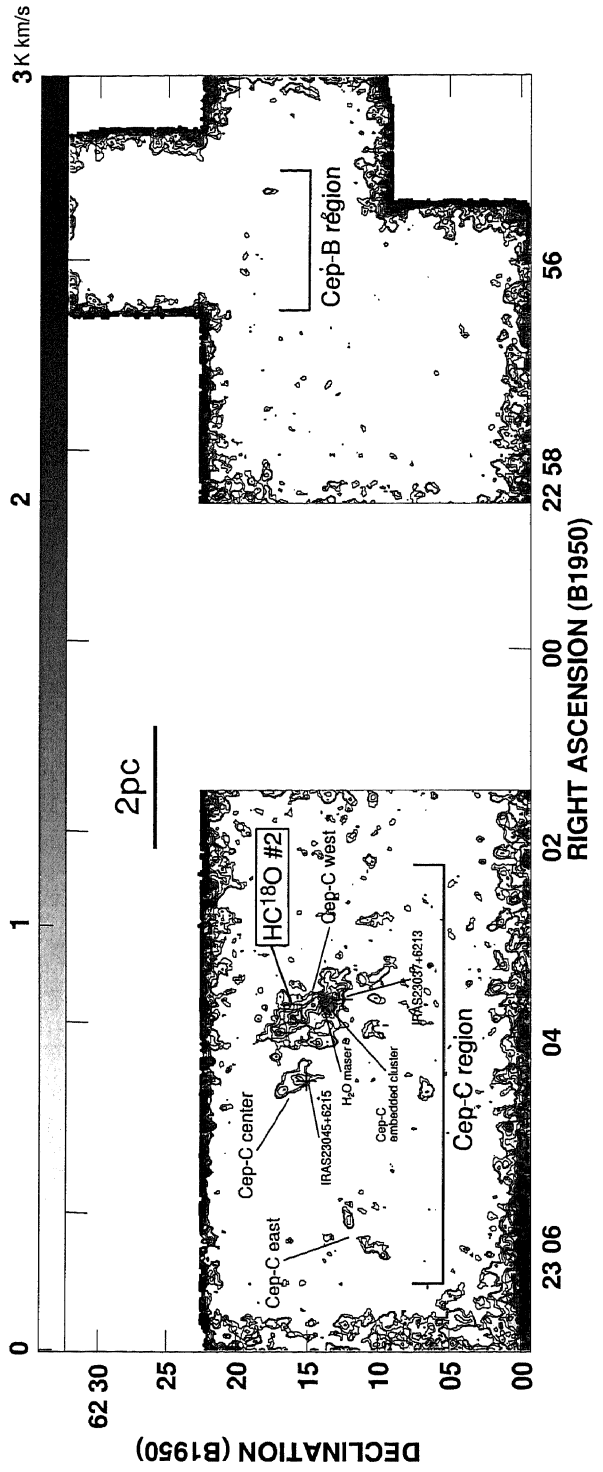

Figure 3.12 Total integrated intensity map of the $H^{13}CO^+(J = 1-0)$ emission ($v_{LSR} = -15$ - -5 km s^{-1}) of the Cep-B and Cep-C regions in the Cepheus OB3 cloud. The contour intervals are 0.08 K km s^{-1} (correspoinding to 3σ) starting at 0.24 K km s^{-1}. The unit of the grey scale is K km s^{-1}.

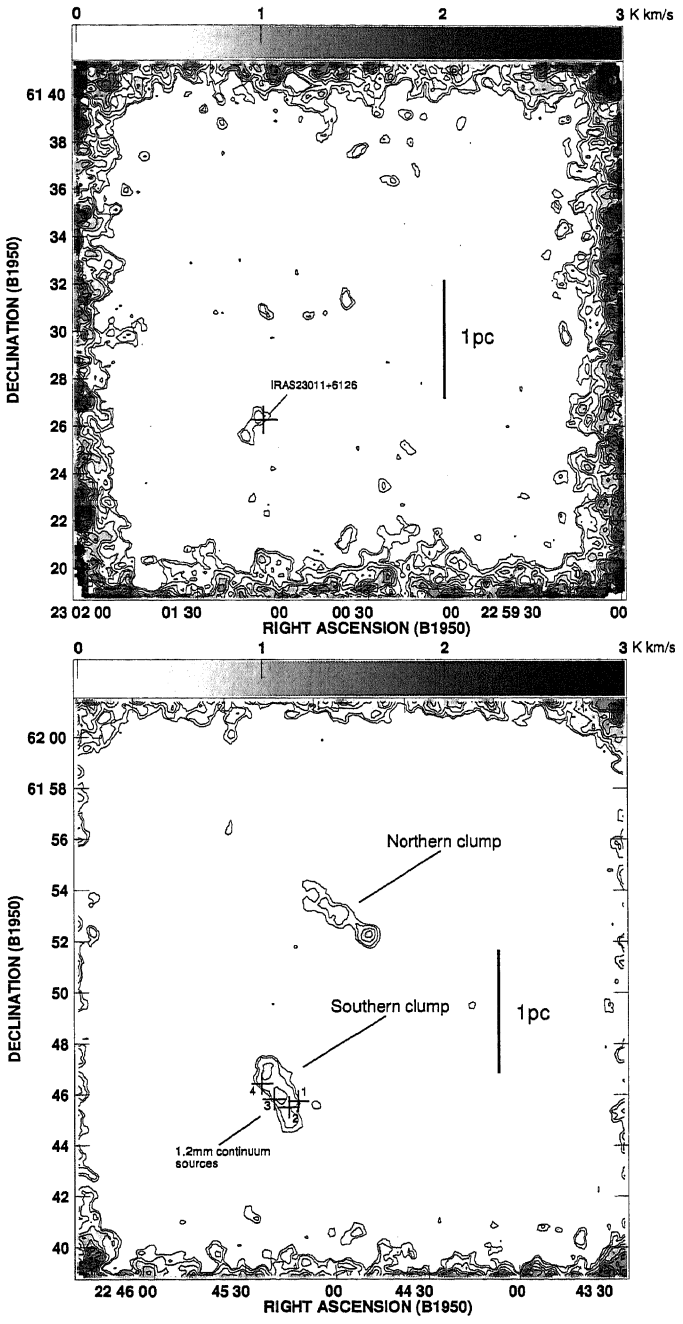

Figure 3.13 (*Top*) Total integrated intensity map of the $H^{13}CO^+(J = 1 - 0)$ emission ($v_{LSR} = -15$ - -5 km s^{-1}) of the Cep-E region in the Cepheus OB3 cloud. The contour intervals are 0.08 K km s^{-1} (correspoinding to 3σ) starting at 0.24 K km s^{-1}. The unit of the grey scale is K km s^{-1}. (*Bottom*) Total integrated intensity map of the $H^{13}CO^+(J = 1 - 0)$ emission ($v_{LSR} = -15$ - -5 km s^{-1}) of the L1211 region in the Cepheus OB3 cloud. The contour intervals are 0.3 K km s^{-1} (correspoinding to 3σ) starting at 0.3 K km s^{-1}. The unit of the grey scale is K km s^{-1}.

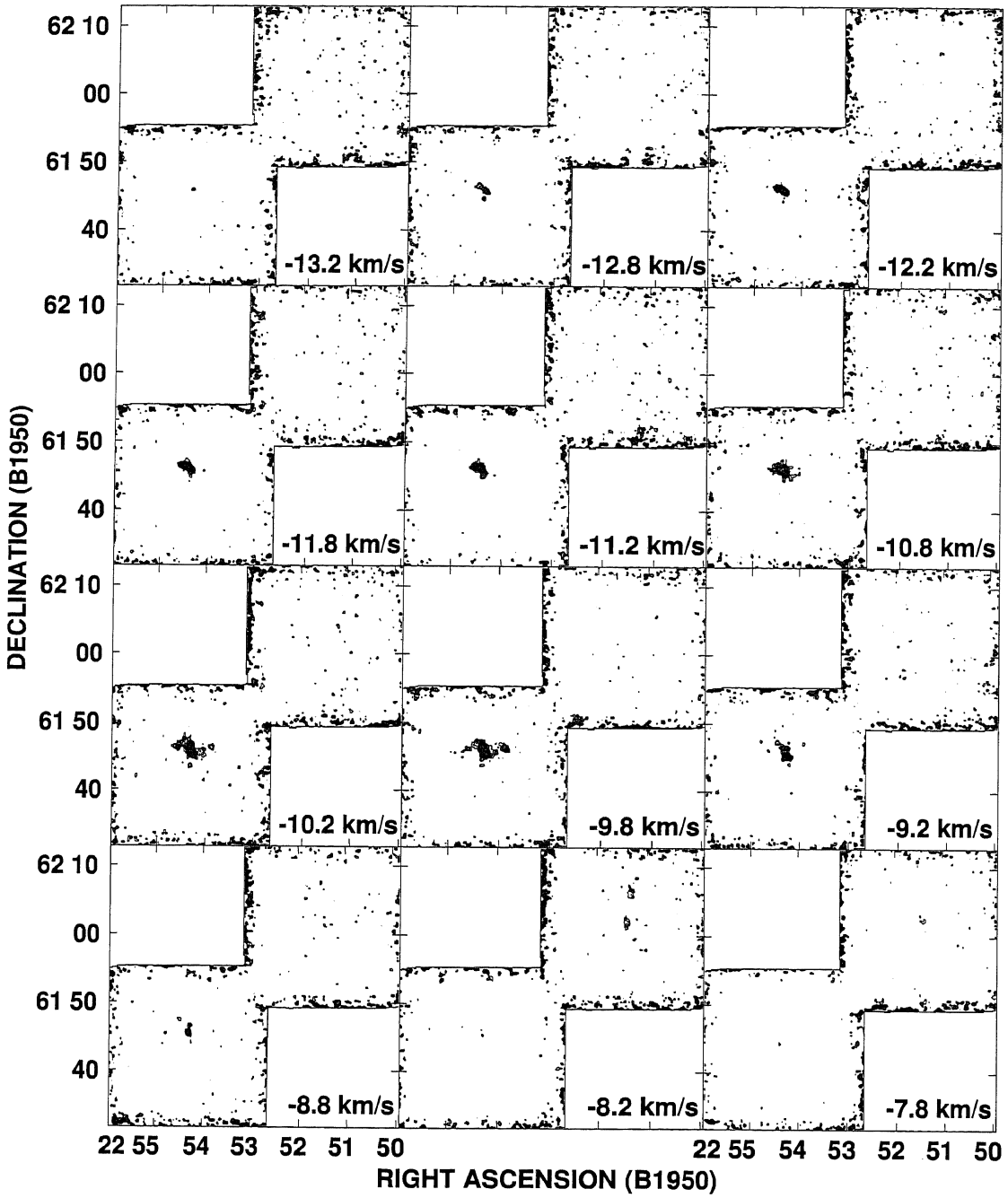

Figure 3.14 Velocity channel maps of the $H^{13}CO^+$ emission in the Cep-A/Cep-F regions. The contour intervals are 0.08 K (correspoinding to 1σ) starting at 0.24 K. The LSR velocity is indicated at the bottom right-hand corner of each panel, and the velocity intervals are 0.5 km s^{-1}.

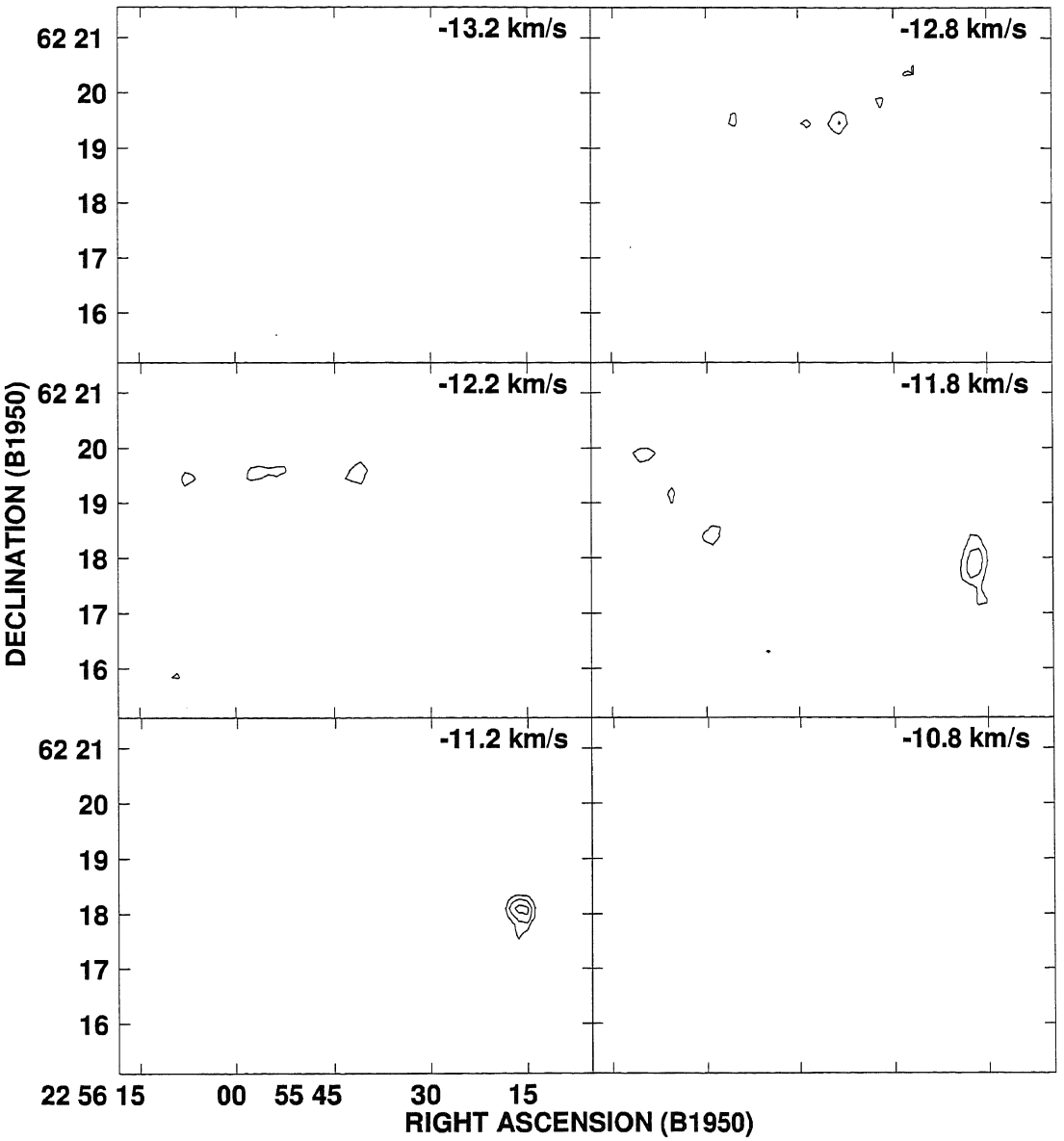

Figure 3.15 Velocity channel maps of the $H^{13}CO^+$ emission in the Cep-B region. The contour intervals are 0.08 K (correspoinding to 1σ) starting at 0.24 K. The LSR velocity is indicated at the top right-hand corner of each panel, and the velocity intervals are 0.5 km s^{-1}.

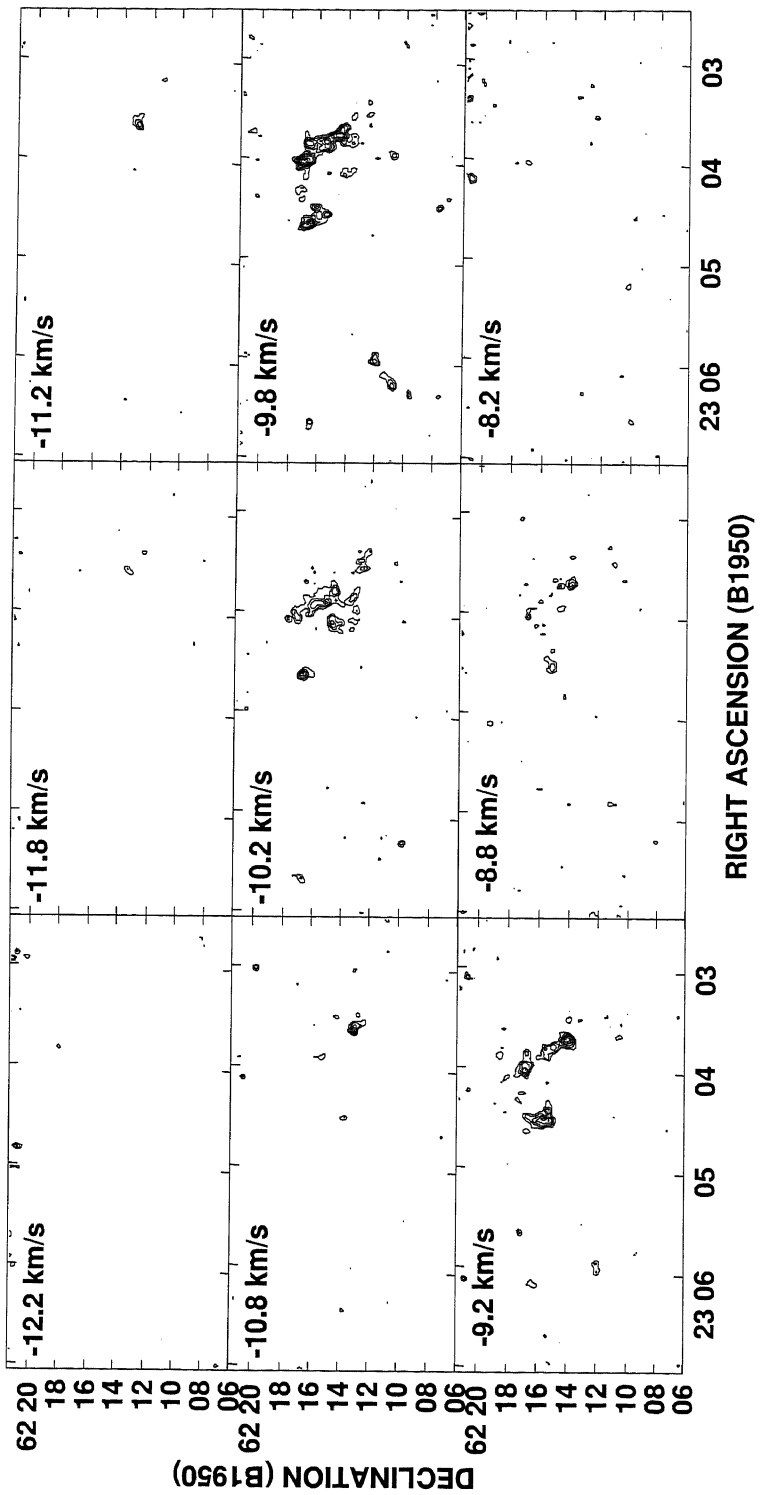

Figure 3.16 Velocity channel maps of the $H^{13}CO^+$ emission in the Cep-C region. The contour intervals are 0.08 K (correspoinding to 1σ) starting at 0.24 K. The LSR velocity is indicated at the top left-hand corner of each panel, and the velocity intervals are 0.5 km s^{-1}.

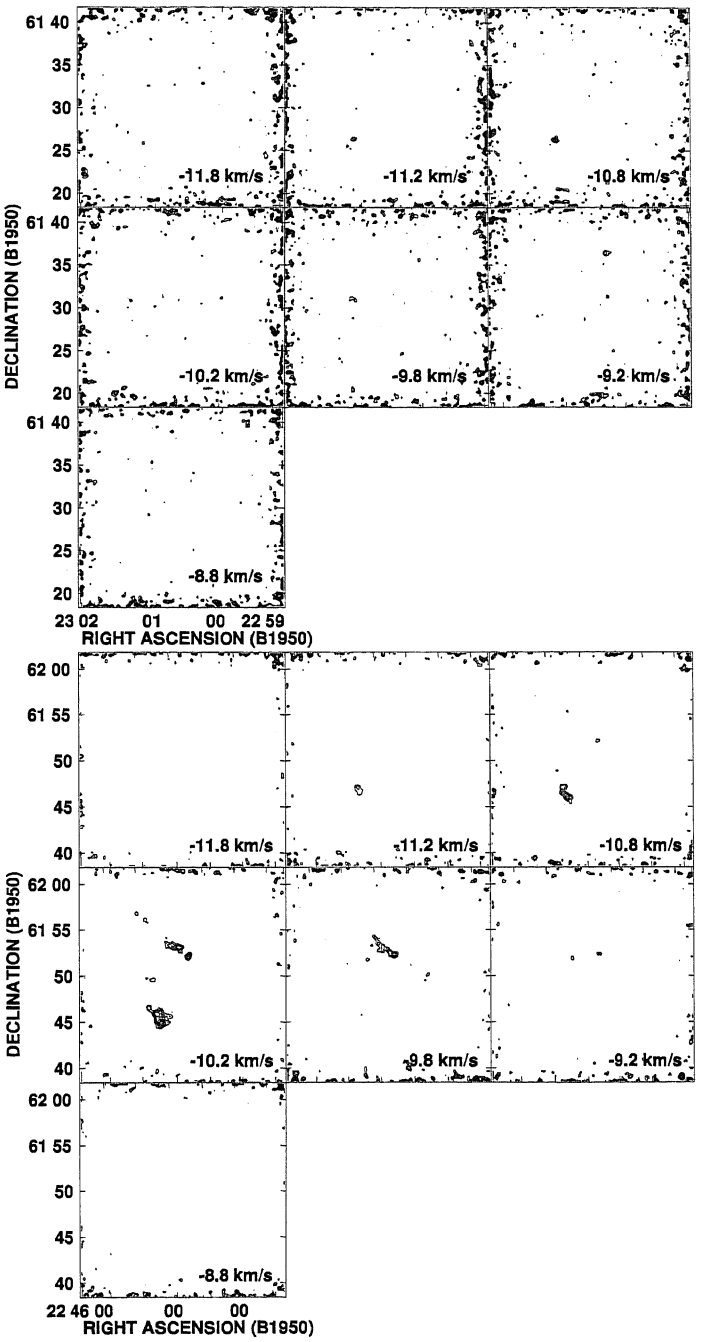

Figure 3.17 Velocity channel maps of the $H^{13}CO^+$ emission in the Cep-E (*Top*) and L1211 region (*Bottom*). The contour intervals are 0.08 K (corrospoinding to 1σ) starting at 0.24 K. The LSR velocity is indicated at the botom right-hand corner of each panel, and the velocity intervals are 0.5 km s^{-1}.

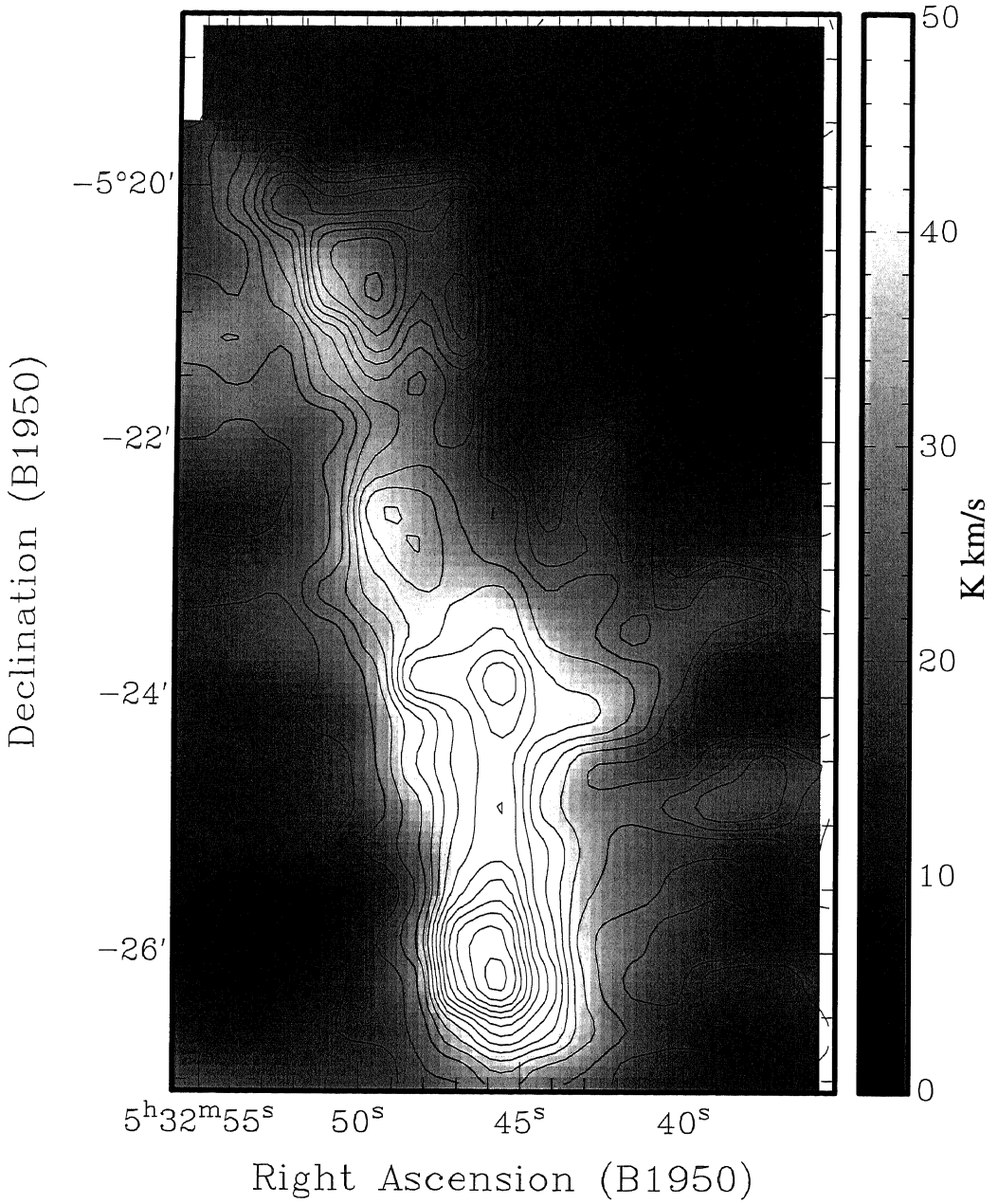

Figure 3.18 Region of that we estimated the optical depth of the $H^{13}CO^+(1-0)$ emission in the Orion A. The grey scale and contour map show the integrated intensity distribution of the $H^{12}CO^+(1-0)$ and $H^{13}CO^+(1-0)$ emission, respectively. The contour starts at 0.3 K km s^{-1}, corresponding to 3 σ, and the interval is 0.3 K km s^{-1}.

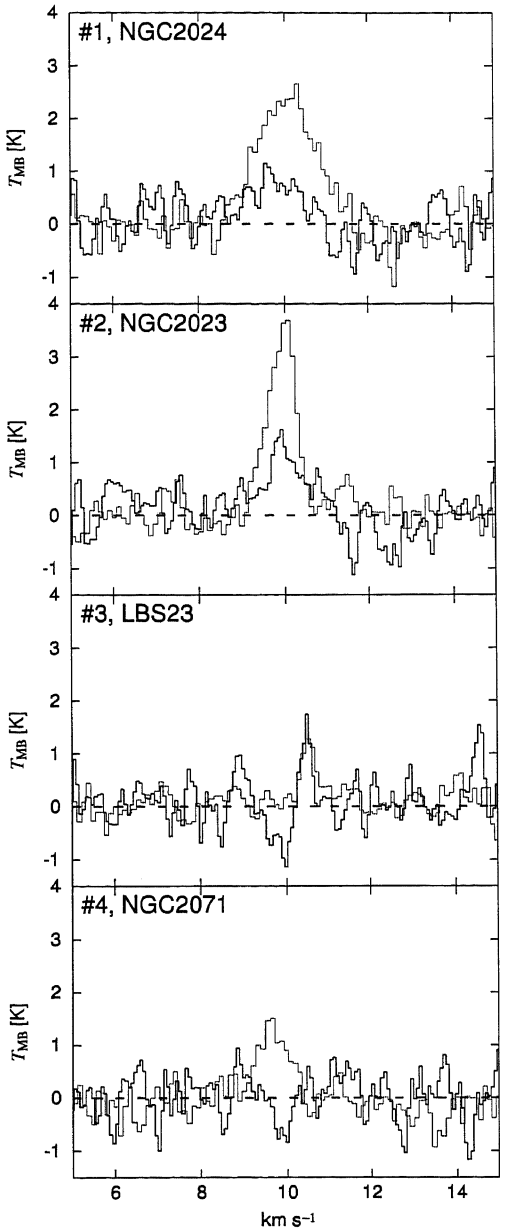

Figure 3.19 Spectra of the $HC^{18}O^+$ (thick-color) and $H^{13}CO^+$ emission (thin-color). The intensities of the $HC^{18}O^+$ emission are multiplied by 5.5.

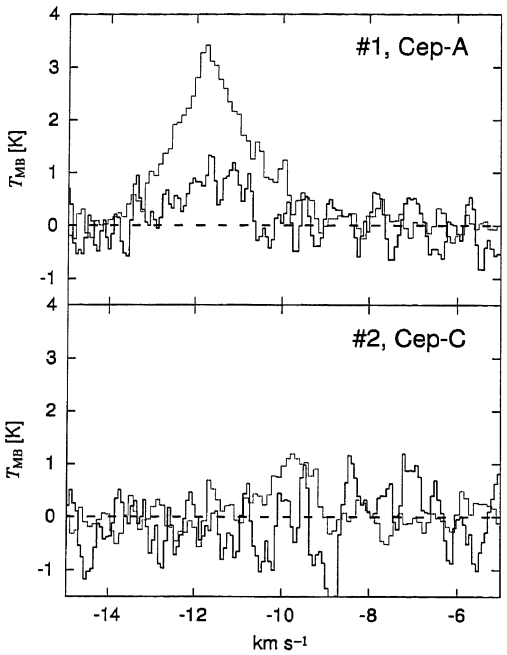

Figure 3.20 Spectra of the $HC^{18}O^+$ (thick-color) and $H^{13}CO^+$ emission (thin-color). The intensities of the $HC^{18}O^+$ emission are multiplied by 5.5.

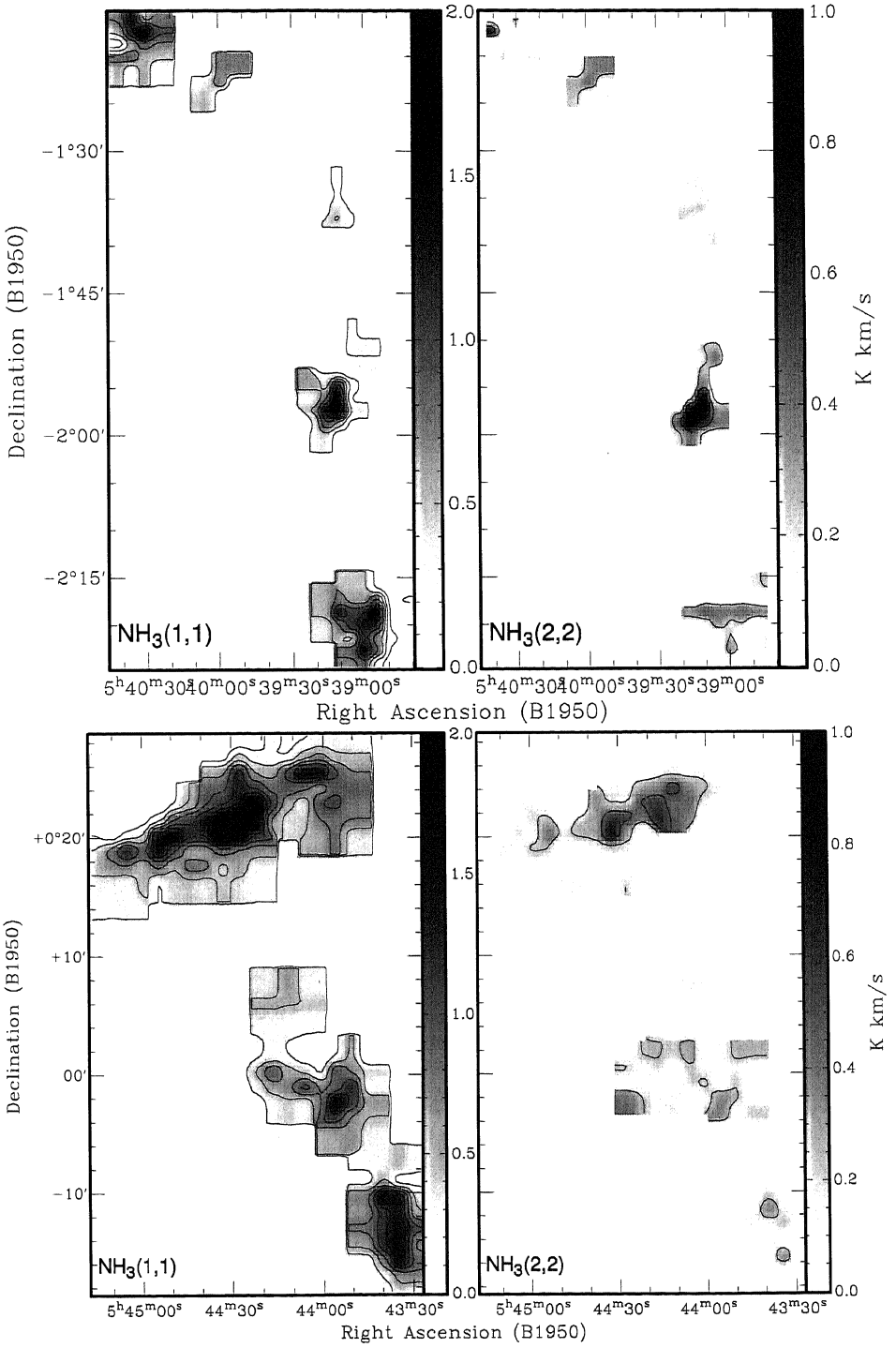

Figure 3.21 Total integrated intensity maps of the (1,1) and (2,2) inversion line of the NH_3 molecule in the NGC 2024/2023 regions (*Top*) and in the NGC 2068/2071 regions (*bottom*). The contour interval is 0.24 K km s^{-1}, corresponding 3 σ, starting at 0.24 K km s^{-1}.

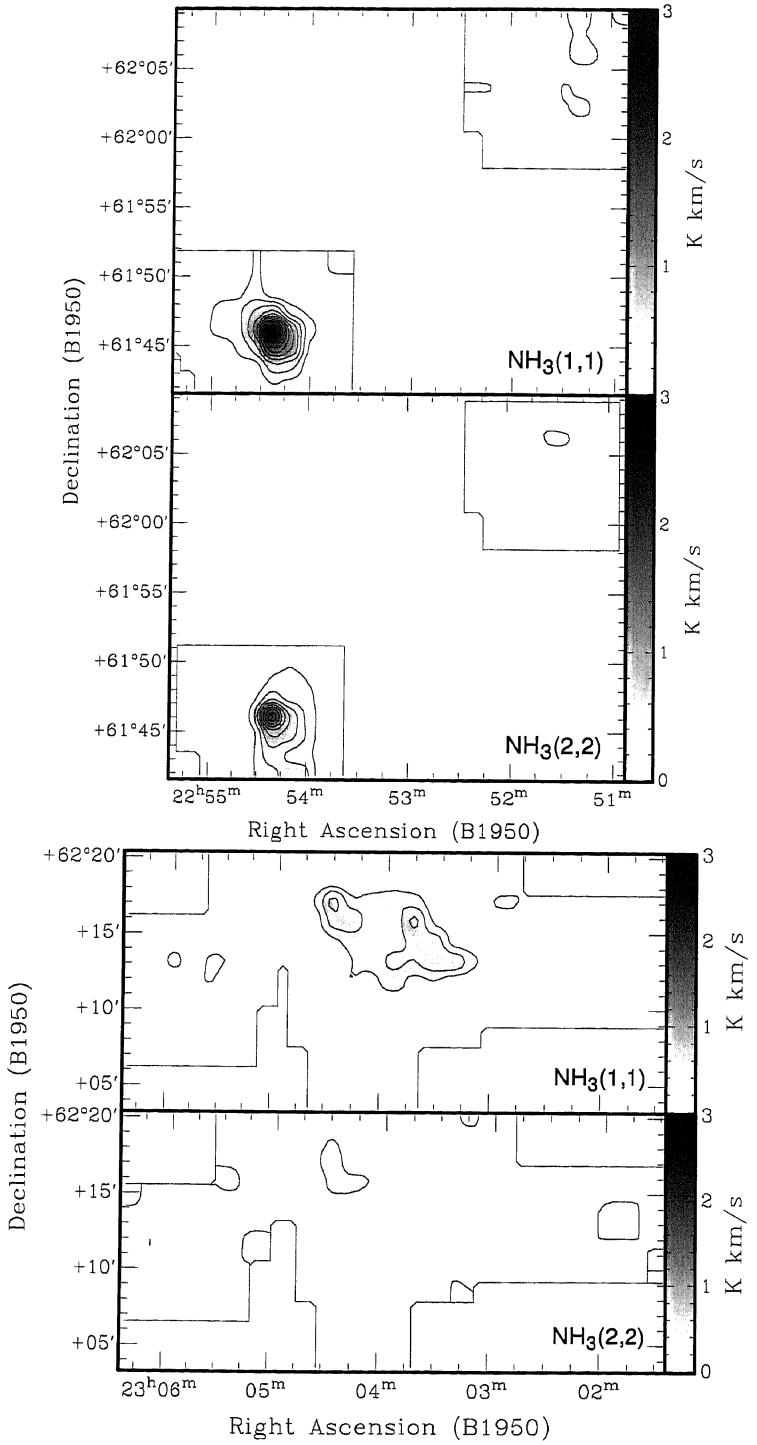

Figure 3.22 Total integrated intensity maps of the (1,1) and (2,2) inversion line of the NH_3 molecule in the Cep-A/F regions (*Top*) and in the Cep-C region (*bottom*). The contour interval is 0.24 K km s^{-1}, corresponding 3 σ, starting at 0.24 K km s^{-1}.

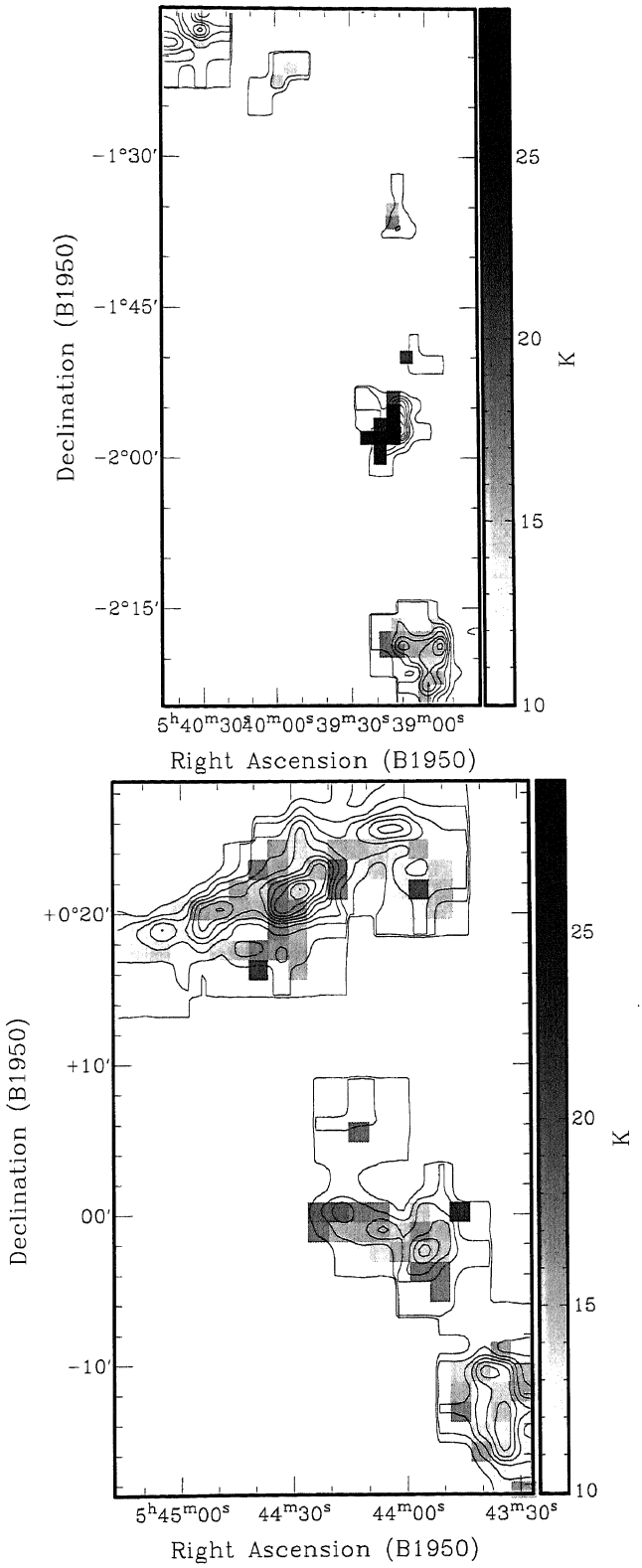

Figure 3.23 Rotational temperature distributions in the NGC 2024/2023 regions (*Left*) and in the NGC 2068/2071 regions (*Right*) are shown with the greyscale. The (1,1) total integtated intensity is also shown with the contour, starting at 0.24 K km s^{-1}, corresponding to 3 σ, and the interval of 0.24 K km s^{-1}, corresponding to 3 σ.

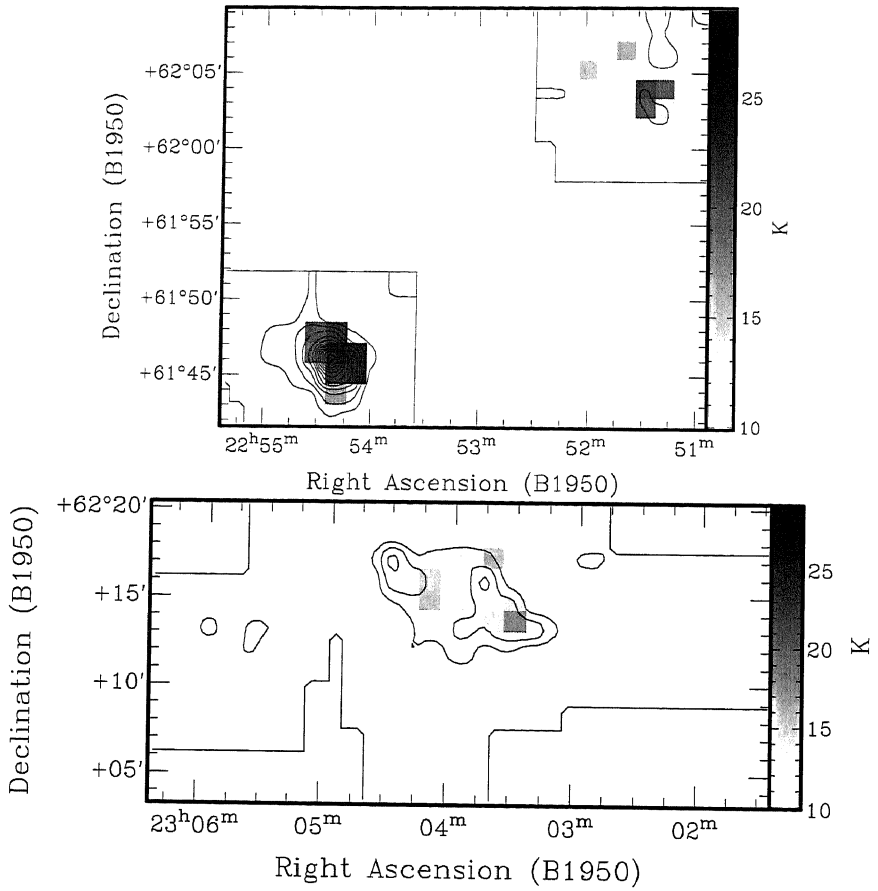

Figure 3.24 Rotational temperature distributions in the Cep-A/F regions (*Top*) and in the Cep-C region (*Bottom*) are shown with the greyscale. The (1,1) total integtated intensity is also shown with the contour, starting at 0.24 K km s^{-1}, corresponding to 3 σ, and the interval of 0.24 K km s^{-1}, corresponding to 3 σ.

Table 3.1. Observing points and intensity of the $HC^{18}O^+$ emission

Cloud	#	R.A.(B1950)	Dec.(B1950)	$T_{MB,H^{13}CO^+}$ K	$T_{MB,HC^{18}O^+}$ K	R.M.S. in T_{MB} K
Orion B	1	$5^h39^m11^s$	-1°55′45″	2.5	0.15*	0.075
	2	$5^h39^m9^s$	-2°18′50″	3.6	0.23	0.075
	3	$5^h43^m37^s$	-0°14′40″	1.2	0.29	0.083
	4	$5^h44^m32^s$	0°19′50″	1.4	undetected	0.075
Cepheus	1	$22^h54^m25^s$	61°46′0″	2.8	0.18*	0.066
	2	$23^h3^m53^s$	62°17′10″	0.94	undetected	0.10

*Marginal ($< 3\sigma$) detection.

Chapter 4

$H^{13}CO^+$ Core Catalog

In this chapter we describe the $H^{13}CO^+$ core catalog. The identification of the cores from the $H^{13}CO^+$ data cube, the mass detection limit, and the derivation of core physical properties are presented first. Next we show the property distributions, correlations, and CMFs through the comparison with the previous results and between the three clouds.

4.1 Core Identification

To identify dense cores from the $H^{13}CO^+$ 3-D ($\alpha - \delta - v_{\rm LSR}$) data, we used the clumpfind algorithm (Williams et al., 1994) . Williams et al. (1994) showed that misidentification of cores is minimized by taking the threshold contour level of 2σ, where 1σ is the rms noise level of the data. We, therefore, adopted the threshold level of 0.17 K, 0.28 K, and 0.26 K for the Orion A, Orion B, and Cepheus OB3 clouds, respectively. The clumpfind automatically rejected core candidates in which the number of pixels in the core is less than 4 as fake cores due to noise. Among the clumpfind-identified core candidates, we rejected core candidates located at the edge of the observed region. Furthermore, we rejected ambiguous or fake core candidates whose size and velocity width are smaller than the spatial and velocity resolutions, respectively: a core must

contain 2 or more continuous velocity channels, each of which has at least 3 pixels which have intensities above 3 σ level, and the pixels must be connected to each other in both the space and velocity domains. Following the above procedure, we have finally identified 236, 98, and 31 cores in the Orion A, Orion B, and Cepheus OB3 clouds, respectively. Table 4.1 summarizes the parameters for the clumpfind and the core-identification results. Figures 4.1 and 4.2, for example, show the mimimum mass (# A168 of table A.1 described in sect. 4.2.1) and maximum mass (# A142) cores in the Orion A, respectively. Some ($\sim$ 6 %) of the core candidates that the clumpfind identified contain a few isolated pixels. For such core candidates, we did not use the isolated pixels for further analysis. The total mass of the identified cores is 2500 $M_\odot$, 872 $M_\odot$, and 698 $M_\odot$ in Orion A, the Orion B, and Cepheus OB3, respectively. The total core masses are about 60 % of the total mass traced by the $H^{13}CO^+$ emission.

Next, we estimate the mass detection limit in our identification. According to our definition of the dense core, a core with the detection limit mass has six pixels above the 3 σ level over two velocity channels and all the 3-σ level pixels are surrounded by three to five 2-σ level pixels. There are 21 possible configurations of the six 3-σ level pixels, and Figure 4.3 shows six representative patterns out of 21 possible configurations. The total intensity of the minimum mass core becomes the 58 and 62 σ levels for the eleven and ten patterns, respectively. Therefore the cores whose mass is the mass detection limit have the total intensity, $\sum T$, of 58 σ. Using Eqs. 4.5, the corresponding masses are 1.58 $M_\odot$ in the Orion A, 1.3 $M_\odot$ in the Orion B, and 3.6 $M_\odot$ in the Cepheus OB3 cloud. It should be noted that the mass detection limit is *not* the completeness limit in our survey. If several cores with similar radial velocities overlap each other, we would mis-identify such a group as one core. We refer to this effect as confusion in the following and discuss the influence of the confusion effect on the CMF in sect. 5.3.

4.2 Core Properties

4.2.1 Derivation of Core Properties

We show all of the physical properties of the $H^{13}CO^+$ cores in Tables A.1, A.2, and A.3 in the Orion A, Orion B and Cepheus OB3 clouds, respectively. We summarize the minimum, maximum and mean values of each quantity in Table 4.2, 4.3, and 4.4. In this subsection we describe the definition and derivation of the core physical properties.

The position and LSR velocity of each core are those of the most intense pixel with $T^*_{\rm A,peak}$ in the core. The aspect ratio is defined as the ratio of the major to minor axis length, which are derived by 2-D Gaussian fitting to the total integrated intensity map of each core with a 2-σ level threshold. We define the apparent core radius $R_{\rm obs}$ as,

$$R_{\rm obs} = \left(\frac{A}{\pi}\right)^{1/2}, \tag{4.1}$$

assuming the core is a sphere. Here A is the projected area of the integrated intensity map of each core, derived by the clumpfind. Assuming a Gaussian intensity profile, we estimate the core radius $R_{\rm core}$ by correcting for the telescope beam as follows,

$$R_{\rm core} = \left\{ R^2_{\rm obs} - \left[\frac{\Delta\theta_{\rm eff}/2}{\sqrt{2\ln 2}} \left(2\ln \frac{I_{\rm peak}}{\Delta I} \right)^{1/2} \right]^2 \right\}^{1/2}, \tag{4.2}$$

where $I_{\rm peak}$ is the peak intensity of the core, and ΔI the threshold level in core identification (see appendix A of Williams et al., 1994).

To derive the apparent velocity width in FWHM $dv_{\rm obs}$, we first calculated a velocity dispersion within the core. Then we multiplied the velocity dispersion by $2\sqrt{2\ln 2}$ to convert to the FWHM assuming a Gaussian velocity

profile. Therefore $dv_{\rm obs}$ is given by

$$dv_{\rm obs} = 2\sqrt{2\ln 2}\left[\frac{\sum_i v_i^2 I_i}{\sum_i I_i} - \left(\frac{\sum_i v_i I_i}{\sum_i I_i}\right)^2\right]^{1/2}, \quad (4.3)$$

where v_i and I_i are the radial velocity and intensity of the i-th pixel in each core, respectively. As in the case of $R_{\rm core}$, the core velocity width $dv'_{\rm core}$ should be corrected for the velocity resolution, $dv_{\rm spec}$ of the spectrometers as follows,

$$dv'_{\rm core} = \left(dv^2_{\rm obs} - dv^2_{\rm spec}\right)^{1/2}, \quad (4.4)$$

where $dv_{\rm spec} = 0.13$ km s^{-1}. Furthermore, we corrected for the line broadening due to the hyperfine splitting of $H^{13}CO^+$ with a separation of 0.13 km s^{-1} and an intrinsic intensity ratio of 3:1 (Schmid-Burgk et al., 2004) considering that the $H^{13}CO^+$ emission is optically thin. Since the hyperfine separation is almost the same as our velocity resolution, the influence of the line broadening on $dv_{\rm core}$ is found to be small: $dv'_{\rm core} - dv_{\rm core} \leq 0.04$ km s^{-1}, which is significantly smaller than the velocity resolution of 0.13 km s^{-1}.

Assuming the optically thin $H^{13}CO^+(J = 1$ - $0)$ emission as described in sect. 3.4 and Local Thermodynamic Equilibrium (LTE), we estimated the core mass as follows,

$$M_{\rm LTE} = 9.91\times10^{-2}\left(\frac{X_{\rm H^{13}CO^+}}{4.8\times10^{-11}}\right)^{-1} T_{\rm ex}e^{4.16/T_{\rm ex}} \left(\frac{D}{480{\rm pc}}\right)^2\left(\frac{\Delta\theta_{\rm grid}}{20''.55}\right)^2\left(\frac{\eta}{0.51}\right)^{-1}\left(\frac{\Sigma_i T^*_{{\rm A},i}\Delta v_i}{\rm K\ km\ s^{-1}}\right) \quad [M_\odot] \quad (4.5)$$

where $X_{\rm H^{13}CO^+}$ is the fractional abundance of $H^{13}CO^+$ relative to H_2, $T_{\rm ex}$ the excitation temperature, D the distance to the clouds, $\Delta\theta_{\rm grid}$ the spatial grid size of the 3-D cube, and $\Sigma_i T^*_{{\rm A},i}\Delta v_i$ the total integrated intensity of the core. For D, we adopted 480 pc (Genzel et al., 1981) in the Orion A, 470 pc (Wilson et al., 2005) in the Orion B, and 730 pc (Garmany, 1973) in the

Cepheus OB3 cloud. For T_{ex}, we used the rotational temperature T_R derived from the NH_3 observations. In the Orion A, the uniform T_R of 20 K derived from the NH_3 observations of the ISF by Cesaroni & Wilson (1994) was adopted. Since the south region is far from heating sources such as the OB associations and the H II region, this assumption might lead to overestimate of the core mass in the south region by a factor of two. For the Orion B and Cepheus OB3 clouds, we used T_R derived from our NH_3 observations (see Section 3.5). Of course, the whole of the observed region does not have enough quality to derive T_R accurately. In such positions we used the mean value of the derived T_R of 16.1 K and 17.0 K, in the Orion B and Cepheus OB3 clouds, respectively.

However, the most ambiguous factor in estimating the mass is $X_{H^{13}CO^+}$. Butner et al. (1995) obtained $[H^{13}CO^+]/[H_2] = 3 \times 10^{-11}$ to 4×10^{-10} for 27 low-mass cores. The region-to-region scatter of the abundance is a factor of ~10. In the Orion A, Ungerechts et al. (1997) derived $[HCO^+]/[^{12}CO] = (3.4 \pm 2.1) \times 10^{-5}$. This value can be converted to the fractional abundance $X_{H^{13}CO^+}$ of 4.8×10^{-11}, by using $[^{13}CO]/[H_2] = 1.4 \pm 10^{-6}$ (Frerking et al., 1982) and $[^{13}CO]/[^{12}CO] \sim [^{13}C]/[^{12}C] = 43 \pm 7$ (Savage et al., 2002). In the Orion B, we used the same value of $X_{H^{13}CO^+}$ in the Orion A because the positions of the Orion B and the Orion A in the Galaxy are almost the same and environments around them is expected to be very similar. In the Cepheus OB3 cloud, Bergin et al. (1997) derived $[HCO^+]/[^{12}CO] = (3 \pm 2) \times 10^{-5}$. Since this value is almost the same as that in the Orion A, we also have $X_{H^{13}CO^+}$ of 4.8×10^{-11} in the Cepheus OB3 cloud. Since the converted values falls in the range by Butner et al. (1995), we adopt $X_{H^{13}CO^+}$ of 4.8×10^{-11} with uncertainty of a factor of 2 - 3. Therefore, our mass estimation involves the uncertainties of a factor of 3.

The virial mass M_{vir} can be estimated from the core radius R_{core} and the

velocity width $dv_{\rm core}$ as follows,

$$M_{\rm vir} = 209 \left(\frac{R_{\rm core}}{\rm pc}\right) \left(\frac{dv_{\rm core}}{\rm km\ s^{-1}}\right)^2 \quad [M_\odot]. \tag{4.6}$$

In addition, the mean number density of the core $\bar{n}$ is given by

$$\bar{n} = \frac{3M_{\rm LTE}}{4\pi\mu m_{\rm H} R_{\rm core}^3}, \tag{4.7}$$

where μ is the mean molecular weight of 2.33 and $m_{\rm H}$ the mass of a hydrogen atom.

4.2.2 Comparison of Our Core Properties with Previous Ones

In this subsection we describe the physical properties of the $H^{13}CO^+$ cores. First, we compare the properties of the $H^{13}CO^+$ cores in the Orion A with the previous molecular line studies of the cloud and discuss the validity of our core identification and estimate of the core properties. Next, we compare the cores in the Orion B with those in the Orion A to reveal the region-to-region difference of the $H^{13}CO^+$ cores. In addition, since in the Orion B a dust continuum core survey (Johnstone et al., 2001) is available, we compare our $H^{13}CO^+$ cores with the dust continuum cores directly. Finally, we describe the core properties in the Cepheus OB3 cloud. Since the Cepheus OB3 cloud is 1.5 times as far as the Orion clouds, we compare the cores in the Cepheus OB3 cloud with those identified from the low-resolution maps of Orion.

4.2.2.1 Orion A Cloud

We compare our core properties with the previous results of the Orion A cloud in CS (J = 1 - 0) (Tatematsu et al., 1993) and $H^{13}CO^+$(J = 1 - 0) (Aso et al., 2000) in Table 4.5. Note that the two studies were done with

the same telescope (Nobeyama 45 m) as in our study and that the latter one used the same line, $H^{13}CO^+(J = 1 - 0)$. In the following, we describe each physical parameter of the $H^{13}CO^+$ cores through the comparison.

The radius of the $H^{13}CO^+$ cores in the Orion A seems to have a single peak at 0.13 pc, as shown in the top panel of Figure 4.4. The mean radius of 0.14±0.03 pc is larger than the $H^{13}CO^+$ radius in the OMC-2/3 regions by Aso et al. (2000), but comparable to the CS radius by Tatematsu et al. (1993). The agreement between the radii in $H^{13}CO^+$ and CS, however, is not real. This is because the definition of the CS radius is different from ours; they used a threshold of the 5 σ level (1.7 K) to identify a clump and derived the radius as the half of the FWHM size of the clump. If we re-identify the $H^{13}CO^+$ cores following their study, the core radius becomes smaller by a factor of 2 or more. This clearly means that the $H^{13}CO^+$ cores are smaller than the CS clumps, suggesting that the $H^{13}CO^+$ emission typically traces the denser parts of the CS clumps owing to different critical densities. Furthermore, the smaller radius of the $H^{13}CO^+$ cores in the OMC-2/3 regions by Aso et al. (2000) also can be explained by a different definition of the core radius; they defined A in Equation 4.1 as the area higher than the half of the peak intensity of the core. If we adopt their definition of the core radius and the distance of 450 pc, we obtain the mean radius of 0.10 ± 0.03 pc, consistent with their radius.

The distribution of the velocity widths of the $H^{13}CO^+$ cores, shown in the middle panel of Figure 4.4, has a mean of 0.52 ± 0.17 km s^{-1} and shows a remarkable high-velocity-width tail, extends from 1.0 km s^{-1} to 1.5 km s^{-1}. The velocity widths are apparently dominated by the non-thermal velocity component because the thermal velocity width of the $H^{13}CO^+$ emission is 0.18 km s^{-1} with 20 K. Myers et al. (1991) classified cores into the two groups of "thermal core" and "turbulent core" on the basis of the critical

velocity width, $dv_{\rm cr}$, which is expressed by

$$dv_{\rm cr} = \left[8 \ln 2kT \left(\frac{1}{\mu m_{\rm H}} + \frac{1}{m_{\rm obs}}\right)\right]^{1/2}, \quad (4.8)$$

where $m_{\rm obs}$ is the mass of the observed molecule. The critical velocity width of $H^{13}CO^+$ is 0.6 km s^{-1} with 20 K, shown by the vertical broken line of the middle panel of Figure 4.4: 20 % of the cores are turbulent. Furthermore, we found that three cores of # A112, A114, and A131 have velocity widths significantly larger than the mean value by 3 σ or more, corresponding to the high-velocity-width tail from 1.0 to 1.5 km s^{-1}. Since the three cores have the potential for producing massive stars owing to their large effective sound velocities, we refer to the cores as "large-dv cores" and discuss them in terms of star formation activity over the Orion A in subsect. 4.3.

Table 4.5 shows that the mean velocity width of the $H^{13}CO^+$ cores is much smaller than that for the CS clumps. Since the $H^{13}CO^+$ emission is thought to trace the inner dense parts of the CS clumps, the turbulence might be dissipated in some degree within the dense cores, which are surrounded with tenuous gas traced by CS. It is possible that the formation of the dense cores is caused by dissipation of the turbulence. On the other hand, the mean velocity width in our study is smaller than that by Aso et al. (2000) by a factor of 2. This is because their core identification by eye could not separate well spatially overlapped cores in some cases. For example, one of their core AC03 is separated into two cores (# A142, $dv_{\rm core}$ = 0.66km s^{-1} and # A135, $dv_{\rm core}$ = 0.48km s^{-1}) in our study.

The LTE mass of the $H^{13}CO^+$ cores in the Orion A has a mean of 12 $\pm$ 12 $M_\odot$ and a wide range of 2 to 80 $M_\odot$, as shown in the bottom panel of Figure 4.4. The mass distribution has a broad peak at $\sim 5M_\odot$ with a high-mass tail in the range of 25 to 80 $M_\odot$: the number of the cores in the tail is 10 % of the total number. There are five "high-mass cores" (# A112, A118, A119, A142, and A163) significantly more massive than the mean mass by 3 σ or

more, corresponding to the high-mass tail. Note that the high-mass cores are distributed over the OMC-1 and 3 regions. The high-mass tail-like feature is not seen in low-mass star forming regions, such as Taurus (Onishi et al., 2002), and are possibly related to the massive star formation in the Orion A. The mean mass of the $H^{13}CO^+$ cores is much smaller than that of the CS clumps by Tatematsu et al. (1993, see Table 4.5), probably because the $H^{13}CO^+$ cores are the denser parts of the CS cores. On the other hand, our mean mass is consistent with that (18 $\pm$ 9.0 $M_\odot$) in the OMC-2/3 regions by Aso et al. (2000), because the mean mass of our cores identified only in the OMC-2/3 regions is calculated to be 14 $\pm$ 12 $M_\odot$. The mean number density of our $H^{13}CO^+$ cores in the Orion A is typically 2×10^4 cm^{-3} (see Table 4.2), which is consistent with the critical density of the $H^{13}CO^+(J = 1$ - 0) line emission (8×10^4 cm^{-3}), because the uncertainty of the mean number density estimation is of a factor of 4, derived from the uncertainties in $M_{\rm LTE}$ and $R_{\rm core}$.

The virial ratio, $M_{\rm vir}/M_{\rm LTE}$, with a mean of 1.0 $\pm$ 0.6 (see Table 4.2) suggests that almost all the $H^{13}CO^+$ cores in the Orion A are in virial equilibrium. Furthermore, both the turbulent and thermal cores are in the equilibrium, as shown in Figure 4.5: the mean ratios for the turbulent and thermal cores are 1.4$\pm$0.9 and 0.9$\pm$0.5, respectively. We can expect that the turbulent cores in virial equilibrium have the potential to produce massive stars, because the mass infall rate is proportional to the third power of the effective sound speed.

4.2.2.2 Orion B Cloud

In the following, we describe each physical parameter of the $H^{13}CO^+$ cores in the Orion B through the comparison with the results in the Orion A. In addition, since the data of an 850 μm continuum survey in the NGC2068, NGC2071 and LBS 23 regions (Johnstone et al., 2001) are available, we also compare the $H^{13}CO^+$ core properties with those of the 850 μm cores.

Although two large-scale surveys with CS ($J = 2$ - 1, Lada et al., 1991a) and $H^{13}CO^+$ ($J = 1$ - 0, Aoyama et al., 2001) were carried out in the region, the resolutions of the two surveys are not sufficient enough to compare directly with our data. Table 4.6 summarizes the mean core parameters of the studies.

Before we compare the properties of the $H^{13}CO^+$ cores with those of the 850 μm cores, we examine whether each $H^{13}CO^+$ cores is associated with the 850 μm cores or not. If the position of the 850 μm cores are associated with peaks seen in the velocity channel maps of the $H^{13}CO^+$ cores considering the spatial resolution of 27″, we regarded the 850 μm cores as associated ones with the $H^{13}CO^+$ cores. We found 21 $H^{13}CO^+$ cores associated with the 850 μm ones, which we refer to "dust-associated" cores, and the remaining 20 cores are not associated with the 850 μm ones in the survey area of Johnstone et al. (2001). We found three types of how the 850 μm cores are associated with the $H^{13}CO^+$ cores: 17 cases of that one 850 μm core is located at the center of the most-intense peak of a $H^{13}CO^+$ core (type A), 2 cases (#B57 and #B75) of that one 850 μm core is not associated with the most-intense peak, but associated with less-intense peak of a $H^{13}CO^+$ core (type B), and 2 cases (#B77 and #B80) of that two 850 μm cores are placed around the most-intense peak of a $H^{13}CO^+$ core (type C). The dust-associated cores are listed in Table 4.7.

Most of the dust-associated cores (type A, 17/21) seem to have one-to-one relations with the 850 μm cores. On the other hand, half of the $H^{13}CO^+$ cores are not associated with the dust emission. This may be explained by the evolution of prestellar core. In the earlier stage of the evolution, the density concentration of a gravitationally-bound, collapsing prestellar core is expected to be lower, and as the core evolves, the density concentration would become higher (Kandori et al., 2005). According to this, we can consider that the $H^{13}CO^+$ cores not associated with the dust emission correspond to prestellar cores still having lower density concentration not enough to be observed with the dust continuum emission, i.e., less evolved cores, and the

type A cores are more evolved ones. If this holds, clear differences would be found in their density profile. Unfortunately, we cannot discuss their inner density structures further due to our insufficient spatial resolution of 27″. In addition, four of the dust-associated cores (type B and C) seem to have spatial offset between the $H^{13}CO^+$ and dust emission peaks, as shown in Figures 4.6 and 4.7. The origin of the offset is still unclear. To reveal the nature of such cores, we may need more detailed studies of each individual cores. Anyway, we did not use the type B and C cores in the following discussion for the relation between the $H^{13}CO^+$ and 850 μm cores. The existence of them does not affect the following discussion because their number is small (4/21).

The radius of the $H^{13}CO^+$ cores in the Orion B seems to have a distribution with a single peak at 0.09 pc, as shown in the top panel of Figure 4.8. A tail feature toward the larger radius, reaching 0.2 pc, can be seen. In fact, there are two cores whose radii are larger than the mean radius by 3 σ (0.19 pc) or more (0.19 pc for # B2 and 0.20 pc for # B27). However, since the uncertainty in the radius estimation is 0.04 pc, the presence of such large cores is suspected. The mean radius of 0.11±0.03 pc and the peak of the radius histogram seem to be smaller than those in the Orion A. We checked the significance of the difference of the radius distribution using the Kolmogorov-Smirnov (K-S) test (Press et al., 1992): a null hypothesis that the two observed distributions is originated from the same distribution is rejected with the significant level of less than 1 %, i.e., the two distribution is considerably different from each other. This is because the number of the cores whose sizes are 0.14 - 0.23 pc is relatively smaller than that in the Orion A.

On the other hand, the mean radius of 0.11 pc seems to be twice larger than the 850 μm dust continuum core radius by Johnstone et al. (2001). In fact, the associated pairs of the 850 μm and $H^{13}CO^+$ cores have the mean radius ratio of 0.5±0.3. Since Johnstone et al. (2001) used the clumpfind as the core identification method, the definition of the radius is thought to be

the same as ours. The difference can be explained if we consider that the 850 μm cores are the inner dense parts of the $H^{13}CO^+$ cores. If we consider a density profile of a singular isothermal sphere of $\rho(r) \propto r^{-2}$, the radius of the 850 μm core is expected to be one-third of the $H^{13}CO^+$ one because the dust continuum emission traces the region which have a density of above 10^6 cm^{-3}, an order of magnitude higher than that of the $H^{13}CO^+$ cores. This is roughly consistent with the $H^{13}CO^+$ - 850 μm core radius ratio of 0.5$\pm$0.3. We note that there is no difference between the radii of the dust-associated and not-associated cores: the mean radii of them are 0.11 $\pm$ 0.02 pc and 0.11 $\pm$ 0.03 pc, respectively.

The velocity width of the $H^{13}CO^+$ cores has a mean of 0.50 $\pm$ 0.13 km s^{-1}, almost the same as that in the Orion A. As in the Orion A, the velocity width is turbulent. The critical velocity width, dv_{cr}, at 16.1 K is 0.54 km s^{-1} and the fraction of the turbulent cores are 32 %, comparable to that in the Orion A. The middle panel of Figure 4.8 shows the velocity width distribution. A peak of the distribution at 0.5 km s^{-1} is very similar to those in the Orion A, although the high-velocity-width tail of 1 - 1.6 km s^{-1}, in the Orion A, cannot be seen in the Orion B: we applied the K-S test, but we cannot find the difference with the significance level of 1 %. The probability to find the large-dv cores in the Orion A is 1.3 %. Then the expected number of the large-dv cores in the Orion B is estimated to be 1.2$\pm$1.1 if we assume this probability holds also in the Orion B cloud, because the velocity-width distribution of the Orion B cores is not considerably different from that of the Orion A cores. Therefore the absence of the large-dv cores in the Orion B cloud is marginal because of the large statistical uncertainties. The velocity widths of the dust-associated and not-associated cores have good agreement with each other: the mean velocity widths of them are 0.51 $\pm$ 0.09 km s^{-1} and 0.53 $\pm$ 0.12 km s^{-1}, respectively.

The LTE masses of the $H^{13}CO^+$ cores has a mean of 8.9 $\pm$ 7.7 $M_\odot$, consistent with that in the Orion A of 12.3 $M_\odot$. The distribution has a

broad peak at $\sim$ 6 $M_{\odot}$, and shows a high-mass tail toward 50 $M_{\odot}$ (Figure 4.8); The highest mass core is # B27, 52 $M_{\odot}$, located in the NGC2023 region. Although the peak mass is about two times smaller than that of the Orion A and much higher mass ($> 60M_{\odot}$) cores cannot be found, the shape of the distribution is consistent with that of the Orion A: we applied the K-S test, and we cannot find significant difference with the significance level of 1 % (see also Section 4.3). In addition, the probability to find massive $> 50M_{\odot}$ cores in the Orion A is 2.1 %, leading to the expected number of cores $> 50M_{\odot}$ in the Orion B is 2.1$\pm$1.4, assuming the same mass distribution in the Orion B and A clouds. This is consistent with the observed massive core number in the Orion B. Therefore we cannot conclude that there are less number of massive ($> 50M_{\odot}$) cores in the Orion B than in the Orion A cloud.

The mean LTE mass is five times larger than that of the 850 μm cores. Actually, the mean mass ratio of the 850 μm cores to the dust-associated $H^{13}CO^{+}$ cores is 0.22$\pm$0.14. This difference can be explained by the density structure of the cores. The mass of a core which has a density profile of $\rho(r) \propto r^{-2}$ scales inversely as the square root of density. If the 850 μm continuum emission traces an order of magnitude denser part than the $H^{13}CO^{+}$ emission, the 850 μm cores are expected to have one third of the $H^{13}CO^{+}$ masses, and this is consistent with the mass ratio of 0.22 within the uncertainties. We note that the mean mass of the dust-associated cores of 11 $\pm$ 5.8 $M_{\odot}$ is not significantly differ from that of not-associated cores of 8.4 $\pm$ 7.9 $M_{\odot}$.

The virial ratio in the Orion B has a mean of 0.9 $\pm$ 0.5. This suggests that almost all the $H^{13}CO^{+}$ cores in the Orion B are in virial equilibrium, just like the case of the Orion A. In addition, both the turbulent and thermal cores are in the equilibrium, as shown in Figure 4.9: the mean ratios for the turbulent and thermal cores are 1.1$\pm$0.7 and 0.8$\pm$0.4, respectively.

In summary, the differences between the $H^{13}CO^{+}$ cores in the Orion B and A clouds is the distribution of the core radius of >0.14 pc. The distributions and the typical values of the velocity widths and masses are consistent with

each other. Note that there is no large-dv core in the Orion B cloud, although the statistical scatter may explain this absence. Except the above feature, the majority of the cores show the properties which are very similar to each other. The $H^{13}CO^+$ cores in the Orion B cloud are gravitationally bound as well as those of the Orion A. On the other hand, through the comparison with the continuum core survey, one $H^{13}CO^+$ core contains one 850 μm core. This suggests that the 850 μm cores correspond to the inner denser ($\geq 10^6$ cm^{-3}) parts of the $H^{13}CO^+$ cores. The radius and mass of the $H^{13}CO^+$ cores are respectively three and five times larger than those of the 850 μm cores. We can explain this discrepancy considering the density strucuture of $\rho(r) \propto r^{-2}$.

4.2.2.3 Cepheus OB3 Cloud

In the Cepheus OB3 cloud, there have been no large-scale and systematic dense gas survey with a resolution enough to be directly compared with our results. Then we describe the core physical properties in Cepheus through the comparison with low-resolution results of the Orion A and B in our study.

We made 41″.2 resolution 3-D cubes of the Orion A and B. The effective spatial resolution $\Delta\theta_{\rm eff}$ of the map of the Cepheus OB3 cloud is 27″.1 with $\Delta\theta_{\rm grid}$ of 9″ and a spheroidal function of $m = 6$ and $\alpha = 1$ as a GCF. Since the distances of the Orion A, B, and Cepheus OB3 are 480 pc, 470 pc, and 730 pc, respectively, $\Delta\theta_{\rm eff}$ in the Orion clouds should be 41″.2 to compare the maps with the same linear resolution in the Cepheus cloud, 0.10 pc. For the Orion A, a Gaussian with a FWHM of 33″.9 is used as a GCF, and the resulting typical RMS of the 3-D cube is 0.06 K. For the Orion B, a Bessel×Gaussian function (Mangum, 1999) with a FWHM of 37″.1 is used and the typical RMS becomes 0.12 K. We identified the cores with the clumpfind algorithm just as the same manner as the case of the high-resolution maps described in Section 4.1. Finally 69 and 47 cores were identified in the Orion A and B, respectively. The mass detection limits are 3.5 $M_\odot$ and 3.5 $M_\odot$, respectively,

almost the same as that for the Cepheus OB3 map of 3.6 $M_{\odot}$.

We summarized the core properties of the Cepheus, Orion A, and Orion B cores in Table 4.8. The mean radius in the Cepheus cloud of 0.18±0.04 pc is consistent with those in the Orion A (0.23±0.06 pc) and Orion B (0.18±0.03 pc). The mean velocity width is 0.60±0.17 km s^{-1}, which is also consistent with those in the other two clouds. The mean LTE mass of $23\pm32M_{\odot}$ is similar to those in the Orion B of $21\pm14M_{\odot}$ and in the Orion A of $36\pm34M_{\odot}$. Note that the highest core mass of 162 $M_{\odot}$ in the Cepheus OB3 is consistent with that of 176 $M_{\odot}$ in the Orion A cloud, while the highest core mass of 82 $M_{\odot}$ in the Orion B is twice smaller than those in the Cepheus and Orion A.

Figure 4.10 shows that the core property histograms of the radius, velocity width, and mass in the left, middle, and right panels, respectively. The radius panels show that the distribution of the radius in the Cepheus cloud is very similar to that in the Orion B, while the two distributions are considerably different from that in the Orion A: we applied the K-S test and found that the radius distributions for the Orion B and Cepheus cores cannot be considered to be different to each other, while the differences are siginificant between the Cepheus and Orion A cores, and between the Orion B and Orion A ones with the significance level of less than 1 %. The cores whose radii are between 0.28 and 0.4 pc are only found in the Orion A. In other words, in the range from 0.05 to 0.28 pc, the distributions of the three clouds seem not to differ from each other.

In the velocity width panels, the distributions seem to be consistent with each other: we cannot find any significant difference among them using the K-S test with the significance level of 1 %. On the other hand, there are a few cores with large velocity widths (>1.0 km s^{-1}) can be found in the Cepheus and Orion A clouds. In the Cepheus cloud, we found one core # C15, whose velocity width satisfies the criterion of the large-*dv* cores. Core # C15 is located at the center of Cep-A region.

In the mass panels, the shape of the Cepheus histogram is rather similar

to that of the Orion B although the peak of the Cepheus histogram is about twice smaller than that of the Orion B. However, this is possibly caused by the smaller sample number in the Cepheus: through the K-S test, the distributions of the Cepheus and Orion B cannot be considered to be different from each other with the significance level of 1 %. On the other hand, the Orion A histogram is apparently different from those of the Cepheus and Orion B. The peak mass is $\sim$ 35 $M_\odot$, twice and four times larger than those of the Orion B and Cepheus, respectively. Furthermore, the K-S test shows the Orion A histogram is considerably different from those of the Cepheus and Orion B with the significance level of 1 %. One may think that this is a discrepancy because the mass distributions of the Orion A and B from the high-resolution data is consistent with each other as shown in the last subsection. This discrepancy is possibly caused by core merging due to the insufficient spatial resolution. Since in the Orion A the cores are more crowded than the Orion B (see Section 5.3), the misidentification of neighbor cores as a more massive one would be more severe, and cause the histogram peak shift toward more massive.

In summary, among the cores in the three clouds identified from the low-resolution data, the majority of the cores are the common ones which have radii of 0.1 - 0.27 pc, velocity widths of 0.2 - 0.8 km s^{-1}, and masses of 5 - 180$M_\odot$. On the other hand, there are several peculiar cores: the cores which have larger radii of $>$ 0.28 pc only found in the Orion A and which have larger velocity widths of $>$ 1.0 km s^{-1} only found in the Cepheus and Orion A. The latter corresponds to the large-*dv* cores: in the Cepheus cloud, we found one large-*dv* core of # C15.

4.2.3 Correlation Among the Core Properties

In this section we show correlation plots among the core physical properties. The property correlations of the structures in molecular clouds having various scales, i.e., clumps and cores, have been investigated by many au-

thors. The most famous work was done by Larson (1981). He found the Larson's laws, the power-law relations between the linear-extent of clouds, clumps, and cores L and the three-dimensional velocity dispersion σ , and between the LTE mass M and σ: $(\sigma/\mathrm{km\ s^{-1}}) = 1.10(L/\mathrm{pc})^{0.38}$ and $(\sigma/\mathrm{km\ s^{-1}}) = 0.42(M/M_{\odot})^{0.20}$ with very wide ranges of $0.1 < (L/\mathrm{pc}) < 100$ and $1 < (M/M_{\odot}) < 10^5$, respectively. In core scales of 0.1 pc, Caselli & Myers (1995) compiled eight low-mass dense core samples, whose radii fall in the range of 0.03 to 1 pc, and found the correlation between the non-thermal FWHM velocity width, dv_{NT}, and radius: $(dv_{\mathrm{NT}}/\mathrm{km\ s^{-1}}) = (1.51\pm0.21)(R/\mathrm{pc})^{0.53\pm0.07}$. We discuss the property correlations in the Orion A throuth the comparison with the previous results by Larson (1981) and Caselli & Myers (1995). Next we compare the correlations in the Orion A with those in the Orion B and Cepheus OB3 clouds to investigate the region-to-region variations.

4.2.3.1 Correlation in the Orion A Cloud

Figure 4.11 shows the correlations in the Orion A. The plots of velocity width vs radius and LTE mass are presented in the top panels. Power-law functions are applied to these plots and the best-fit results are listed in Tables 4.9 and 4.10: $(dv_{\mathrm{core}}/\mathrm{km\ s^{-1}}) = (1.55\pm0.27)(R_{\mathrm{core}}/\mathrm{pc})^{0.55\pm0.09}$ with a correlation coefficient of 0.37 and $(dv_{\mathrm{core}}/\mathrm{km\ s^{-1}}) = (0.34\pm0.02)(M_{\mathrm{LTE}}/M_{\odot})^{0.19\pm0.02}$ with 0.48. We also plotted the Larson's laws (Larson, 1981) with dotted lines in Figure 4.11. Note that we converted σ and L to dv_{core} and R_{core} in our definition, respectively. Although both our correlations are weak, the best-fit relations seem to differ from those by Larson (1981): the velocity widths of the $H^{13}CO^+$ cores tend to be smaller and the power-law index of the dv_{core}-R_{core} relation is somewhat larger. The former suggests that the turbulence within the dense cores, traced by $H^{13}CO^+$, is more efficiently dissipated than that within the tenuous objects in the larson's sample, mainly observed with lower-density tracers such as ^{13}CO. For the latter, our relation is quite similar to that between dv_{NT} and radius for low-mass dense core samples compiled

by Caselli & Myers (1995). Actually, the best-fit relation of the $dv_{\rm NT}$ vs $R_{\rm core}$ of our $H^{13}CO^+$ cores is $(dv_{\rm NT}/{\rm km\ s^{-1}}) = (1.59 \pm 0.29)(R_{\rm core}/{\rm pc})^{0.58\pm0.10}$ with a correlation coefficient of 0.37. We note that not only the power-law index but also the coefficient is very similar to Caselli & Myers's. This agreement suggests that even in the GMC, more turbulent than low-mass star forming regions, the turbulence within a 0.1 pc-scale dense core is dissipated as well.

The difference between the power-law indices of the $dv_{\rm core}$-$R_{\rm core}$ relation in the top-left panel of Figure 4.11 is emphasized in the $M_{\rm LTE}$-$R_{\rm core}$ correlation, shown in the bottom-left panel of Figure 4.11. The best-fit power-law function is given by $(M_{\rm LTE}/M_\odot) = (6.6 \pm 2.4) \times 10^3 (R_{\rm core}/{\rm pc})^{3.34\pm0.21}$ with a correlation coefficient of 0.70 (see also Tables 4.9 and 4.10). Note that the $M_{\rm LTE}$-$R_{\rm core}$ relation can be roughly derived from the $dv_{\rm core}$-$R_{\rm core}$ and $dv_{\rm core}$-$M_{\rm LTE}$ relations. The strong correlation with the power-law index of ~ 3 suggests that the density is uniform all over the cores, because a single molecular line tends to trace the gas having the critical density of the line. Actually, our coefficient of the $M_{\rm LTE}$-$R_{\rm core}$ relation, roughly the mass density, based on $H^{13}CO^+$ ($n_{\rm crit} \sim 10^{4\sim5}$ cm^{-3}) is an order of magnitude larger than that by Larson (1981) mainly based on ^{13}CO ($n_{\rm crit} \sim 10^3$ cm^{-3}).

The bottom-right panel of Figure 4.11 shows the $(M_{\rm vir}/M_{\rm LTE})$ vs $M_{\rm LTE}$ plot with a weak negative correlation. The best-fit power-law function is given by $M_{\rm vir}/M_{\rm LTE} = (1.89 \pm 0.21)(M_{\rm LTE}/M_\odot)^{-0.32\pm0.06}$ with a correlation coefficient of 0.38. The corresponding Larson's relation is $M_{\rm vir}/M = 0.40(M/M_\odot)^{-0.07}$, whose power-law index is smaller than ours. Although almost all the cores seem to be in virial equilibrium, the cores with larger masses tend to have smaller virial ratios, i.e., gravitationally unstable. Similar correlations are also found in previous studies. The CS clumps in Orion have an index of -0.35 ± 0.05 (Tatematsu et al., 1993). Willams et al. (1995) found a steeper index of -0.64 for the ^{13}CO clumps in the Rosette molecular cloud. The steeper relation, however, can be explained by "pressure-confined clumps", which are far from gravitationally bound state and are confined by

surrounding ambient pressure. Bertoldi & McKee (1992) found that the virial ratio of the pressure-confined clumps is proportional to $M^{-2/3}$. In contrast, the shallower relation ($\propto M^{-0.32}$) for the $H^{13}CO^+$ cores suggests that the Orion A cores are not pressure-confined but are gravitationally bound.

4.2.3.2 Correlation in the Orion B Cloud

Now we are going to compare the correlations in Orion B with those of the Orion A cloud. Figure 4.12 shows the $dv_{\rm core}$ - $R_{\rm core}$, $dv_{\rm core}$ - $M_{\rm LTE}$, $M_{\rm LTE}$ - $R_{\rm core}$, and virial ratio - $M_{\rm LTE}$ relations of the Orion B clouds. Power-law functions are applied to these plots and the best-fit results are listed in Tables 4.9 and 4.10: $(dv_{\rm core}/{\rm km\ s^{-1}}) = (1.26 \pm 0.30)(R_{\rm core}/{\rm pc})^{0.42\pm0.11}$ with a correlation coefficient of 0.37, $(dv_{\rm core}/{\rm km\ s^{-1}}) = (0.35 \pm 0.02)(M_{\rm LTE}/M_\odot)^{0.18\pm0.03}$ with 0.52, $(M_{\rm LTE}/M_\odot) = (1.5 \pm 0.7) \times 10^3 (R_{\rm core}/{\rm pc})^{2.35\pm0.23}$ with 0.70, and $M_{\rm vir}/M_{\rm LTE} = (1.58 \pm 0.23)(M_{\rm LTE}/M_\odot)^{-0.32\pm0.08}$ with 0.39. We also plotted the correlations of the Orion A clouds with thin-color symbols in the figures. The correlation plots allow us to recognize more easily the region-to-region difference already seen in Section 4.2.2.2 as follows:

- the cores in the Orion B seem to have smaller radii of < 0.14 pc, while the velocity widths and masses of the two clouds are similar to each other.
- the cores whose velocity widths are larger than 1 km s^{-1} are only found in the Orion A.

We can also recognize on the correlation plots that the majority of the cores are the ordinary ones, from the fact that the best-fit results of $dv_{\rm core}$ - $R_{\rm core}$, $dv_{\rm core}$ - $M_{\rm LTE}$, and $M_{\rm vir}/M_{\rm LTE}$ - $M_{\rm LTE}$ relations are very consistent with those in the Orion A (see Tables 4.9 and 4.10).

On the other hand, the power-law index of the $M_{\rm LTE}$ - $R_{\rm core}$ relation is considerably different from that in the Orion A. For the cores whose masses are higher than $10M_\odot$, the $M_{\rm LTE}$ - $R_{\rm core}$ relations of the two clouds are

consistent. On the other hand, for the cores of $< 10M_\odot$, there are ten and several cores whose masses are about $5M_\odot$ but radii are about 0.15 pc, relatively larger than those in the Orion B. Such cores would provide the shallower power-law index in the Orion A. This difference, however, is suspect considering the uncertainty of the radius of 0.04 pc. Furthermore, these cores having larger radii seem not to show the other remarkable point, such as in the spatial distribution and in the CMF. Because of this, we do not discuss these larger radius cores further.

4.2.3.3 Correlation in the Cepheus OB3 Cloud

Figure 4.13 shows the correlations in the Cepheus OB3 cloud, comparing to the low-resolution data of the other two clouds. Power-law functions are applied to these plots and the best-fit results are listed in Tables 4.9 and 4.10: $(dv_{\rm core}/{\rm km\,s^{-1}}) = (1.82 \pm 0.54)(R_{\rm core}/{\rm pc})^{0.66\pm0.17}$ with a correlation coefficient of 0.61, $(dv_{\rm core}/{\rm km\,s^{-1}}) = (0.32 \pm 0.03)(M_{\rm LTE}/M_\odot)^{0.22\pm0.04}$ with 0.75, $(M_{\rm LTE}/M_\odot) = (1.8 \pm 1.4) \times 10^3 (R_{\rm core}/{\rm pc})^{2.79\pm0.43}$ with 0.60, and $M_{\rm vir}/M_{\rm LTE} = (2.20 \pm 0.56)(M_{\rm LTE}/M_\odot)^{-0.35\pm0.09}$ with 0.44. We also show the best-fit results of the low-resolution data in the Orion clouds in Figure 4.13 and Tables 4.9 and 4.10. We note that the $dv_{\rm core}$ - $R_{\rm core}$ relation of the low-resolution data in the Orion A is different from that of the high-resolution data (see 4.9 and 4.10), and are rather similar to that of the massive core samples compiled by Caselli & Myers (1995) of $dv \propto R^{0.21\pm0.03}$. Since the Orion A is the most spatially crowded region among the three clouds, the lower-resolution may efficiently blend the neighboring cores and the radii would become larger, resulting in the shallower power-law index of dv - R relation. In fact, Caselli & Myers's massive core samples were mainly obtained with spatial resolutions of 0′.7 - 2′.7, comparable to or larger than those of our lower-resolution data. On the other hand, the power-law index of dv - M relation is thought to be insensitive to the blending because the mass is proportional to about the one third power of the radius.

The correlation plots of the cores in the Cepheus OB3 have a good agreement with those in the Orion B. This is consistent with the results shown in Section 4.2.2.3. However the best-fit result of the $dv_{\rm core}$ - $R_{\rm core}$ relation seems to be different from those of the Orion A and B clouds. This may be caused by the small core number in the Cepheus OB3 cloud of 31, which is 9 and 3 times smaller than that of the Orion A and B clouds, respectively. Therefore, the similarity of the correlation plots between the Cepheus and Orion B clouds suggests that the almost all of the cores in the Cepheus and Orion B have similar properties. Furthermore, we already showed that the core properties of the Orion A and B is very similar to each other using the high-resolution data. Combining the above two results, we conclude that the majority of the cores over the three clouds are similar to each other.

4.3 $H^{13}CO^+$ CMF

The CMF is usually expressed in the following differential power-law form,

$$\frac{dN}{dM} \propto M^{-\gamma}, \tag{4.9}$$

and the cumulative form,

$$N(>M) = kM^{-\alpha} + c \qquad (\alpha = \gamma - 1). \tag{4.10}$$

The former differential expression allows us to easily recognize the behavior of the CMF, i.e., the steepness of the slope and the presence of a turnover. However, the differential form is thought to be sensitive to mass bins adopted. On the other hand, the latter cumulative form never depend on the mass bins, although the behavior of the CMF is not easily recognized. In this study, we consider a case that a CMF has a turnover, which separates low-mass flat and high-mass steep parts, as suggested by many authors, and apply a power-law function with a turnover to our derived CMF.

Figures 4.14, 4.15, and 4.16 show the $H^{13}CO^+$ CMFs in the Orion A, Orion B and Cepheus OB3 clouds, respectively. The left panels of the figures show the $H^{13}CO^+$ CMFs in the differential form. It is clear that there exist flat and steep parts separated by a turnover at $\sim$ 10-15 $M_\odot$. Since our mass detection limit is as small as $1.6M_\odot$ in the Orion and $3.6M_\odot$ in the Cepheus OB3, the turnover is most likely to be real. We will discuss the turnover in detail in Section 5.3. The best-fit results in the Orion A cloud are as follows: a turnover mass of 9.3±0.5 $M_\odot$, γ = 0.40±0.04 in the flat low-mass part, and γ = 2.25± 0.10 in the steep high-mass part (see the two straight lines in Figure 4.14). In the Orion B, the best-fit results are: a turnover mass of 7.7±0.5 $M_\odot$, γ = 0.10±0.05 in the flat low-mass part, and γ = 2.40± 0.21 in the steep high-mass part. In the Cepheus OB3, the best-fit results are as follows: a turnover mass of 16.9±2.6 $M_\odot$, γ = 0.50±0.06 in the flat low-mass part, and γ = 2.10± 0.41 in the steep high-mass part. To check the validity of the mass bins adopted for the differential CMFs, we also estimated the $H^{13}CO^+$ CMF in the cumulative form, as in the right panels of the figures. Here we show the case of the Orion A. The best-fit results are as follows: a turnover mass of $12 \pm 5M_\odot$, γ=0.56±0.30 in the flat low-mass part, and γ=2.45±0.20 in the steep high-mass part (see the grey curve in the right panel of Figure 4.14). These best-fit values agree well with those in the differential form. Consequently, the mass bins we adopted in the differential CMF are justified. For the other two clouds we also confirmed the validity of the adopted mass bins in the same way.

Our $H^{13}CO^+$ CMF in the three clouds are consistent with the CMFs derived in various star forming regions in the sense that the power-law index γ falls the plausible range from 2.0 to 3.0 in the high-mass parts. We summarized several CMFs including ours in Table 4.11. In the Orion B cloud, Johnstone et al. (2000) made mapping observations in dust continuum emission, one of the best tracers of the dense cores, and cataloged 75 dust cores. In the ρ Ophiuchi cloud, Motte et al. (1998) and Johnstone et al. (2000)

identified 60 and 55 dust cores, respectively. Testi & Sargent (1998) detected 26 dust cores toward the Serpens region. Furthermore, Onishi et al. (2002) surveyed dense cores in Taurus with $H^{13}CO^+(J = 1 - 0)$ and identified 23 cores. Table 4.11 clearly shows that our sample number in the Orion A is much larger than those in the previous studies, resulting in a good statistical case. On the other hand, the γ values in Table 4.11 are generally larger than those with lower critical-density tracers such as CO and CS. Kramer et al. (1998) showed that the CMFs of nearby 7 dark clouds and GMCs have a common power-law index of 1.6 using the ^{12}CO, ^{13}CO and $C^{18}O$ emission. The CS mass function in the Orion A also has the smaller power-law index of 1.6 (Tatematsu et al., 1993).

Our $H^{13}CO^+$ CMFs have turnovers separating the low-mass flat and high-mass steep parts at 8 - 17 $M_\odot$, far above the mass detection limit. In fact, some authors showed that the CMF has a turnover, which could not be considered as an artifact due to the incompleteness of core survey. Motte et al. (1998) derived a dust CMF and found that the CMF becomes flat ($\gamma = 1.5$) below 0.5 $M_\odot$, i.e., there is a turnover at 0.5 $M_\odot$ with a mass-detection limit ranging from 0.04 to 0.1 $M_\odot$. They concluded that the turnover is real considering the uncertainties in the mass estimation and the detection limit. Onishi et al. (2002) also showed that the CMF has a turnover at $\sim$ 3.5 $M_\odot$, three times larger than a completeness limit mass of $1M_\odot$, which they estimated from their observation grid size and sensitivity. They argued that the turnover cannot be explained by the incompleteness of their survey. Furthermore, the turnover masses in the three clouds are significantly larger than those in the ρ Ophiuchi and Taurus clouds, although the power-law index γ on the high-mass side has similar values in the six clouds (see Table 4.11). The large turnover masses might charactarize the massive star formation in the three clouds, in constrast to the low- and intermediate-mass star forming regions.

4.4 Chapter Summary

We cataloged the $H^{13}CO^+$ cores in the nearby massive star- and cluster-forming GMCs, the Orion A, Orion B, and Cepheus OB3 clouds. For core identification, we used the clumpfind algorithm, which minimizes mis-identification and allows us to compare the cores fairly among the cloud. The identified 236, 98, and 31 cores in the Orion A, Orion B, and Cepheus OB3 clouds, respectively, show the mean radius of $\sim$ 0.12 pc, the mean velocity width of $\sim$ 0.5 km s^{-1}, and the mean mass of $\sim$ 10 $M_\odot$. Among the three clouds, the majority of the cores are the ordinary and common ones, because the correlations among core properties and the CMFs are similar to each other, and are consistent with the previous studies. On the other hand, there are several peculiar cores such as the large-*dv* and high-mass cores, found in the Orion A and Cepheus. In the Orion B, however, such peculiar cores cannot be found, possibly due to the large statistical scatter.

In the Orion A, we found that the $H^{13}CO^+$ cores are the substructures of the CS(1 - 0) clumps. The power-law index of the CMF of the $H^{13}CO^+$ cores is considerably different from that of the CS clumps, but is similar to those of the CMFs obtained by the dust continuum observations, which are thought to be one of the best methods to observe prestellar cores. This suggests that the $H^{13}CO^+$ cores are the structures more closely related to star formation than the CS clumps. In the Orion B we showed that each of the $H^{13}CO^+$ cores contains typically one 850 μm dust continuum cores. This seems to suggest that the dense and compact 850 μm cores correspond to the inner dense parts of the $H^{13}CO^+$ cores. In fact, power-law index of the high-mass part of the CMFs of the $H^{13}CO^+$ and 850 μm cores are very similar to each other.

The turnover masses in the $H^{13}CO^+$ CMFs seem to have physical meaning, because they are significantly larger than the mass detection limit. It is shown that the turnover masses in the three clouds are considerably larger than those in the low- and intermediate-mass star forming regions, suggesting

that the larger turnover mass is an indicator of massive star formation.

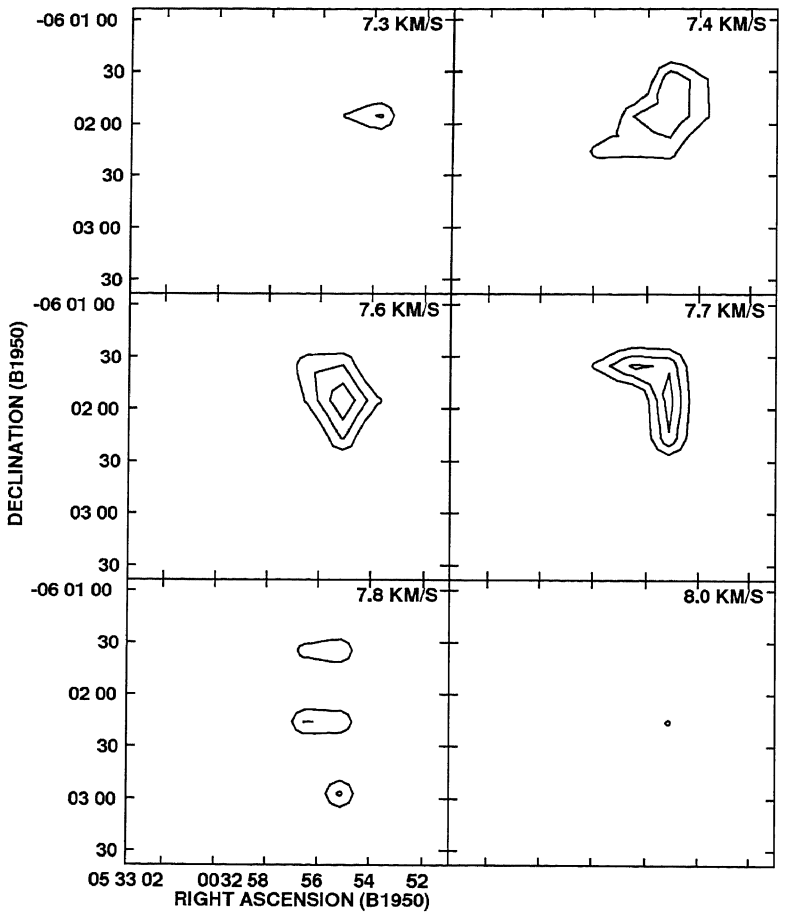

Figure 4.1 Velocity channel maps of the minimum-mass core that we identified. The lowest contour level is 0.17 K (corresponding to 2 σ) and the contour interval is 0.085 K. The LSR velocity is shown at the top right-hand corner of each panel.

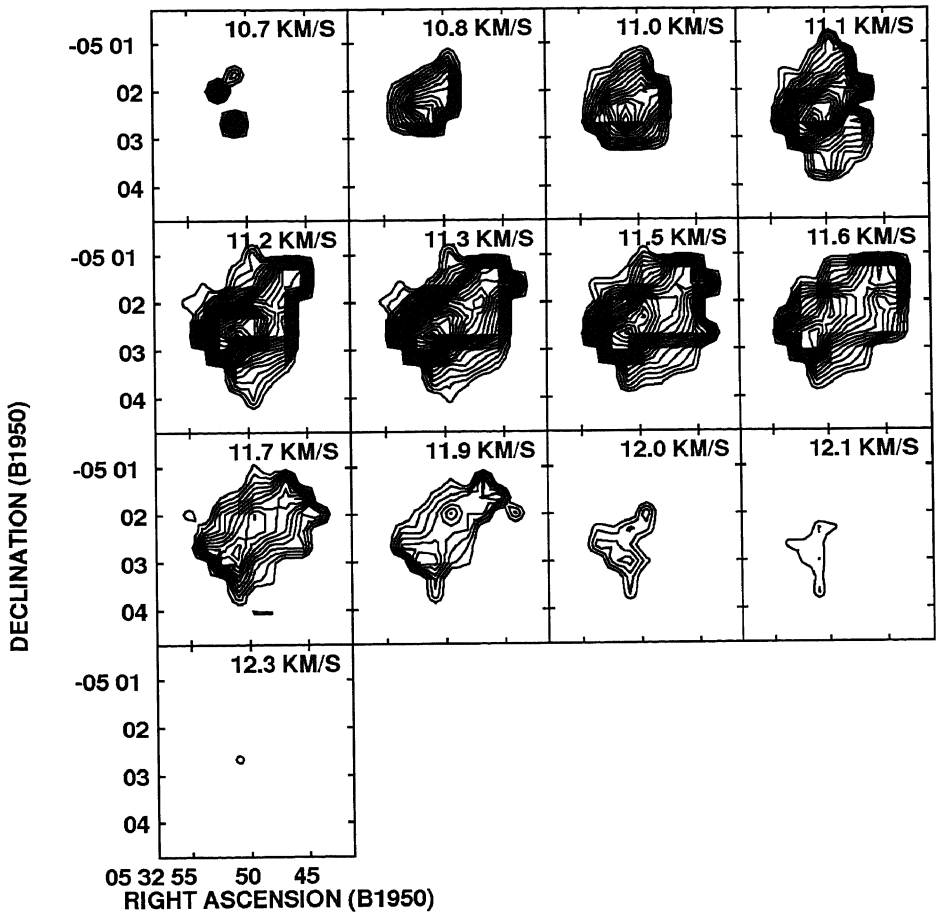

Figure 4.2 Velocity channel maps of the maximun-mass core that we identified. The map parameters are the same as in Figure 4.1.

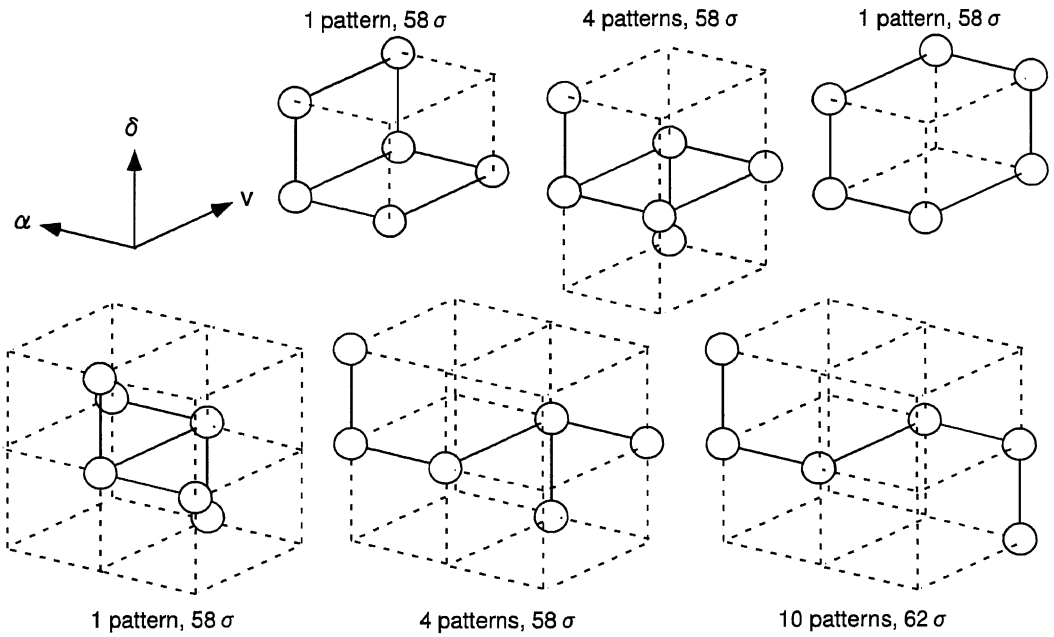

Figure 4.3 Representative patterns of the possible configurations of the 3 σ level spatially-independent pixels for the minimum-mass case. The open circles show the 3 σ level pixels. The surrounding 2 σ level pixels and dependent pixels are omitted.

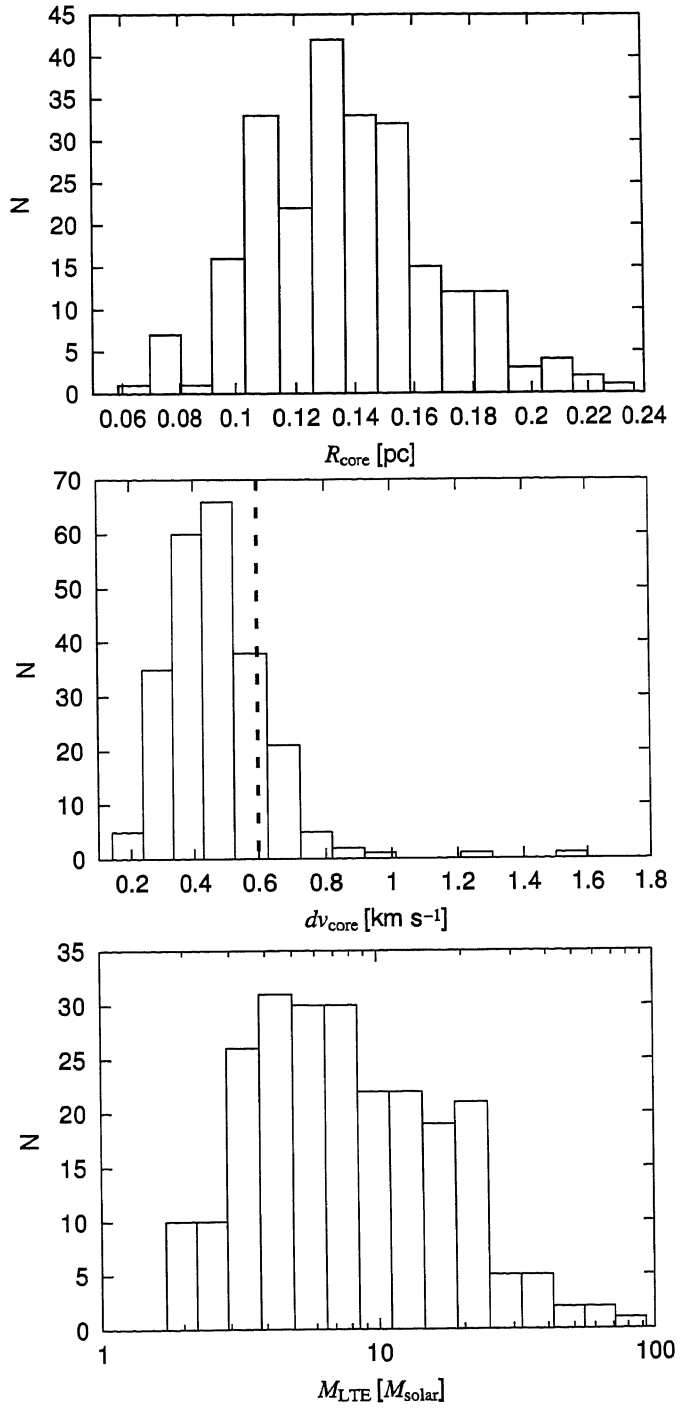

Figure 4.4 Histograms of the radius (*Top*), velocity width (*Middle*), and LTE mass (*Bottom*) of the $H^{13}CO^+$ cores in the Orion A. In the velocity width panel, the thermal and turbulent cores are divided by the vertical dashed line at 0.6 km s^{-1}.

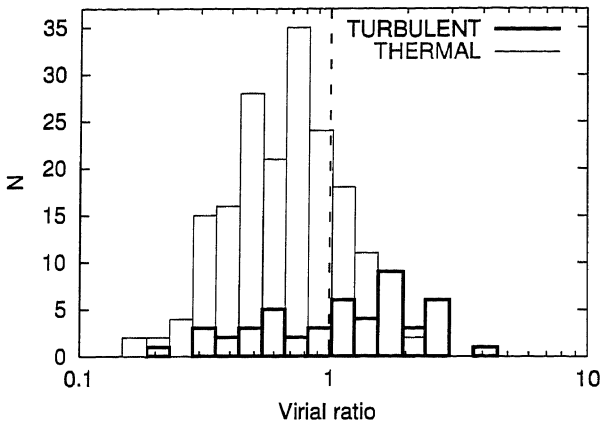

Figure 4.5 Histogram of the virial ratio ($M_{\rm vir}/M_{\rm LTE}$) of the $H^{13}CO^+$ cores in the Orion A. The thick and thiin histograms indicate the turbulent and thermal cores, respectively.

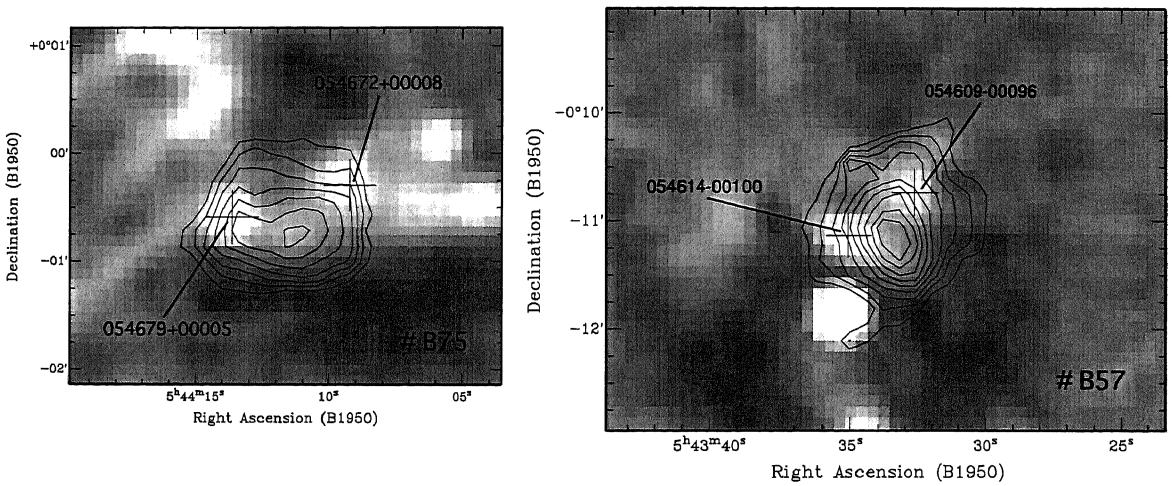

Figure 4.6 Integrated intensity map of # B75 (left) and # B57 (right panel), which are categorized as type B, are shown with contour. Both the contour interval and starting level are 1.2 K km s^{-1}. The grayscale in each panel shows the 850 μm continuum map (Johnstone et al., 2001). The cross marks shows the position of the 850 μm dust cores.

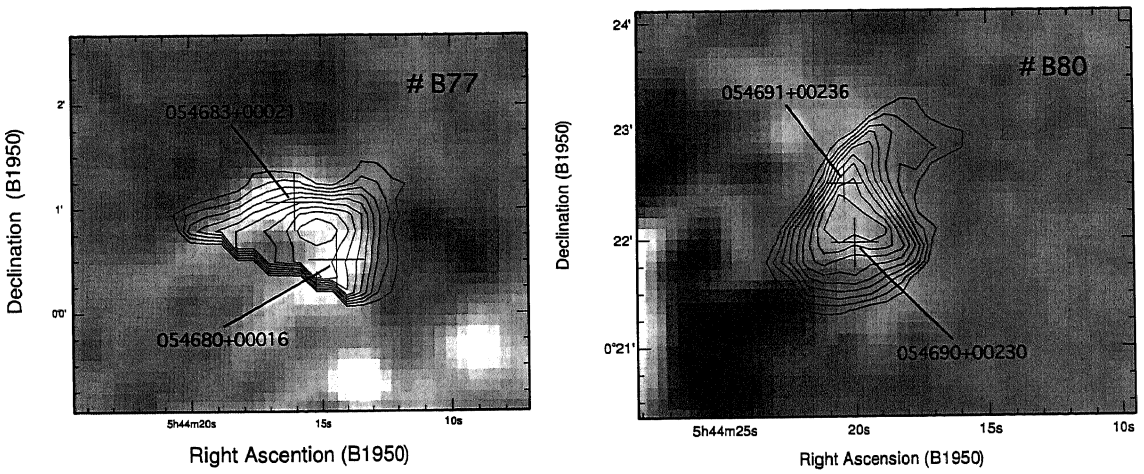

Figure 4.7 Integrated intensity map of # B77 (left) and # B80 (right panel), which are categorized as type C, are shown with contour. The contouring paramters are the same as Figure 4.6. The grayscale in each panel shows the 850 μm continuum map (Johnstone et al., 2001). The cross marks shows the position of the 850 μm dust cores.

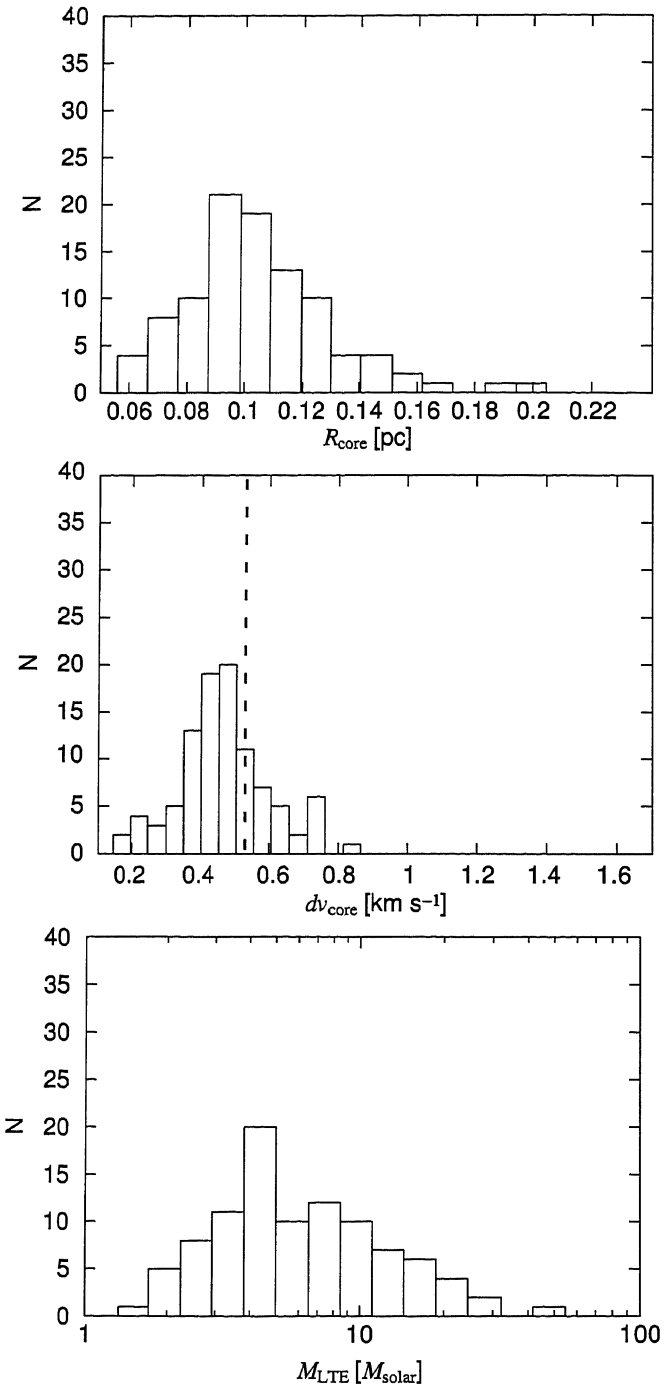

Figure 4.8 Histograms of the radius (*Top*), velocity width (*Middle*), and LTE mass (*Bottom*) of the $H^{13}CO^+$ cores in the Orion B. In the velocity width panel, the thermal and turbulent cores are divided by the vertical dashed line at 0.6 km s^{-1}.

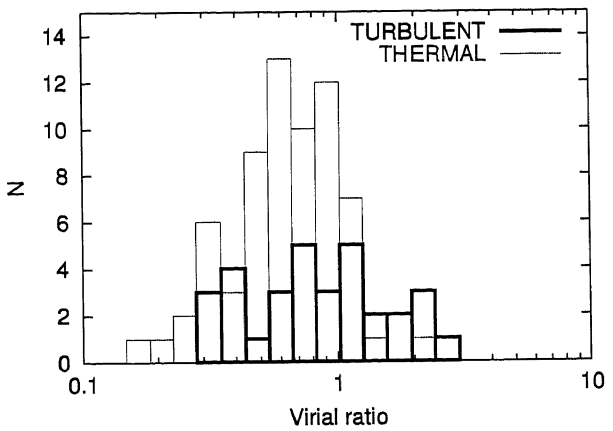

Figure 4.9 Histogram of the virial ratio ($M_{\rm vir}/M_{\rm LTE}$) of the $H^{13}CO^+$ cores in the Orion B. The thick and thin histograms indicate the turbulent and thermal cores, respectively.

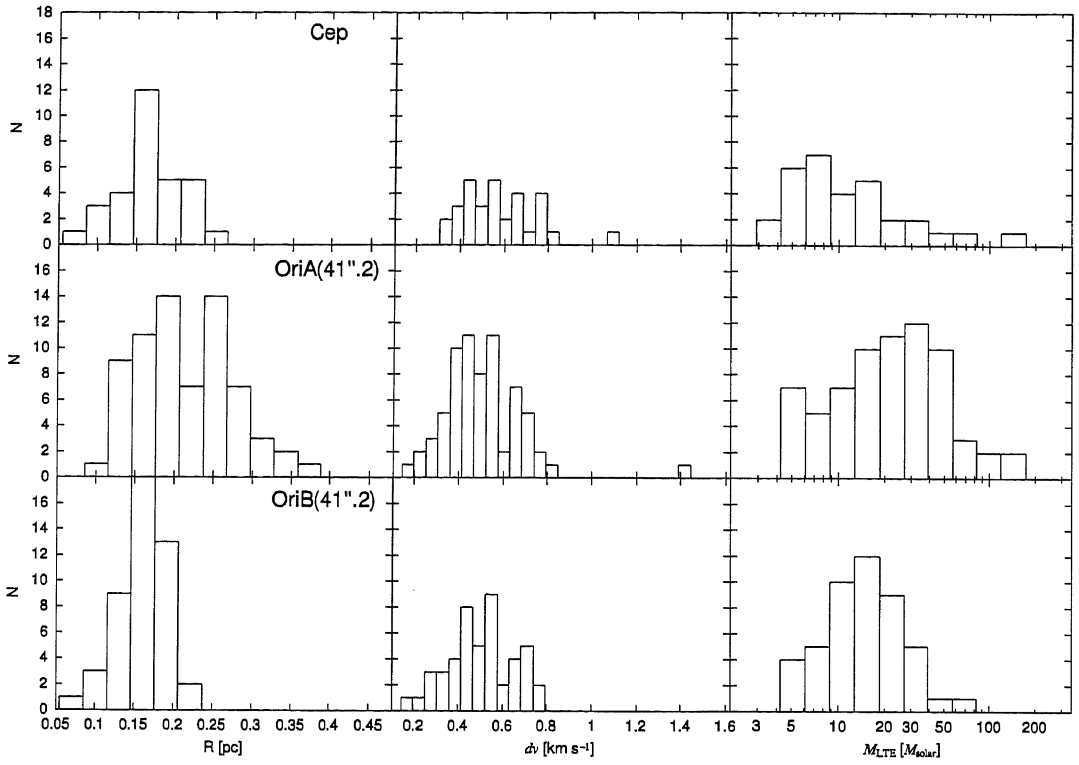

Figure 4.10 Histograms of the core properties in the Cepheus OB3 cloud (*top row*), the resolution-reduced results in the Orion A (*middle row*), and those in the Orion B cloud (*bottom row*). The left, middle, right columns respectively shows the radius, velocity width, and mass distributions.

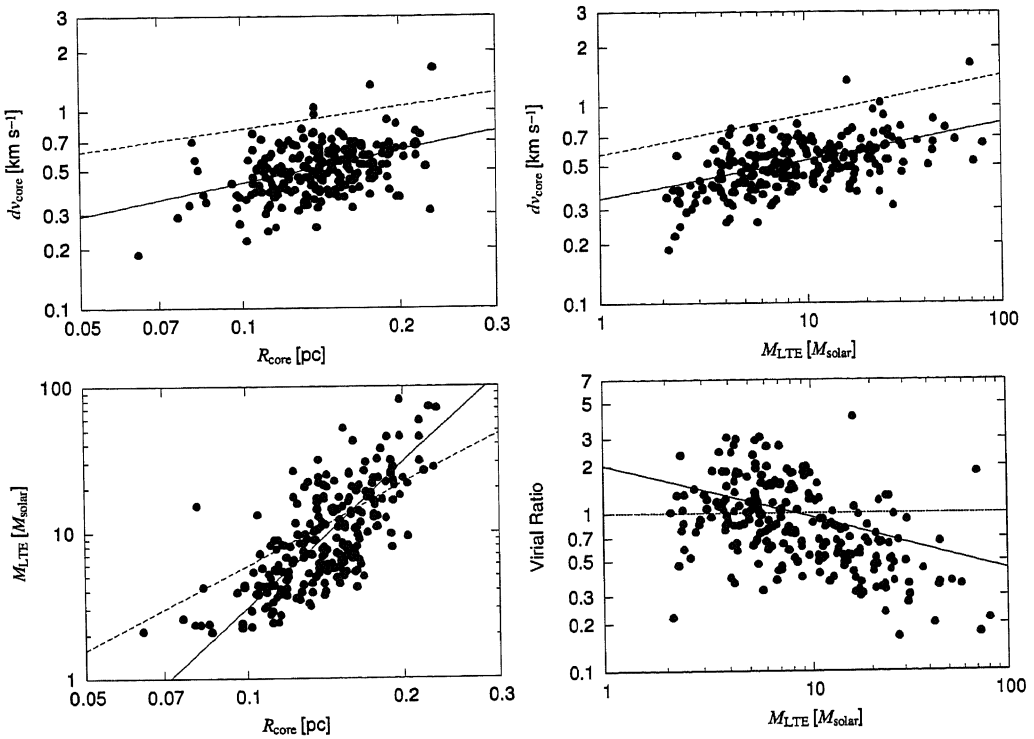

Figure 4.11 Velocity width-radius (*top-left*), velocity width-mass (*top-right*), mass-radius (*bottom-left*), and virial ratio (M_{vir}/M_{LTE})-mass (*bottom-right*) relations of the $H^{13}CO^+$ cores. The solid and dashed lines in each panel represent the best-fit solution and the Larson's relation, respectively. The horizontal dotted line in the virial ratio-mass relation panel represents the virial equilibrium.

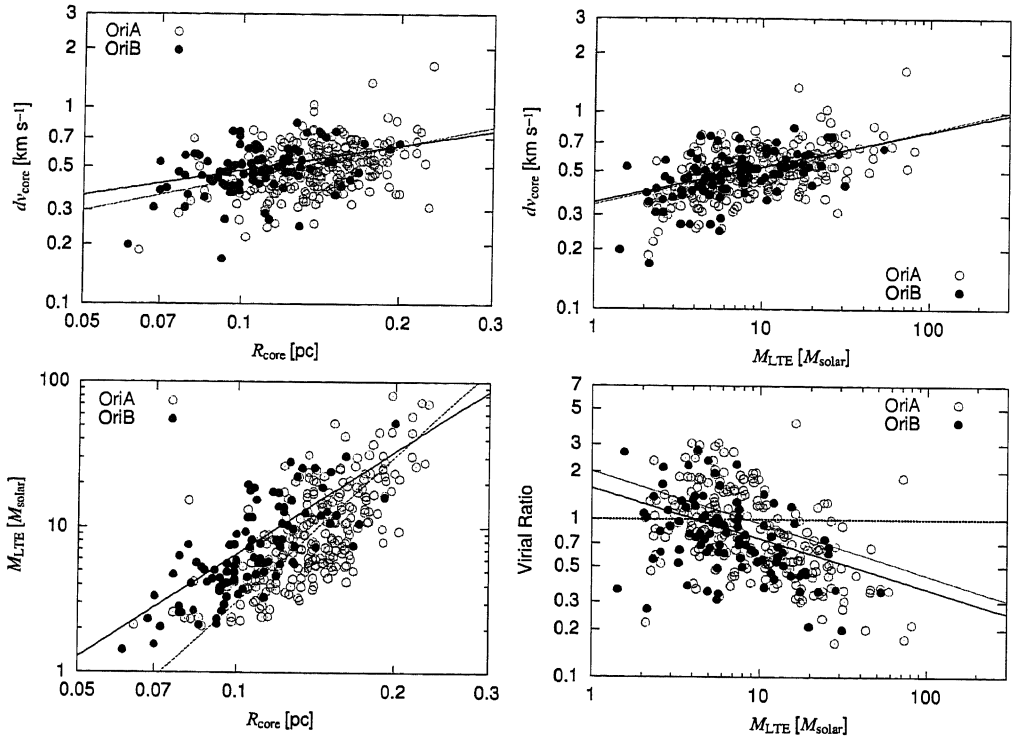

Figure 4.12 Velocity width-radius (*top-left*), velocity width-mass (*top-right*), mass-radius (*bottom-left*), and virial ratio-mass (*bottom-right*) relations of the $H^{13}CO^+$ cores in the Orion B cloud with thick-color symbols. The same relations in the Orion A cloud are shown with thin-color symbols. The solid lines in thick- and thin-color in each panel represent the best-fit solutions in the Orion B and Orion A, respectively. The horizontal dotted line in the virial ratio-mass relation panel represents the virial equilibrium.

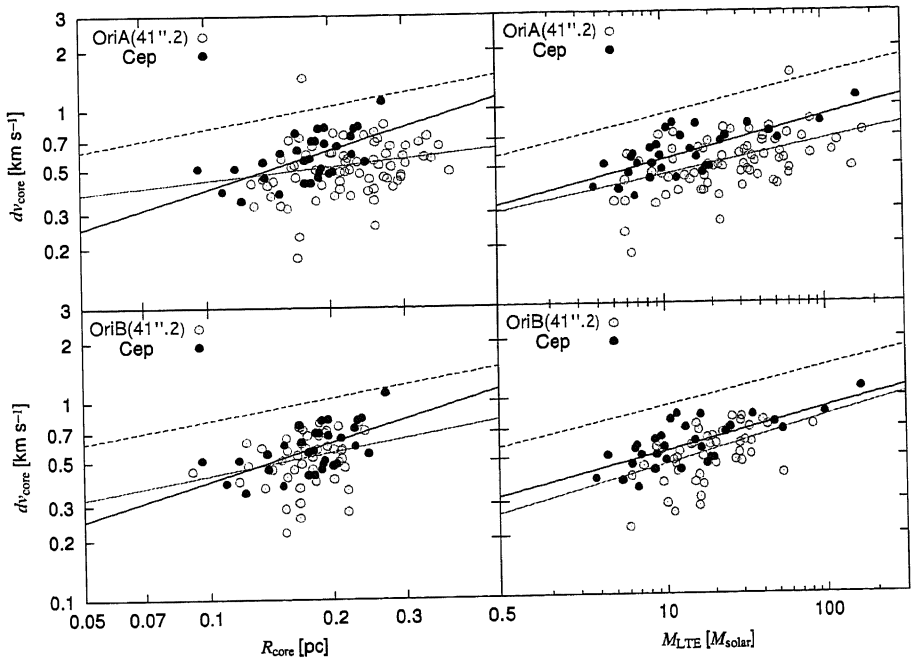

Figure 4.13 Velocity width-radius (*Left-column*) and velocity width-mass (*Right-column*) relations of the $H^{13}CO^+$ cores in the Cepheus OB3 cloud with thick-color symbols. Thin-color symbols show the same relations in the resolution-reduced results in the Orion A and B cloud in the upper-row and lower-row panels, respectively. The solid lines in thick- and thin-color in each panel represent the best-fit solutions in the Cepheus OB3 and the other clouds, respectively. The dashed line in each panel shows the corresponding Larson's relation.

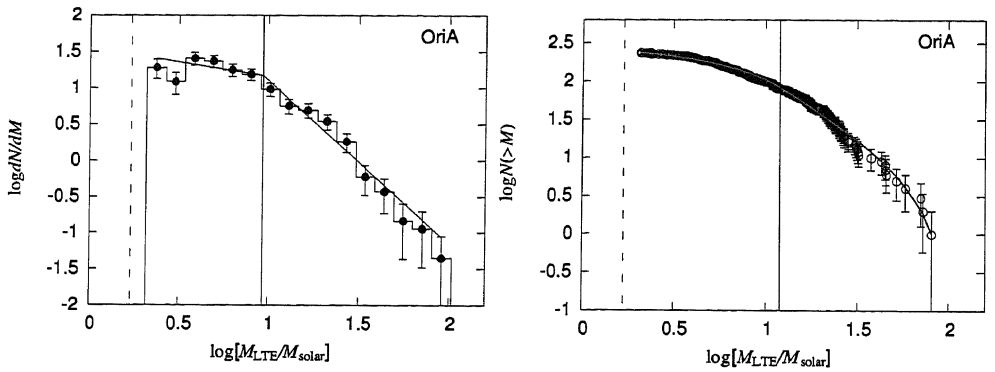

Figure 4.14 (*Left*) $H^{13}CO^+$ CMF in the Orion A cloud. The two solid lines represent the best-fit power-law functions. The vertical dashed and solid lines show the mass detection limit of our observations and the turn over mass, respectively. (*Right*) $H^{13}CO^+$ cumulative CMF in the Orion A cloud. The thin-color solid curve shows the best-fit power-law functions with two indices and the best-fit turn over mass is indicated by a vertical solid line. The vertical dashed line indicates the mass detection limit. The error bars in each panel show the statistical uncertainty of $\sqrt{N}$, where N is the sample number in each mass bin.

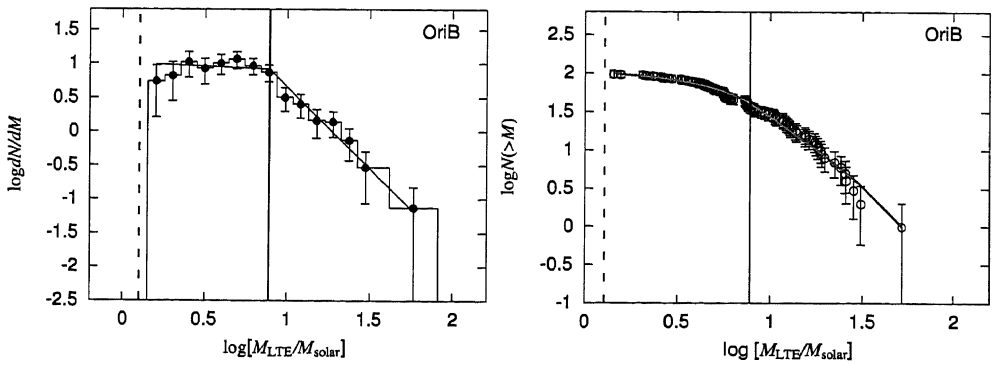

Figure 4.15 $H^{13}CO^+$ CMF (*Left*) and $H^{13}CO^+$ cumulative CMF (*Right*) in the Orion B cloud. The symbols in the panels are plotted as the same manner as Figure 4.14.

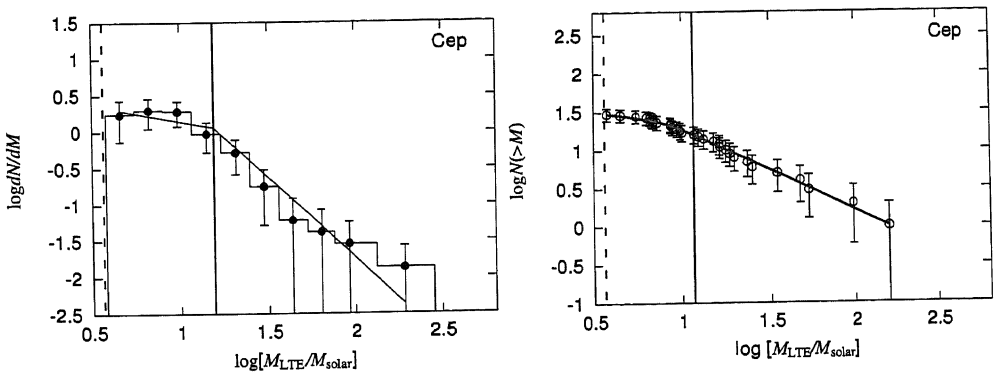

Figure 4.16 $H^{13}CO^+$ CMF (*Left*) and $H^{13}CO^+$ cumulative CMF (*Right*) in the Cepheus OB3 cloud. The symbols in the panels are plotted as the same manner as Figure 4.14.

Table 4.1. Parameters for CLUMPFIND and the mass detection limit

Cloud	$\Delta\theta_{\rm eff}$ arcsec	ΔT K	Number of cores	Area degree^2	Mass detection limit $M_\odot$
Orion A	23.4	0.17	236	1.5	1.6
Orion B	27.1	0.28	98	1.4	1.3
Cepheus	27.1	0.25	31	1.4	3.6
Orion A	41.2	0.12	69	1.5	3.5
Orion B	41.2	0.24	47	1.4	3.5

Table 4.2. Summary of the physical properties of the $H^{13}CO^+$ cores in the Orion A cloud

	min	max	mean[a]
$R_{\rm core}$ [pc]	0.06	0.23	0.14 ± 0.03
$dv_{\rm core}$ [km s^{-1}]	0.19	1.65	0.52 ± 0.17
$M_{\rm LTE}$ [$M_\odot$]	2.1	81	12 ± 12
$M_{\rm vir}/M_{\rm LTE}$	0.2	4.1	1.0 ± 0.6
$\bar{n}$ [cm^{-3}]	4.2×10^3	1.2×10^5	$(1.6\pm1.2)\times10^4$

[a]With standard deviation

Table 4.3. Summary of the physical properties of the $H^{13}CO^+$ cores in the Orion B cloud

	min	max	mean[a]
$R_{\rm core}$ [pc]	0.06	0.20	0.11 ± 0.03
$dv_{\rm core}$ [km s^{-1}]	0.17	0.84	0.50 ± 0.13
$M_{\rm LTE}$ [$M_\odot$]	1.4	52	8.9 ± 7.7
$M_{\rm vir}/M_{\rm LTE}$	0.2	2.8	0.9 ± 0.5
$\bar{n}$ [cm^{-3}]	6.8×10^3	7.0×10^4	$(2.6\pm1.3)\times10^4$

[a]With standard deviation

Table 4.4. Summary of the physical properties of the $H^{13}CO^+$ cores in Cepheus OB3

	min	max	mean[a]
$R_{\rm core}$ [pc]	0.10	0.27	0.18 ± 0.04
$dv_{\rm core}$ [km s^{-1}]	0.35	1.11	0.60 ± 0.17
$M_{\rm LTE}$ [$M_\odot$]	3.8	162	23 ± 32
$M_{\rm vir}/M_{\rm LTE}$	0.3	2.3	1.0 ± 0.5
$\bar{n}$ [cm^{-3}]	4.3×10^3	3.5×10^4	$(1.3\pm0.8)\times10^4$

[a]With standard deviation

Table 4.5. Comparison of our results with other works in the Orion A

Line	$H^{13}CO^{+a}$	$H^{13}CO^{+b}$	CS[c]
R [pc]	0.14	0.06	0.16
dv [km s^{-1}]	0.52	0.94	1.21
M_{LTE} [$M_\odot$]	12	18	79
M_{vir}/M_{LTE}	1.0	1.1	0.5

[a]Our study

[b]Aso et al. (2000)

[c]Tatematsu et al. (1993)

Note. — The listed values are the mean values in each region.

Table 4.6. Comparison of our results with other works in the Orion B

Cloud Line/Wavelength	Orion B $H^{13}CO^{+}$[a]	Orion B 850 μm[b]	Orion A $H^{13}CO^{+}$[c]
R [pc]	0.11	0.05	0.14
dv [km s^{-1}]	0.50	-	0.52
$M_{\rm LTE}$ [M$_\odot$]	8.9	1.6	12
$M_{\rm vir}/M_{\rm LTE}$	0.9	-	1.0

[a]Our study

[b]Johnstone et al. (2001)

[c]Our study, in the Orion A cloud

Note. — The listed values are the mean values in each region.

Table 4.7. Dust-associated $H^{13}CO^+$ cores in the Orion B

I.D.	Type of association	Associated dust core name[a]
B54	A	054607−00123
B55	A	054609−00143
B57	B	054610−00096
B59	A	054613−00119
B60	A	054614−00124
B61	A	054615−00108
B62	A	054617−00123
B64	A	054623−00055
B68	A	054639−00135
B70	A	054647−00017
B73	A	054667+00006
B74	A	054676+00073
B75	B	054679+00005
B77	C	054680+00016 , 054683+00021
B80	C	054690+00230 , 054691+00236
B82	A	054696+00245
B85	A	054703+00181
B88	A	054706+00202
B91	A	054717+00213
B92	A	054719+00231
B94	A	054728+00228

[a]The nomenclature is given by Johnstone et al. (2001).

Table 4.8. Comparison of the Cepheus cores with the low-resolution results in the Orion A and B

Clouds	Cepheus	Orion A	Orion B
R [pc]	0.18	0.23	0.18
dv [km s^{-1}]	0.60	0.53	0.53
$M_{\rm LTE}$ [$M_\odot$]	23	36	21
$M_{\rm vir}/M_{\rm LTE}$	1.0	0.6	0.6

Note. — The listed values are the mean values in each region.

Table 4.9. Best-fit parameters for the power-law fitting 1. Coefficients

	Coefficients C		
	$dv_{\rm core} = CR_{\rm core}^{\beta}$	$dv_{\rm core} = CM_{\rm LTE}^{\beta}$	$M_{\rm LTE} = CR_{\rm core}^{\beta}$
Orion A	1.55±0.27	0.34±0.02	(6.6±2.4)×10^3
Orion B	1.26±0.30	0.35±0.02	(1.5±0.7)×10^3
Cepheus	1.82±0.54	0.32±0.03	(1.8±1.4)×10^3
Orion A (41″.2)	0.75±0.17	0.30±0.05	(2.7±0.9)×10^3
Orion B (41″.2)	1.06±0.41	0.26±0.05	(2.0±1.8)×10^3
Larson (1981)	1.95	0.57	4.7×10^2

Note. — The units of $R_{\rm core}$, $dv_{\rm core}$, and $M_{\rm LTE}$ are pc, km s^{-1}, and $M_{\odot}$, respectively.

Table 4.10. Best-fit parameters for the power-law fitting 2. Power-law indices

	Power-law index β		
	$dv_{\rm core} = CR_{\rm core}^{\beta}$	$dv_{\rm core} = CM_{\rm LTE}^{\beta}$	$M_{\rm LTE} = CR_{\rm core}^{\beta}$
Orion A	0.55±0.09	0.19±0.02	3.34±0.21
Orion B	0.42±0.11	0.18±0.03	2.35±0.23
Cepheus	0.66±0.17	0.22±0.04	2.79±0.43
Orion A(41″.2)	0.23±0.15	0.18±0.04	3.10±0.27
Orion B(41″.2)	0.39±0.22	0.24±0.06	2.67±0.53
Larson (1981)	0.38	0.20	1.9

Note. — The units of $R_{\rm core}$, $dv_{\rm core}$, and $M_{\rm LTE}$ are pc, km s^{-1}, and $M_{\odot}$, respectively.

Table 4.11. Comparison among the power-law indices in the high-mass sides of various mass functions

region	Number of cores	power-law index γ	fitting range	Lines or wavelengths	References
Cepheus	31	2.1 ± 0.4	$> 17 M_\odot$*	$H^{13}CO^+(1-0)$	1
Cepheus	31	2.1 ± 0.9	$> 11 M_\odot$*	$H^{13}CO^+(1-0)$	2
Orion A	236	2.3 ± 0.1	$> 9.3 M_\odot$*	$H^{13}CO^+(1-0)$	1
Orion A	236	2.5 ± 0.2	$> 12 M_\odot$*	$H^{13}CO^+(1-0)$	2
Orion B	98	2.4 ± 0.2	$> 7.7 M_\odot$*	$H^{13}CO^+(1-0)$	1
Orion B	98	2.7 ± 0.7	$> 8.3 M_\odot$*	$H^{13}CO^+(1-0)$	2
Orion B	75	2.5 - 3.0	$> 1.0 M_\odot$	850 μm	3
ρ Ophiuchi	60	2.5	$> 0.5 M_\odot$*	1.3 mm	4
ρ Ophiuchi	55	2.0 - 2.5	$> 0.6 M_\odot$	850 μm	5
Serpens	26	2.1	$> 0.5 M_\odot$	3 mm	6
Taurus	23	2.5 ± 0.3	$> 3.5 M_\odot$*	$H^{13}CO^+(1-0)$	7

References. — (1) Our study, differential form; (2) Our study, cumulative form; (3) Johnstone et al. 2001; (4) Motte et al. 1998; (5) Johnstone et al. 2000; (6) Testi & Sargent 1998; (7) Onishi et al. 2002.

*The lowest mass is also the turnover mass.

Chapter 5

Physical Relation between the $H^{13}CO^+$ CMF and the IMF

In this chapter we investigate the physical relation between the $H^{13}CO^+$ CMF and dust CMF and finally the IMF. First, we show that the dust continuum CMF derived by Johnstone et al. (2001) in the northern part of the Orion B cloud can be well reproduced from the $H^{13}CO^+$ CMF considering that the dust cores are internal structures of the $H^{13}CO^+$ cores. This suggests that the shape of the dust CMF have been simultaneously determined at the $H^{13}CO^+$ core formation phase. Next, we compare the $H^{13}CO^+$ CMF to the stellar IMF through the reproduction of the IMF from the CMF. There is a major disagreement between the predicted and real IMFs: paucity of stars in the low-mass side. We show that this disagreement can be explained by considering the confusion along the line of sight, which also makes the turnover in the CMF disappear. The implication of these results is discussed in conjunction with the origin of the IMF.

5.1 Relation between the $H^{13}CO^+$ and Dust CMF

Johnstone et al. (2001) derived the dust CMF in the northern part of the Orion B cloud, including NGC2068/NGC2071/LBS23 regions, in the Orion B cloud. In the same region, we have identified 39 $H^{13}CO^+$ cores. The left panel of Figure 5.1 shows the $H^{13}CO^+$ CMF of the 39 cores and the dust CMF. Although Figures 8 and 9 in Johnstone et al. (2001) presented the dust CMF in the cumulative form, we convert it to a differential CMF to compare the two CMFs more easily. Note that the best-fit results of the dust CMF in the differenital form by us are consistent with theirs: a turnover mass of $1.6\pm0.2M_\odot$, $\gamma = 0.2 \pm 0.14$ in the low-mass flat part, and $\gamma = 2.6 \pm 0.25$ in the high-mass steep part, which is consistent with their ranges of 2.5 to 3.0 in the cumulative form. The high-mass part γ is consistent with their γ in the range from 2.5 to 3.0 in the cumulative form. On the other hand, the $H^{13}CO^+$ CMF has the following best-fit results: a turnover mass of $8.6\pm0.9M_\odot$, $\gamma = 0.20\pm0.07$ in the flat low-mass part, and $\gamma = 2.20\pm0.25$ in the steep high-mass part. The high-mass part γ is consistent with that of the dust CMF within the uncertainty, suggesting that the two CMFs have a physical relation between them.

To produce the dust CMF from the $H^{13}CO^+$ CMF, we assume that dust cores are the inner denser ($\sim 10^6$ cm^{-3}) parts of the $H^{13}CO^+$ cores with densities of $\sim 10^{4-5}$ cm^{-3} and the masses of the dust cores are the one third of those of the $H^{13}CO^+$ cores, as described in Section 4.2.2.2. The right panel of Figure 5.1 shows the reproduced dust CMF from our $H^{13}CO^+$ CMF. The two CMFs are remarkably similar to each other, not only for the high-mass part slope but also for the turnover mass. We note that in the NGC2068/2071/LBS23 regions the velocity structure of the $H^{13}CO^+$ emission is not a complex one, i.e., the $H^{13}CO^+$ emission lines show no apparent multiple peaks (see Figure 3.9), leading to the similarity between the $H^{13}CO^+$

and dust CMFs. This suggests that the CMF of the denser dust cores, which are thought to be the direct sites of star formation (Motte et al., 1998), has been simultaneously determined at the formation of $H^{13}CO^+$ cores. In other words, we can get the insight into the origin of the IMF only from the $H^{13}CO^+$ CMF.

5.2 Relation between the CMF and IMF

In the last chapter we showed that the γ values of the CMF obtained with the $H^{13}CO^+$ and dust continuum emission, including ours, fall in the range from 2.0 to 3.0, which is consistent with the IMF, such as Salpeter's (2.35) and Miller & Scalo's (2.6) (Motte et al., 1998; Onishi et al., 2002). Furthermore, in the last section the dense gas traced by $H^{13}CO^+$ emission is most likely to be closely related to star formation as well as that by the dust continuum emission. These facts strongly suggest a physical relation between the IMF and the $H^{13}CO^+$ CMF. In this section we examine the similarity between the IMF and the CMF in more detail and discuss a possible physical relation between them.

5.2.1 Similarity between the CMF and the IMF

In Orion A, the IMF of the ONC has been derived by Hillenbrand (1997); $\gamma = 2.94$ for $M > 0.3M_\odot$. To directly compare the CMF of the $H^{13}CO^+$ cores with the ONC IMF, we should re-estimate the CMF in the formation area of the ONC, which is expected to be more compact than the present extent of the cluster. Kroupa et al. (2001) studied the dynamical evolution of the ONC using an N-body calculation method. According to their model B, the radius of the core part of the ONC was initially 0.1 pc, and become 0.16 pc at 1 Myr, which agrees well with the observations (Hillenbrand & Hartmann, 1998). If we assume that the whole extent of the ONC is proportional to the radius of the cluster core, the extent of the ONC at their formation is expected to

be 63 % of the present size. Figure 5.2 shows the 63 %-reduced version of the surface density map obtained by Hillenbrand & Hartmann (1998). The reduced area includes 57 $H^{13}CO^+$ cores, and we re-estimated a CMF for the 57 cores (hereafter we refer to the new CMF as "ONC CMF") as shown in Figure 5.3. The best-fit results of the ONC CMF based on a power-law function are as follows: a turnover mass of $6.7 \pm 0.7 M_\odot$, $\gamma = 0.3 \pm 0.1$ in the flat low-mass part, and $\gamma = 1.8 \pm 0.2$ in the steep high-mass part. The latter index is strikingly similar to that of the ONC IMF ($\gamma = 1.94$).

For the whole of the Orion A cloud and the other GMCs, however, no IMFs have been derived with such a very wide mass range as the ONC IMF. Then we used the Galactic-field averaged IMF (GFIMF) defined by Kroupa (2001): he complied the IMFs of the clusters and OB associations in the Milky Way and the Large Magellanic Cloud in the literature and derived the averaged IMF as the GFIMF. He found that the GFIMF is a power-law function which has two turnover masses of $\sim 0.5\ M_\odot$ and $\sim 0.08\ M_\odot$:

$$\frac{dN}{dM} = C_* M^{-\gamma}, \tag{5.1}$$

where

$$\begin{aligned} \gamma &= 0.3 \pm 0.8 \quad \text{for} \quad 0.01 \leq M/M_\odot < 0.08, \\ &= 1.3 \pm 0.5 \quad \text{for} \quad 0.08 \leq M/M_\odot < 0.50, \\ &= 2.3 \pm 0.3 \quad \text{for} \quad 0.50 \leq M/M_\odot < 1.00, \\ &= 2.3 \pm 0.7 \quad \text{for} \quad 1.00 \leq M/M_\odot, \end{aligned} \tag{5.2}$$

and C_* is a constant or a dN/dM value for $M = 1 M_\odot$. The power-law index of the steep part ($> 1 M_\odot$) of the GFIMF, $\gamma = 2.3 \pm 0.7$, is consistent with those of our CMFs in the three clouds within the uncertainties: 2.3 ± 0.1 for the Orion A, 2.4 ± 0.2 for the Orion B, and 2.1 ± 0.4 for the Cepheus OB3 (see Table 4.11).

To directly compare the GFIMF with the CMFs, we scale the GFIMF by the number of stars associated with the GMCs. The total stellar number, N_*, can be obtained by

$$N_* = \int_{M_{*,\min}}^{M_{*,\max}} \frac{dN}{dM} dM, \tag{5.3}$$

where $M_{\min}$ and $M_{\max}$ are the minimum and maximum masses of stars to be counted, respectively. Note that N_* is insensitive to $M_{*,\max}$ because $\gamma > 1$ for $M > 0.01 M_\odot$. First, we consider the case of the ONC. Since the completeness limit mass of the ONC IMF is 0.1 $M_\odot$ and the total number of stars above 0.1 $M_\odot$ is 896 (Hillenbrand, 1997), resulting in $C_* = 127.8$. We show the GFIMF of $C_* = 127.8$ and the ONC IMF in Figure 5.4. The figure also shows the Trapezium cluster IMF obtained by Muench et al. (2002), scaled by the observed area ratio of Hillenbrand's and Muench et al's. Since the scaled GFIMF have a good agreement with the ONC and Trapezium IMFs, the scaling of the GFIMF by the total stellar number is likely to be a good method to estimate the IMF in each GMC. Second, we consider the whole of the Orion A cloud, not only the ONC. In the Orion A GMC, the stellar members are well studied: 70 % of the stellar members are the distributed population, 23 % are the members of the clusters such as the ONC and L1641S clusters, and 7 % are the members of the aggregates (Strom et al., 1993). Note that the underlying IMF for the three different stellar populations seems to be very similar to each other (Strom et al., 1993). Assuming that these fractions do not vary in the Orion A GMC, we estimate N_* of the Orion A cloud to be 3900 from the total stellar number of the ONC (Hillenbrand, 1997). According to Equation 5.3, C_* is derived to be 555.7. Third, for the Orion B case, Lada et al. (1991a) found that 96 % of the stellar members associated with the cloud belong to the four clusters, NGC2024, NGC2023, NGC2068, and NGC2071. Then N_* and M_* is estimated to be the total steller number of these clusters of 627 (Lada & Lada, 2003), multiplied by 1.04, i.e., $N_* = 650$. and we have

C_* of 87.5. Finally, for the Cepheus OB3 cloud case, the stellar members has not been studied as well as in the Orion A and B. Therefore we use the sum of the parameters of the associated clusters Cep-A and C: N_* of 690 (Lada & Lada, 2003) and we have C_* of 85.3.

Figure 5.5 shows the scaled GFIMFs and the $H^{13}CO^+$ CMFs in each region. We can see the similarity between the γ values in the high-mass parts of the $H^{13}CO^+$ CMFs and the IMFs in the three clouds: the γ of the GFIMF $> 1.0M_\odot$ is 2.3±0.7, and those of the best-fit results of the ONC IMF, Orion A, Orion B, and Cepheus CMFs are 1.8±0.2, 2.3±0.1, 2.4±0.2, and 2.1±0.4, respectively, all of which are consistent with the GFIMF within the uncertainties. This similarity strongly suggests that the $H^{13}CO^+$ cores we identified are direct sites of star formation, i.e., a physical link between the CMF and the IMF. To discuss the possible physical relation, we try to predict the IMF from the CMF through a simple model described in the following.

5.2.2 Physical Relation between the CMF from the IMF

Considering that the CMF is directly linked to the IMF, we can predict an IMF from the $H^{13}CO^+$ CMF by introducing the two parameters of the star formation efficiency (SFE), defined by the mass ratio of stars to their natal core, and the stellar multiplicity in a core (SMC), defined by the number of stars to be formed in a core. In calculating the predicted IMF, we assume that the SFE is constant for all the cores and all the cores have the same SMC, because the γ value of the CMF in the high-mass part is almost the same as that of the IMF. If the SFE varies over individual cores, then the slope of the predicted IMF considerably differs from that of the real IMF. As for the SMC, it seems quite natural to consider that more massive cores have larger SMC. If this is the case, however, the slope of the predicted IMF becomes steeper than that of the IMF.

We can take the SMC value from the studies of the stellar multiplicity. For main sequence stars, Duquennoy & Mayor (1991) surveyed G dwarf multiple systems in the solar neighborhood and found that the fractions of single star, binary, and triple or more systems are 0.57, 0.38 and 0.05, respectively. Fischer & Marcy (1992) also found a similar trend in their M dwarf sample. The above studies show that the formations of single star and binary system are dominant in nearby star forming regions. For pre-main-sequence stars (PMS), Mathieu et al. (2000) compiled the PMS binary surveys and found that the PMS binary fraction ranges from 0.03 to 0.4. Therefore, we consider the following two extreme cases of SMC = 1 and 2. In the case of binary formation, we should also need the mass ratio of the secondary to primary, q. For main-sequence stars, Duquennoy & Mayor (1991) found that the q distribution has a broad Gaussian shape which has a peak at ~ 0.23 with a standard deviation of 0.42. For pre-main-sequence stars, Woitas et al. (2001) showed that the q distribution is fairly flat without any distinct peak, although their sensitivity at small q was not sufficient. For massive stars earlier than O type, Mason et al. (1998) argued that high-mass stars tend to have similar mass companions, i.e., $q \sim 1$, compared to solar-type stars. Therefore, in this study, we consider the two cases of q=0.23 and 1.0. Furthermore, we assume that all the cores have the same q for simplicity.

For the case of $q < 1.0$, note that the completeness limit of the predicted IMF is larger than the low-mass end of the predicted IMF. Let $M_{\rm min}$ be the mass detection limit of the core survey. The minimum-mass core produces two stars with masses of $M_{\rm min} \times {\rm SFE}/(1+q)$ and $M_{\rm min} \times {\rm SFE} \times q/(1+q)$, and the minimum-stellar mass of the predicted IMF is the latter mass. On the other hand, stars whose masses fall into a range from $M_{\rm min} \times {\rm SFE} \times q/(1+q)$ to $M_{\rm min} \times {\rm SFE}/(1+q)$ can also be produced within the cores of $< M_{\rm min}$. However, in our model, the cores of $< M_{\rm min}$ are ignored , leading to the underestimation of the predicted IMF below $M_{\rm min} \times {\rm SFE}/(1+q)$. Hence we call this the completeness limit of the predicted IMF.

We consider the three models A (SMC = 1), B (SMC = 2 and q=1.0), and C (SMC = 2 and q=0.23) to estimate IMFs from the CMFs and to fit the predicted IMFs to the real ONC IMF/GFIMF by treating the SFE as a free parameter. First, we discuss the relation between the ONC IMF and the ONC CMF. The predicted IMFs can be quite well fitted to the ONC IMF on the high-mass side, as shown in Figure 5.6. The completeness limits of the predicted IMFs are also indicated with the vertical dashed lines. For model A, the fitting in the high-mass range of $M > 1M_{\odot}$ requires the SFE of 0.37±0.05. In the case of binary formation (models B and C) the predicted IMF moves toward the low-mass side with the same γ as in the single star case: the best-fit SFE is 0.37±0.05 and 0.39±0.04 for models B and C, respectively. Note that the SFE does not sensitivily depend on our adopted models. Next, we show the results for the scaled GFIMFs of the Orion A, Orion B, and Cepheus clouds in Figure 5.7. As for the ONC case, the high-mass parts of the predicted IMFs can be fitted well to those of the scaled GFIMFs with the best-fit SFE of 0.25 - 0.46. Note that the best-fit SFE for the ONC GFIMF, 0.37 - 0.39, have a good agreement with the ONC IMF case. The best-fit SFEs of the Orion B and Cepheus OB3 regions, 0.25 - 0.32, are similar to each other, but they are 1.4 times smaller than those of the ONC and Orion A regions (0.34 - 0.46).

Our derived SFE of 0.25 - 0.46 seems to be consistent with the theoretical prediction by Nakano et al. (1995). We applied their model to our $H^{13}CO^+$ data as follows. First, we plotted the $H^{13}CO^+$ cores on Figure 1 by Nakano et al. (1995), as shown in Figure 5.8: the dense cores are located in the regime where the stellar mass is determined by an outflow. Therefore, we calculated model-predicted stellar masses using Equation 11 of Nakano et al. (1995) and obtained a model-predicted SFE of 0.26 for the ONC CMF, 0.30 for the Orion A, 0.24 for the Orion B, and 0.30 for the Cepheus OB3. Since the IMF can be well reproduced from the CMF with reasonable SFE, we conclude that the IMF is most likely to be determined at the $H^{13}CO^+$ core

formation.

There are two mismatched points in the fitting in Figures 5.6 and 5.7. First, the number of the high mass ($M \geq 10M_{\odot}$) stars in the predicted IMF seems to be smaller than that in the ONC IMF even for model A. Second, the predicted IMF becomes significantly smaller than the IMF in the low-mass part even if we consider the completeness of the predicted IMF. For the first point, we can consider the following two possible causes of the paucity of the high mass stars: (1) the SFE is not uniform but high (0.50 - 0.70) for the massive cores of $> 30M_{\odot}$, or (2) there are no massive cores to produce such high-mass stars in the present time: only one or two cores are required. Anyway, we believe that the disagreement is not serious because of the large statistical scatters around the high-mass end.

For the second disagreement, we indicate the shortage of stellar number with the shadowed areas in Figures 5.6 and 5.7. The shortage can be seen below the turnover mass of the predicted IMF, $M_{*,\mathrm{turn}}$, falls in a range from 0.5 - 2.5 $M_{\odot}$ and the corresponding shortage of stellar mass, $M_{*,\mathrm{short}}$, is estimated to be 60 - 500 $M_{\odot}$. Table 5.1 summarizes $M_{*,\mathrm{turn}}$ and $M_{*,\mathrm{short}}$ for the three models in each region. These mass shortages could be explained by a very large SMC of >10. The large SMC, however, drastically decreases the number of high-mass stars, resulting in the disagreement with the IMF even if we consider the large statistical uncertainties around the high-mass end. Another possible cause is a very low value of q. If we take such a very low q, a large number of low-mass stars can be produced. However, the predicted IMF is only stretched horizontally toward the low-mass side, keeping the position of the high-mass part, which cannot be well fitted to the IMF. We show two examples for $q = 0.1$ and 0.2 in Figure 5.9: the behavior is essentially the same for much lower values of $q \sim 0$. As a more likely cause of the mass shortage, we discuss the confusion effect in core identification in the next section.

5.3 Turnover in the CMF and Confusion

The CMFs of the $H^{13}CO^+$ cores in the three clouds and the ONC CMF have the turnover in 8 - 17 $M_\odot$ and at $6.7M_\odot$, respectively, far above the mass detection limit. Although the presence of a turnover in a CMF has been found by the previous studies, the physical meaning of the turnover has been little understood up to now. In this subsection, we examine whether the turnover in our CMF is an artifact due to the confusion in core identification or not.

The core identification based on 2-D mapping data is intrinsically affected by the confusion. The confusion means a blending, i.e., misidentifying several cores with similar sizes as a larger one owing to overlap along the line of sight, and a shadowing, i.e., overlooking several smaller cores owing to obscuration by a larger one. Therefore, the confusion is likely to considerably decrease the number of smaller (or less massive) cores to be identified and to slightly increase the number of large massive ones, producing a turnover in an estimated CMF: the low-mass part below the turnover mass becomes flatter than the high-mass part. Williams et al. (1994) discussed the influence of the blending on the slope of the CMF and showed that the slope of the CMF becomes shallower as the blending becomes more severe. However, no one has discussed the influence of the confusion on the turnover up to now.

First, we examine the influence of the confusion on the projected shape of the cores on the sky plane. If the blending is severe, one can expect that the core shape is considerably different from the original one. If the shadowing is serious, the core shape would be unchanged. Figure 5.10 shows the histograms of the core aspect ratio in the ISF and in the other regions and clouds. The confusion in the ISF is likely to be more severe than that in the other regions and clouds, because $A_{\rm core}/A_{\rm obs} = 2.5$ for the ISF, significantly larger than those of 1.0, 1.2, 0.3 for the other regions in the Orion A, for the Orion B, and for the Cepheus OB3 clouds, respectively, where $A_{\rm obs}$ is the observed total area above the 2-σ level and $A_{\rm core}$ the total projected area of

the cores on the sky plane. The histograms clearly show that the core aspect ratio in the most crowded region ISF is similar to those in the other regions: we applied the K-S test, and found that the aspect ratio distributions cannot be considered to be different significantly with the significance level of 1 %. This fact suggests that the blending is not dominant in the confusion. We, however, cannot completely rule out the contribution of the blending, because the core aspect ratio depends on how the cores overlap each other, and because we do not know the original shapes of the cores. In this study, for simplicity, we discuss only the shadowing for the confusion.

To quantitatively estimate the shadowing, we adopt the following simple model considering the $H^{13}CO^+$ emission is optically thin. Only cores with smaller masses than the turnover mass are assumed to be shadowed by cores with higher masses than the turnover, and the cores are assumed not to be obscured by similar-mass cores. This assumption needs that the total core mass to be obscured, i.e., the mass shortage, should be smaller than the total mass to hide them, i.e., total core mass above the turnover. Actually, the total masses (800 - 2500 $M_\odot$) of the cores above the turnover at 3.8 - 9.7 $M_\odot$ in the CMFs are larger than the core mass shortages of 200 - 1100 $M_\odot$ below the turnover. Furthermore, the total mass shadowed by a massive core is assumed to be proportional to the projected area of the core on the sky plane. Since the mass-radius relation has $M_{\rm LTE} \propto R_{\rm core}^{\beta}$ with $\beta = 3.3$, the shadowed mass is given by $const. \times M^{2/\beta}$. Under these assumptions, we have

$$M_{{\rm obs},i} = M_{0,i} + \Delta M_i, \tag{5.4}$$

$$\Delta M_i = C {M_{0,i}}^{2/\beta}, \tag{5.5}$$

$$\sum^{i} \Delta M_i = M_{\rm shadowed}, \tag{5.6}$$

where $M_{{\rm obs},i}$ is our estimated mass of the i-th core on the high-mass side above the turover, $M_{0,i}$ the true core mass, ΔM_i the apparent mass increase due to the shadowing, C a constant, and $M_{\rm shadowed}$ the total missing core mass on the

low-mass side below the turnover, which can be obtained by $M_{\rm shadowed} = M_{*,\rm short}/{\rm SFE}$. Since $M_{{\rm obs},i}$ and β are known from our observations, and $M_{\rm shadowed}$ can be obtained through the comparison between the IMF and the CMF, we can determine $M_{0,i}$ and C by applying the above model to the CMFs.

Next, we should re-construct the CMFs on the low-mass side by adding the recovered mass. To put the shadowed cores separately into their original mass bins below the turnover, we assume that ΔM_i can be split into the representative core masses in individual mass bins below the turnover. Let $M_{{\rm bin}j}$ and $N_{{\rm bin}j,i}$ be the representative core mass in the j-th bin and the number of the cores in the j-th bin shadowed by the i-th massive core, respectively. Then we have

$$\Delta M_i = \sum_j M_{{\rm bin}j} N_{{\rm bin}j,i}. \quad (5.7)$$

Practically, we must search the best combination of $N_{{\rm bin}j,i}$ that minimizes $(\Delta M_i - \sum_j M_{{\rm bin}j} N_{{\rm bin}j,i})^2$ for each ΔM_i, because $N_{{\rm bin}j,i}$ is an integer variable. The typical difference between ΔM_i and $\sum_j M_{{\rm bin}j} N_{{\rm bin}j,i}$ is 0.3 - 1 $M_\odot$, much smaller than the minimum mass of $M_{\rm bin,1}$ of 2.8 - 4.6 $M_\odot$. The total sum $\sum_{i,j} M_{{\rm bin}j} N_{{\rm bin}j,i}$ have a good agreement with $M_{\rm shadowed}$: the difference is less than 10 %, as shown in Figure 5.11. These results do not considerably change even for the mass bins smaller than our adopted ones by a factor of 0.5.

The CMFs corrected for the shadowing based on the comparsion with the ONC IMF and the GFIMFs are shown in the left panels of Figure 5.12 and in Figure 5.13, respectively. In Figure 5.13, we only show the results for model A, because the shadowing-corrected CMFs for the three models are almost identical. Note that the turnover disappears in the corrected CMF. Therefore, the shadowing of smaller cores by a larger one is most likely to apparently produce the turnover and low-mass flat part in the ONC CMF, i.e., the turnover we found does not seem to have any physical meanings.

The predicted IMF from the corrected CMF can be well fitted to the IMFs, as shown in the right panels of Figure 5.12 and in Figure 5.14. The

best-fit SFE is 0.40 - 0.46 for the ONC, 0.45 - 0.55 for the Orion A, 0.31 - 0.32 for the Orion B, and 0.36 - 0.38 for the Cepheus OB3. These SFEs are slightly larger than those without the shadowing correction, because the core mass on the high-mass side decreases owing to the shadowing correction. Note that the shadowing model does not change the slope of the predicted IMF considerably. The excellent agreement in Figures 5.12 and 5.14 strongly suggests that the steep part of the IMF is determined at the time of the core formation, but the turnover of the IMF does not correspond to that of the observed CMF.

5.4 Generalization of the Shadowing Model

In the last section we showed that the shadowing model can work well and that the predicted IMF from the CMF corrected for the shadowing can well reproduce the real IMF. In this section, we try to generalize the shadowing model in order to derive the shadowing-free CMF only from the $H^{13}CO^+$ cores, or, try to estimate $M_{\rm shadowed}$ independently of the IMF. On the other hand, it is natural to consider that the severeness of the shadowing should be connected to the 3-dimensional distribution of the $H^{13}CO^+$ cores. In the model, it is assumed implicitly that the low-mass cores of $< M_{\rm turn}$ are distributed uniformly in the α-δ-$v_{\rm LSR}$ space, where $M_{\rm turn}$ is the turnover mass of the $H^{13}CO^+$ CMF. According to this assumption, the mass "density" of the low-mass cores, ρ, can be derived as

$$\rho = \frac{M_{\rm app}}{\sum_{<M_{\rm turn}} V_{{\rm obs},i}}, \tag{5.8}$$

where $M_{\rm app} = \sum_{<M_{\rm turn}} M_{{\rm obs},i}$ is the observed total mass of the low-mass cores, $V_{{\rm obs},i}$ the observed "volume" in the α-δ-$v_{\rm LSR}$ space occupied by the i-th core.

Therefore the total mass of the shadowed cores, $M_{\rm s,p}$, can be obtained by

$$M_{\rm s,p} = \rho \times \sum_{>M_{\rm turn}} V_{0,i}, \tag{5.9}$$

where $V_{0,i}$ is the true volume of the i-th core.

Next, we should find a method to estimate $M_{\rm s,p}$ only from the $H^{13}CO^+$ data. The shadowing generally enlarges the volume of the massive core. If we assume that the shadowing does not broaden the velocity width of the massive core, the volume of the core is proportional to the projected area of the core on the sky plane, or $V \propto M^{2/\beta}$. This assumption would be valid because the shadowed low-mass cores, whose intensities are much weaker than those of the massive cores, cannot contribute much to the velocity width of the massive ones. Actually, the relation of $V \propto M^{2/\beta}$ is supported by our $H^{13}CO^+$ data as follows. If $V \propto M^{2/\beta}$ holds, the relation of $M_{\rm LTE} \propto V I_{\rm mean}$ (see Equation 4.5), where $I_{\rm mean}$ is the mean intensity within a core, lead us to the relation of $I_{\rm mean} \propto M^{1-2/\beta}$, which roughly holds for the $H^{13}CO^+$ cores: the $H^{13}CO^+$ cores have relations of $I_{\rm mean} \propto M_{\rm LTE}^{0.17-0.30}$, consistent with the expected power-law index range of $1 - 2/\beta = 0.16 - 0.40$. Consequently, we use the approximation,

$$\frac{V_{0,i}}{V_{{\rm obs},i}} \simeq \left(\frac{M_{0,i}}{M_{{\rm obs},i}} \right)^{2/\beta}. \tag{5.10}$$

Furthermore, an approximation of

$$\frac{\sum_{>M_{\rm turn}} V_{0,i}}{\sum_{>M_{\rm turn}} V_{{\rm obs},i}} \simeq \overline{\left(\frac{M_{0,i}}{M_{{\rm obs},i}} \right)^{2/\beta}}, \tag{5.11}$$

holds, because the scatter of $M_{0,i}/M_{{\rm obs},i}$ over the massive cores is found to be small; The errors of the above relations are 7 % for the ONC, 5 % for the Orion A, 1 % for the Orion B, and 4 % for the Cepheus OB3. Using

Equations 5.8, 5.9, and 5.11 we finally have

$$M_{\rm s,p} = \frac{\sum_{>M_{\rm turn}} V_{{\rm obs},i}}{\sum_{<M_{\rm turn}} V_{{\rm obs},i}} \overline{\left(\frac{M_{0,i}}{M_{{\rm obs},i}}\right)^{2/\beta}} M_{\rm app}. \quad (5.12)$$

Using Equation 5.12 and $M_{0,i}$ derived in Section 5.3, we calculated $M_{\rm s,p}$ for each region, and compared with $M_{\rm shadowed}$ in Figure 5.15. We can see a good agreement between $M_{\rm s,p}$ and $M_{\rm shadowed}$ within the uncertainties. In other words, $M_{\rm s,p}$ can be a good estimator of $M_{\rm shadowed}$. Equation 5.12 allows us to estimate $M_{\rm shadowed}$ without comparison between the CMF and IMF because $V_{{\rm obs},i}$, $M_{{\rm obs},i}$, $M_{\rm turn}$, and β can be obtained only from our $H^{13}CO^+$ observations. Therefore, solving Equations 5.4, 5.5, 5.6, 5.7 and 5.12 numerically, we can apply this generalized shadowing model to any CMFs in regions where the stellar IMF has not been derived yet.

Figure 5.16 shows the CMF corrected for the confusion on the basis of the generalized shadowing model. The new CMFs are found not to be very much different from the CMFs in Section 5.3: the new CMFs do not have any turnovers and can be well described by power-law functions. The best-fit power-law indices are summarized in Table 5.2. The γ values obtained with the original and the generalized shadowing model have a good agreement with each other. Furthermore, all of the corrected CMFs are consistent with that of the GFIMF (2.3±0.7).

In more detail, the index for the ONC is smaller than those of the others considering the uncertainties although the indices for the Orion A, Orion B, and Cepheus OB3 are very similar to each other within the uncertainties. This flatter high-mass slope of the ONC CMF possibly implies that there exists the mass segregation of the $H^{13}CO^+$ cores: the ONC CMF, constructed by the cores extracted from the central region of the Orion A cloud, is expected to have flatter high-mass slope if more massive cores tend to be located near the center of the cloud. The mass segregation of the $H^{13}CO^+$ cores is possibly the origin of the mass segregation of the stellar members in

the ONC (Hillenbrand & Hartmann, 1998). Hillenbrand & Hartmann (1998) showed that the stellar mass segragation cannot be explained by gravitational relaxation, and concluded that the segregation is primordial one: more massive stars are preferred to be formed in the central region of the cluster. Our results of the existence of the mass segregation of the $H^{13}CO^+$ cores and the physical relation between the IMF and the $H^{13}CO^+$ CMF support their conclusion.

Figure 5.17 shows the predicted IMFs corrected for the confusion with the generalized shadowing model. As for the original model, the predicted IMFs can be fitted to the GFIMFs very well: The best-fit γ values of the predicted IMFs are 2.11±0.22, 2.62±0.09, 2.44±0.11, and 2.00±0.18 for the ONC, Orion A, Orion B, and Cepheus clouds, respectively and all of the γ are consistent with that of the GFIMF of 2.3±0.7. In addition, the best-fit SFEs are similar to those for the original model, shown in Table 5.3. It is also apparent that the SFE for the ONC and Orion A is 1.5 times larger than those of the Orion B and Cepheus OB3. However, since the fitting uncertainty of the SFE is typically 0.05, and the uncertainties of C_* of the scaled GFIMFs are relatively large, a factor of 2 or more, the uncertainties of the SFEs are as large as a factor of two or more. Considering this large uncertainties, all of the SFEs are consistent with each other, and it is unclear whether or not this variation of the SFE is related to the variation of the star formation activities among the clouds. The comparison between the predicted IMF and GFIMF also suggests that we cannot rule out the possibility that the CMFs have true turnovers corresponding to the turnovers at $\sim$ 0.3 $M_\odot$ in the IMFs. From the best-fit SFEs of 0.32 - 0.55, the core masses at the turnovers are 0.7 - 3.2 $M_\odot$, which are below our mass detection limits. Actually, in the low- and intermediate-mass star-forming regions, Ophiuchus and Taurus, respectively, where the confusion is thought not to be severe, the observed CMFs also seem to have turnovers at 0.5 - 3.5$M_\odot$ (Motte et al., 1998; Onishi et al., 2002), which is consistent with the above rough calculations. Therefore, more

sensitive and higher resolution observations are needed to examine whether the true turnover exists or not in the three clouds. In addition, it is also necessary to study the influence of the confusion on the CMF in detail even in the low- and intermediate-mass star-forming regions.

Apart from the turnover, our analysis clearly shows that single power-law form of the $H^{13}CO^+$ CMF holds in the wide mass range of $1.3 \leq M/M_\odot \leq 110$. Furthermore, the power-law indices are found not to vary considerably over the three clouds, which have various star-forming activities. Although there exists such arguments based on the lower-density tracers such as ^{12}CO and ^{13}CO (Kramer et al., 1998), our study is the first one based on the high-density tracer of $\sim 10^{4-5}$ cm^{-3}, more closely related to star-formation processes. Furthermore, we found that the power-law indices of the $H^{13}CO^+$ CMFs agree with that of the IMF. In contrast, Kramer et al. (1998) showed that the power-law indices of the CO CMFs have a mean of 1.69±0.06, significantly smaller than ours and the IMF, over the wider mass range of $2 \times 10^{-4} \leq M/M_\odot \leq 10^4$. These facts imply that the high-mass slope universality of the IMF originates in the formation process of the dense core with densities of $\sim 10^{4-5}$ cm^{-1}, but not in the tenuous gas with $\sim 10^{2-3}$ cm^{-1}.

5.5 Chapter Summary

We have shown that the CMF of the $H^{13}CO^+$ dense cores can be converted into that of the 850 μm dust cores assuming the core density structure of $\rho \propto r^{-2}$, and that the predicted IMF from the $H^{13}CO^+$ CMF can be well fitted to the IMF through the simple model considering binary formation and confusion with a best-fit SFE of ~ 40 %. These results suggest that the physical processes of the dense gas of $\sim 10^{4-5}$ cm^{-3}, rather than the denser gas traced by the dust continuum emission, are more closely related to star formation and determine the IMF.

We found that the turnover in the CMF disappears after the correction of the shadowing, suggesting that the apparent turnover in the observed CMF is not connected to any physical processes. However, we cannot completely rule out the existence of the turnover in the CMF, because the mass of the natal core for the turnover seen in the IMF is expected to be smaller than our mass detection limit. In addition, the apparent turnover is known in the low-mass star forming regions, where the confusion effect is thought to be small. Not only more sensitive and high-resolution observations of the GMCs but also the detailed examination of the turnover in low-mass star forming regions are needed to reveal whether the turnover is real or not.

We also found that the power-law indices of the confusion-corrected CMFs are very similar to each other (~ 2.5) over a wide core mass range of $1.3 \leq M/M_{\odot} \leq 110$ in spite of various star-forming activities in the three clouds. This suggests that a common process of the dense core formation, which is insensitive to various environmental effects, must exists.

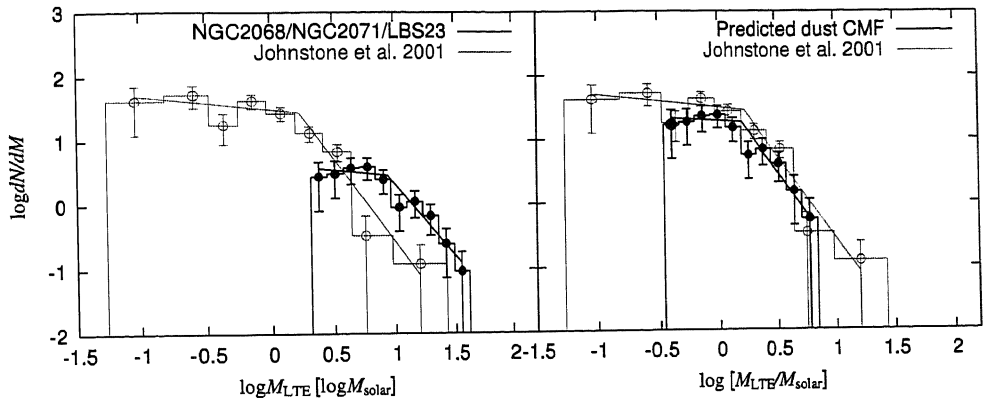

Figure 5.1 (*Left*) Dust CMF (thin-color open circles and histogram, Johnstone et al., 2001) and CMF of the 39 $H^{13}CO^+$ cores in the NGC2068/NGC2071/LBS23 regions (thick-color filled circles and histogram). The best-fit results are indicated using solid lines in each color. (*Right*) Dust CMF (thin-color open circles and histogram, Johnstone et al., 2001) and predicted dust CMF from the CMF of the 39 $H^{13}CO^+$ cores (thick-color filled circles and histogram).

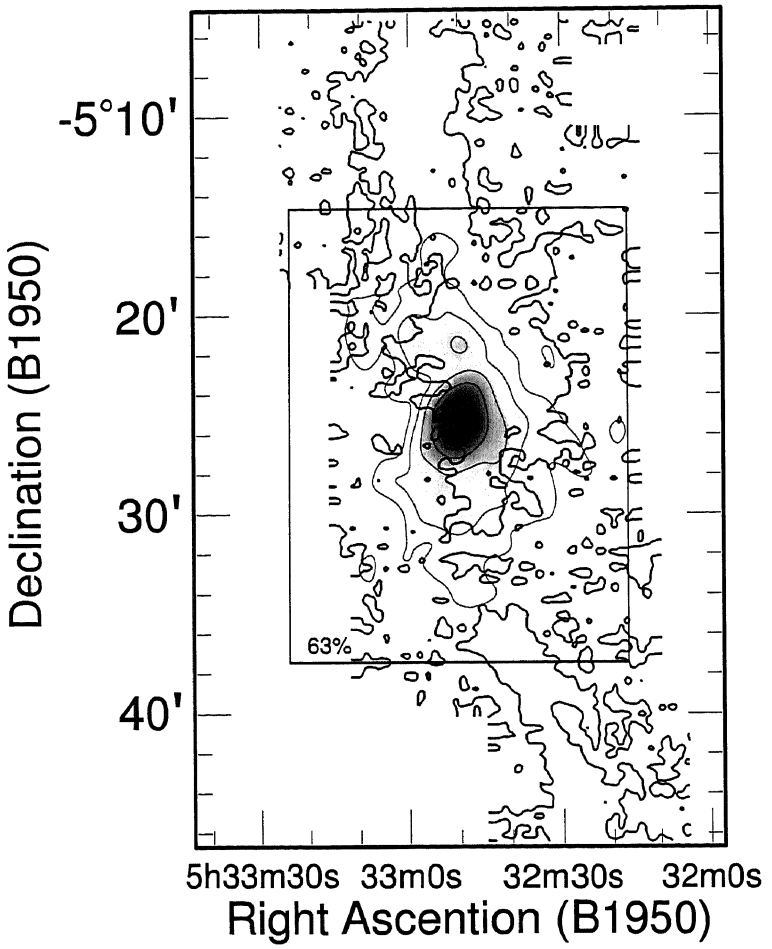

Figure 5.2 Comparison between the $H^{13}CO^+$ total integrated intensity map (thick contour at the 2-σ level shows the outline) and the 63 %-reduced surface density map by Hillenbrand & Hartmann(1998) (thin contour and gray scale).

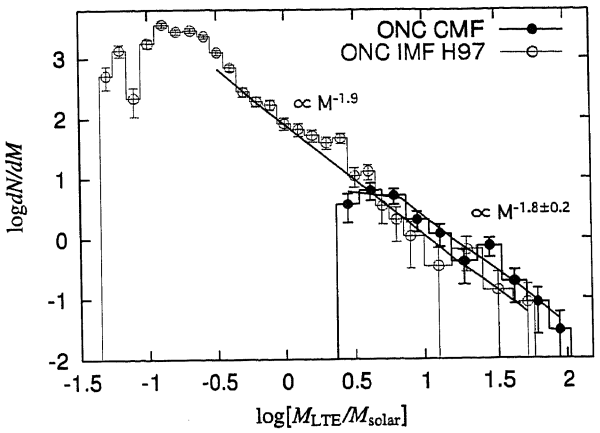

Figure 5.3 ONC CMF (*thick-color filled circles and histogram*, see text) and ONC IMF (Hillenbrand 1997, *thin-color open circles and histogram*) The best-fit power-law functions in the high-mass sides are shown by the two solid lines. The error bars show the statistical uncertainty of $\sqrt{N}$.

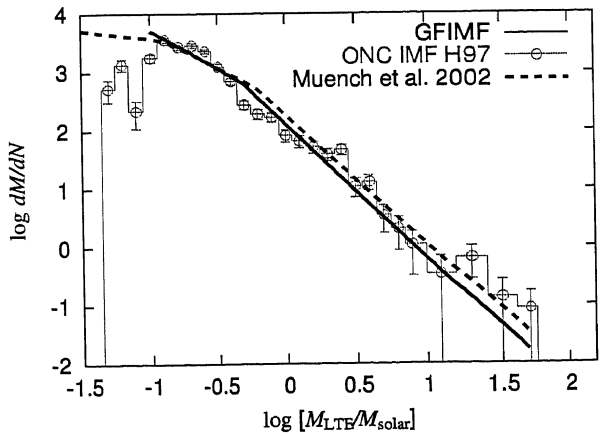

Figure 5.4 GFIMF is shown with the thick-color solid lines. ONC IMF (Hillenbrand 1997, *thin-color open circles and histogram*) and Trapezium IMF (Muench et al. 2002, *thick-color dashed lines*) are overplotted.

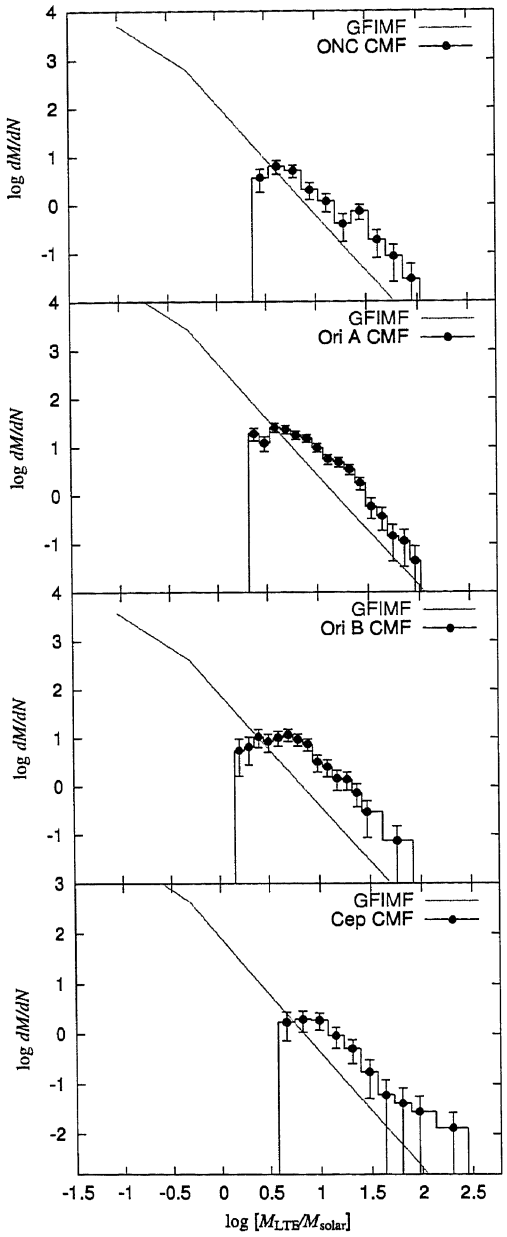

Figure 5.5 GFIMFs for the ONC, Orion A, Orion B, and Cepheus OB3 are indicated with the thin-color solid lines in the panels from the top to the bottom. The corresponding $H^{13}CO^+$ CMFs are shown with the thick-color filled circles and histograms.

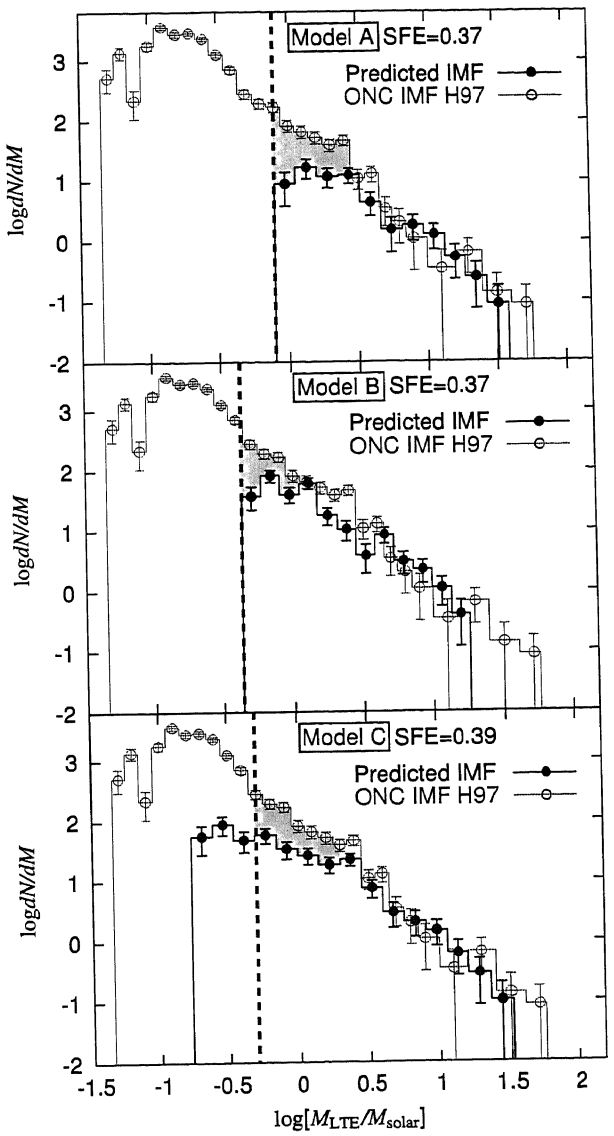

Figure 5.6 ONC IMF (Hillenbrand 1997, *thin-color open circles and histogram*) and IMF predicted from the ONC CMF (*thick-color filled circles and histogram*). The top, middle, and bottom panels show the results of models A, B, and C, respectively. The best-fit SFE for each case is indicated at the top of each panel. The vertical dashed lines indicate the completeness limits of the predicted IMFs (see text). The hatched region in each panel represents the mass shortage of the predicted IMF (see text).

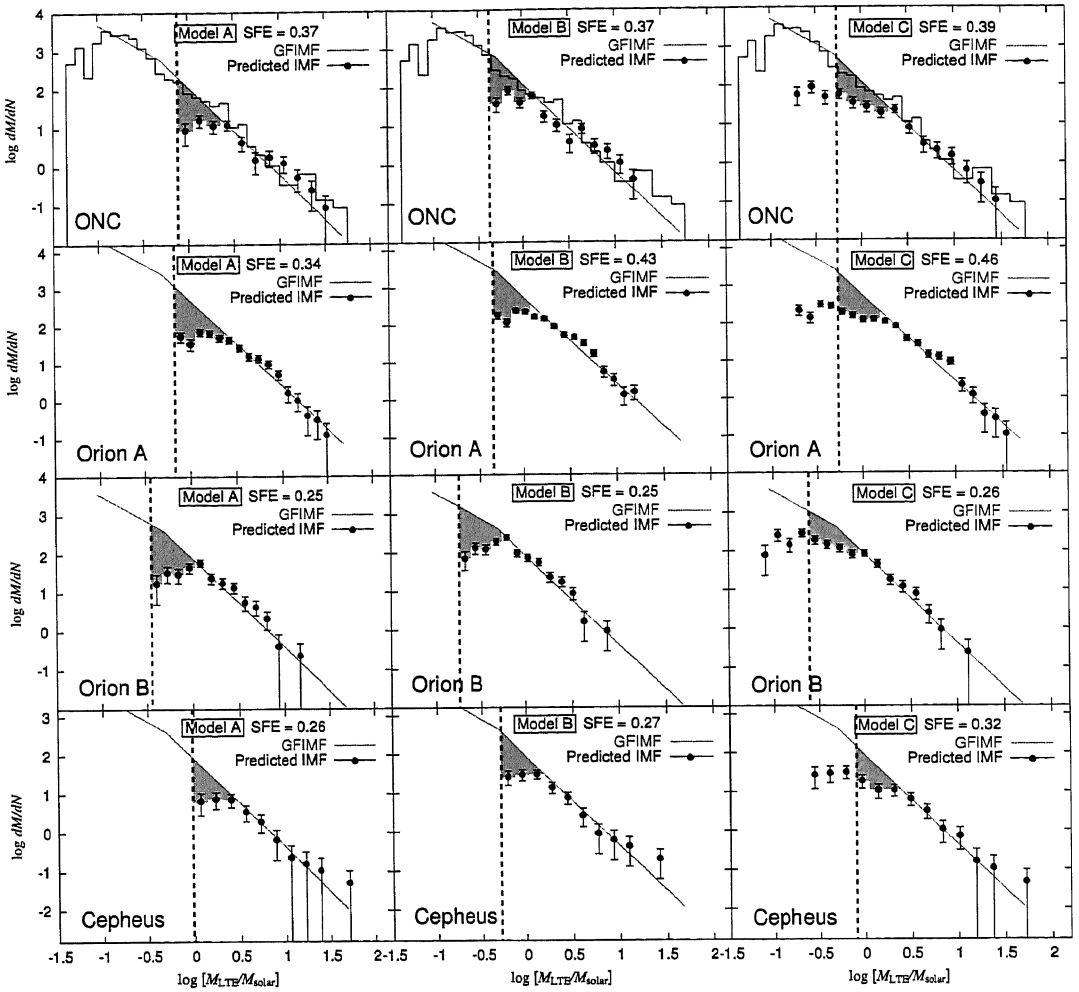

Figure 5.7 GFIMFs (*thin-color solid lines*) and IMFs predicted from the CMFs (*thick-color filled circles*). The left, center, and right panels show the results of models A, B, and C, respectively. The best-fit SFE for each case is indicated at the top of each panel. The vertical dashed lines indicate the completeness limits of the predicted IMFs (see text). The hatched region in each panel represents the mass shortage of the predicted IMF (see text).

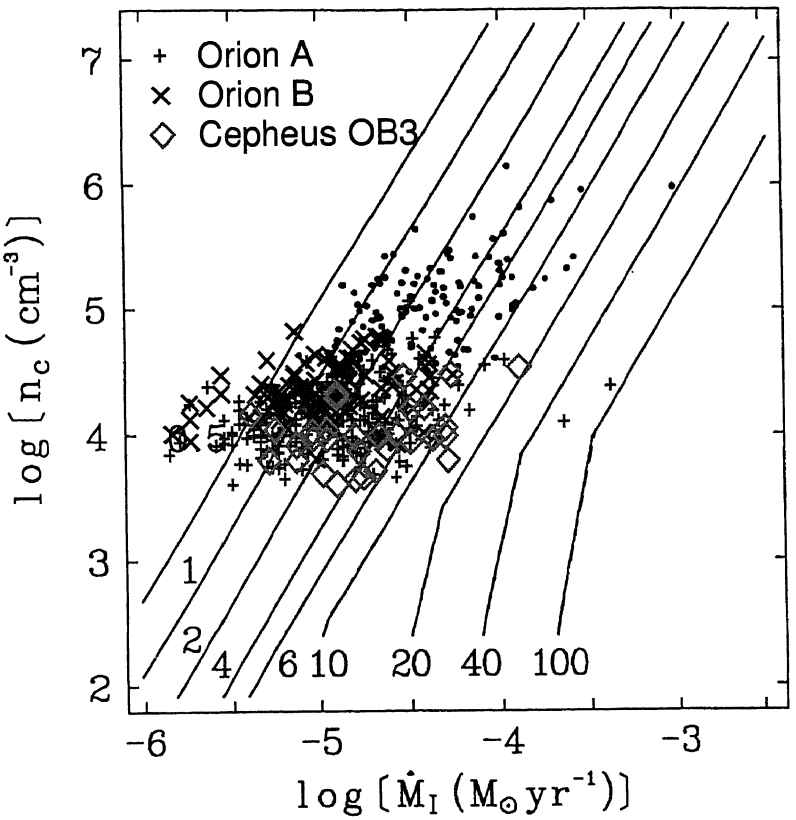

Figure 5.8 Plot of the $H^{13}CO^+$ cores in the Orion A (plus signs), Orion B (crosses), and Cepheus OB3 (diamonds) on Figure 1 of Nakano et al.(1995). The numbered solid lines show the estimated stellar mass in $M_\odot$, and the filled circles represent the CS clumps by Tatematsu et al.(1993).

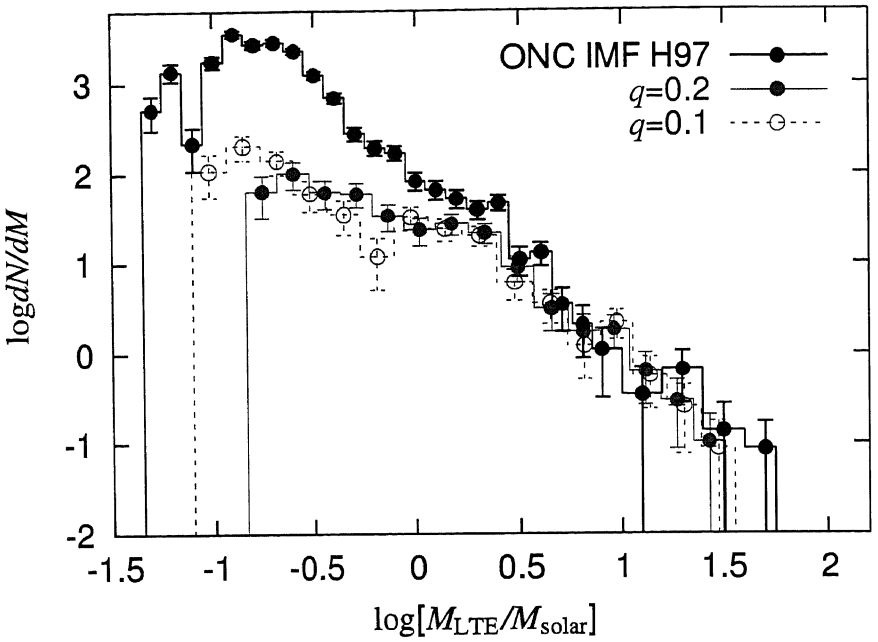

Figure 5.9 ONC IMF (Hillenbrand 1997, *thick-color filled circles and histogram*) and predicted IMFs assuming $q = 0.2$ (thin-color filled circles and solid histogram) and 0.1 (thin-color open circles and dashed histogram). The predicted IMFs are derived assuming BF = 1 and SFE = 0.37.

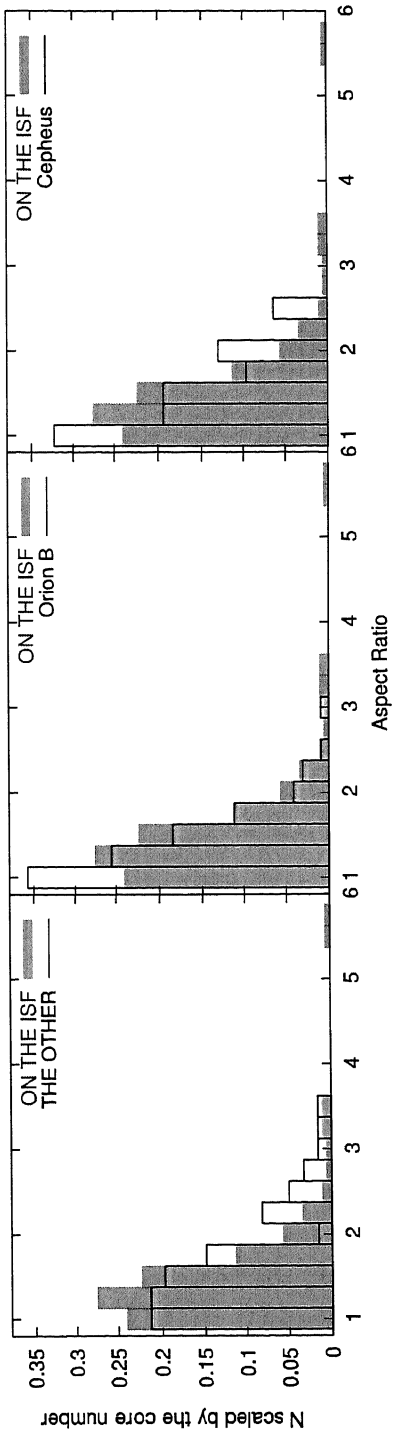

Figure 5.10 Comparison between the core aspect ratio of the $H^{13}CO^+$ cores on the ISF (thin-color filled histograms) and that in the other regions in the Orion A, in the Orion B, and in the Cepheus OB3 clouds (thick-color open histograms) in the left, middle, and right panels, respectively.

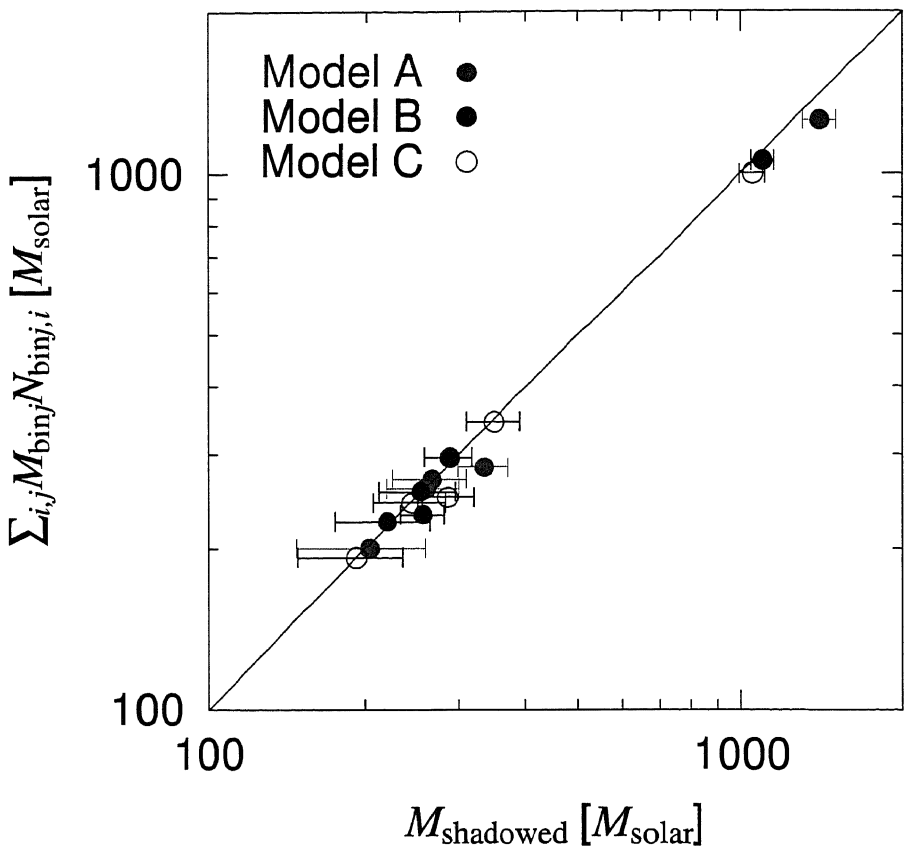

Figure 5.11 Correlation between M_{shadowed} and $\sum_{i,j} M_{\mathrm{bin}j} N_{\mathrm{bin}j,i}$. The thin-color filled, thick-color filled, and thick-color open circles respectively show the results for models A, B, and C. The diagonal solid line shows an relation that the both values are equal.

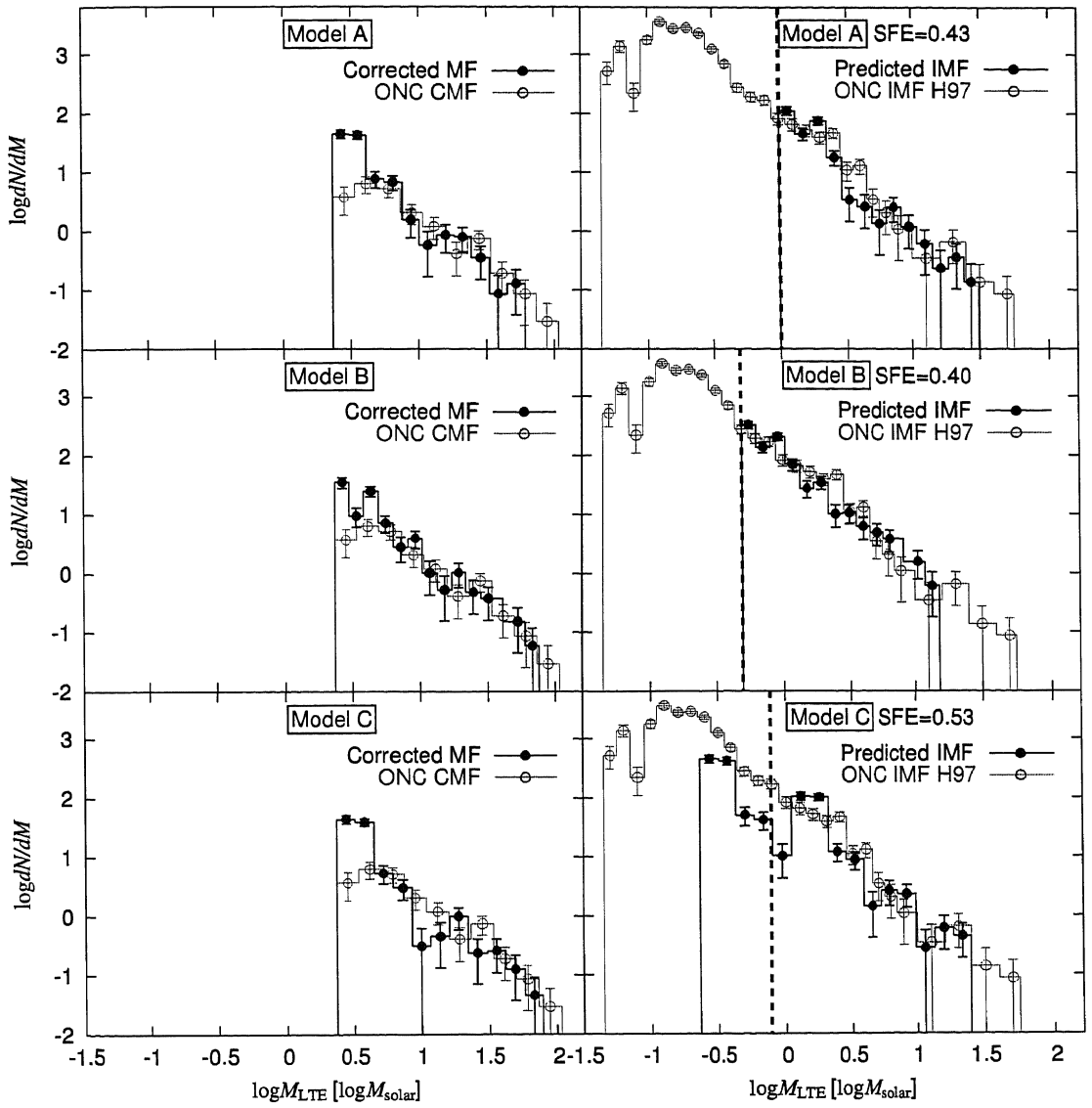

Figure 5.12 (*Left column*) ONC CMFs with (thick-color filled circles and histogram) and without (thin-color) the correction for the confusion effect. (*Right column*) Predicted IMFs corrected for the confusion (thick-color filled circles and histogram) and OMC IMF (thin-color). The top, middle, and bottom rows, respectively, correspond to models A, B, and C. The best fit SFE for each case is indicated at the top of each right panel.

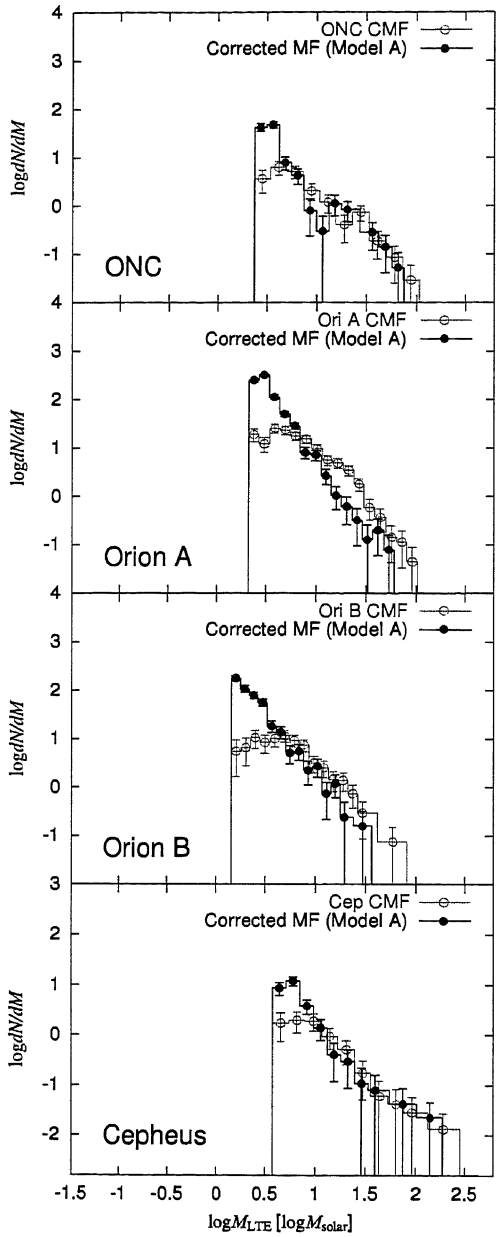

Figure 5.13 CMFs with (thick-color filled circles and histogram) and without (thin-color open circles and histogram) the correction for the confusion effect based on the comparison with the GFIMF. The thick-color solid line in each panel shows the best-fit result of the corrected CMF.

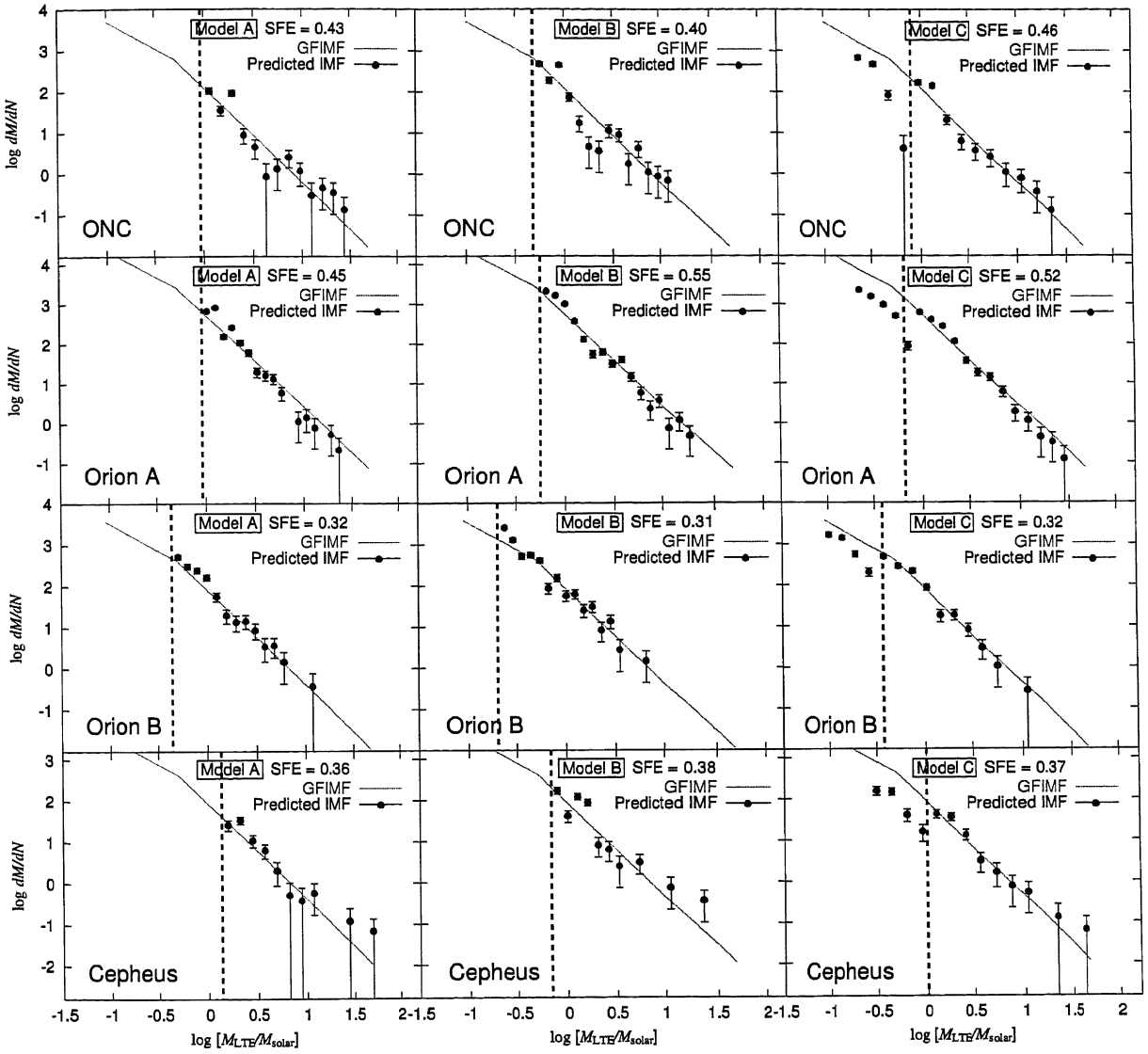

Figure 5.14 GFIMFs (*thin-color solid lines*) and predicted IMFs corrected for the shadowing (*thick-color filled circles*). The left, center, and right panels show the results of models A, B, and C, respectively. The best-fit SFE for each case is indicated at the top of each panel. The vertical dashed lines indicate the completeness limits of the predicted IMFs (see text).

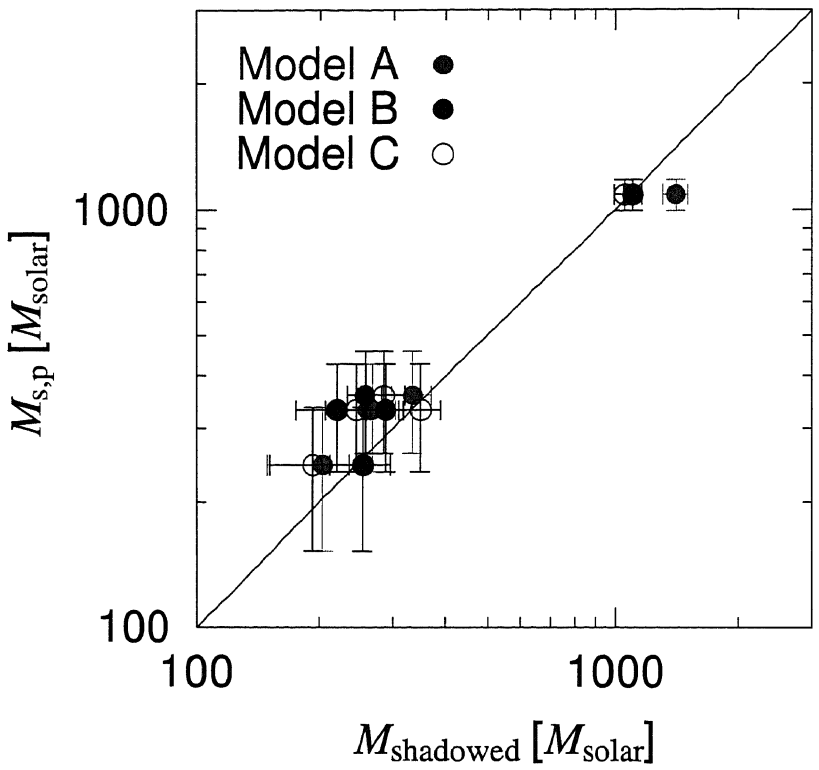

Figure 5.15 Correlation between $M_{s,p}$ and $M_{shadowed}$. The thin-color filled, thick-color filled, and thick-color open circles show the result for models A, B, and C, respectively. The error bars correspond to the statistical uncetainties of the IMF and CMF. The diagonal solid line shows an relation that the both values are equal.

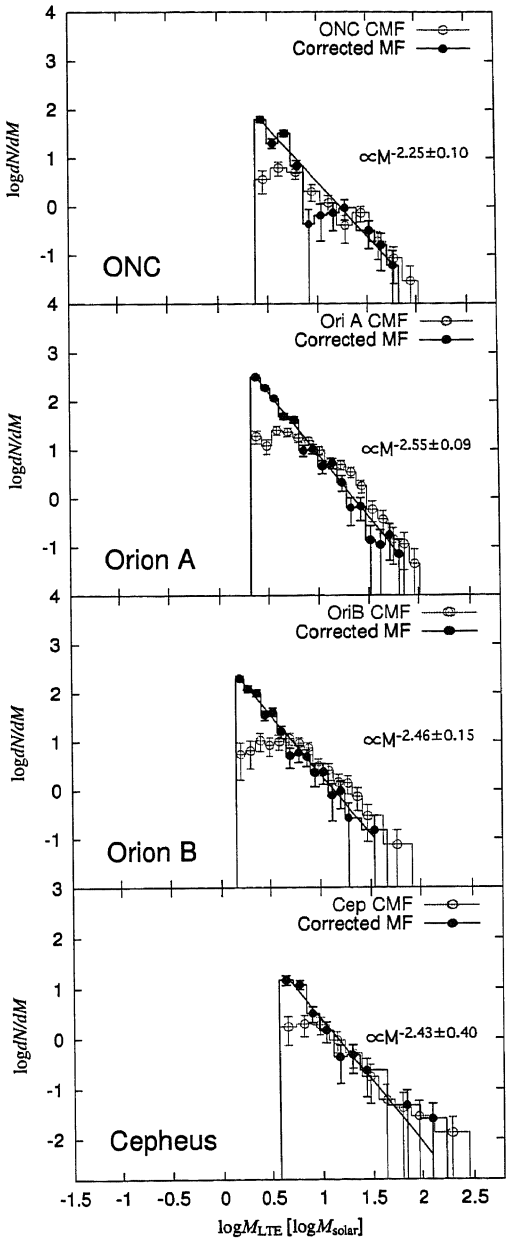

Figure 5.16 CMFs with (thick-color filled circles and histogram) and without (thin-color open circles and histogram) the correction for the confusion effect with the modified shadowing model. The panels from top to bottom respectively show the results for the ONC, Orion A, Orion B, and Cepheus OB3. The thick-color solid line in each panel shows the best-fit result of the corrected CMF.

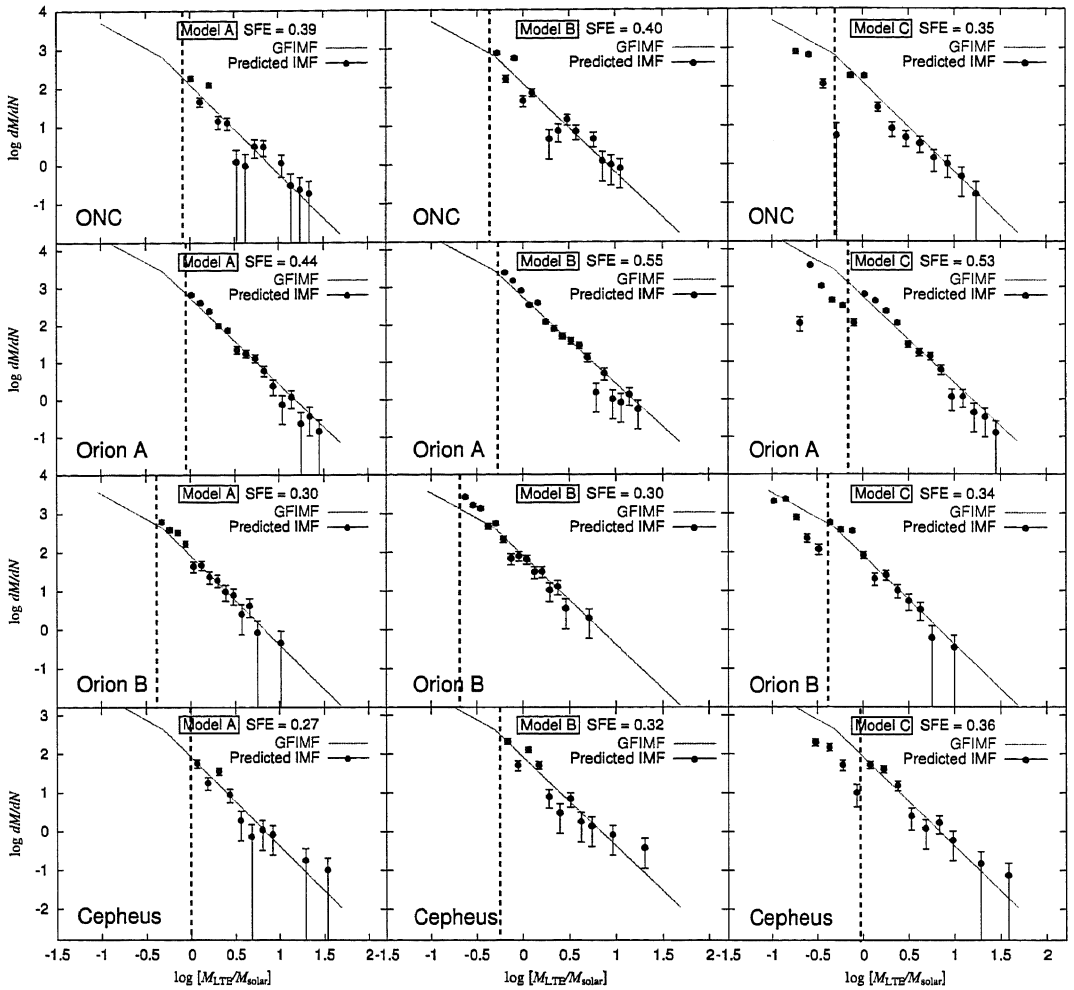

Figure 5.17 GFIMFs (*thin-color solid lines*) and predicted IMFs corrected for the confusion with the modified shadowing model (*thick-color filled circles*). The left, center, and right panels show the results of models A, B, and C, respectively. The best-fit SFE for each case is indicated at the top of each panel. The vertical dashed lines indicate the completeness limits of the predicted IMFs (see text).

Table 5.1. Shortage of stars in the predicted IMFs

Region/Model	A		B		C	
	$M_{*,\mathrm{turn}}$	$M_{*,\mathrm{short}}$	$M_{*,\mathrm{turn}}$	$M_{*,\mathrm{short}}$	$M_{*,\mathrm{turn}}$	$M_{*,\mathrm{short}}$
	— with the ONC IMF —					
ONC	1.9	99±15	1.8	81±17	1.2	96±15
	— with the GFIMF —					
ONC	1.9	96±15	1.0	107±11	1.6	136±16
Orion A	2.1	478±33	1.1	473±24	1.4	484±27
Orion B	0.9	83±9	0.5	64±6	0.8	74±9
Cepheus OB3	2.5	53±15	1.3	69±11	1.4	62±14

Note. — The unit is $M_{\odot}$.

Table 5.2. Best-fit power-law indices of the CMFs corrected for the confusion effect

	Power-law index γ	
Shadowing model	Original	Generalized
ONC	2.32±0.09	2.25±0.10
Orion A	2.61±0.09	2.55±0.09
Orion B	2.47±0.07	2.46±0.15
Cepheus OB3	2.32±0.13	2.43±0.40

Table 5.3. Best-fit SFEs of the predicted IMFs corrected for the confusion with the original and generalized shadowing models

Model	A		B		C	
Shadowing model	org[1]	gen[2]	org	gen	org	gen
ONC	0.43	0.39	0.40	0.40	0.46	0.35
Orion A	0.45	0.44	0.55	0.55	0.52	0.53
Orion B	0.32	0.30	0.31	0.30	0.32	0.34
Cepheus OB3	0.36	0.27	0.38	0.32	0.37	0.36

[1]With the original shadowing model.

[2]With the generalized shadowing model.

Note. — The typical uncertainty of the fitting is 0.05.

Chapter 6

Relation between the Core Properties and Star Formation Activities

In Chapter 4 we showed that there are several peculiar cores whose velocity widths and masses are significantly larger than the other ones with good statistics, i.e., large-*dv* and high-mass cores in the Orion A and Cepheus OB3 clouds. In the following we discuss such peculiar cores, especially the large-*dv* cores, in the context of the influence of nearby stellar activities. We show that the large-*dv* cores may be connected to the most massive star in the cloud and the formation of the high-mass end of the IMF.

6.1 Large-*dv* Cores in the Orion A and Cepheus OB3 Clouds

Both the gravitationally bound state of the $H^{13}CO^+$ cores and the similarity between the CMF and the IMF indicated that the core properties are likely to provide the initial conditions for star formation. Then, what determines the

core properties? To address this question, the large-dv cores are thought to be a key. This is because, in the Orion A, all the large-dv cores (# A112, A114, and A131) are located within 1 pc from the center of the M42 H II region i.e., the position of the exciting star, Ori θ_1C, at $5^h32^m50^s$ and $-5°25'17''$ (see Figure 6.1), and in the Cepheus OB3, a large-dv core # C15 seems to be associated with the centimeter continuum sources excited by the shock from a compact H II region at the center of Cep-A (see Figure 6.2). These facts strongly suggest that the shock caused by nearby OB stars produces large-dv cores in gravitationally bound state, leading to massive star formation. In addition, high-mass cores in the Orion A also have the potential for massive star formation. However, they are distributed uniformly over the OMC-1 and 3 regions, and can be statistically explained in the power-law CMF, as shown in Figure 4.14. In other words, these high-mass cores are not likely to be physical link to local stellar activities.

6.2 Energy Sources for the Large-dv Cores

We can show that the energy input from the (compact) H II regions through shocks is sufficient to drive the turbulent motions within the cores as follows: first of all, the energy required to produce the turbulent motion in the i-th large-dv core, E_i, is given by

$$E_i = 10^{43} \left(\frac{M_{\mathrm{LTE},i}}{M_\odot} \right) \left(\frac{dv^2_{\mathrm{core},i}}{\mathrm{km^2 s^{-2}}} \right) \quad [\mathrm{erg}], \tag{6.1}$$

where $M_{\mathrm{LTE},i}$ and $dv_{\mathrm{core},i}$ are the LTE mass and velocity width of the i-th large-dv core, respectively. E_i is calculated to be $0.2 - 2 \times 10^{45}$ erg. Since the turbulence is thought to be dissipated on the timescale of the order of the eddy turnover time (Kolmogorov, 1941), the energy dissipation rate of the turbulence can be estimated by $E_i/(2R_{\mathrm{core,i}}/dv_{\mathrm{core},i})$, where $R_{\mathrm{core,i}}$ is the radius of the i-th large-dv core. Dividing the dissipation rate by the projected

area of the core, we finally obtained the turbulence dissipation rate per unit area, $\dot{E}_{\mathrm{dis},i}$, of $0.5 - 1.3 \times 10^{33}$ erg s^{-1} pc^{-2}.

The ionization shock due to UV photons and the neutral shock due to stellar wind are considered as the energy sources. First, we estimate the energy input rate from M42, where the stellar content is well known. the kinetic energy to be supplied to the ambient cloud through the passage of the ionization shock is about 0.01 % of the total energy of the Lyman photons emitted from an ionizing star (Dyson & Williams, 1997). Among the stellar members of the ONC listed in Hillenbrand (1997), we consider the three earliest O stars (one O6 and two O9 stars) having the UV photon fluxes of $\sim 10^{48\sim49}$photons s^{-1} as the energy sources, because five B stars in the ONC have negligible UV photon fluxes of $\sim 10^{47}$photons s^{-1} compared with the O stars. Then the UV photon flux from M42 is estimated to be 2×10^{49} photons s^{-1} (Osterbrock, 1989), resulting in the energy supply rate of 8.8×10^{34} erg s^{-1}. Next, the kinetic energy transfer efficiency to the cloud through the stellar wind is 20 % (Dyson & Williams, 1997). Lamers & Leitherer (1993) showed that the mean mass loss rate and wind velocity of the stellar wind from an O type star are $1.2 \times 10^{-6} M_{\odot}\mathrm{yr}^{-1}$ and 2800 km s^{-1}, respectively. Using these values, we estimated the energy output rate of 2.9×10^{36} erg s^{-1} by the stellar wind from the earliest O6 star Ori θ_1C, resulting in the kinetic energy supply rate of 5.8×10^{35} erg s^{-1}. The contribution by the O9 stars is negligible because the mass loss rate of a O9 star is two orders of magnitude smaller than that of an O6 star (Vink et al., 2000). Consequently the total kinetic energy supply rate from M42 is estimated to be 6.7×10^{35} erg s^{-1}, dominated by the contribution of the stellar wind (Mac Low & Klessen, 2004). Considering that the separation between M42 and OMC-1 is 1.5 pc, which is the projected extent of M42, the kinetic energy supply rate to the cloud per unit area, $\dot{E}_{\mathrm{sup}}$, is calculated to be 2.4×10^{34} erg s^{-1} pc^{-2}.

For the Cep-A case, the spectral type of the most earliest star is not well known. However, Garay et al. (1996) showed that jets emerged from the

center of the Cep-A should have the mass loss rate of $2\times10^{-6}M_{\odot}$ yr^{-1} and the wind velocity of 1900 km s^{-1} to explain their centimeter radio continuum fluxes. The resulting energy output rate of 2.3×10^{36} erg s^{-1} is comparable to that of the M42 case. Since the projected separation between the core # C15 and the exciting sources ($22^{h}54^{m}19^{s}$ and $61°45'43''$, Garay et al., 1996) are 0.4 pc, $\dot{E}_{\rm sup}$ is calculated to be 9×10^{34} erg s^{-1} pc^{-2} considering the inclination angle of the jets from the Cep-A of $\sim 45°$ (Ho et al., 1982).

Next, we should know the fraction of the supplied energy to be converted to the turbulent motions, $\eta_{\rm turb}$. Theoretically, Kornreich & Scalo (2000) showed that the ratio of the typical turbulent velocity generated in a core to the shock speed in the ambient gas is of the order of 0.1, when the ionization and neutral shocks from a H II region passed across the core. Since the shock velocity is $\sim$ 10 km s^{-1}, of the order of the sound velocity in H II regions, the excited turbulent velocity width is expected to be $\sim$ 1 km s^{-1}, consistent with that of the large-dv cores. The velocity ratio can be converted into the $\eta_{\rm turb}$ value of $\sim$ 0.01. In addition, Mac Low & Klessen (2004) derived the fraction of $\sim$ 0.05 for the turbulence excited by a protostellar wind. If we adopt $\eta_{\rm turb}$ = 0.01 - 0.05, the relation of $\dot{E}_{{\rm dis},i} \simeq \eta_{\rm turb}\dot{E}_{\rm sup}$ holds. Therefore, we conclude that the turbulence in the large-dv cores can be excited and maintained by the energy input from the nearby OB stars, such as the M42 H II region and the Cep-A compact H II region.

6.3 Formation of the Most Massive Stars within the Large-dv Cores

It is possible that the large-dv cores produce the most massive stars, because the cores are gravitationally bound and because the mass infall rate of the core is proportional to the third power of the effective sound velocity, including the turbulent motions (Mckee & Tan, 2003). The mass infall rates of the large-dv cores of 1 - $4\times10^{-4}M_{\odot}$yr^{-1} are one order of magnitude larger

than the mean mass infall rate of the other cores of $2 \times 10^{-5} M_{\odot} \mathrm{yr}^{-1}$. The expected stellar masses from the large-*dv* cores, i.e., the mass infall rate multiplied by the free-fall time, are 17 - $90 M_{\odot}$, possibly corresponding to the high-mass end of the ONC IMF. These rough estimates are consistent with the predicted stellar masses of 13 - 80 $M_{\odot}$ from the large-*dv* cores based on the theoretical model by Nakano et al. (1995).

On the other hand, the most massive, but not the large-*dv* core, # A142, is expected to form a star of 32 - $41 M_{\odot}$ with the SFEs of 0.40 - 0.50, derived in Section 5.3. This argument suggests that the most massive star forms not in the most massive core, but in the large-*dv* cores, i.e., the SFE for the large-*dv* cores is higher than that of the others. The enhanced SFE for the large-*dv* cores, however, is likely to be acceptable in our proposed physical relation between the CMF and IMF under the constant SFE, because the number of the large-*dv* cores is very small (4/365), resulting in the large statistical uncertainties of the IMF at the high-mass end. In addition, the large uncertainties at the high-mass end might prevent us from knowing the true form of the IMF, i.e., the IMF might also have a turnover at the most high-mass side $\geq 30 M_{\odot}$ and the slope might become flatter. In fact, the high-mass end ($\geq 10 M_{\odot}$) of the ONC IMF seems to be slightly larger than that of the GFIMF while both of them are very similar to each other in the mass range of $1 \leq M/M_{\odot} \leq 10$ (see Figure 5.4).

Consequently, in addition to the CMF-IMF relation, we propose another hypothesis that a nearby H II region makes cores more turbulent, leading to the formation of the most massive stars, where one can explain the well-known fact that massive star formation always occurs near H II regions (e.g., Dobashi et al., 2001). The hypothesis predicts the high-mass turnover on the IMF.

6.4 Energy Input to the Cores in the Orion B Cloud?

In the Orion B, there are energetic stellar activities such as H II regions and outflows, expected to also suppy turbulent energy to the $H^{13}CO^+$ cores. However, there are no significant large-*dv* cores. We showed in Section 4.2.2.2 that we cannot conclude that the absence of large-*dv* cores in the Orion B is significant because of the large statistical uncertainties. On the other hand, it is certain that the energy sources in the Orion B cloud are less energetic than those in the Orion A and Cepheus OB3: the most earliest star in the Orion B cloud is an O8 star, exciting the NGC2024 II region (Bik et al., 2003). This may be another possibility to explain the abcense of large-*dv* cores. In fact, the energy input from the O8 star causes $\dot{E}_{\rm sup}$ of 3×10^{33} erg s^{-1} pc^{-2}, one order of magnitude smaller than that of the M42 H II region. This energy supply rate will cause the velocity widths of the typical core in the Orion B of $M_{\rm LTE} \sim 9M_\odot$, $R_{\rm core} \sim 0.01$ pc to be 0.75 km s^{-1}, larger by only 2σ more than the mean value. There are six cores whose velocity widths are larger than 0.75 km s^{-1}. All of them seem to be associated with the stellar sources of the NGC2024 H II region (# B29, Figure 6.3), the NGC2023 reflection nebula (# B16, B19, and B22, Figure 6.4), and the NGC2071 embedded cluster and its outflows (# B87 and B92, Figure 6.5).

On the other hand, the expected stellar masses from the cores are estimated to be 6 - 10 $M_\odot$ by the mass infall rate multiplied by the free fall time. In contrast to the case of the Orion A, these are less massive than 17 $M_\odot$, from the most massive core in the Orion B, # B27, with the constant SFE of 0.32 (see Section 5.3). This is because the energy input to them are not large enough to excite turbulence within the cores that achieves large-mass infall rates of 10^{-4} $M_\odot$yr^{-1}. This argument suggests that the stellar energy sources earlier than O7 - 6 should be needed to create the large-*dv*, most massive star-formimg cores and to produce the turnover in the high-mass

end of the IMF.

6.5 Chapter Summary

We found several cores in the Orion A and Cepheus OB3 cloud whose velocity widths are significantly larger by 3σ or more than the mean value, referred to as large-*dv* cores. The large-*dv* cores are located only near the M42 H II region and the compact H II region at the center of the Cep-A region, suggesting that the large velocity width of the cores are caused by the interaction with the stellar activities from the (compact) H II regions. We examined the energy balance between the energy input rate through the shock produced by the stellar wind from O stars in the H II regions and the energy dissipation rate estimated by the dissipation of turbulence. Finally we found that the energy input from the H II regions can excite and maintain the velocity widths of the large-*dv* cores with a reasonable energy fraction to be converted into the turbulence, $\eta_{\rm turb}$. We estimated the expected stellar mass produced by the large-*dv* cores as the mass infall rate multiplied by the free fall time of the cores and found that the large-*dv* cores can be expected to produce the most massive stars in the clouds. This enhancement of the SFE for the large-*dv* cores can be acceptable in our proposed CMF-IMF relation under the constant SFE because of the large statistical uncertainties in the high-mass end of the IMF.

On the other hand, in the Orion B, there is no large-*dv* core in spite of the existence of the active stellar sources such as the NGC2024 H II region. although there is a tendency that larger velocity widths can be found near the stellar sources. This is because the energy input rate from NGC2024, excited by an O8 star, is not sufficient to broaden the velocity widths of the cores significantly, and only causes moderate mass infall rates. This may indicate that there is a threshold of spectral types (about O7 - 6) to be able to influence the formation of the next stellar population through the excitation

of turbulence within the cores.

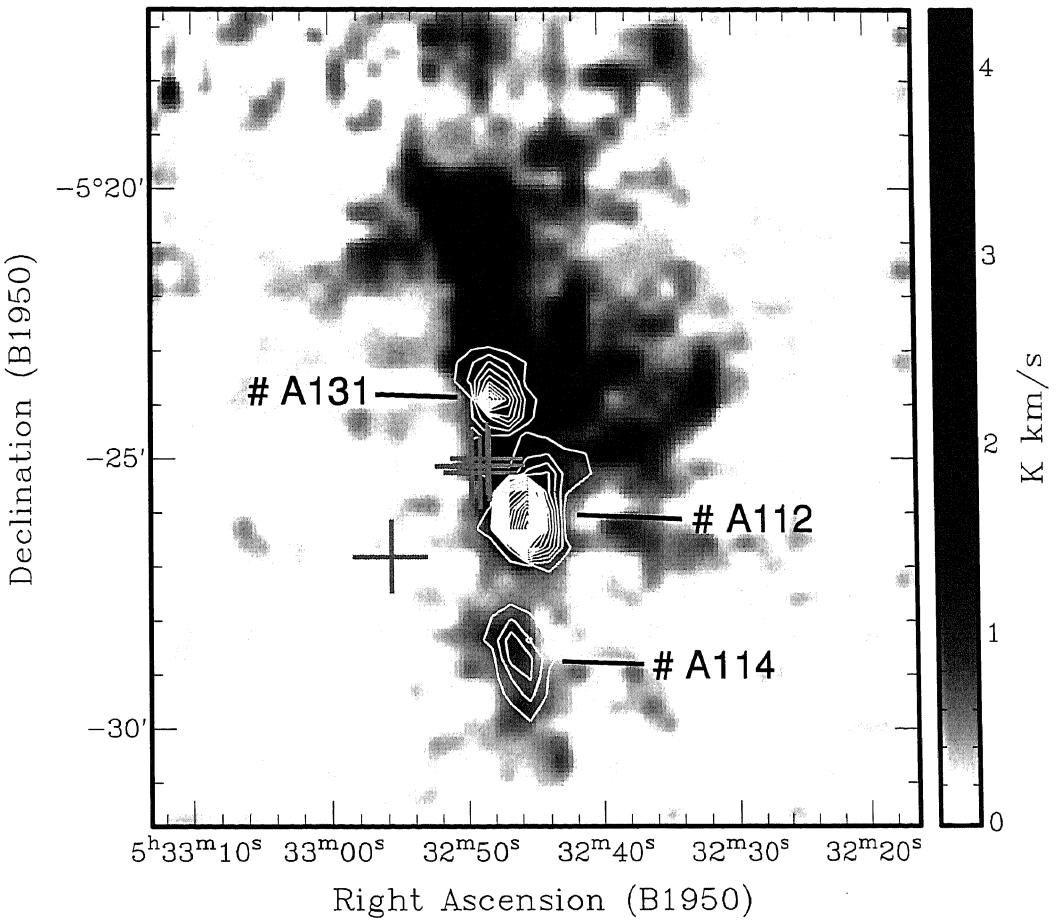

Figure 6.1 Positions of the three large-dv cores in the Orion A. The contours show the total integrated intensity of the large-dv cores with intervals of 0.09 K km s^{-1} (corresponding to 2 σ level) starting at 0.13 K km s^{-1}. The grayscale shows the total integrated intensity map. The grey crosses indicate the positions of the trapezium stars.

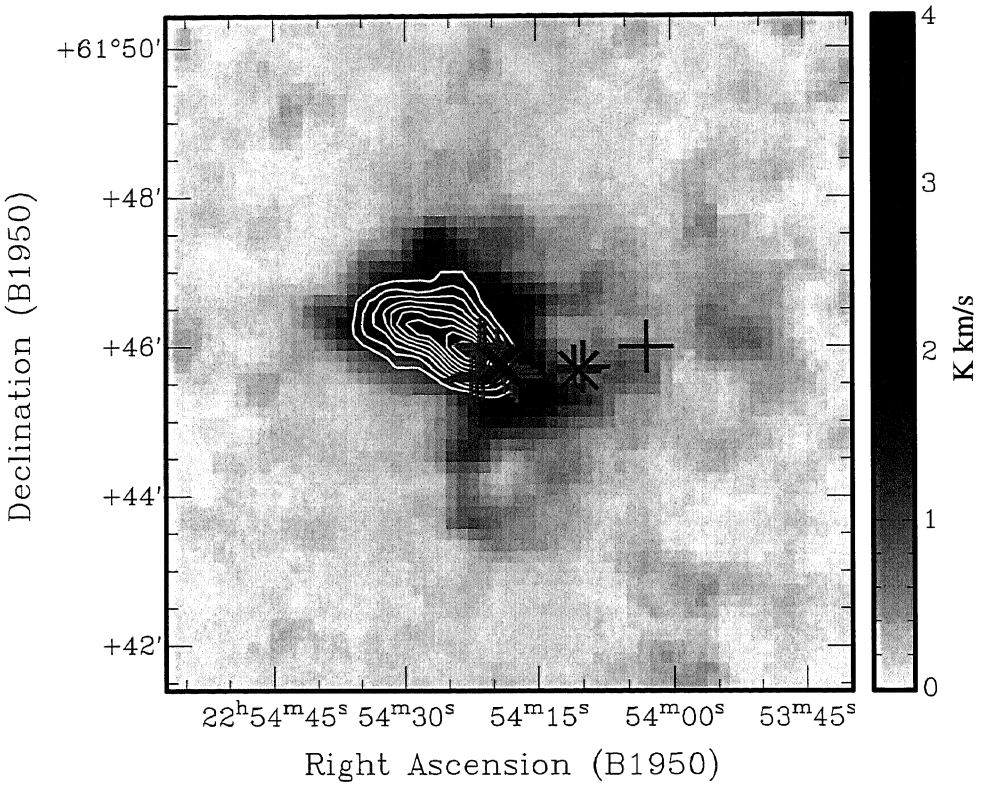

Figure 6.2 Position of the large-dv core # C15 in the Cep-A region. The contour shows the total integrated intensity of the core # 15 with intervals of 0.09 K km s^{-1} (corresponding to 2 σ level), starting at 0.13 K km s^{-1}. The grayscale shows the total integrated intensity map. The thin-color grey crosses and thick-color X marks indicate the positions of the centimeter continuum sources from the shocks and the exciting stars (Hughes, 1988), respectively.

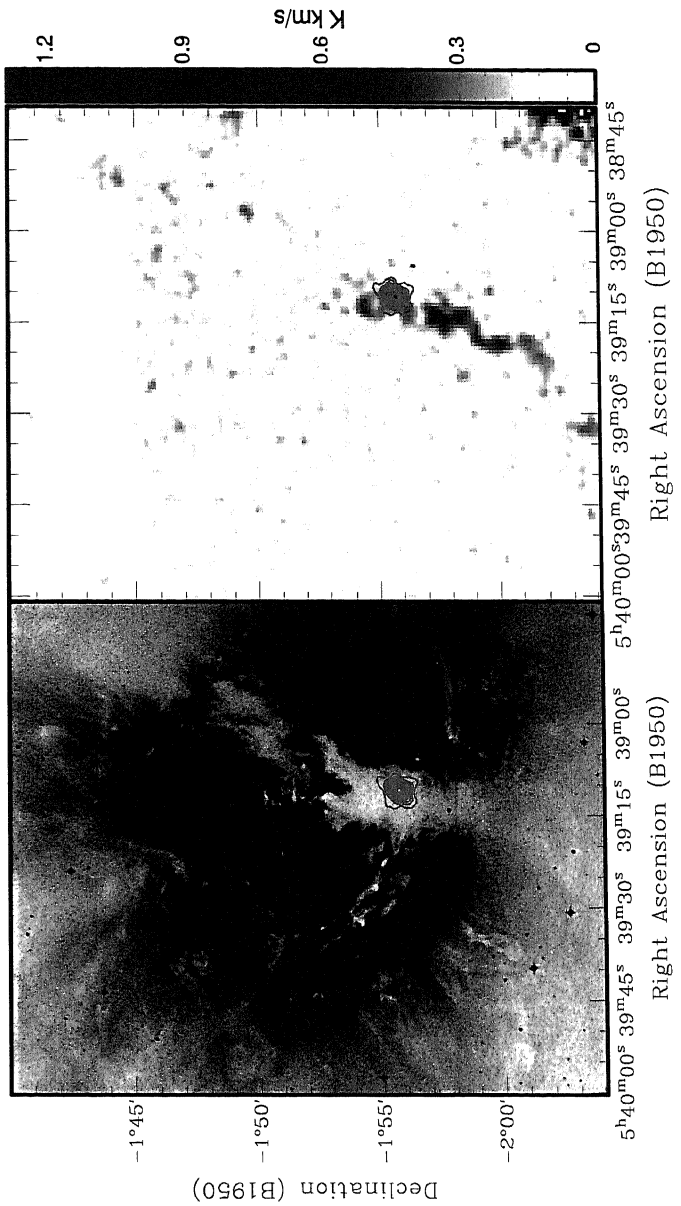

Figure 6.3 Positions of the cores whose velocity widths are greater than 0.75 km s^{-1} in the NGC2024 region in the Orion B. The grey solid contours in both panel show the total integrated intensity of the large-*dv* cores with intervals of 0.09 K km s^{-1} (corresponding to 2 σ level) starting at 0.13 K km s^{-1}. The grayscale in the right panel shows the total integrated intensity map. The grayscale in the left panel shows the optical image of the NGC 2024 H II region taken from the DSS.

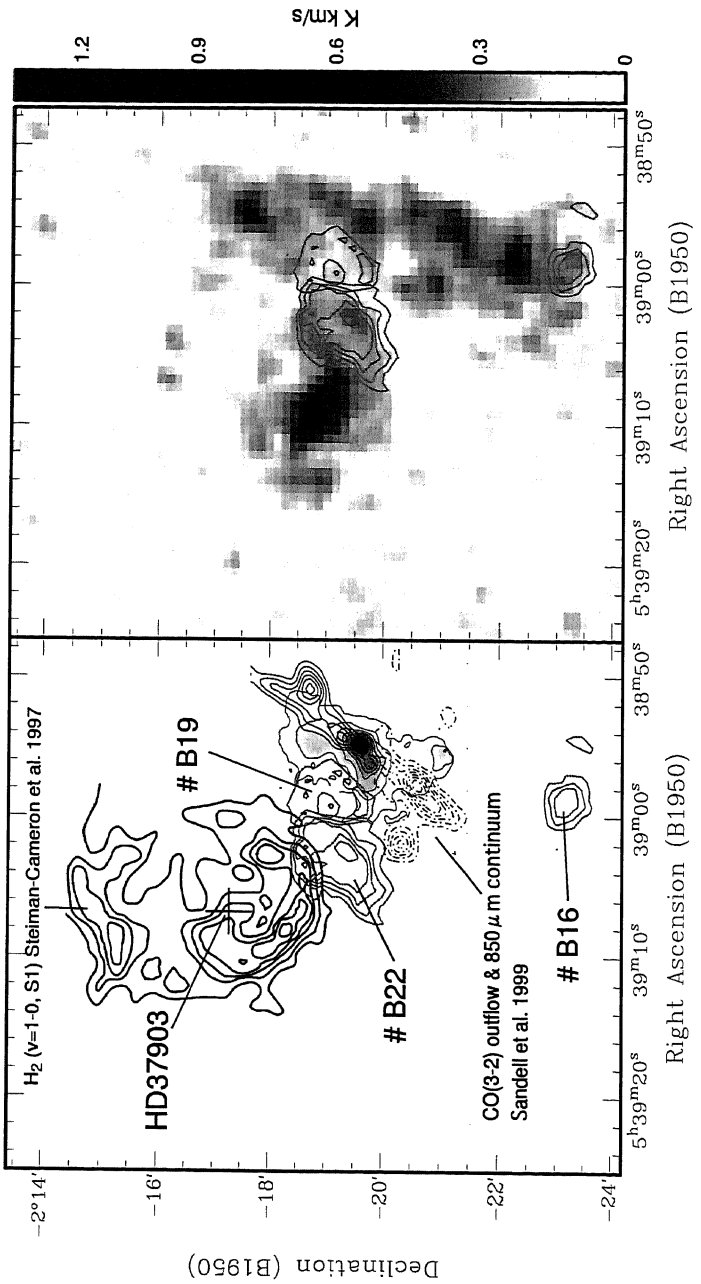

Figure 6.4 Positions of the cores whose velocity widths are greater than 0.75 km s^{-1} in the NGC2023 region in the Orion B. The grey solid contours in both panel show the total integrated intensity of the large-dv cores with intervals of 0.09 K km s^{-1} (corresponding to 2 σ level) starting at 0.13 K km s^{-1}. The grayscale in the right panel shows the total integrated intensity map. The thick solid contour in the right panel indicates the shocked H_2 emission (Steiman-Cameron et al., 1997). The thin solid and dot-dashed contours and the grayscale in the right panel show the CO(3 - 2) outflow lobes and the 850μm continuum emission, respectively (Sandell et al., 1999).

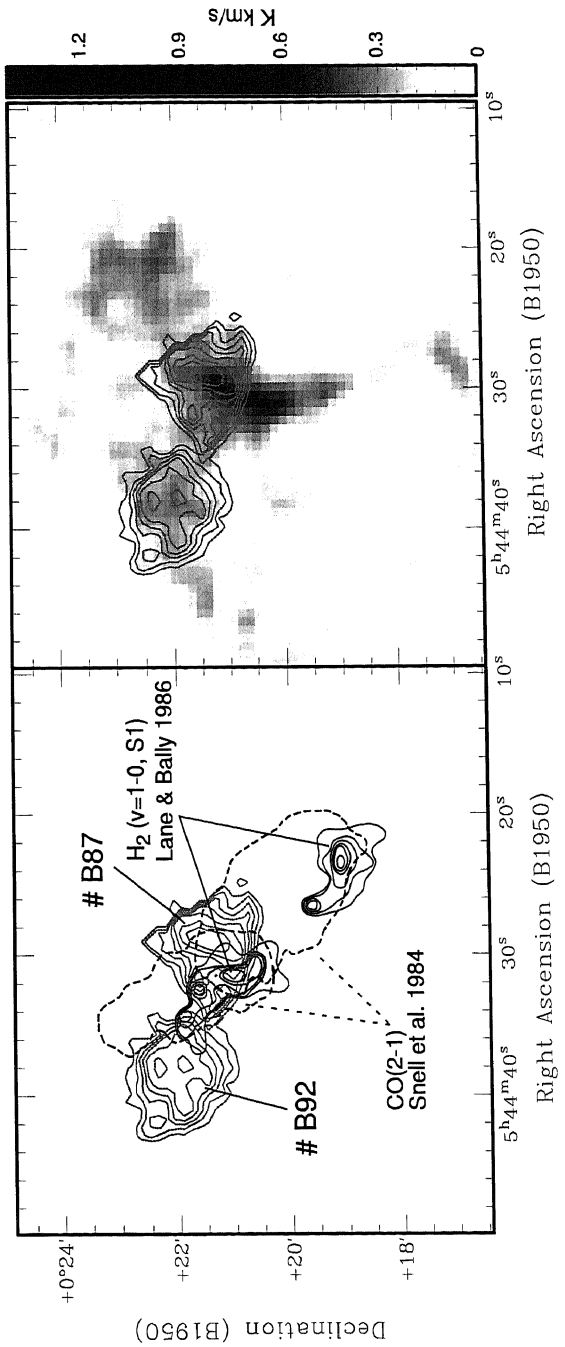

Figure 6.5 Positions of the cores whose velocity widths are greater than 0.75 km s^{-1} in the NGC2071 region in the Orion B. The grey solid contours in both panel show the total integrated intensity of the large-*dv* cores with intervals of 0.09 K km s^{-1} (corresponding to 2 σ level) starting at 0.13 K km s^{-1}. The grayscale in the right panel shows the total integrated intensity map. The solid and dashed black contours in the right panel indicate the shocked H_2 emission (Lane & Bally, 1986) and the CO(2 -1) high-velocity lobes (Snell et al., 1984), respectively.

Chapter 7

On the Formation Processes of the $H^{13}CO^+$ Cores

We showed that the IMF is likely to determinde at the formation stage of the $H^{13}CO^+$ cores. Several possible processes of the dense core formation have been proposed. Here we discuss the formation processes of the dense cores on the basis of our results, leading to the understanding of the origin of the IMF.

7.1 Gravitational Fragmentation

The gravitational fragmentation is the most basic and important physical process to generate gravitationally-bound condensations. The representative mass and scale due to the gravitational fragmentation is the Jeans mass and length, or

$$M_{\rm J} = 35 \left(\frac{C_{\rm eff}}{\rm km\ s^{-1}}\right)^3 \left(\frac{n}{10^5 {\rm cm}^{-3}}\right)^{-1/2} \quad [M_\odot], \tag{7.1}$$

$$\lambda_{\rm J} = 0.19 \left(\frac{C_{\rm eff}}{\rm km\ s^{-1}}\right) \left(\frac{n}{10^5 {\rm cm}^{-3}}\right)^{-1/2} \quad [{\rm pc}], \tag{7.2}$$

respectively, where $C_{\rm eff}$ is the effective sound speed including the turbulent motion and n the gas number density. The gravitational fragmentation is suggested as one of the processes to determine the characteristic mass of the CMF, i.e., turnover mass (Bonnell et al., 2006), if it exists. The variation of $C_{\rm eff}$ and n produces some range of the core mass but are of the order of a $M_\odot$: for example, if we adopt $C_{\rm eff} = 0.5$ km s^{-1}, mean velocity width of the $H^{13}CO^+$ emission and $n = 10^5$ cm^{-3} in Equations 7.1 and 7.2, we have $M_{\rm J}$ of 4.4 $M_\odot$ and $\lambda_{\rm J}$ of 0.095 pc.

However, the gravitational fragmentation alone cannot produce the power-law mass distribution with a wide mass range across two orders of magnitude because $C_{\rm eff}$ and n in the star-forming regions do not vary over the corresponding wide ranges. In addition, in a gravitationally bound cloud, even if gravitationally-unstable condensations are formed, the whole of cloud is expected to collapse much quickly and the condensations will be marged together at the center of the cloud because the $t_{\rm ff}$ of the whole cloud is shorter than those of the condensations. To avoid this, there should be exist sufficient internal pressure, such as the turbulent one (Klessen et al., 1998), in the cloud which makes the global $t_{\rm ff}$ longer than the local one.

7.2 Coalescence by Mutual Collision

The coalescence of smaller dense condensations which are produced by the gravitational fragmentation can produce a power-law like mass distribution (e.g., Yoshii & Saio, 1985; Murray & Lin, 1996). The cross section of the collision between two cores, σ, can be obtained from

$$\begin{aligned}\sigma &= \pi (R+r)^2 \left\{ 1 + \frac{2GM}{v^2(R+r)} \right\} \\ &= 0.03 \left(\frac{R+r}{0.1{\rm pc}} \right)^2 \left\{ 1 + 0.10 \left(\frac{M}{M_\odot} \right) \left(\frac{v}{{\rm km\ s^{-1}}} \right)^{-2} \left(\frac{R+r}{0.1{\rm pc}} \right)^{-1} \right\} \end{aligned} \quad [{\rm pc}^2] \quad (7.3)$$

where R and M are the radius and mass of a target core, respectively, and r and v the radius and relative velocity of a colliding core, respectively. Then the probability of the collision per unit time is estimated to be $n_{\rm core}\sigma v$, where $n_{\rm core}$ is the number density of the cores. Finally, the expected number of collision during the core lifetime, i.e., the order of the free fall time, $t_{\rm ff}$, becomes $n_{\rm core}\sigma v t_{\rm ff}$.

Here we consider a case that the $H^{13}CO^+$ cores were formed by the collision of the gravitationally-fragmented condensations having the Jeans mass of 4.4 $M_\odot$. For $R+r$ we used $\lambda_{\rm J}$ of 0.095 pc. For v, we adopted the typical velocity width of GMCs of 2 - 4 km s^{-1} (Lada, 1999) as the upper limit, because GMCs are generally in virial equilibrium (Blitz, 1999). The lower limit is the relative velocities among the $H^{13}CO^+$ cores, because the kinetic energy of the condensations would be dissipated during the coalescence through the collision. The $H^{13}CO^+$ core relative velocity can be estimated from the deviation of the global velocity gradient: 0.98 km s^{-1} in the Orion A, 0.80 km s^{-1} in the Orion B, and 0.95 km s^{-1} in the Cepheus OB3. Now the velocity v has a range from 1 to 4 km s^{-1}. To estimate $n_{\rm core}$, we assumed that the total volume occupied by the $H^{13}CO^+$ cores is the three second power of the cloud area above the 2-σ level: the surface number density of the $H^{13}CO^+$ cores has a mean of 29.4 pc^{-2} over the three clouds, and then the volume density of them is estimated to be 28.1 pc^{-3}. Furthermore we assumed that the number ratio of the condensations to the $H^{13}CO^+$ cores is the mass ratio of one $H^{13}CO^+$ core to one condestaion, i.e., the total mass should be conserved. Then the number density of the condensations is estimated to be 67.1 pc^{-3}. Consequently, we can expect 0.4 - 1.2 collisions during the core life time.

This implies even if the sticking probability is assumed to be one, the expected core mass to be formed is only 5 $M_\odot$ or less, much smaller than the mean mass of the $H^{13}CO^+$ cores of about 10 $M_\odot$. This estimate is rather rough, but suggest that it is difficult to form the $H^{13}CO^+$ cores by the

coalescence of the gravitationally-fragmented condensations.

7.3 Accretion Process

The accretion from the surrounding lower-density gas reservoir is another process to be frequently considered. The gravitational fragmentation processes can produce numerous low-mass stars of an order of 1 $M_\odot$ with the timescale of $t_{\rm ff}$. The cluster of these low-mass stars would be still surrounded by their remaining natal gas and the accretion onto them would occur. Since the accretion is though to be competitive (Bonnell et al., 1997), the power-law like stellar mass distribution can be realized. Numerical simulations (e.g., Bonnell et al., 2003) showed that the power-law mass distribution is similar to the IMF.

To apply the accretion model to the dense core formation, we treat the mass accretion onto the gravitationally-fragmented condensations from the lower-density gas reservoir. Since the total mass traced by the $H^{13}CO^+$ emission is one fifth or less than that traced by the $C^{18}O$ or ^{13}CO emission in the three clouds (Nagahama et al., 1998; Aoyama et al., 2001; Yu et al., 1996), it is possible to form the $H^{13}CO^+$ cores. This scenario, however, seems inconsistent with our conclusion that the power-law shape IMF is already formed at the formation time of the CMF. This is because the gravitationally-fragmented condensations cannot be survive until the accretion phase ends, with timescale of several $\times$ $t_{\rm ff}$ (Bonnell et al., 2003), and must collapse to form low-mass protostars. Therefore, the accretion process cannot explain the formation of "dense cores".

7.4 Turbulent Fragmentaion

One of the most promising processes is the turbulent fragmentation. The turbulence in interstellar medium is generally supersonic: the sound speed in

molecular clouds is 0.2 - 0.3 km s^{-1}, while the typical velocity width of the cloud is of the order of 1 km s^{-1}. This implies that the turbulence compresses interstellar medium and creates density strucutures. The properties of the strucutures are thought to be closely related to the power spectrum of the turbulence. The power spectrum has a power-law form until the smallest scale where the energy cascade ends (Kolmogorov, 1941). Then it is natural to consider that the power-law index of the power spectrum characterizes the self-similar nature of the molecular cloud strucutures, such as the Larson's relations and the high-mass part of the CMF.

Padoan & Nordlund (2002) showed analytically that the fragmentation by the turbulence having a power spectrum of $E(k) \propto k^{-\beta_{\rm turb}}$, where k is the wavenumber of the turbulence, leads to the Larson's relation of $dv_{\rm core} \propto R_{\rm core}^{(\beta_{\rm turb}-1)/2}$ and a power-law form CMF of $dN/dM \propto M^{-(7-\beta_{\rm turb})/(4-\beta_{\rm turb})}$, In other words, the power-law index of dv - R relation β (see Section 4.2.3) and that of the CMF γ can be linked to each other as,

$$\beta = \frac{3}{2}\left(1 - \frac{1}{\gamma - 1}\right), \tag{7.4}$$

if the cores were formed by the turbulent fragmentation. Figure 7.1 shows the shadowing-corrected γ - β correlations in the three clouds. We note that the shadowing model does not considerably change β. The data points seem to follow Equation 7.4 within the uncertainties. Furthermore, the corresponding $\beta_{\rm turb}$ falls in a plausible range: Boldyrev et al. (2002) performed numerical simulations of supersonic MHD turbulence and found $\beta_{\rm turb} = 1.74$; Blunt & Heyer (2002) derived a $\beta_{\rm turb}$ range from 1.72 to 2.9 with the mean value of 2.17 observationally. These agreements strongly suggest that the turbulent fragmentation plays an important role in the core formation process. In addition, it is interesting that the dependence of γ on $\beta_{\rm turb}$ is weak in the relevant range, leading to the universality of γ: the γ range considering the uncertainties, from 2.0 to 2.8, can be explained by the $\beta_{\rm turb}$ range from 0.7

to 2.3, and the plausible values of $\beta_{\rm turb}$, such as the Kolmogorov turbulence of 5/3, the mean value of the observed $\beta_{\rm turb}$ of 2.17 (Blunt & Heyer, 2002), and the numerical simulation result of 1.74 (Boldyrev et al., 2002) fall in this $\beta_{\rm turb}$ range.

The turbulent fragmentation model predicts that the *IMF* should gradually flatten below approximately 2 $M_\odot$, because at about 2 $M_\odot$ the probability of the star-forming cores created by turbulence begins to decrease (Klessen et al., 1998; Padoan & Nordlund, 2002). This prediction is consistent with the ONC IMF and the GFIMF. In contrast, the turnover does not have to appear in the *CMF*, because the turbulent fragmentation would produce very low-mass cores continuously down to $\sim$ 0.0003 $M_\odot$ (Padoan & Nordlund, 2002) following the power-law relation of $dN/dM \propto M^{-(7-\beta_{\rm turb})/(4-\beta_{\rm turb})}$. Therefore, we should carry out more sensitive and high-spatial-resolution core surveys with smaller mass detection limit to examine the existence of the turnover in the CMF, and to test whether the turbulent fragmentation is suitable or not.

7.5 Chapter Summary

We examined gravitational fragmentation, coalescence by collision, competitive accretion, and turbulent fragmentation as the core formation process on the basis of our results. The gravitational instability is important to form gravitationally-bound cores, but cannot produce the power-law shape of the CMF with a wide mass range over two orders of magnitude. The core collision is estimated to occur only 0.4 - 1.2 times during the core lifetime, suggesting that it is difficult to explain the observed $H^{13}CO^+$ core mass. The mass accretion is not suitable for the dense core formation process because the timescale of the power-law shape mass distribution by the accretion is too long for the cores to survive, which is inconsistent with the power-law form of the CMFs. We conclude that the turbulent fragmentation is the

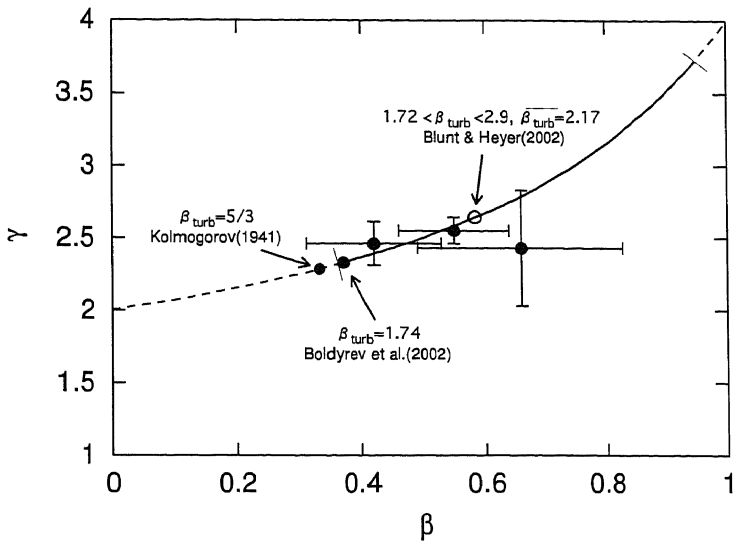

Figure 7.1 Relations between the power-law indices of the $dv_{\rm core}$ - $R_{\rm core}$ relations β and the shadowing-corrected CMFs γ in the Orion A, Orion B, and Cepheus OB3 clouds are indicated with the filled circles with errorbars. The dashed curve shows Equation 7.4, the expected relation for the turbulent fragmentation (Padoan & Nordlund, 2002), and the solid part and the open circle on the curve respectively show the range and the mean value of $\beta_{\rm turb}$ derived by Blunt & Heyer (2002). The filled ciecles on the curve indicates the cases of $\beta_{\rm turb} = 5/3$ (Kolmogorov, 1941) and $\beta_{\rm turb} = 1.74$ (Boldyrev et al., 2002).

most plausible process for the $H^{13}CO^+$ core formation, because the turbulent fragmentation can well predict the observed β and γ. On the other hand, the CMF produced by the turbulent fragmentation is expected to have no turnover. Although we showed that the power-law form of the confusion-corrected CMF continues as small as $1.3M_\odot$, higher-spatial-resolution and higher-sensitive observations should be needed to confirm this conclusion.

Chapter 8

Summary

In this chapter we summarize this thesis. First, we describe our main results and discussion on the origin of the IMF. Next we show the unsolved issues of the IMF origin and propose future observations to resolve them.

8.1 Summary

8.1.1 Distribution of the Dense Gas

We made the mapping observations of the dense parts of the nearby massive star-/cluster-forming GMCs, Orion A, Orion B, and Cepheus OB3, covering very large areas of 1.5°, 1.4°, and 1.4°, respectively. The observations were carried out in the $H^{13}CO^+(J = 1 - 0)$ line emission with the Nobeyama 45 m radio telescope.

In the Orion A cloud, the $H^{13}CO^+(J = 1 - 0)$ emission is relatively strong in the northern part ($-5° < decl. < -5°.8$) and shows the remarkable filamentary structure called "Integral Shaped filament", which is very similar to that of the dust continuum emission at millimeter and submillimeter wavelengths. We also found a large-scale velocity gradient along the Integral Shaped Filament, almost consistent with the previous studies. On the other

hand, in the southern part ($-5°.8 < decl. < -6°.5$) of the cloud, the emission is much weaker than that of the northern part and no filamentary structure was found.

In the Orion B cloud, we found five distinct clumps named NGC2023, NGC2024, NGC2068, NGC2071, and LBS23. The $H^{13}CO^+$ morphologies of the NGC2068, NGC2071, and LBS23 clumps are very similar to those of the 850μm dust continuum emission. We revealed that the molecular ridge associated with the NGC2024 H II region shows a local velocity gradient. The other regions in the Orion B, on the other hand, do not show any distinct velocity structures.

In the Cepheus OB3 cloud, our $H^{13}CO^+$ map is the first one of the dense gas covering the large area of $1°.4^2$ with a high-spatial resolution of $27''$. Although the emission is relatively weaker than those of the other two clouds, the total mass is comparable to that of the Orion A.

8.1.2 Core Catalog

We used the clumpfind algorithm to identify molecular cloud cores and finally identified 236, 98, and 31 cores in the Orion A, B, and Cepheus OB3, respectively. The cores show the mean radius of ~ 0.12 pc, the mean velocity width of ~ 0.5 km s^{-1}, and the mean mass of $\sim 10\ M_\odot$. Although the fractional abundance of $H^{13}CO^+$ relative to H_2 has not been well determined, almost all of the cores seem to be gravitationally bound and to have potential for forming stars. The radius, velocity width, and mass of the cores are smaller than those of the CS clumps by Tatematsu et al. (1993), while each of the $H^{13}CO^+$ cores contains typically one dust core of $\geq 10^6$ cm^{-3}.

The distributions of the core velocity width in the Orion A and Cepheus OB3 clouds have large velocity-width tails of 1 - 1.5 km s^{-1}, i.e., the large-dv cores, which are not seen in low-mass star forming regions. Furthermore, there exists several high-mass cores of $> 60 M_\odot$ in the Orion A and Cepheus OB3 clouds. The existence of such peculiar cores with the large velocity width

and high mass would be related to active and massive cluster formation. On the other hand, the majority of the cores are similar to each other, and are consistent with those in the previous dense core studies.

8.1.3 Relation between the $H^{13}CO^+$ CMF and the IMF

The $H^{13}CO^+$ CMFs have turnovers in the range from 8 to 17 $M_\odot$, which separate steep high-mass parts and flat low-mass ones. The power-law indices in the high-mass side are quite similar to those of the dust CMF and the stellar IMF. In addition, we showed that the dust CMF can be well produced from the $H^{13}CO^+$ CMF considering the dust cores are the denser internal strucutures of the $H^{13}CO^+$ cores, suggesting that the high-mass slope of the IMF has been formed at the formation time of the $H^{13}CO^+$ CMF. Through the comparison between the $H^{13}CO^+$ CMFs and the IMFs, we found that the star formation efficiencies in the core are $\sim$ 0.4 - 0.5, and that the number of stars expected from the CMFs are much smaller than the IMFs on the low-mass side.

We showed that the mass shortage on the low-mass side of the CMFs can be explained by the confusion, mainly due to core shadowing. Actually, the expected IMF from the confusion-corrected CMFs agree well with the IMFs. On the other hand, the corrected CMFs are found to have no turnover, and thus, the turnovers seen in the CMFs directly derived from our observations are not likely to correspond to those of the IMFs and do not represent some physical processes. Furthermore, the power-law indices of the corrected CMFs in the three clouds are similar to each other in the mass range from $1.3 \leq M/M_\odot \leq 110$, in spite of their different star-forming activities. This suggests that the universality of the IMF high-mass slope have already emerged at the $H^{13}CO^+$ core formation time.

8.1.4 Large-dv Cores and the Formation of the Most Massive Star

The massive star formations in the GMCs are likely to be related to the associated OB stars with H II regions, because the large-dv cores are found to be located near the M42 H II region and the Cep-A compact H II region. The large-dv cores have the potential for massive-star formation because the mass infall rate is proportional to the third power of the velocity width. We propose that such cores are produced by the shock form the OB stars and produce the high-mass turnover of the IMF.

8.1.5 Core Formation Processes

We found that the IMF can be determined at the core formation. This implies that revealing the origin of the IMF is equivalent to investigating the formation processes of the CMF. We examined proposed core formation processes of the gravitational fragmentation, the coalescence by collision, the accretion process, and the turbulent fragmentation on the basis of our results. We concluded that the most plausible processes is the turbulent fragmentation because the turbulent fragmentation model (Padoan & Nordlund, 2002) can wel reproduced the $dv_{\rm core}$ - $R_{\rm core}$ relation and the power-law CMF.

8.2 Future Work

Last we summarize the unsolved problems for the origin of the IMF and future plans to resolve them.

The correction method of the confusion effect we developed is only based on the shadowing. The confusion, however, involves the shadowing and the blending, as mentioned in Section 5.3. If we consider the confusion effect in more distant clouds, where we cannot achieve a sufficient spatial resolution, the contribution of the blending cannot be ignored and $M_{\rm s,p}$ would be un-

derestimated. Therefore, the modeling of the blending should be needed to investigate more active massive-star forming regions, usually located at > 1 kpc.

To examine whether the turnover in the CMF corresponding to the confusion-free turnover in the IMF exists or not, we need to carry out more sensitive and higher resolution observations to reduce the mass detection limit down to the order of $0.1 M_{\odot}$. It is also important to check whether the turbulent fragmentation, which predicts the CMF without the turnover, is suitable for the core formation process or not.

When the universal high-mass power-law slope of the IMF originates is still unclear. We showed that the CMF slopes seem to show the universality for the cores of 10^{4-5} cm^{-3}. Figure 8.1 shows the γ values derived with various tracers as a function of the representative densities of the tracers. Figure 8.1 indicates that the CMFs derived by the less dense (10^{2-4} cm^{-3}) tracers of the ^{12}CO and ^{13}CO emission have similar indices of 1.7 (Kramer et al., 1998) but the indices are far from that of the IMF of 2.3 - 2.7. The less dense CMFs, however, should be re-examined because their spatial resolution is as coarse ($\sim$ 1′ - 10′), corresponding to linear resolutions of 0.3 - 0.8 pc. The γ values derived with coarser resolution tend to become smaller, and hence we cannot fairly compare their γ values with ours (spatial resolution of 0.05 pc). Therefore, to seek the origin of the IMF slope universality, it is needed to survey the clouds with tracers of modelate density of 10^{3-4} cm^{-3}, such as C^{18}O(1 - 0), and with sufficient resolution as high as 0.1 pc, to derive the mass function of the modelate-density structure with a good statistics as well as our H^{13}CO^{+} CMFs.

The sample number of the large-dv cores are only four. To statistically confirm the relation between the energy input from the stellar sources and the most-massive star formation, and we should search such cores in other star-forming regions where the interaction between stellar activities and dense gas is expected.

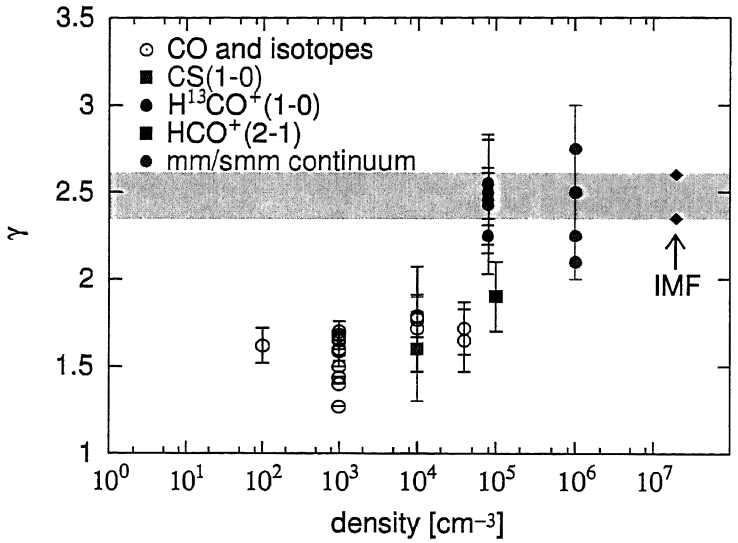

Figure 8.1 γ values of the high-mass part of the CMF derived with various tracers, as function of the density. The diamonds in the left of the figure show the γ of the IMFs: 2.6 (Miller & Scalo, 1979) and 2.35 (Salpeter, 1955) is indicated with the upper and lower symbols, respectively. The horizontal shadowed band roughly shows the range of the IMF γ. *References* – CO and isotopes: Sanders et al. (1985); Blitz (1993); Langer et al. (1993); Williams et al. (1994); Brand & Wouterloot (1995); Dobashi et al. (1996); Kramer et al. (1998); CS(1 - 0): Tatematsu et al. (1993); $H^{13}CO^+$(1 - 0): present study, Onishi et al. (2002); HCO^+(2 - 1): Hobson et al. (1994); mm/submm continuum: Motte et al. (1998); Testi & Sargent (1998); Johnstone et al. (2000, 2001).

References

Aoyama, H., Mizuno, N., Yamamoto, H., Onishi, T., Mizuno, A. & Fukui, Y. 2001, PASJ, 53, 1053

Aso, Y., Tatematsu, K., Sekimoto, Y., Nakano, T., Umemoto, T., Koyama, K. & Yamamoto, S. 2000, ApJS, 131, 465

Bally, J., Langer, W. D., Stark, A. A. & Wilson, R. W. 1987, ApJ, 312, L45

Bally, J., Langer, W. D. & Liu, W. 1991, ApJ, 383, 645

Barranco, J. A. & Goodman, A. A. 1998, ApJ, 504, 207

Beichman, C. A., Myers, P. C., Emerson, J. P., Harris, S., Matheu, R., Benson, P. J. & Jennings, R. E. 1986, ApJ, 307, 337

Bergin, E. A., Ungerechts, H., Goldsmith, P. F., Snell, R. L., Irvine, W. M. & Schloerb, F. P. 1997, ApJ, 482, 267

Bertoldi, F. & McKee, C. F. 1992, ApJ, 395,140

Bik, A., Lenorzer, A., Kaper, L., Comerón, F., Waters, L. B. F. M., de Koter, A. & Handson, M. M. 2003, A&A, 404, 249

Blaauw, A. 1991 in The Physics of Star Formation and Early Stellar Evolution, eds. Lada, C. J. and Kylafis, N. D., (Kluwer Academic Publishers: Dordrecht), p. 125

Blitz, L. 1993, in Protostars and Planets III, eds. Levy, E. H. & Lunine, J. I. (The University of Arizona Press)

Blitz, L. & Williams, J. P. 1999, in The Origin of Stars and Planetary Systems, eds. Lada, C. J. & Kylafis, N. D. (Kluwer Academic Publishers)

Blunt, C. M. & Heyer, M. H. 2002, ApJ, 566, 289

Boldyrev, S., Nordlund, A. & Padoan, P. 2002, ApJ, 573, 678

Bondi, H. & Hoyle, F. 1944, MNRAS, 104, 273

Bonnell, I. A., Bate, M. R., Clarke, C. J. & Pringle, J. E. 1997, MNRAS, 285, 201

Bonnell, I. A. 1999, in The formation of stars and planetary systems, ed. Lada, C. J. & Kylafis, N. D.

Bonnell, I. A., Bate, M. R., Clarke, C. J. & Pringle, J. E. 2001, MNRAS, 323, 785

Bonnell, I. A., Clarke, C. J., Bate, M. R. & Pringle, J. E. 2001, MNRAS, 324, 573

Bonnell, I. A., Bate, M. R. & Vine S. G. 2003, MNRAS, 343, 413

Bonnell, I. A., Larson, R. B. & Zinnecker, H. 2006, in Protostars and Planets V, eds. Reipurth, B., Jewitt, D. & Keil K. (The University of Arizona Press)

Brand, J. & Wouterloot, J. G. A. 1995, A&A, 303, 851

Brown, A. G. A., de Geus, E. J. & de Zeeuw, P. T. 1994, A&A, 289, 101

Butner, H. M., Lada, E. A. & Loren, R. B. 1995, ApJ, 448, 207

Caselli, P. & Myers, P. C. 1995, ApJ, 446, 665

Caselli, P., Benson, P.J., Myers, P. C. & Tafalla, M. 2002, ApJ, 572, 238

Cesaroni, R. & Wilson, T. L. 1994, A&A, 281, 209

Chandler, C. J. & Carlstrom, J. E. 1996, ApJ, 466, 338

Chini, R., Reipurth, B., Ward-Thompson, D., Barry, J., Nyman, L.-Å.,Sievers, A. & Billawala, Y. 1997, ApJ, 474, L135

Dame, T. M., Hartmann, D. & Thaddeus, P. 2001, ApJ, 547, 792

Di Francesco, J., Evans, N. J. II, Caselli, P., Myers, P. C., Shirley, Y., Aikawa, Y. & Tafalla, M. 2006, in Protostars and Planets V, eds. Reipurth, B., Jewitt, D. & Keli, K. (The University of Arizona Press)

Dobashi, K., Bernerd, J. P. & Fukui, Y. 1996, ApJ, 466, 282

Dobashi, K., Yonekura, Y., Matsumoto, T., Momose, M., Sato, F., Bernard, J-P & Ogawa, H. 2001, PASJ, 53, 85

Duquennoy, A. & Mayor, M. 1991, A&A, 248, 485

Dutrey, A., Langer, W. D., Bally, J., Duvert, G., Castets, A. & Wilson, R. W. 1991, A&A, 247, 9

Dyson, J. E. & Williams, D. A. 1997, The physics of the interstellar medium, eds. Tayler, R. J., Elvis, M. (Institute of Physics Publishing)

Elmegreen, B. G. & Lada, C. J. 1997, ApJ, 214, 725

Emerson, D. T. & Gräve, R., 1988, A&A, 190, 353

Felli, M., Churchwell, E., Wilson, T. L. & Taylor, G. B. 1993, A&AS, 98, 137

Fischer, D. A. & Marcy, G. W. 1992, ApJ, 396, 178

Frerking, M. A., Langer, W. D. & Wilson, R. W. 1982, ApJ, 262, 590

Garay, G., Ramírez, S., Rodríguez, L. F., Curiel, S. & Torrelles, J. M. 1996, ApJ, 459, 193

Garmany, C. 1973, ApJ, 78, 185

Genzel, R., Reid, M. J., Moran, M. J. & Downes, D. 1981, ApJ, 244, 884

Harju, J., Walmsley, C. M. & Wouterloot, J. G. A. 1993, A&AS, 98, 51

Harjunpää, P., Lehtinen, K. & Haikala,L. K. 2004, A&A, 421, 1087

Harten, R. H., Thum, C. & Felli, M. 1981, A&A, 94, 231

Hillenbrand, L. A. 1997, AJ, 113, 173

Hillenbrand, L. A. & Carpenter, J. M. 2000, ApJ, 540, 236

Hillenbrand, L. A. & Hartmann, L. W. 1998, ApJ, 492, 540

Ho, P. T. P., Moran, J. M. & Rodriguez, L. F. 1982, ApJ, 262, 619

Ho, P. T. P. & Townes, 1983, ARA&A, 21, 239

Hobson, M. P., Jenness, T., Padman, R & Scott P. F. 1994, MNRAS, 266, 972

Hogerheijde, M. R., Van Dishoeck, E. F., Blake, G. A. & Langevelde, H. J. 1997, ApJ, 489, 293

Hughes, V. A. 1988, ApJ, 333, 788

Johnstone, D. & Bally, J. 1999, ApJ, 510, L49

Johnstone, D., Wilson, C. D., Moriaty-Schieven, G., Joncas, G., Smith, G., Gregersen, E. & Fich, Michel 2000, ApJ, 545, 327

Johnstone, D., Fich, M., Mitchell, G. F. & Moriaty-Schieven, G. 2001, ApJ, 559, 307

Kandori, R., Nakajima, Y., Tamura, M., Tatematsu, K., et al. 2005, AJ, 130, 2166

Klessen, R. S., Burkert, A. & Bate, M. R. 1998, ApJ, 501, L205

Kolmogorov, A. 1941, Dokl. Akad. Nauk SSSR, 31, 538

Kornreich, P., & Scalo, J. 2000, ApJ, 531, 366

Kramer, C., Stutzki, J., Röhrig, R & Corneliussen, U. 1998, A&A, 329, 249

Kroupa, P., Tout, C. A. & Gerard, G. 1993, MNRAS, 262, 545

Kroupa, P. 1995, MNRAS, 277, 1522

Kroupa, P., Aarseth, S. & Hurley, J. 2001, MNRAS, 321, 699

Kroupa, P. 2001, MNRAS, 322, 231

Kutner, M. & Thaddeus, P. 1971, ApJ, 168, 67

Kutner, M. L., Machnik, D. E., Mead, K. N. & Evans, N. J., II 1985, ApJ, 299, 351

Lada, C. J. 1999, in The Origin of Stars and Planetary Systems, eds. Lada, C. J. & Kylafis, N. D. (Kluwer Academic Publishers)

Lada, E. A., Bally, J. & Stark, A. A. 1991, ApJ, 368, 432

Lada, E. A., DePoy, D. L., Evans, N. J. II & Gatley, I. 1991, ApJ, 371, 171

Lada, C. J., Young, E. T. & Greene, T. P. 1993, ApJ, 408, 471

Lada, E. A. & Lada, C. J. 1995, ApJ, 109, 1682

Lada, C. J. & Lada, E. A. 2003, ARA&A, 41, 57

Lamers, H. J. G. L. M. & Leitherer, C. 1993, ApJ, 412, 771

Lane, A. P. & Bally, J. 1986, ApJ, 310, 820

Langer, W. D., Wilson, R. W. & Anderson, C. H. 1993, ApJ, 408, L45

Larson, R. B. 1981, MNRAS, 194, 809

Lis, D. C., Serabyn, E., Keene, J., Dowell, C. D., Benford, D. J., Phillips, T. G., Hunter, T. R. & Wang, N. 1998, ApJ, 509, 299

Maddalena, R. J., Morris, M., Moscowitz, J. & Thaddeus, P. 1986, ApJ, 303, 375

Mangum, J. 1999, On The Fly Observing at the 12 Meter

Mac Low, M.-M. & Klessen, R. S. 2004, Rev. Mod. Phys. 76, 125

Mason, B. D., Gies, D. R., Hartkopf, W. I, Bagnuolo, W, G, T. T. Brummelaar, & McAlister, H. A. 1998, ApJ, 115, 821

Massey, P., Johnson, K. E. & DeGioia-Eastwood K. 1995, ApJ, 454, 151

Mathieu, R. D., Ghez, A. M., Jensen, E. L. N. & Simon, M. 2000, in Protostars and Planets IV, eds. Mannings, V., Boss, A. P. & Russell, S. S. (The University of Arizona Press)

Mazeh, T., Goldberg, D., Duquennoy, A. & Mayor, M. 1992, ApJ, 401, 265

McKee, C. F. & Tan, J. C. 2003, ApJ, 585, 850

McMullin, J. P., Mundy, L. G. & Blake, G. A. 1993, ApJ, 405, 599

Miller, G. E. & Scalo, J. M. 1979, ApJS, 41, 513

Minchin, N. R., Ward-Thompson, D. & White, G. J. 1992, A&A, 265, 733

Motoyama, K. & Yoshida, T. 2003, MNRAS, 344, 461

Motte, F., André, P. & Neri, R. 1998, A&A, 336, 150

Muench, A. A., Lada, E. A. & Lada, C. J. 2000, ApJ, 533, 358

Muench, A. A., Lada, E. A. & Lada, C. J. 2002, ApJ, 573, 366

Muench, A. A., Lada, E. A., Lada, C. J., Elston, R. J., Alves, J. F., Horrobin, M., Huard, T. H., Levine, J. L., Raines, S. N., Román-Zúñiga, C. 2003, AJ, 125, 2029

Murata, Y., Kawabe, R.,Ishiguro, M., Morita, K., Kasuga, T.,Takano, T. & Hasegawa, T. 1990, ApJ, 359, 125

Murray, S. D. & Lin, D. N. 1996, ApJ, 467, 728

Myers, P. C., Ladd, E. F. & Fuller, G. A. 1991, ApJ, 372, 95

Nagahama, T., Mizuno, A., Ogawa, H. & Fukui, Y 1998, AJ, 116, 336

Nakano, T., Hasegawa, T. & Norman, C. 1995, ApJ, 450, 183

Nielbock, M., Chini, R. & Müller, S. A. H. 2003, A&A, 408, 245

Onishi, T., Mizuno, A., Kawamura, A., Tachihara, K. & Fukui, Y. 2002, ApJ, 575, 950

Osterbrock, D. E. 1989, Astrophysics of gaseous nebulae and active galactic nuclei (University Science Books)

Ostriker, J. 1964, ApJ, 140, 1056

Padoan, P. & Nordlund, A. 2002, ApJ,576, 870

Petr, M. G., Coudé du Foresto, V., Beckwith, S. V. W., Richichi, A., & McCaughrean, M. J. 1998, ApJ, 500, 825

Reid, I. N., Gizis, J. E. & Hawley, S. L. 2002, ApJ, 124, 2721

Press, W. H., Teukolsky, S. A., Vetterling, W. T. & Flannery, B. P. 1992, Numerical Recipes in C, (Cambridge Univ. Press)

Rodríguez-Franco, A., Martín-Pintado, J., Gómez-González, J. & Planesas, P. 1992, A&A, 264, 592

Rodríguez-Franco, A., Martín-Pintado, J. & Fuente, A. 1998, A&A, 329, 1097

Saito, T. 2002, Master thesis

Salpeter, E. E. 1955, ApJ, 121, 161

Sandell, G., Avery, L. W., Baas, F., Coulson, I., Dent, W. R. F., Friberg, P., Gear, W. P. K., Greavees, J., Holland, W., Jennings, T., Jewell, P., Lightfoot, J., Matthews, H. E., Moriarty-Schieven, G., Prestage, R., Robson, E. I., Stevens, J., Tilanus, R. P. J. & Watt, G. D. 1999, ApJ, 519, 236

Sanders, D. B., Scoville, N. Z. & Solomon, P. M. 1996, ApJ, 289, 373

Sargent, A. I. 1977, ApJ, 218, 736

Sargent, A. I., van Duinen, R. J., Nordh, H. L., Fridlund, C. V. M, Aalders, J. W. G. & Beintema, D. 1983, AJ, 88, 1236

Savage, C., Apponi, A. J., Ziurys, L.M. & Wyckoff, S. 2002, ApJ, 578, 211

Schmid-Burgk, J., Muders, D., Müller, H.S.P., & Brupbacher-Gatehouse, B. 2004, A&A, 419, 949

Schwab, F. R. 1984, Optimal Gridding of Visibility Data in Radio Interferometry, in Indirect Imaging, Robert, J. A., Ed., pp.333-346

Smith, M. D., Froebrich, D. & Eislöffel, J. 2001, ApJ, 592, 245

Snell, R. L, Scoville, N. Z., Sanders, D. B. & Erickson, N. R., 1984, ApJ, 284, 176

Sorai, K., Sunada, K., Iwasa, T., Tanaka, T., Natori, K. & Onuki, H. 2000, Proc. SPIE, 4015, 86

Stanke, T., McCaughrean, M. J. & Zinnecker, H. 2002, A&A, 392, 239

Steimen-Cameron, T. Y., Haas, M. R. & Tielens, A. G. G. M. 1997, ApJ, 478, 261

Strom, K. M., Strom, S. E. & Merrill, K. M. 1993, ApJ, 412, 233

Stutzki, J. & Güsten, R. 1990, ApJ, 356, 513

Sunada, K., Yamaguchi, C., Nakai, N., Sorai, K., Okumura, S. & Ukita, N. 2000, Proc. SPIE, 4015, 237

Tafalla, M., Myers, P. C., Mardones, D. & Bachiller, R. 1999, A&A, 348, 479

Tatematsu, K., Umemoto, T., Kameya, O., Hirano, N., Hasegawa, T., Hayashi, M., Iwata, T., Kaifu, N., Mikami, H., Murata, Y., Nakano, M., Nakano, T., Ohashi, N., Sunada, K., Takaba, H. & Yamamoto, S. 1993, ApJ, 404, 643

Testi, L., Olmi, L., Hunt, L., Tofani, G., Felli, M. & Goldsmith, P. 1995, A&A, 303, 881

Testi, L. & Sargent, I. 1998, ApJ, 508, L91

Tsujimoto, M., Koyama, K., Kobayashi, N., Goto, M., Tsuboi, Y. & Tokunaga, A. T. 2003, AJ, 125, 1537

Ungerechts, H., Bergin, E. A., Goldsmith, P. F., Irvine, W. M., Schloerb, F. P. & Snell, R. L. 1997, ApJ, 482, 245

Vink, J. S., de Koter, A. & Lamers, H. J. G. L. M. 2000, A&A, 362, 295

Williams, J. P., de Geus, E. J. & Blitz, L. 1994, ApJ, 428, 693

Williams, J. P., Blitz, L. & Stark, A. A. 1995, ApJ, 451, 252

Wilson, B. A., Dame, T. M., Masheder, M. R. W. & Thaddeus, P. 2005, A&A, 430, 523

Wiseman, J. J. & Ho, P. T. P. 1998, ApJ, 502, 676

Woitas, J., Leinert, Ch. & Köhler, R. 2001, A&A, 376, 982

Yamaguchi, C., Sunada, K., Iizuka, Y., Iwashita, H. & Noguchi, T. 2000, Proc. SPIE, 4015, 614

Yoshii, Y. & Saio, H. 1985, ApJ, 295, 521

Yu, Z.-Y., Nagahama, T. & Fukui, Y. 1996, ApJ, 471, 867

Zapata, L. A., Rodríguez, L. F., Kurtz, S. E., O'Dell, C. R & Ho, P. T. P. 2004, ApJ, 610, L121

Zinnecker, H., McCaughrean, M. & Wilking, B. A. 1993, in Protostars and Planets III, eds. Levy, H. & Lunine, J. I., (The University of Arizona Press)

Ziurys, L. M., Martin, R. N., Pauls, T. A. & Wilson, T. L. 1981, A&A, 104, 288

Appendix A

Lists of the $H^{13}CO^+$ Cores

The typical uncertainty of each quantity is as follows: $R_{\rm core}$. 0.04 pc in the Orion A and B clouds, and 0.06 pc in the Cepheus OB3 cloud, derived from the uncertainty in the estimation of the core projected area; $dv_{\rm core}$. 0.13 km s^{-1}, corresponding to the velocity resolution; $M_{\rm LTE}$. A factor of 3 (see text); $M_{\rm vir}$. A factor of 3, derived from the uncertainties in $R_{\rm core}$ and $dv_{\rm core}$; $M_{\rm vir}/M_{\rm LTE}$. A factor of 4, derived from the uncertainties in $M_{\rm LTE}$ and $M_{\rm vir}$; $\bar{n}$. A factor of 4, derived from the uncertainties of $R_{\rm core}$ and $M_{\rm LTE}$.

Table A.1. Physical properties of the $H^{13}CO^+$ cores in the Orion A cloud

I.D.	α (B1950)			δ (B1950)			v_{LSR}	$T^*_{A,peak}$	Aspect Ratio	R_{core}	dv_{core}	M_{LTE}	M_{vir}	M_{vir}/M_{LTE}	$\bar{n}$
	h	m	s	°	′	″	km s^{-1}	K		pc	km s^{-1}	$M_\odot$	$M_\odot$		10^4 cm^{-3}
A1	5	32	9.7	−5	42	45	8.0	0.7	1.3	0.15	0.64	6.1	13	2.1	0.86
A2	5	32	11.1	−5	47	53	8.4	0.5	1.2	0.16	0.66	8.0	15	1.8	0.80
A3	5	32	15.2	−5	43	26	7.7	0.5	1.1	0.11	0.51	4.3	5.8	1.4	1.5
A4	5	32	17.9	−5	46	31	9.0	0.8	1.1	0.18	0.45	13	7.3	0.6	1.0
A5	5	32	17.9	−5	48	55	8.9	0.8	1.1	0.15	0.63	15	12	0.8	2.0
A6	5	32	20.7	−4	57	32	10.7	1.4	1.1	0.13	0.57	16	8.5	0.5	3.4
A7	5	32	20.7	−5	47	53	8.6	1.2	1.3	0.15	0.48	15	7.5	0.5	1.8
A8	5	32	22.1	−5	43	26	7.2	0.6	1.5	0.13	0.35	5.2	3.3	0.6	0.97
A9	5	32	22.1	−5	46	31	8.4	0.7	1.6	0.12	0.32	4.1	2.6	0.6	1.0
A10	5	32	22.1	−5	47	12	9.3	1.1	1.1	0.15	0.38	12	4.5	0.4	1.5
A11	5	32	22.1	−5	48	13	7.7	0.6	1.2	0.14	0.67	10	12	1.2	1.7
A12	5	32	22.1	−5	49	36	9.8	0.4	1.2	0.16	0.56	5.4	10	1.9	0.61
A13	5	32	22.1	−5	49	56	8.7	0.5	1.9	0.16	0.56	6.7	11	1.6	0.70
A14	5	32	23.5	−5	40	0	6.8	0.5	1.1	0.13	0.52	7.1	7.6	1.1	1.3
A15	5	32	23.5	−5	41	2	7.7	1.0	1.1	0.11	0.52	8.2	6.3	0.8	2.5
A16	5	32	23.5	−5	44	27	7.8	0.7	1.3	0.08	0.50	4.2	4.4	1.0	3.2
A17	5	32	23.5	−5	45	9	8.5	0.7	1.2	0.15	0.43	11	5.8	0.5	1.2
A18	5	32	23.5	−5	46	10	9.3	0.8	1.0	0.15	0.42	11	5.7	0.5	1.3
A19	5	32	24.8	−5	46	10	8.1	0.8	1.4	0.13	0.33	7.1	3.1	0.4	1.3
A20	5	32	24.8	−5	47	53	8.9	1.2	1.1	0.17	0.53	27	9.9	0.4	2.3
A21	5	32	24.9	−4	58	34	11.1	1.0	1.4	0.13	0.40	8.4	4.1	0.5	1.8
A22	5	32	26.2	−4	59	15	10.8	1.1	1.2	0.12	0.49	8.0	6.2	0.8	1.9
A23	5	32	26.2	−5	43	26	9.1	0.8	1.0	0.17	0.68	19	16	0.8	1.7
A24	5	32	26.2	−5	45	29	7.8	0.9	1.7	0.14	0.40	11	4.6	0.4	1.7
A25	5	32	27.6	−4	56	51	11.1	0.6	1.1	0.11	0.45	5.6	4.8	0.9	1.6

Table A.1 (cont'd)

I.D.	α (B1950)			δ (B1950)			$v_{\rm LSR}$	$T^*_{A,\rm peak}$	Aspect Ratio	$R_{\rm core}$	$dv_{\rm core}$	$M_{\rm LTE}$	$M_{\rm vir}$	$M_{\rm vir}/M_{\rm LTE}$	$\bar{n}$
	h	m	s	°	′	″	km s^{-1}	K		pc	km s^{-1}	$M_\odot$	$M_\odot$		10^4 cm^{-3}
A26	5	32	27.6	−5	42	4	9.3	0.8	1.3	0.13	0.68	9.7	12	1.2	2.1
A27	5	32	27.6	−5	45	29	8.7	0.8	1.3	0.14	0.45	11	5.9	0.5	1.7
A28	5	32	27.6	−5	46	10	7.3	1.2	1.4	0.16	0.42	17	5.7	0.3	1.9
A29	5	32	27.6	−5	47	12	7.8	1.0	1.6	0.12	0.49	12	6.2	0.5	2.6
A30	5	32	27.6	−5	48	13	7.8	1.3	1.2	0.15	0.50	23	7.7	0.3	3.0
A31	5	32	27.6	−5	49	56	8.9	0.4	2.5	0.11	0.57	4.3	7.7	1.8	1.3
A32	5	32	29.0	−5	1	18	11.3	0.4	1.2	0.14	0.39	3.7	4.4	1.2	0.57
A33	5	32	29.0	−5	4	44	9.9	0.4	1.1	0.11	0.30	2.8	2.1	0.8	0.85
A34	5	32	29.0	−5	35	54	6.7	0.4	1.4	0.11	0.77	4.4	13	3.0	1.6
A35	5	32	29.0	−5	43	26	7.6	0.6	1.3	0.14	0.55	6.1	9.0	1.5	0.89
A36	5	32	29.0	−5	44	27	8.9	0.8	1.1	0.16	0.52	14	8.9	0.6	1.5
A37	5	32	29.0	−5	47	53	7.3	1.2	1.1	0.16	0.45	21	7.0	0.3	2.0
A38	5	32	29.0	−5	50	37	7.3	1.1	1.2	0.19	0.61	22	14	0.6	1.5
A39	5	32	30.3	−5	22	12	8.7	0.3	1.1	0.08	0.56	2.3	5.5	2.4	1.8
A40	5	32	30.3	−5	38	18	6.7	1.0	1.1	0.16	0.61	19	12	0.6	1.9
A41	5	32	30.3	−5	44	27	7.3	0.6	1.5	0.14	0.36	6.1	3.6	0.6	1.0
A42	5	32	30.3	−5	45	50	7.1	1.3	1.2	0.14	0.47	18	6.5	0.4	2.7
A43	5	32	30.3	−5	51	18	8.5	0.4	1.1	0.11	0.61	3.6	8.9	2.5	1.0
A44	5	32	31.7	−5	0	37	10.8	1.2	1.1	0.15	0.48	15	7.2	0.5	2.0
A45	5	32	31.7	−5	23	34	8.6	1.4	1.3	0.14	0.96	22	26	1.2	3.6
A46	5	32	31.7	−5	42	24	9.3	0.5	1.9	0.14	0.66	5.3	12	2.4	0.85
A47	5	32	31.7	−5	47	12	6.9	1.4	1.5	0.16	0.63	25	13	0.5	2.7
A48	5	32	33.1	−5	17	24	10.0	0.4	1.0	0.14	0.35	4.0	3.6	0.9	0.59
A49	5	32	33.1	−5	21	51	8.0	0.5	2.5	0.14	0.65	8.0	12	1.5	1.2
A50	5	32	33.1	−5	49	56	6.9	0.7	1.2	0.15	0.41	11	5.3	0.5	1.2

Table A.1 (cont'd)

I.D.	α (B1950)			δ (B1950)			$v_{\rm LSR}$	$T^*_{A,\rm peak}$	Aspect Ratio	$R_{\rm core}$	$dv_{\rm core}$	$M_{\rm LTE}$	$M_{\rm vir}$	$M_{\rm vir}/M_{\rm LTE}$	$\bar{n}$
	h	m	s	°	′	″	km s^{-1}	K		pc	km s^{-1}	$M_\odot$	$M_\odot$		10^4 cm^{-3}
A51	5	32	33.1	−5	51	18	6.9	0.5	1.1	0.15	0.37	8.4	4.2	0.5	1.0
A52	5	32	33.1	−5	55	25	7.4	0.6	1.2	0.10	0.56	5.4	6.9	1.3	2.1
A53	5	32	34.5	−5	0	58	10.6	1.5	1.0	0.13	0.57	8.4	8.9	1.1	1.7
A54	5	32	34.5	−5	17	24	9.4	1.0	1.5	0.18	0.60	13	13	1.0	1.0
A55	5	32	34.5	−5	19	48	8.5	0.6	1.0	0.11	0.54	4.3	6.8	1.6	1.4
A56	5	32	34.5	−5	40	0	8.7	0.9	1.0	0.17	0.60	19	13	0.7	1.5
A57	5	32	34.5	−5	40	21	6.8	0.6	1.5	0.13	0.46	7.4	5.7	0.8	1.5
A58	5	32	34.5	−5	48	55	6.8	0.3	1.4	0.11	0.51	3.3	6.2	1.9	1.0
A59	5	32	34.5	−5	57	28	8.1	0.7	1.1	0.10	0.27	4.2	1.5	0.4	1.8
A60	5	32	34.5	−5	57	49	8.5	0.7	1.1	0.11	0.39	3.1	3.4	1.1	1.0
A61	5	32	35.8	−5	37	57	7.1	1.5	1.1	0.16	0.64	26	13	0.5	2.8
A62	5	32	35.9	−4	57	12	11.1	1.2	1.2	0.13	0.46	11	6.0	0.5	2.1
A63	5	32	35.9	−4	59	35	11.5	1.1	1.0	0.18	0.38	16	5.2	0.3	1.3
A64	5	32	35.9	−5	17	45	8.1	0.5	1.1	0.09	0.38	2.4	2.5	1.1	1.7
A65	5	32	35.9	−5	22	32	8.5	0.7	1.2	0.15	0.46	11	7.0	0.6	1.3
A66	5	32	35.9	−5	24	56	9.0	0.4	1.2	0.15	0.55	6.4	9.6	1.5	0.79
A67	5	32	35.9	−5	25	37	10.6	0.4	1.5	0.16	0.76	7.0	19	2.7	0.79
A68	5	32	37.2	−4	56	30	11.2	0.7	1.0	0.12	0.40	6.4	4.0	0.6	1.5
A69	5	32	37.2	−4	58	34	11.2	1.4	1.1	0.12	0.45	18	5.3	0.3	4.0
A70	5	32	37.2	−5	22	32	8.9	0.5	1.0	0.15	0.44	8.2	6.1	0.7	0.98
A71	5	32	37.2	−5	24	56	8.5	0.5	1.4	0.15	0.66	11	14	1.2	1.4
A72	5	32	37.2	−5	26	18	8.6	0.6	1.1	0.13	0.33	3.3	3.1	1.0	0.61
A73	5	32	37.2	−5	26	18	8.4	0.5	1.8	0.16	0.57	7.1	11	1.6	0.71
A74	5	32	37.2	−5	36	55	7.2	1.2	1.0	0.17	0.53	17	10	0.6	1.5
A75	5	32	37.2	−5	38	59	8.9	0.7	1.0	0.12	0.47	6.2	5.6	0.9	1.4

Table A.1 (cont'd)

I.D.	α (B1950)			δ (B1950)			$v_{\rm LSR}$	$T^*_{A,\rm peak}$	Aspect Ratio	$R_{\rm core}$	$dv_{\rm core}$	$M_{\rm LTE}$	$M_{\rm vir}$	$M_{\rm vir}/M_{\rm LTE}$	$\bar{n}$
	h	m	s	°	′	″	km s^{-1}	K		pc	km s^{-1}	$M_\odot$	$M_\odot$		10^4 cm^{-3}
A76	5	32	37.2	−5	53	22	6.5	0.9	1.2	0.12	0.69	8.2	12	1.4	2.1
A77	5	32	38.6	−5	17	45	9.9	0.5	1.2	0.10	0.38	3.8	3.0	0.8	1.4
A78	5	32	38.6	−5	18	46	9.5	0.6	1.1	0.14	0.32	6.9	3.0	0.4	1.1
A79	5	32	38.6	−5	24	56	6.7	1.2	1.2	0.19	0.90	25	32	1.3	1.6
A80	5	32	40.0	−5	17	45	9.3	0.6	1.4	0.12	0.37	3.9	3.3	0.8	1.0
A81	5	32	40.0	−5	53	22	6.5	0.9	1.1	0.14	0.60	11	11	0.9	1.7
A82	5	32	41.4	−5	0	16	11.1	1.1	1.0	0.18	0.46	24	7.8	0.3	1.7
A83	5	32	41.4	−5	1	59	11.7	0.3	1.5	0.15	0.41	5.1	5.3	1.0	0.60
A84	5	32	41.4	−5	19	48	9.1	1.2	1.5	0.16	0.53	21	9.5	0.5	2.2
A85	5	32	41.4	−5	22	12	8.0	1.9	1.1	0.17	0.66	30	15	0.5	2.6
A86	5	32	41.4	−5	22	53	9.5	0.5	1.4	0.19	0.53	13	11	0.9	0.84
A87	5	32	41.4	−5	35	54	6.5	0.5	1.1	0.16	0.47	6.5	7.6	1.2	0.62
A88	5	32	41.4	−5	37	16	8.2	1.2	1.3	0.13	0.60	21	9.6	0.5	4.0
A89	5	32	41.4	−5	57	49	7.1	0.6	1.2	0.13	0.40	3.5	4.1	1.2	0.74
A90	5	32	41.4	−6	1	55	8.0	0.6	2.1	0.17	0.60	10	12	1.2	0.93
A91	5	32	42.7	−5	0	16	10.7	1.2	1.2	0.14	0.42	13	5.0	0.4	2.1
A92	5	32	42.7	−5	2	20	10.7	1.2	1.2	0.18	0.67	37	17	0.4	2.7
A93	5	32	42.7	−5	17	3	8.6	0.4	2.1	0.17	0.41	5.0	5.9	1.2	0.45
A94	5	32	42.7	−5	23	54	10.6	0.4	1.1	0.13	0.67	3.9	12	3.0	0.81
A95	5	32	42.7	−5	24	15	9.0	0.4	1.4	0.15	0.40	6.1	4.9	0.8	0.84
A96	5	32	42.7	−5	24	15	6.9	1.2	1.0	0.20	0.37	24	5.6	0.2	1.2
A97	5	32	42.7	−5	24	15	7.2	1.2	1.2	0.23	0.31	28	4.6	0.2	0.98
A98	5	32	42.7	−5	25	37	8.6	0.3	1.1	0.11	0.46	3.9	4.8	1.2	1.4
A99	5	32	42.7	−5	26	39	8.7	0.4	1.6	0.14	0.42	5.0	4.9	1.0	0.84
A100	5	32	42.7	−5	26	59	9.4	0.4	1.2	0.11	0.42	3.0	4.0	1.3	1.0

Table A.1 (cont'd)

I.D.	α (B1950)			δ (B1950)			$v_{\rm LSR}$	$T^*_{A,\rm peak}$	Aspect Ratio	$R_{\rm core}$	$dv_{\rm core}$	$M_{\rm LTE}$	$M_{\rm vir}$	$M_{\rm vir}/M_{\rm LTE}$	$\bar{n}$
	h	m	s	°	′	″	km s^{-1}	K		pc	km s^{-1}	$M_\odot$	$M_\odot$		10^4 cm^{-3}
A101	5	32	42.7	−5	35	54	6.1	0.8	1.4	0.16	0.63	9.7	13	1.3	1.1
A102	5	32	42.7	−5	55	4	8.0	0.6	1.6	0.12	0.67	5.4	11	2.1	1.3
A103	5	32	42.7	−6	0	33	8.0	1.0	1.3	0.18	0.48	24	8.4	0.4	1.9
A104	5	32	44.1	−5	19	7	9.3	0.7	1.0	0.14	0.57	12	9.6	0.8	1.8
A105	5	32	44.1	−5	20	29	8.0	0.7	1.2	0.16	0.57	7.8	11	1.4	0.79
A106	5	32	44.1	−5	29	23	9.9	0.5	1.4	0.15	0.54	5.7	9.0	1.6	0.76
A107	5	32	44.1	−5	35	13	6.7	0.6	1.1	0.11	0.59	4.4	8.0	1.8	1.3
A108	5	32	44.1	−5	36	14	8.2	1.6	1.2	0.14	0.77	17	17	1.0	2.8
A109	5	32	44.1	−5	57	28	7.6	0.7	1.2	0.11	0.33	5.5	2.6	0.5	1.6
A110	5	32	44.7	−6	17	56	5.9	0.5	2.3	0.13	0.37	4.5	3.8	0.8	0.80
A111	5	32	45.5	−5	23	54	7.8	1.9	1.0	0.19	0.66	45	17	0.4	3.0
A112	5	32	45.5	−5	25	58	6.3	1.8	1.5	0.23	1.64	71	130	1.8	2.4
A113	5	32	45.5	−5	26	18	7.8	0.8	1.5	0.22	0.79	31	28	0.9	1.3
A114	5	32	45.5	−5	28	42	8.4	0.5	1.3	0.18	1.34	16	67	4.1	1.2
A115	5	32	45.5	−6	1	14	8.6	0.4	1.0	0.16	0.32	4.2	3.5	0.8	0.42
A116	5	32	46.9	−4	59	15	11.0	0.4	1.8	0.13	0.51	3.9	7.2	1.8	0.70
A117	5	32	46.9	−5	20	8	10.3	1.7	1.2	0.18	0.51	32	9.7	0.3	2.4
A118	5	32	46.9	−5	20	49	9.8	2.8	1.1	0.22	0.52	73	13	0.2	2.7
A119	5	32	46.9	−5	22	12	8.6	1.4	1.5	0.22	0.68	58	21	0.4	2.5
A120	5	32	46.9	−5	24	56	8.5	1.1	1.7	0.19	0.69	28	19	0.7	1.7
A121	5	32	46.9	−5	25	17	9.7	0.5	1.3	0.14	0.50	7.1	7.3	1.0	1.1
A122	5	32	46.9	−5	25	58	9.4	0.5	1.1	0.14	0.48	5.4	6.7	1.2	0.89
A123	5	32	46.9	−5	29	23	9.3	0.4	1.0	0.16	0.45	7.1	6.7	0.9	0.72
A124	5	32	46.9	−5	55	4	8.0	0.7	1.1	0.12	0.26	4.1	1.6	0.4	1.1
A125	5	32	46.9	−5	59	52	7.2	0.6	1.1	0.14	0.44	5.4	5.9	1.1	0.80

Table A.1 (cont'd)

I.D.	α (B1950)			δ (B1950)			$v_{\rm LSR}$	$T^*_{A,\rm peak}$	Aspect Ratio	$R_{\rm core}$	$dv_{\rm core}$	$M_{\rm LTE}$	$M_{\rm vir}$	$M_{\rm vir}/M_{\rm LTE}$	$\bar{n}$
	h	m	s	°	′	″	km s^{-1}	K		pc	km s^{-1}	$M_\odot$	$M_\odot$		10^4 cm^{-3}
A126	5	32	48.2	−5	14	19	10.3	0.4	1.7	0.15	0.40	4.5	5.0	1.1	0.55
A127	5	32	48.2	−5	14	40	10.8	0.5	2.4	0.11	0.50	5.7	5.6	1.0	1.9
A128	5	32	48.2	−5	16	22	9.9	0.7	1.9	0.10	0.37	4.4	2.8	0.6	1.9
A129	5	32	48.2	−5	17	24	10.3	1.0	1.0	0.14	0.44	8.9	5.5	0.6	1.5
A130	5	32	48.2	−5	18	5	10.4	1.1	1.3	0.11	0.43	7.7	4.5	0.6	2.2
A131	5	32	48.2	−5	23	54	10.3	1.5	1.3	0.14	1.04	24	31	1.3	4.0
A132	5	32	48.2	−6	0	33	7.6	0.7	1.1	0.13	0.31	6.7	2.5	0.4	1.4
A133	5	32	48.9	−6	15	10	6.9	0.5	1.3	0.10	0.22	2.3	1.1	0.5	0.79
A134	5	32	49.6	−5	1	18	10.0	0.4	1.4	0.16	0.44	5.5	6.5	1.2	0.54
A135	5	32	49.6	−5	3	42	10.4	1.1	1.6	0.19	0.46	31	8.5	0.3	2.0
A136	5	32	49.6	−5	11	55	11.2	0.7	1.3	0.13	0.46	8.9	5.9	0.7	1.6
A137	5	32	49.6	−5	17	45	10.8	0.7	1.2	0.13	0.31	4.4	2.6	0.6	0.89
A138	5	32	49.6	−5	22	32	10.2	1.5	1.0	0.20	0.86	46	30	0.7	2.5
A139	5	32	49.6	−5	28	1	10.0	0.6	1.1	0.14	0.78	5.7	17	3.1	0.94
A140	5	32	49.6	−5	32	49	6.4	0.5	1.3	0.15	0.59	7.0	11	1.5	0.89
A141	5	32	49.6	−6	1	55	7.4	0.5	1.1	0.14	0.40	6.0	4.6	0.8	0.92
A142	5	32	51.0	−5	2	40	11.2	2.0	1.0	0.20	0.65	81	17	0.2	4.5
A143	5	32	51.0	−5	6	6	9.9	0.9	1.4	0.14	0.26	5.8	1.9	0.3	0.92
A144	5	32	51.0	−5	6	6	10.3	0.7	1.1	0.20	0.37	18	5.6	0.3	0.99
A145	5	32	51.0	−5	6	47	9.3	0.9	1.1	0.13	0.81	9.1	18	2.0	1.7
A146	5	32	51.0	−5	11	14	11.1	0.7	1.2	0.12	0.48	6.8	5.8	0.9	1.7
A147	5	32	51.0	−5	14	40	11.7	0.4	1.1	0.15	0.52	4.9	8.4	1.7	0.64
A148	5	32	51.0	−5	14	40	10.8	0.8	2.5	0.14	0.49	16	6.9	0.4	2.7
A149	5	32	51.0	−5	17	3	10.7	0.7	1.5	0.11	0.39	7.1	3.3	0.5	2.5
A150	5	32	51.0	−5	20	29	11.2	0.6	1.1	0.14	0.70	7.6	15	1.9	1.1

Table A.1 (cont'd)

I.D.	α (B1950)			δ (B1950)			$v_{\rm LSR}$	$T^*_{A,\rm peak}$	Aspect Ratio	$R_{\rm core}$	$dv_{\rm core}$	$M_{\rm LTE}$	$M_{\rm vir}$	$M_{\rm vir}/M_{\rm LTE}$	$\bar{n}$
	h	m	s	°	′	″	km s^{-1}	K		pc	km s^{-1}	$M_\odot$	$M_\odot$		10^4 cm^{-3}
A151	5	32	52.4	−5	7	7	11.3	1.4	1.2	0.14	0.74	25	16	0.6	3.7
A152	5	32	52.4	−5	20	8	9.1	1.9	1.0	0.22	0.60	45	16	0.3	1.9
A153	5	32	52.4	−6	1	14	7.6	0.6	1.5	0.11	0.49	5.2	5.5	1.1	1.7
A154	5	32	52.4	−6	3	18	6.9	0.4	1.1	0.15	0.56	5.8	10	1.8	0.71
A155	5	32	53.7	−5	5	4	11.2	0.7	1.1	0.16	0.74	16	18	1.1	1.8
A156	5	32	53.7	−5	7	49	11.3	1.5	1.1	0.14	0.63	32	11	0.4	5.2
A157	5	32	53.7	−5	10	12	11.0	1.2	1.1	0.19	0.53	26	11	0.4	1.6
A158	5	32	53.7	−5	12	16	11.5	1.0	1.2	0.15	0.55	17	9.7	0.6	2.2
A159	5	32	53.7	−5	16	43	10.7	0.6	1.1	0.13	0.56	10	8.9	0.9	1.8
A160	5	32	53.7	−5	21	10	8.5	0.5	1.1	0.18	0.52	11	10	0.9	0.82
A161	5	32	53.7	−6	0	33	7.1	0.4	1.5	0.10	0.38	2.2	2.9	1.3	1.0
A162	5	32	53.7	−6	2	16	6.1	0.4	1.8	0.10	0.32	2.4	2.1	0.9	1.1
A163	5	32	55.1	−5	3	21	11.2	1.9	1.4	0.15	0.78	52	19	0.4	6.1
A164	5	32	55.1	−5	6	47	12.0	1.0	1.1	0.20	0.59	22	14	0.7	1.1
A165	5	32	55.1	−5	9	11	11.6	1.4	1.0	0.12	0.71	26	13	0.5	6.0
A166	5	32	55.1	−5	10	54	11.5	0.7	1.2	0.11	0.39	8.9	3.5	0.4	2.6
A167	5	32	55.1	−5	14	40	10.8	0.8	1.7	0.14	0.48	14	6.7	0.5	2.4
A168	5	32	55.1	−6	1	55	7.4	0.4	1.4	0.09	0.35	2.1	2.1	1.0	1.4
A169	5	32	55.8	−6	14	49	5.5	1.1	1.5	0.12	0.41	4.7	4.1	0.9	1.2
A170	5	32	56.5	−5	14	19	10.2	0.8	1.4	0.13	0.51	7.0	7.4	1.1	1.2
A171	5	32	56.5	−5	15	0	10.3	0.7	1.0	0.14	0.47	7.7	6.4	0.8	1.2
A172	5	32	56.5	−5	21	10	7.8	0.4	1.2	0.12	0.39	3.6	3.9	1.1	0.79
A173	5	32	57.9	−5	5	4	11.1	1.5	1.0	0.14	0.54	21	8.8	0.4	3.0
A174	5	32	57.9	−5	10	54	11.6	1.1	1.4	0.14	0.56	17	9.5	0.6	2.6
A175	5	32	57.9	−5	54	3	7.3	0.8	1.1	0.12	0.49	8.9	5.9	0.7	2.4

Table A.1 (cont'd)

I.D.	α (B1950)			δ (B1950)			$v_{\rm LSR}$	$T^*_{A,\rm peak}$	Aspect Ratio	$R_{\rm core}$	$dv_{\rm core}$	$M_{\rm LTE}$	$M_{\rm vir}$	$M_{\rm vir}/M_{\rm LTE}$	$\bar{n}$
	h	m	s	°	′	″	km s^{-1}	K		pc	km s^{-1}	$M_\odot$	$M_\odot$		10^4 cm^{-3}
A176	5	32	57.9	−5	55	4	7.3	0.6	1.0	0.12	0.46	6.5	5.4	0.8	1.5
A177	5	32	57.9	−6	1	14	7.2	0.5	1.2	0.12	0.43	5.0	4.6	0.9	1.2
A178	5	32	59.2	−5	5	45	11.1	1.6	1.0	0.13	0.73	22	14	0.6	4.2
A179	5	32	59.2	−5	7	28	11.5	2.0	1.2	0.16	0.50	43	8.6	0.2	4.3
A180	5	32	59.2	−5	9	52	11.6	0.9	1.6	0.08	0.70	15	8.3	0.5	12
A181	5	32	59.2	−5	13	17	11.2	0.7	1.0	0.15	0.50	14	7.8	0.5	1.8
A182	5	33	0.6	−5	2	40	10.4	0.8	1.1	0.17	0.47	12	7.6	0.6	1.1
A183	5	33	0.6	−5	9	11	11.6	1.0	1.1	0.11	0.64	13	8.9	0.7	4.8
A184	5	33	0.6	−5	11	55	11.2	1.1	1.2	0.14	0.62	21	11	0.5	3.2
A185	5	33	0.6	−5	13	58	10.4	0.9	1.5	0.16	0.40	11	5.4	0.5	1.1
A186	5	33	2.0	−5	0	16	11.6	0.9	1.0	0.16	0.56	14	11	0.8	1.3
A187	5	33	2.0	−5	0	58	12.4	0.9	1.0	0.15	0.72	9.2	16	1.7	1.2
A188	5	33	2.0	−5	1	39	11.7	0.8	1.1	0.19	0.40	17	6.4	0.4	0.99
A189	5	33	2.0	−5	2	20	11.1	0.5	1.9	0.15	0.43	7.9	5.9	0.7	0.90
A190	5	33	2.0	−5	4	44	10.6	0.7	1.1	0.18	0.54	13	11	0.8	0.97
A191	5	33	2.0	−5	12	16	12.1	0.3	1.4	0.11	0.25	2.4	1.4	0.6	0.73
A192	5	33	2.0	−5	55	25	7.7	0.7	1.1	0.18	0.49	17	9.4	0.6	1.2
A193	5	33	2.0	−6	1	14	7.3	0.7	1.5	0.16	0.37	8.2	4.3	0.5	0.91
A194	5	33	2.8	−6	7	13	7.7	0.4	1.3	0.12	0.40	2.7	3.9	1.4	0.73
A195	5	33	3.4	−5	6	26	11.0	0.9	1.2	0.15	0.61	14	11	0.8	1.9
A196	5	33	3.4	−5	11	55	11.1	0.8	1.4	0.16	0.57	13	11	0.8	1.4
A197	5	33	3.4	−5	54	23	7.3	0.8	1.1	0.15	0.38	5.7	4.3	0.8	0.77
A198	5	33	4.7	−5	8	9	11.7	1.2	1.7	0.17	0.53	22	10	0.5	1.7
A199	5	33	4.8	−6	3	59	7.2	0.6	1.2	0.10	0.43	3.9	3.8	1.0	1.9
A200	5	33	6.1	−5	1	59	11.3	0.6	1.2	0.16	0.51	7.5	8.8	1.2	0.78

Table A.1 (cont'd)

I.D.	α (B1950)			δ (B1950)			$v_{\rm LSR}$	$T^*_{A,\rm peak}$	Aspect Ratio	$R_{\rm core}$	$dv_{\rm core}$	$M_{\rm LTE}$	$M_{\rm vir}$	$M_{\rm vir}/M_{\rm LTE}$	$\bar{n}$
	h	m	s	°	′	″	km s^{-1}	K		pc	km s^{-1}	$M_\odot$	$M_\odot$		10^4 cm^{-3}
A201	5	33	6.1	−5	8	50	12.4	1.3	1.6	0.18	0.54	15	11	0.7	1.2
A202	5	33	6.1	−5	12	16	10.8	0.9	1.1	0.18	0.45	11	7.4	0.7	0.82
A203	5	33	8.9	−5	12	57	10.4	0.4	2.4	0.12	0.37	2.4	3.2	1.3	0.68
A204	5	33	9.7	−6	7	55	7.8	0.6	2.1	0.11	0.43	3.8	4.0	1.1	1.4
A205	5	33	11.6	−5	14	40	9.3	0.5	1.6	0.14	0.52	4.5	8.1	1.8	0.69
A206	5	33	12.5	−6	30	1	8.9	0.6	1.1	0.15	0.39	7.3	4.7	0.6	0.94
A207	5	33	13.0	−5	4	44	11.7	0.5	1.2	0.16	0.70	9.0	17	1.8	0.86
A208	5	33	13.0	−6	1	35	9.0	0.5	1.3	0.16	0.69	5.4	16	2.9	0.56
A209	5	33	13.9	−6	7	55	6.4	0.5	1.6	0.17	0.69	6.1	16	2.7	0.57
A210	5	33	15.7	−5	9	31	12.0	0.4	1.4	0.13	0.38	3.1	3.9	1.2	0.58
A211	5	33	25.0	−6	12	3	8.1	0.5	1.7	0.11	0.72	4.3	12	2.7	1.4
A212	5	33	25.1	−6	30	1	8.6	0.6	1.5	0.19	0.60	7.9	14	1.8	0.48
A213	5	33	43.1	−6	12	24	8.4	0.7	1.7	0.06	0.19	2.1	0.47	0.2	3.4
A214	5	33	43.1	−6	12	24	8.1	0.6	1.5	0.08	0.33	2.4	1.8	0.8	1.9
A215	5	33	45.9	−6	12	45	8.2	0.6	1.1	0.08	0.29	2.6	1.4	0.5	2.5
A216	5	33	50.1	−6	13	47	8.2	0.4	1.0	0.10	0.36	2.9	2.7	0.9	1.1
A217	5	33	50.1	−6	25	53	6.9	0.5	1.5	0.19	0.67	9.8	18	1.8	0.61
A218	5	33	51.5	−6	24	30	6.5	0.4	1.4	0.14	0.45	5.5	5.9	1.1	0.81
A219	5	33	51.5	−6	25	11	6.8	0.5	1.7	0.11	0.32	2.9	2.4	0.9	0.86
A220	5	33	52.9	−6	24	9	7.1	0.8	1.6	0.13	0.44	9.7	5.2	0.5	1.9
A221	5	33	54.2	−6	14	49	8.7	0.6	1.2	0.12	0.41	6.0	4.0	0.7	1.7
A222	5	33	55.6	−6	14	29	8.2	0.6	1.2	0.11	0.46	4.9	5.0	1.0	1.5
A223	5	33	55.6	−6	23	48	7.6	0.6	1.2	0.16	0.70	11	17	1.5	1.1
A224	5	33	57.0	−6	25	11	6.0	0.6	1.1	0.15	0.55	6.3	9.8	1.6	0.73
A225	5	33	58.4	−6	16	12	8.4	0.7	1.2	0.12	0.51	8.2	6.4	0.8	2.2

Table A.1 (cont'd)

I.D.	α (B1950)			δ (B1950)			$v_{\rm LSR}$	$T^*_{A,\rm peak}$	Aspect Ratio	$R_{\rm core}$	$dv_{\rm core}$	$M_{\rm LTE}$	$M_{\rm vir}$	$M_{\rm vir}/M_{\rm LTE}$	$\bar{n}$
	h	m	s	°	′	″	km s^{-1}	K		pc	km s^{-1}	$M_\odot$	$M_\odot$		10^4 cm^{-3}
A226	5	33	58.4	−6	24	30	7.2	1.1	1.8	0.17	0.48	14	8.1	0.6	1.3
A227	5	33	58.4	−6	26	55	6.4	1.0	1.8	0.19	0.61	23	15	0.7	1.4
A228	5	34	2.6	−6	16	54	8.6	0.5	1.3	0.11	0.50	3.9	5.8	1.5	1.3
A229	5	34	6.8	−6	28	18	7.1	0.7	1.1	0.22	0.76	26	26	1.0	1.1
A230	5	34	9.6	−6	27	57	6.0	0.4	1.1	0.20	0.66	9.4	19	2.0	0.46
A231	5	34	10.9	−6	15	10	8.4	0.4	2.1	0.12	0.64	4.1	10	2.4	1.0
A232	5	34	13.7	−6	27	57	6.5	0.7	1.1	0.19	0.63	21	16	0.7	1.3
A233	5	34	17.9	−6	28	59	6.8	0.4	1.2	0.12	0.52	3.7	6.9	1.9	0.92
A234	5	34	22.1	−6	29	41	6.1	0.4	1.0	0.15	0.48	5.4	7.3	1.4	0.64
A235	5	34	23.5	−6	30	22	6.5	0.7	1.2	0.12	0.38	5.4	3.6	0.7	1.4
A236	5	34	24.9	−6	31	45	6.1	0.8	1.4	0.11	0.40	5.5	3.7	0.7	1.6

Table A.2. Physical properties of the $H^{13}CO^+$ cores in the Orion B cloud

I.D.	α (B1950)			δ (B1950)			v_{LSR}	$T^*_{A,peak}$	Aspect Ratio	R_{core}	dv_{core}	M_{LTE}	M_{vir}	M_{vir}/M_{LTE}	$\bar{n}$
	h	m	s	°	′	″	km s^{-1}	K		pc	km s^{-1}	$M_\odot$	$M_\odot$		10^4 cm^{-3}
B1	5	38	35.6	−2	28	36	10.3	0.7	1.4	0.09	0.41	2.4	3.3	1.4	1.3
B2	5	38	40.5	−1	49	9	8.9	1.0	1.9	0.19	0.62	16	15	1.0	0.97
B3	5	38	50.7	−1	44	12	8.3	1.0	1.2	0.09	0.44	4.4	3.6	0.8	2.6
B4	5	38	53.1	−2	18	6	9.8	0.9	1.1	0.13	0.50	7.4	6.7	0.9	1.5
B5	5	38	53.7	−2	18	33	9.3	1.0	1.1	0.11	0.65	7.3	9.4	1.3	2.6
B6	5	38	54.3	−2	20	39	10.2	1.2	1.6	0.11	0.54	8.2	6.5	0.8	2.8
B7	5	38	54.3	−2	17	21	9.4	1.1	1.0	0.15	0.71	12	16	1.3	1.7
B8	5	38	54.3	−1	46	18	8.6	0.8	1.2	0.06	0.20	1.4	0.52	0.4	2.6
B9	5	38	55.5	−2	19	45	9.5	1.1	1.1	0.10	0.52	8.9	5.7	0.6	3.8
B10	5	38	56.1	−2	19	36	10.6	0.7	2.2	0.10	0.46	3.5	4.5	1.3	1.4
B11	5	38	56.7	−2	18	24	9.2	0.9	1.6	0.09	0.53	5.3	5.0	1.0	3.5
B12	5	38	57.3	−2	22	18	9.3	1.0	1.2	0.11	0.41	6.2	3.8	0.6	2.1
B13	5	38	57.3	−2	20	57	9.1	0.6	1.3	0.09	0.47	2.7	4.4	1.7	1.3
B14	5	38	57.9	−2	21	33	8.9	0.9	1.1	0.10	0.50	4.1	5.1	1.2	1.9
B15	5	38	57.9	−2	21	24	9.7	0.9	1.3	0.10	0.37	5.6	2.8	0.5	2.7
B16	5	38	58.5	−2	23	21	9.7	0.7	2.0	0.10	0.76	4.3	12	2.8	1.9
B17	5	38	58.5	−2	22	18	9.9	1.0	1.2	0.10	0.65	7.6	8.8	1.2	3.3
B18	5	38	58.5	−2	20	39	9.4	0.6	1.3	0.08	0.45	2.9	3.3	1.1	2.5
B19	5	38	58.5	−2	19	9	9.5	0.6	1.6	0.10	0.76	4.9	12	2.4	2.3
B20	5	38	59.1	−2	25	18	11.3	0.9	1.1	0.11	0.29	5.7	1.9	0.3	1.8
B21	5	39	0.3	−2	20	39	10.2	0.8	1.9	0.10	0.41	4.4	3.5	0.8	1.9
B22	5	39	2.1	−2	19	18	9.7	0.9	1.4	0.13	0.84	15	19	1.2	3.1
B23	5	39	4.5	−2	22	36	11.1	0.7	1.4	0.11	0.47	4.7	5.0	1.1	1.5
B24	5	39	6.9	−1	37	45	10.0	1.0	1.2	0.08	0.45	5.7	3.5	0.6	4.0
B25	5	39	8.1	−1	54	6	9.7	0.9	2.0	0.09	0.40	3.8	3.1	0.8	2.0

Table A.2 (cont'd)

I.D.	α (B1950)			δ (B1950)			$v_{\rm LSR}$	$T^*_{A,\rm peak}$	Aspect Ratio	$R_{\rm core}$	$dv_{\rm core}$	$M_{\rm LTE}$	$M_{\rm vir}$	$M_{\rm vir}/M_{\rm LTE}$	$\bar{n}$
	h	m	s	°	′	″	km s^{-1}	K		pc	km s^{-1}	$M_\odot$	$M_\odot$		10^4 cm^{-3}
B26	5	39	8.1	−1	36	51	10.0	1.0	3.1	0.13	0.45	9.8	5.3	0.5	2.0
B27	5	39	9.3	−2	18	42	10.1	2.0	1.3	0.20	0.66	52	18	0.4	2.7
B28	5	39	9.9	−2	17	39	9.5	0.6	1.7	0.14	0.74	7.3	16	2.2	1.1
B29	5	39	11.1	−1	55	36	10.3	1.4	1.2	0.13	0.75	26	16	0.6	4.6
B30	5	39	11.1	−1	54	24	9.5	1.3	1.7	0.15	0.53	19	8.5	0.5	2.5
B31	5	39	13.5	−1	58	27	10.6	1.4	1.7	0.13	0.54	22	7.9	0.4	4.3
B32	5	39	13.5	−1	57	24	10.3	1.0	1.5	0.13	0.47	10	5.8	0.6	2.2
B33	5	39	13.5	−1	57	15	11.0	1.2	1.3	0.11	0.61	18	8.3	0.5	6.3
B34	5	39	18.3	−2	1	9	11.3	1.5	1.2	0.11	0.49	12	5.3	0.5	4.3
B35	5	39	18.3	−1	59	48	11.5	2.1	1.4	0.13	0.62	28	10	0.4	5.9
B36	5	39	21.3	−2	1	36	11.4	1.6	1.4	0.10	0.52	9.3	5.8	0.6	3.5
B37	5	39	25.5	−2	2	30	11.4	1.2	1.2	0.09	0.40	4.5	3.1	0.7	2.3
B38	5	39	30.9	−2	8	57	12.1	0.9	1.2	0.08	0.58	4.1	5.7	1.4	3.1
B39	5	39	32.7	−2	3	42	10.9	1.4	1.5	0.16	0.40	12	5.2	0.4	1.4
B40	5	39	32.7	−2	3	15	11.3	1.2	1.1	0.10	0.51	5.9	5.5	0.9	2.5
B41	5	39	36.3	−1	54	33	11.9	0.7	1.5	0.07	0.53	1.6	4.2	2.7	1.9
B42	5	39	56.7	−1	23	21	9.9	0.9	1.5	0.11	0.46	4.6	4.6	1.0	1.6
B43	5	39	57.3	−1	21	51	9.1	1.0	1.6	0.09	0.42	4.2	3.2	0.8	2.6
B44	5	39	57.3	−1	20	39	8.8	0.7	1.3	0.09	0.35	2.1	2.2	1.0	1.5
B45	5	39	59.7	−1	23	48	9.7	0.9	2.1	0.07	0.31	2.3	1.3	0.6	3.2
B46	5	40	0.3	−1	22	27	9.4	1.0	1.2	0.09	0.47	5.1	4.1	0.8	2.8
B47	5	40	0.9	−1	27	6	9.9	0.8	1.2	0.08	0.31	2.6	1.6	0.6	2.3
B48	5	40	12.3	−1	17	30	8.5	0.9	1.3	0.13	0.25	5.6	1.7	0.3	1.1
B49	5	40	13.5	−1	17	57	8.7	0.7	1.7	0.11	0.27	3.3	1.8	0.5	0.97
B50	5	40	29.7	−1	17	48	9.3	0.9	1.4	0.17	0.47	7.5	7.7	1.0	0.68

Table A.2 (cont'd)

I.D.	α (B1950)			δ (B1950)			$v_{\rm LSR}$	$T^*_{A,\rm peak}$	Aspect Ratio	$R_{\rm core}$	$dv_{\rm core}$	$M_{\rm LTE}$	$M_{\rm vir}$	$M_{\rm vir}/M_{\rm LTE}$	$\bar{n}$
	h	m	s	°	′	″	km s^{-1}	K		pc	km s^{-1}	$M_\odot$	$M_\odot$		10^4 cm^{-3}
B51	5	40	34.5	−1	15	60	9.1	0.7	1.5	0.09	0.17	2.2	0.57	0.3	1.2
B52	5	40	36.9	−1	20	39	9.4	0.9	2.0	0.15	0.36	11	4.0	0.4	1.3
B53	5	40	44.7	−1	20	12	9.5	0.8	2.6	0.11	0.27	4.9	1.8	0.4	1.4
B54	5	43	29.6	−0	13	1	10.2	0.7	1.2	0.11	0.48	5.7	5.4	1.0	1.6
B55	5	43	31.4	−0	15	25	10.5	1.0	1.1	0.12	0.41	5.8	4.0	0.7	1.6
B56	5	43	33.2	−0	12	16	10.4	1.0	1.4	0.10	0.38	4.9	3.0	0.6	2.1
B57	5	43	33.2	−0	11	13	10.1	1.2	1.2	0.12	0.54	13	7.4	0.6	2.9
B58	5	43	33.8	−0	15	7	10.1	0.6	1.1	0.12	0.47	5.6	5.7	1.0	1.3
B59	5	43	33.8	−0	13	1	10.3	1.0	1.4	0.08	0.57	6.3	5.2	0.8	5.7
B60	5	43	34.4	−0	13	37	10.5	0.9	1.4	0.12	0.51	8.2	6.6	0.8	2.1
B61	5	43	35.6	−0	11	49	9.8	0.9	1.1	0.11	0.49	6.1	5.6	0.9	1.9
B62	5	43	36.8	−0	13	28	10.2	1.1	1.2	0.12	0.62	11	9.7	0.9	2.5
B63	5	43	37.4	−0	9	34	10.1	0.7	1.3	0.13	0.60	5.8	9.5	1.7	1.2
B64	5	43	39.8	−0	6	34	9.4	1.1	1.2	0.08	0.47	4.7	3.6	0.8	4.6
B65	5	43	40.4	−0	11	4	10.4	1.0	1.4	0.12	0.47	8.3	5.7	0.7	1.9
B66	5	43	42.8	−0	12	34	10.3	0.7	1.2	0.11	0.48	5.7	5.3	0.9	1.8
B67	5	43	47.6	−0	1	19	9.9	0.6	2.1	0.07	0.39	2.1	2.3	1.1	2.3
B68	5	43	50.0	−0	14	31	10.8	0.9	1.6	0.10	0.37	2.9	2.6	0.9	1.5
B69	5	43	53.6	−0	3	7	10.8	0.9	1.8	0.09	0.43	5.1	3.3	0.7	3.2
B70	5	43	53.6	−0	2	40	10.9	1.0	1.2	0.10	0.51	7.5	5.2	0.7	3.4
B71	5	43	54.8	0	25	32	8.6	0.7	1.1	0.10	0.40	3.3	3.2	1.0	1.6
B72	5	43	59.0	0	26	17	9.2	0.8	1.9	0.15	0.53	13	8.7	0.7	1.6
B73	5	44	6.2	−0	0	34	10.5	1.5	1.2	0.11	0.55	15	6.8	0.4	4.9
B74	5	44	11.0	0	6	20	10.7	1.3	1.1	0.12	0.53	14	7.1	0.5	3.4
B75	5	44	11.6	−0	0	43	10.7	1.4	1.3	0.12	0.50	17	6.2	0.4	4.5

Table A.2 (cont'd)

I.D.	α (B1950)			δ (B1950)			$v_{\rm LSR}$	$T^*_{A,\rm peak}$	Aspect Ratio	$R_{\rm core}$	$dv_{\rm core}$	$M_{\rm LTE}$	$M_{\rm vir}$	$M_{\rm vir}/M_{\rm LTE}$	$\bar{n}$
	h	m	s	°	′	″	km s^{-1}	K		pc	km s^{-1}	$M_\odot$	$M_\odot$		10^4 cm^{-3}
B76	5	44	11.6	0	24	11	9.1	0.6	1.9	0.17	0.66	11	15	1.5	0.89
B77	5	44	15.8	0	0	47	11.0	1.9	2.0	0.11	0.43	20	4.1	0.2	7.0
B78	5	44	17.0	0	0	2	11.0	1.9	1.2	0.16	0.43	31	6.3	0.2	3.1
B79	5	44	19.4	0	23	26	10.3	0.8	1.3	0.10	0.62	3.8	8.3	2.2	1.5
B80	5	44	20.6	0	22	14	9.4	1.3	1.7	0.12	0.58	14	8.5	0.6	3.1
B81	5	44	22.4	0	22	32	9.3	1.4	1.3	0.08	0.58	7.6	5.7	0.8	6.0
B82	5	44	23.0	0	23	17	9.7	0.9	2.5	0.12	0.39	7.9	3.9	0.5	1.9
B83	5	44	24.2	0	22	5	9.3	0.9	2.3	0.11	0.64	12	9.1	0.8	4.0
B84	5	44	26.0	0	20	53	8.8	0.7	1.3	0.09	0.47	3.6	4.3	1.2	1.9
B85	5	44	27.8	0	16	50	9.7	1.3	1.2	0.14	0.49	13	6.9	0.5	2.2
B86	5	44	28.4	0	24	47	9.7	0.8	1.8	0.08	0.57	2.7	5.7	2.1	2.0
B87	5	44	29.0	0	21	20	9.3	1.6	1.2	0.14	0.76	26	17	0.7	3.8
B88	5	44	30.2	0	19	32	9.7	1.6	2.1	0.12	0.55	17	7.6	0.4	4.2
B89	5	44	30.8	0	20	8	9.5	1.9	1.2	0.11	0.62	19	8.8	0.5	6.2
B90	5	44	33.8	0	23	8	9.5	0.7	1.9	0.12	0.51	4.6	6.5	1.4	1.2
B91	5	44	36.8	0	19	59	9.7	0.7	1.6	0.09	0.52	4.0	5.3	1.3	2.0
B92	5	44	38.0	0	21	56	9.3	1.3	1.2	0.15	0.76	24	18	0.8	3.0
B93	5	44	42.8	0	20	26	9.4	0.7	1.7	0.10	0.72	5.4	11	2.0	2.4
B94	5	44	45.2	0	21	20	9.7	1.0	1.8	0.11	0.44	7.7	4.4	0.6	2.4
B95	5	44	52.4	0	19	50	9.5	0.9	1.4	0.07	0.38	3.4	2.1	0.6	4.2
B96	5	44	56.6	0	19	41	9.2	0.8	1.0	0.08	0.36	2.6	2.2	0.8	2.2
B97	5	45	7.4	0	36	38	8.7	0.7	1.7	0.09	0.27	3.7	1.4	0.4	1.9
B98	5	45	11.0	0	37	41	9.1	0.9	1.2	0.12	0.54	7.4	7.3	1.0	1.8

Table A.3. Physical properties of the $H^{13}CO^+$ cores in the Cepheus OB3

I.D.	α (B1950)			δ (B1950)			v_{LSR}	$T^*_{A,peak}$	Aspect Ratio	R_{core}	dv_{core}	M_{LTE}	M_{vir}	M_{vir}/M_{LTE}	$\bar{n}$
	h	m	s	°	′	″	km s^{-1}	K		pc	km s^{-1}	$M_\odot$	$M_\odot$		10^4 cm^{-3}
C1	22	44	48.6	61	52	42	−9.8	0.6	1.7	0.15	0.61	8.5	12	1.4	1.0
C2	22	44	54.7	61	53	18	−10.2	0.7	1.3	0.12	0.51	8.8	6.4	0.7	2.3
C3	22	45	13.9	61	45	3	−10.3	0.8	1.7	0.19	0.46	18	8.3	0.5	1.1
C4	22	45	16.2	61	45	57	−10.5	0.8	1.9	0.19	0.49	19	9.6	0.5	1.2
C5	22	45	18.3	61	47	9	−11.0	0.5	1.3	0.17	0.77	11	21	2.0	0.98
C6	22	51	23.8	62	2	39	−7.8	0.6	1.6	0.20	0.48	10	9.5	1.0	0.53
C7	22	51	26.6	62	1	18	−8.6	0.6	2.7	0.19	0.51	7.2	10	1.4	0.43
C8	22	51	26.5	62	1	36	−8.2	0.5	2.1	0.17	0.63	9.3	14	1.5	0.82
C9	22	53	52.9	61	46	9	−9.8	1.0	1.5	0.21	0.66	23	19	0.8	1.1
C10	22	54	17.0	61	45	24	−9.3	1.3	1.1	0.23	0.74	47	26	0.6	1.7
C11	22	54	17.0	61	45	33	−9.7	1.3	1.2	0.20	0.68	53	19	0.4	3.0
C12	22	54	17.0	61	46	27	−9.3	1.0	1.7	0.23	0.81	35	32	0.9	1.2
C13	22	54	19.6	61	43	36	−10.3	0.6	1.4	0.20	0.82	12	27	2.3	0.66
C14	22	54	19.5	61	46	27	−10.1	1.3	1.5	0.24	0.83	98	34	0.3	3.1
C15	22	54	24.6	61	46	9	−11.8	1.8	1.7	0.27	1.11	162	69	0.4	3.5
C16	22	54	31.0	61	46	45	−12.7	0.5	1.3	0.18	0.70	13	19	1.4	0.93
C17	22	54	30.9	61	46	54	−10.4	0.5	1.9	0.19	0.81	16	26	1.6	1.0
C18	22	54	34.8	61	46	18	−10.4	0.8	1.3	0.19	0.70	25	19	0.8	1.7
C19	23	1	8.8	61	26	27	−11.0	0.6	1.3	0.10	0.51	4.5	5.2	1.2	2.1
C20	23	3	41.3	62	14	3	−9.3	0.8	1.6	0.18	0.43	12	6.9	0.6	0.89
C21	23	3	44.1	62	14	39	−9.7	0.9	2.5	0.20	0.49	20	10	0.5	0.98
C22	23	3	47.6	62	13	18	−9.9	0.6	1.8	0.18	0.57	6.7	12	1.8	0.49
C23	23	4	0.2	62	16	54	−9.4	0.8	1.4	0.17	0.43	8.5	6.7	0.8	0.67
C24	23	4	0.3	62	17	12	−9.7	1.0	1.3	0.25	0.55	16	15	0.9	0.47
C25	23	4	7.3	62	14	39	−10.2	0.6	2.1	0.23	0.60	15	17	1.1	0.55

Table A.3 (cont'd)

I.D.	α (B1950)			δ (B1950)			$v_{\rm LSR}$	$T^*_{A,\rm peak}$	Aspect Ratio	$R_{\rm core}$	$dv_{\rm core}$	$M_{\rm LTE}$	$M_{\rm vir}$	$M_{\rm vir}/M_{\rm LTE}$	$\bar{n}$
	h	m	s	°	′	″	km s^{-1}	K		pc	km s^{-1}	$M_\odot$	$M_\odot$		10^4 cm^{-3}
C26	23	4	29.4	62	15	15	−9.1	0.8	1.2	0.14	0.55	6.5	8.6	1.3	1.0
C27	23	4	29.5	62	15	42	−9.3	0.8	1.2	0.12	0.35	6.8	3.1	0.5	1.6
C28	23	4	36.3	62	16	45	−10.2	0.8	1.3	0.15	0.38	5.5	4.6	0.8	0.67
C29	23	4	37.5	62	16	36	−9.9	0.8	2.1	0.14	0.46	6.3	6.0	1.0	0.99
C30	23	5	55.8	62	11	57	−9.6	0.8	2.1	0.17	0.56	9.8	11	1.2	0.78
C31	23	6	12.2	62	10	54	−9.7	0.7	1.4	0.11	0.39	3.8	3.6	0.9	1.2